②

AFOSR-TR- 89-0275

AN EXPERIMENTAL STUDY OF THE EFFECT
OF STREAMWISE VORTICES ON UNSTEADY
TURBULENT BOUNDARY-LAYER SEPARATION

By

W. W. Humphreys and W. C. Reynolds

Approved for public release;
distribution unlimited.

Report No. TF-42

Thermosciences Division
Department of Mechanical Engineering
Stanford University
Stanford, California 94305

December 1988

AD-A205 462

DTIC
SELECTED
8 MAR 1989
E

REPORT DOCUMENTATION PAGE		Form Approved OMB No. 0704-0188

1a. REPORT SECURITY CLASSIFICATION Unclassified	1b. RESTRICTIVE MARKINGS

2a. SECURITY CLASSIFICATION AUTHORITY	3. DISTRIBUTION / AVAILABILITY OF REPORT Approved for public release. Distribution is unlimited.
2b. DECLASSIFICATION / DOWNGRADING SCHEDULE	

4. PERFORMING ORGANIZATION REPORT NUMBER(S) TF-42	5. MONITORING ORGANIZATION REPORT NUMBER(S) **AFOSR · TR ·** 8 9 - 0 2 7 5

6a. NAME OF PERFORMING ORGANIZATION Stanford University	6b. OFFICE SYMBOL (If applicable)	7a. NAME OF MONITORING ORGANIZATION AFOSR

6c. ADDRESS (City, State, and ZIP Code) Stanford, CA 94305	7b. ADDRESS (City, State, and ZIP Code) Building 410 Bolling Air Force Base, DC 20332-6448

8a. NAME OF FUNDING / SPONSORING ORGANIZATION AFOSR/NA	8b. OFFICE SYMBOL (If applicable) NA	9. PROCUREMENT INSTRUMENT IDENTIFICATION NUMBER F 4962-86-K0020

8c. ADDRESS (City, State, and ZIP Code) Building 410 Bolling Air Force Base, DC 20332-6148	10. SOURCE OF FUNDING NUMBERS			
	PROGRAM ELEMENT NO 61103D	PROJECT NO. 3484	TASK NO A1	WORK UNIT ACCESSION NO.

11. TITLE (Include Security Classification)
An Experimental Study of the Effect of Streamwise Vortices on Unsteady Turbulent Boundary-Layer Separation

12. PERSONAL AUTHOR(S)
W. W. Humphreys and W. C. Reynolds

13a. TYPE OF REPORT Technical	13b. TIME COVERED FROM 9 Dec '88	14. DATE OF REPORT (Year, Month, Day) 1988, December 9	15. PAGE COUNT 272

16. SUPPLEMENTARY NOTATION

17.	COSATI CODES		18. SUBJECT TERMS (Continue on reverse if necessary and identify by block number)
FIELD	GROUP	SUB-GROUP	Flow control, unsteady turbulent boundary layers, Aircraft, vortex generators. JETS

19. ABSTRACT (Continue on reverse if necessary and identify by block number)

This experiment studied the effect of streamwise vortices on unsteady turbulent boundary-layer separation. The objectives were to document the flow field, to characterize the time response of the boundary layer, and to understand the actual mechanisms by which the streamwise vortices modify boundary-layer behavior. A new configuration for non-obtrusive three-component Laser Doppler Anemometry (LDA) determined the phase averaged velocity and Reynolds stress components, in an unsteady water tunnel, at a momentum thickness Reynolds number of 1840. The streamwise vortices were created by three pairs of half-delta wing vortex generators, while the boundary-layer separation was controlled through impulsively initiated opposite-wall suction, which created a strong adverse pressure gradient.

The time response of the freestream velocity demonstrates that convection is the primary mechanism by which vortex generators modify the response of the boundary layer. There is an initial fast response throughout the boundary layer which is unaffected by the presence of vortex generators, followed by a slow or convective response, the magnitude of which is substantially modified by the presence of the vortex generators. In addition, an examination of the transport of spanwise and streamwise vorticity, transport of momentum, and production of turbulent kinetic energy provide new insights which may be helpful to persons attempting to model this very complex unsteady turbulent flow.

20. DISTRIBUTION / AVAILABILITY OF ABSTRACT ☑ UNCLASSIFIED/UNLIMITED ☐ SAME AS RPT ☐ DTIC USERS	21. ABSTRACT SECURITY CLASSIFICATION Unclassified
22a. NAME OF RESPONSIBLE INDIVIDUAL James M. McMichael	22b. TELEPHONE (Include Area Code) (202) 767-4936	22c. OFFICE SYMBOL AFOSR/NA

DD Form 1473, JUN 86   Previous editions are obsolete.

AN EXPERIMENTAL STUDY OF THE EFFECT
OF STREAMWISE VORTICES ON UNSTEADY
TURBULENT BOUNDARY-LAYER SEPARATION

By

W. W. Humphreys and W. C. Reynolds

Report TF-42

Thermoscience Division

Department of Mechanical Engineering

Stanford University

Stanford, California 94305

December 1988

ii
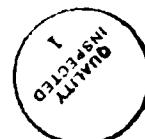
Abstract

This experiment studied the effect of streamwise vortices on unsteady turbulent boundary-layer separation. The objectives were to document the flow field, to characterize the time response of the boundary layer, and to understand the actual mechanisms by which the streamwise vortices modify boundary-layer behavior.

A new configuration for non-obtrusive three-component Laser Doppler Anemometry (LDA) determined the phase averaged velocity and Reynolds stress components, in an unsteady water tunnel, at a momentum thickness Reynolds number of 1840. The streamwise vortices were created by three pairs of half-delta wing vortex generators, while the boundary-layer separation was controlled through impulsively initiated opposite-wall suction, which created a strong adverse pressure gradient.

The time response of the freestream velocity demonstrates that convection is the primary mechanism by which vortex generators modify the response of the boundary layer. Modeling the response with two time scales proved to be a useful technique. There is an initial fast response throughout the boundary layer which is unaffected by the presence of vortex generators, followed by a slow or convective response, the magnitude of which *is* substantially modified by the presence of the vortex generators.

In the presence of an adverse pressure gradient, the strength of the embedded vortex decreased subtantially after several convective time periods. In addition, the spanwise gradient of $\langle u \rangle$ appeared to produce streamwise vorticity of the opposite sign by straining the spanwise vorticity of the boundary layer. All the significant transport of spanwise vorticity appeared to occur in the viscous region of the boundary layer. While the regions of turbulent kinetic energy production were modified by the presence of streamwise vorticity, this did not appear to be a dominant mechanism in the interaction between the streamwise vorticity and the separating boundary layer. These new insights may be helpful to persons attempting to model this very complex unsteady turbulent flow.

Acknowledgements

Table of Contents

List of Tables

List of Figures

Nomenclature

English Letter Symbols

A_∞	amplitude of freestream disturbance (see equation 8.8)
C_f	skin friction coefficient
d	'within pair' vortex generator spacing, cm
D	'between pairs' vortex generator spacing, cm
h	vortex generator height, cm
f	frequency, Hz
H	shape factor (see equation 8.5)
II, III	invariants of the anisotropy tensor (see equation 8.22)
k	turbulent kinetic energy per unit mass, J/kg (see equation 8.20)
ℓ, l	streamwise distance from start of velocity gradient, cm
ℓ_s, ℓ_s^*	Stokes thickness, cm (see equations 3.1 & 3.2)
l_{vg}	vortex generator blade length, cm
p	pressure, N/m^2
q^2	$q^2 = u_i u_i = 2k$, J/kg (see equation 8.20)
Re_x	Reynolds number, $U_0 x/\nu$
Re_θ	momentum thickness Reynolds number, $U_0 \theta/\nu$
S_x	Strouhal number, $\Omega x/U_0$
t	time, sec
u_i	general velocity component in the x_i direction, m/sec
u_τ	friction velocity, $u_\tau = \sqrt{\tau_w/\rho}$, m/sec
u	velocity component in the x direction, m/sec
v	velocity component in the y direction, m/sec
w	velocity component in the z direction, m/sec
x_i	cartesian coordinate direction specified by index i
x	cartesian coordinate direction specified by $i = 1$

y	cartesian coordinate direction specified by $i = 2$
z	cartesian coordinate direction specified by $i = 3$

Greek Letter Symbols

α	angle of attack of vortex generators
Γ	circulation, $\Gamma = -\int \omega \cdot dA$, m^2/sec
δ	boundary-layer thickness, cm
δ^*	displacement thickness, cm (see equation 8.3)
δ_{ij}	isotropic tensor (see equation 2.5)
ϵ_{ijk}	isotropic tensor (see equation 2.6)
θ	momentum thickness, cm (see equation 8.4)
ν	kinematic viscosity, m^2/sec
Π	Coles wake parameter (see equation 5.1)
ρ	density, kg/m^3
τ_w	wall shear stress, N/m^2
Φ	dimensionless velocity change (see equation 8.8)
$\underline{\omega}_x$	vorticity vector, sec^{-1}
ω_i	i^{th} component of vorticity, $\omega_i = \epsilon_{ijk} u_{k,j}$, sec^{-1}
ω_x	vorticity component in the x direction, sec^{-1}
ω_y	vorticity component in the y direction, sec^{-1}
ω_z	vorticity component in the z direction, sec^{-1}
Ω	frequency of oscillation, rad/sec

Other symbols

$\overline{qqq}$	time-averaged quantity
$\langle qqq \rangle$	phase-averaged quantity (see equation 2.2)
$\widetilde{qqq}$	deterministic quantity (see equation 2.3)
q_0	conditions at time, $t = 0$

q_∞	conditions in the freestream
u^+	velocity in wall-coordinate system, $u^+ = u/u_\tau$
y^+	position in wall-coordinate system, $y^+ = yu_\tau/\nu$
$\dot{q}$	time derivative of q
$q_{,x}$	x derivative of q
q'	fluctuating component of q

1. Introduction

1.1 Background

The purpose of this program was to understand the effect of vortex generators on an unsteady, separating, turbulent boundary layer. Vortex generators have been in use on aircraft since the mid-1940's and it is well established that they help delay flow separation. Recently, a number of researchers have studied vortex generators in steady flow to understand the nature of vorticity transport and the changes in the turbulence structure resulting from streamwise vorticity embedded in the boundary layer. While steady flow is the logical first step in understanding the effects of vortex generators, much of the interest in these flow control devices relates to applications in unsteady flow regimes, such as supermaneuverable aircraft. The next logical step, then, is to understand the differences between how vortex generators behave in steady flow and how they behave in unsteady flow. This program was intended to be a first step in that direction.

While vortex generators are presently used primarily as *passive* control devices, future applications may require their use as *active* control devices. During the design of an active control system, engineers need to know the *step response* of the various components of the system. In this program, the portion of the system that is to be controlled is the boundary-layer on a flat surface, and the disturbance to the system is a step change from zero to adverse pressure gradient. The response to this disturbance must be known for the system both with and without vortex generators. The results from this program provide this basic step response information as well as some insight into the mechanisms by which vortex generators modify the nature of an unsteady, separating, turbulent boundary layer.

All the data for this program were obtained in a computer-controlled, unsteady water tunnel, using a compact three-component Laser Doppler Anemometry (LDA)

1

system developed to meet the constraints of this facility. An array of six vortex generators generated streamwise vortices in a steady region of the flow. As these vortices convected downstream, an adverse pressure gradient was impulsively started. Phase-averages of the three-component LDA measurements documented the development of the mean velocities and all six of the normal and shear Reynolds stresses.

1.2 Program Objectives

The specific objectives of this program were as follows:

(1) Describe how vortex generators change the nature of the step response of the boundary layer to an unsteady adverse pressure gradient.

(2) Understand the mechanisms by which streamwise vortices modify the behavior of a boundary layer subjected to an unsteady adverse pressure gradient.

(3) Develop and test a compact three-component LDA system that is compatible with the constraints of the unsteady water tunnel used in this program.

(4) Provide a set of profiles of velocity and Reynolds stresses taken under unsteady flow conditions to supplement the results already published for steady flow.

Chapters 2 and 3 will present the governing equations and previous work published in the literature. Chapter 4 will describe the experimental facility and the LDA configuration, while chapter 5 will discuss the validation of the facility and LDA systems. Chapter 6 will outline the experimental plan, while chapter 7 will present the measured velocity profiles and Reynolds stresses. Finally, chapter 8 will analyze the results in terms of time response and mechanisms. This report will then conclude with a concise summary in chapter 9.

2

2. The Governing Equations

The governing equations can be expressed in many different forms using a variety of notations and symbology, and in fact, they should be expressed in the form that is most useful to the particular study at hand. This chapter provides a brief review of the relevant governing equations, stated in terms that are most relevant to this program.

2.1 Alternate formulations of the governing equations

For steady turbulent flows, the standard practice is to identify each variable as having a time-averaged mean component and an instantaneous fluctuating component. That is,

$$u = U + u', \tag{2.1}$$

where u is the instantaneous velocity composed of U, the time-averaged component, and u', the fluctuating component.

In unsteady flows, the time-averaged value may or may not have significance, depending on the frequency of the unsteadiness and the response time of the flow. What is generally of more interest is the "average" value that would be seen at a particular point or phase of the unsteady event. If the same event is repeated many times, then a *phase-averaged* value can be defined at each phase. That is,

$$u = \langle u \rangle + u', \tag{2.2}$$

where u is the instantaneous velocity composed of $\langle u \rangle$, the phase-averaged velocity and u', the fluctuating component. If the event being described consists of an initial condition followed by a disturbance and a response time, then this double decomposition is probably the appropriate description.

If, on the other hand, the event being described is actually cyclic in nature, then a triple decomposition is appropriate.

$$u = U + \tilde{u} + u' \tag{2.3}$$

In equation 2.3, $\tilde{u}$ is the *deterministic* component of the instantaneous velocity. There is clearly a connection between this component and the phase-averaged velocity, which is

$$\langle u \rangle = U + \tilde{u}. \tag{2.4}$$

In practice, $\tilde{u}$ is found by first obtaining $\langle u \rangle$ and then subtracting the mean velocity, U.

In this experiment, the pressure gradient was suddenly changed and the flow was allowed to fully adjust to that change. Under these conditions, neither the time-averaged values nor the deterministic values have much meaning by themselves. Therefore, the quantities measured and calculated will be expressed as phase-averaged quantities. For comparitive purposes and to establish a baseline for symbology, the phase-averaged equations are presented in section 2.2, and the deterministic equations are summarized in section 2.3.

Cartesian Tensor Notation. Since many of the following equations are lengthy in their most compact form, cartesian tensor notation will frequently be used throughout this report. The conventional orthogonal axes x, y, and z will be indicated as x_1, x_2, and x_3, and an arbitrary direction will be indicated as x_i. In a similar fashion, the conventional velocities u, v, and w, will be indicated as u_1, u_2, and u_3. An overdot, $\dot{u}$, denotes the partial derivative with respect to time, and a comma, $u_{i,j}$, denotes a partial derivative with respect to the direction x_j. Also, in this notation, any indices that are repeated in a given term, such as $u_{i,i}$, indicates a summation of that term over all three directions. When a summation is not intended, Greek indices will be used, such as $u_{\alpha,\alpha}$. This symbology will become clear

4

in the context of the equations that follow. Finally, the isotropic tensors δ_{ij} and ϵ_{ijk} will occasionally be used. They are defined as follows.

$$\delta_{ij} = \begin{cases} 1 & \text{if } i = j \\ 0 & \text{otherwise} \end{cases} \tag{2.5}$$

and

$$\epsilon_{ijk} = \begin{cases} 1 & \text{if } ijk \text{ belongs to } 123123 \\ -1 & \text{if } ijk \text{ belongs to } 321321 \\ 0 & \text{otherwise} \end{cases} \tag{2.6}$$

2.2 The Phase-Averaged Governing Equations

The phase-averaged equations take on the same form as the conventional time-averaged turbulence equations, except that the time-average is replaced in all places by the phase-average. Since the development of these equations is found in many textbooks, they are presented only in summary fashion below. In all cases, the fluid is assumed to be *incompressible*, a very good assumption for this experiment in water.

Continuity

$$\langle u_j \rangle_{,j} = 0, \qquad u'_{j,j} = 0 \tag{2.7}$$

Momentum

$$\langle \dot{u}_i \rangle + \langle u_j u_i \rangle_{,j} = \frac{1}{\rho} \langle p \rangle_{,i} + \nu \langle u_i \rangle_{,jj} - \langle u'_i u'_j \rangle_{,j} \tag{2.8}$$

Evolution of Turbulent Kinetic Energy

$$\frac{1}{2} \langle \dot{u}'_i u'_i \rangle + \left(\langle u_j \rangle \frac{1}{2} \langle u'_i u'_i \rangle \right)_{,j} = P - D - J_{j,j} . \tag{2.9}$$

5

In equation 2.7, P is the production, D is the dissipation, and $J_{j,j}$ is the flux of turbulent kinetic energy in the jth direction.

$$P = -\langle u'_i u'_j \rangle \langle u_i \rangle_{,j}$$

$$D = \nu \langle u'_{i,j} u'_{i,j} \rangle$$

$$J_j = \frac{1}{\rho} \langle u'_j p' \rangle + \frac{1}{2} \langle u'_j u'_i u'_i \rangle - \nu \frac{1}{2} \langle u'_i u'_i \rangle_{,j} \, .$$

Evolution of the Reynolds Stress

$$\langle \dot{u'_i u'_j} \rangle + \left(\langle u_k \rangle \langle u'_i u'_j \rangle \right)_{,k} = P_{ij} + T_{ij} - D_{ij} - J_{ijk,k} \, . \qquad (2.10)$$

In equation (2.8), in addition to the production, dissipation, and flux named previously, T_{ij} is the pressure strain.

$$P_{ij} = -\langle u'_k u'_j \rangle \langle u_i \rangle_{,k} - \langle u'_k u'_i \rangle \langle u_j \rangle_{,k}$$

$$T_{ij} = \frac{1}{\rho} \langle p'(u'_{i,j} + u'_{j,i}) \rangle$$

$$D_{ij} = 2\nu \langle u'_{i,k} u'_{j,k} \rangle$$

$$J_{ijk} = \frac{1}{\rho} \left(\langle p'u'_j \rangle \delta_{ik} + \langle p'u'_i \rangle \delta_{jk} \right) + \langle u_k u'_i u'_j \rangle - \nu \langle u'_i u'_j \rangle_{,k} \, .$$

Evolution of Vorticity

In this study, evolution of both the spanwise vorticity and the streamwise vorticity are of interest. The spanwise vorticity equation characterizes the vorticity embedded in the boundary layer, while the streamwise vorticity equation characterizes the vorticity introduced into the flow by the vortex generators. The following equation applies to both streamwise and spanwise vorticity.

6

$$\langle \dot{\omega_i} \rangle + (\langle u_j \rangle \langle \omega_i \rangle)_{,j} = \langle \omega_j \rangle \langle u_i \rangle_{,j} + \nu \langle \omega_i \rangle_{,jj} + \langle \omega'_j u'_{i,j} \rangle - \langle u'_j \omega'_i \rangle_{,j} . \qquad (2.11)$$

An alternate formulation does not transform the turbulent velocity products into turbulent vorticity terms. It is useful because it expresses the equation in terms of Reynolds stress terms, which can be directly measured in an experiment.

$$\langle \dot{\omega_i} \rangle + (\langle u_j \rangle \langle \omega_i \rangle)_{,j} = \langle \omega_j \rangle \langle u_i \rangle_{,j} + \nu \langle \omega_i \rangle_{,jj} - \epsilon_{ijk} \langle u'_q u'_k \rangle_{,qj} . \qquad (2.12)$$

Equation 2.11 is particularly helpful in that it lends insight into the roles the Reynolds stress terms play in equation 2.12. The Reynolds stress terms are a combination of turbulent convection and turbulent vortex stretching, and will in general be referred to as turbulent transport. The vorticity equation will be expanded term by term and discussed at length for both streamwise and spanwise vorticity in chapter 8.

2.3 The Deterministic Governing Equations

The key deterministic equations governing incompressible, constant property flow are presented below. Following the philosophy expressed in section 2.2, since these equations have been developed in various forms by a number of sources, including Brereton and Reynolds (1987), the resulting equations will not be re-derived but are presented in a summary fashion below.

Continuity

$$U_{j,j} = 0, \qquad \tilde{u}_{j,j} = 0, \qquad u'_{j,j} = 0 \qquad (2.13)$$

Momentum

$$\dot{\tilde{u}}_i + (U_j \tilde{u}_i + \tilde{u}_j U_i + \widetilde{u'_i u'_j} + \widetilde{\tilde{u}_i \tilde{u}_j})_{,j} = -\frac{1}{\rho} \tilde{p}_{,i} + \nu \tilde{u}_{i,jj} \qquad (2.14)$$

7

Evolution of $\widetilde{\tilde{u}_i \tilde{u}_i}$

$$\frac{1}{2}\widetilde{\dot{\tilde{u}_i \tilde{u}_i}} + (U_j \frac{1}{2}\widetilde{\tilde{u}_i \tilde{u}_i})_{,j} = P - D - J_{j,j}. \tag{2.15}$$

where

$$P = \widetilde{u'_j u'_i \tilde{u}_{i,j}} - \widetilde{\tilde{u}_j \tilde{u}_i} U_{i,j} - \widetilde{\tilde{u}_j \tilde{u}_i} \tilde{u}_{i,j} - \widetilde{u'_j u'_i} \tilde{u}_{i,j}$$

$$D = \nu \widetilde{\tilde{u}_{i,j} \tilde{u}_{i,j}}$$

$$J_j = \frac{1}{\rho}\widetilde{\tilde{u}_j \tilde{p}} + \frac{1}{2}\widetilde{\tilde{u}_j \tilde{u}_i \tilde{u}_i} + \widetilde{\tilde{u}_i u'_i u'_j} - \tilde{u}_i \widetilde{\tilde{u}_i \tilde{u}_j} - \nu \widetilde{\tilde{u}_i \tilde{u}_{i,j}}.$$

Evolution of $\widetilde{u'_i u'_i}$

$$\frac{1}{2}\widetilde{\dot{u'_i u'_i}} + \frac{1}{2}(U_j \widetilde{u'_i u'_i})_{,j} = P - D - J_{j,j} \tag{2.16}$$

where

$$P = -\widetilde{u'_i u'_j \tilde{u}_{i,j}} - \widetilde{u'_i u'_j} U_{i,j}$$

$$D = \nu \widetilde{u'_{i,j} u'_{i,j}}$$

$$J_j = \frac{1}{\rho}\widetilde{u'_j p'} + \frac{1}{2}\widetilde{\tilde{u}_j u'_i u'_i} + \frac{1}{2}\widetilde{u'_j u'_i u'_i} - \nu\frac{1}{2}(\widetilde{u'_i u'_i})_{,j}.$$

Evolution of the Reynolds Stress

$$\widetilde{\dot{u'_i u'_j}} + (U_k \widetilde{u'_i u'_j})_{,k} = P_{ij} + T_{ij} - D_{ij} - J_{ijk,k}. \tag{2.17}$$

8

where

$$P_{ij} = -\widetilde{u'_k u'_j \tilde{u}_i{}_{,k}} - \widetilde{u'_k u'_i \tilde{u}_j{}_{,k}} - \widetilde{u'_k u'_j} U_i{}_{,k} - \widetilde{u'_k u'_i} U_j{}_{,k}$$

$$T_{ij} = \frac{1}{\rho}\, \overline{p'(u'_i{}_{,j} + u'_j{}_{,i})}$$

$$D_{ij} = 2\nu\, \overline{u'_i{}_{,k}\, u'_j{}_{,k}}$$

$$J_{ijk} = \frac{1}{\rho}(\overline{p'u'_j}\delta_{ik} + \overline{p'u'_i}\delta_{jk}) + \widetilde{\tilde{u}_k u'_i u'_j} + \widetilde{u'_k u'_i u'_j} - \nu(\widetilde{u'_j u'_i{}_{,k}} + \widetilde{u'_i u'_j{}_{,k}}).$$

Evolution of Vorticity

$$\dot{\tilde{\omega}}_i + (U_j \tilde{\omega}_i){}_{,j} = (\Omega_j \tilde{u}_i{}_{,j} + \tilde{\omega}_k U_i{}_{,j})$$

$$- (\tilde{u}_j \Omega_i + \widetilde{\tilde{u}_j \tilde{\omega}_i} + \widetilde{u'_j \omega'_i}){}_{,j} + (\widetilde{\tilde{\omega}_j \tilde{u}_i} + \widetilde{\omega'_j u'_i}){}_{,j} + \nu \tilde{\omega}_i{}_{,jj}. \tag{2.18}$$

9

Mathematical theories from the happy hunting

grounds of pure mathematics are found suitable

to describe the airflow produced by aircraft ...

— Theodore von Karman, 1954

3. Literature Review

Since this program brings together two technologies, the study of streamwise vortices in steady flows and the study of unsteady separating turbulent flows, the first two sections of this review will be divided in the same manner. In the third section of this review, selected papers will be discussed which consider the combined subjects of vorticity in unsteady flows. Because there is a great deal of literature in each of the first two fields, only the articles which relate most directly to this program will be discussed here. For a broader review of each separate subject area, Pauley and Eaton (1988) reviewed streamwise vortices and Reynolds and Carr (1985) reviewed unsteady, driven, separated flows.

3.1 Streamwise Vorticity in Steady Flows

Vortex generators have been in use on aircraft since the mid-1940's. Schubauer and Spangenberg (1960) attribute the first vortex generator to H. D. Taylor in 1946. Much of the early work was geared toward specific design applications rather than fundamental studies of boundary layer interaction. In addition, since many of the results were of a proprietary nature, they were only published in corporate reports or memos. This section will begin with one of the earliest works published in an engineering journal.

Schubauer and Spangenberg (1960) studied forced mixing to "increase the pressure recovery that a boundary layer will withstand before separation occurs." They evaluated various mixing devices in air, including plows, scoops, twist-interchangers, ramps, tapered fins, domes, shielded sinks, and vortex generators. The vortex generators were of a trapezoidal shape recommended by Taylor in 1948, and were arranged in pairs, producing counter-rotating vortices. They learned that "mixing on a coarse scale by relatively large, widely spaced devices" was far more effective

than fine scale mixing, and that under these conditions multiple rows were less effective than a "single row of devices properly spaced and properly stationed." They concluded that while the mixing devices differ considerably in their effectiveness and drag penalty, they all affect the mechanics of flow in about the same way.

Pearcey (1961) studied the tradeoffs between various vortex generator configurations. He considered co-rotating pairs, counter-rotating pairs, and alternate pairs of co-rotating and counter-rotating which give the so-called biplane effect. He noted that the key design issues are the strength and the disposition of the individual vortices at the location where separation is to occur. The effectiveness of each vortex generator was governed by the initial spacing, height, strength and direction of rotation. In addition, the local effects of the generator blades on the boundary layer itself were important. Co-rotating vortices were effective when their initial spacing was greater than three times the height. Counter-rotating systems of vortices had the characteristic that they moved away from the surface, which limited their effectiveness to generally 20 generator heights. Pearcey recommended dimensional ratios for optimum performance, allowing for trade-offs between maximum effectiveness, range of effectiveness, and minimum drag. As a baseline, he recommended co-rotating pairs because of their greater range of effectiveness and their insensitivity in performance to blade size, incidence, and spacing.

Perkins (1970) evaluated the formation of streamwise vorticity in terms of the steady, incompressible, turbulent vorticity equation. He discussed secondary currents of the *first kind* and *second kind* as originally categorized by Prandtl in 1952. Secondary flows of the *first* kind are caused by vortex stretching due to skewing the mean flow, whereas secondary currents of the *second kind* are caused by turbulent transport and turbulent vortex stretching. Perkins systematically evaluated the relative importance of each of the terms in this vorticity equation. While his treatise emphasized the natural evolution of streamwise vorticity, his conclusions also apply to the growth or decay of vortices that are intentionally introduced into a turbulent

12

boundary layer. The two terms that he found were of major importance were the turbulent transport terms, $\frac{\partial^2}{\partial y \partial z}(\overline{v'^2} - \overline{w'^2})$ and $(\frac{\partial^2}{\partial z^2} - \frac{\partial^2}{\partial y^2})\overline{v'w'}$.

Mehta, Shabaka, Shibl, and Bradshaw (1983) were one of the first to report results for longitudinal vortices embedded in turbulent boundary layers. They looked at an isolated vortex, a vortex pair with "common flow down", and a vortex pair with "common flow up". They introduced the vorticity in the settling chamber of a wind tunnel, then measured mean velocities and the Reynolds stresses after the flow went through a 9 to 1 two-dimensional contraction. They concluded that the longitudinal vorticity drastically altered the turbulence structure. The velocity contours were qualitatively as would be expected due to effects of passive convection by the secondary flow. Triple products suggested that turbulent transport of Reynold's stresses occurred by gradient diffusion, quantification of which they felt would be very difficult.

Shabaka, Mehta and Bradshaw (1985) reported in greater detail on their results from a single vortex embedded in a turbulent boundary layer. They presented contours of the longitudinal vorticity, the Reynolds stress terms, the eddy viscosity, and the turbulent transport of turbulent kinetic energy and shear stress. They observed a region of negative shear stress on the downwash side of the vortex and regions of vorticity of opposite sign surrounding the main vortex. There were large variations in the shear correlation coefficient and the stress-energy ratio, and the correlation coefficients for $\overline{v'w'}$ and $\overline{u'w'}$ were close in value to $\overline{u'v'}$. Finally, they concluded that because contours of the eddy viscosity were far more complex than related contours of the turbulent transport inferred from the triple products, that the concept of a transport velocity is more plausible than the concept of an eddy viscosity. This implies that stress transport models may be needed to successfully compute such flows.

Mehta (1984) studied the interaction of a vortex with a mixing layer. He observed that the vortex induced strong secondary motions and to some degree redistributed

13

the turbulence, in particular $\overline{u'w'}$. In general, there was no active interaction between the vortex and the mixing layer.

Mehta (1985) reported the effect of a longitudinal vortex on a separated boundary layer. He made two-component LDA measurements on an axisymmetric model at subsonic velocities in a transonic wind tunnel and generally saw consistent trends with those reported for the mixing layer. The vortex delayed separation on the downwash side of the vortex but caused earlier separation on the upwash side. Of particular interest was the large diffusion of $\overline{u'v'}$ away from the surface as indicated by the triple correlation $\overline{u'v'^2}$, and the large production of $\overline{u'v'}$, indicated by $\overline{v'^2}(\partial U/\partial y)$. He suggested that the vortex first generates the normal stresses, $\overline{v'^2}$ and $\overline{w'^2}$, which then produce $\overline{u'v'}$ by interaction with the mean strain rates. He also observed a constant value of the shear stress correlation coefficient well into the boundary layer.

Mehta (1986) reported on the same experiment performed at transonic speeds. In contrast to his subsonic results, the vortex reduced the extent of the separated region and caused reattachment to occur sooner. Also in contrast to the subsonic results, the vortex core had much lower values of $\overline{v'^2}$ and there was no increase in $\overline{u'v'^2}$ on the upwash side of the vortex.

Westphal, Eaton, and Pauley (1985) investigated the development of a fairly weak streamwise vortex, embedded within a turbulent boundary layer, in the presence of a moderate pressure gradient. Their study was done in air. They concluded that the vortex could be characterized quite well using the contours of the streamwise vorticity. Second, they observed substantial core growth relative to that expected for a free vortex. While the accelerated core growth was anticipated due to the adverse pressure gradient, the growth was more than could be accounted for by Batchelor's (1967) simple theory. As the core grew, due to interaction with the wall, the core took on an increasingly elliptical shape. In contrast to claims by other authors, the vortex did not meander as it traveled downstream. Although image effects caused the vortex to stray from the center line of the plate, it did so

14

in a consistent and predictable manner. Distortion of the Reynolds stresses were also more pronounced in the presence of the adverse pressure gradient. Finally, they observed an apparent thickening and thinning of the boundary layer on the respective upwash and downwash sides of the vortex.

Eibeck and Eaton (1985) looked at the effects of embedding a single longitudinal vortex in an otherwise two-dimensional turbulent boundary layer. They measured three components of the mean velocity using a 4-hole pressure probe, a 3-hole probe and a single hot wire. They measured shear stress using a 2-component surface fence gauge. In the downwash region, the vortex created a locally thinner boundary layer with subsequently higher skin friction and heat transfer. In the upwash region, it created a locally thicker boundary layer with subsequently lower skin friction and lower heat transfer. While there were 3-dimensional distortions in the outer flow (y^+ values greater than 200), the flow near the wall (y^+ values less than 200) remained essentially 2-dimensional as was evidenced by the log-linear profiles which were similar for the entire flow field.

Liandrat, Aupoix, and Cousteix (1985) computed the effect of longitudinal vortices embedded in a turbulent boundary layer. They found that simple models based on the Boussinesq hypothesis worked well for a single vortex but failed in part for the more complex case of a vortex pair. By integrating the Reynolds stress transport equations along streamlines, and with the help of a simple diffusion model, they obtained better results. Their results emphasized the need for good data in building models for the transport of the Reynolds stress.

Cutler and Bradshaw (1986) studied the interaction between a strong longitudinal vortex and a turbulent boundary layer in air. A full delta wing placed in front of a flat plate allowed the trailing vortices to pass onto the plate while the wake passed under the plate. They measured the mean velocities and pressure, all of the Reynolds stresses, and all of the triple products. In the core of the vortex there was very little mixing. They felt that the high axial velocity in the core, in combination with vortex wandering, could account for all the observed shear stress, $\overline{u'v'_\theta}$, and

15

most of the observed normal stresses, $\overline{u'^2}$, $\overline{v_\theta'^2}$, and $\overline{v_r'^2}$. As the vortices interacted with the boundary layer, secondary vortices of opposite sign first formed along the surface, then broke away and were entrained into the primary vortex. They felt that this breaking away process caused the observed large levels of $\overline{u'w'}$, $\overline{u'^2}$, and $\overline{w'^2}$.

Mehta and Cantwell (1987) studied the mean flow and turbulence structure of a half-delta wing in air in the absence of interactions with other surfaces or shear layers. They felt this was needed as a baseline for comparison with other interaction studies where a similar type vortex was used. They concluded that the vortex was fully developed in a distance of 3 vortex generator heights, because the vorticity and circulation had reached constant values, and because of the coincident location of the maximum vorticity and maximum velocity deficit. They measured and reported contours for all the Reynolds stresses except $\overline{v'w'}$. The turbulence was nearly isotropic as indicated by nearly equal values and time histories of the three normal Reynolds stresses. While contours of the secondary shear stress were complicated in form, the authors felt they were similar in nature to the results reported by others.

Westphal and Mehta (1987) looked at the effect of lateral oscillation of a streamwise vortex, when embedded in a turbulent boundary layer. Their primary objective was to see if the flattening in the vortex core, seen in previous work, could be attributed to vortex meander. They observed that a lateral (spanwise) oscillation of the vortex generator caused a flattening of the vorticity contours when compared with vorticity contours for a stationary generator. They also saw some changes in the Reynolds stresses, particularly $\overline{v'^2}$ and $\overline{u'w'}$. While they concluded that vortex meander will cause flattening in the vortex core, they could not say whether or not this was the cause of flattening in previous studies.

Mehta and Bradshaw (1988) continued their series of studies in a detailed report on a vortex pair with "common flow upward". With this configuration, the pair of vortices tended to rise to a height above the surface equal to approximately

16

twice the boundary-layer thickness. While the distribution of $\overline{u'u'}$ was indicative of "convection of pre-existing boundary-layer turbulence by the vortices", $\overline{v'v'}$ and $\overline{w'w'}$ showed symmetrical maxima in the core regions. In general, turbulent kinetic energy transport appeared to occur from the high energy core region to surrounding regions. Modification of the Reynolds shear stresses appeared to occur by rotation of the fluid around the vortex core. In general, they concluded that the vorticies modify but do not destroy the anisotropy of the turbulence.

Pauley and Eaton (1988) investigated the development of longitudinal vortex pairs embedded in a turbulent boundary layer. Following their earlier work with Westphal *et al.*, they sought to characterize how the history and interaction of vortex pairs varied with pair configuration, spacing, and strength. Configurations studied were counter-rotating with "common flow up" and "common flow down" and co-rotating. Their results confirmed earlier predictions by Pearcey that interaction with the boundary layer would result in rapid diffusion of vorticity accompanied by rapid vortex growth. While Westphal *et al.* found this was true for a single embedded vortex, Pauley and Eaton found an even stronger effect when vortex pairs were placed close enough to influence each other. This effect was the most pronounced for counter-rotating vortices with "common flow up". In contrast to the peak vorticity, the total circulation of the primary vortex (obtained by integration) decreased much more slowly. The primary mechanism for this was skin friction at the wall, which was the strongest in the "common flow down" case where the vortices were the closest to the surface. One final observation regarding the "common flow down" configuration was that varying the strength of the vortices did not change the amount of boundary layer thinning but rather the width of the thinning region, due to compensating effects from the stronger image vortices. With respect to turbulent structure, they discovered that a velocity deficit in the vortex core was associated with an increase in turbulent kinetic energy and that the upwash region exhibits high turbulent kinetic energy production. Finally, they found they could classify the type of strain by plotting the data in terms of the invariants of the anisotropic

17

Reynolds stress tensor. Various Reynolds stress models were tested against their data.

3.2 Unsteady, Separating Turbulent Flows

Perhaps the appropriate starting point for unsteady flow is with the two classic problems posed by Stokes (1851). While the analysis was for laminar flow, the analytical solution for each problem is straight-forward and each solution yields a characteristic length which is very useful in parameterization of unsteady, turbulent flows. Stokes' first problem was a flat plate started abruptly from rest, for which the solution is:

$$\frac{u}{U_0} = \text{erfc}\left(\frac{y}{2\sqrt{\nu t}}\right). \tag{3.1}$$

The equation above defines a characteristic thickness, $\ell_s^* = 2\sqrt{\nu t}$. Stokes' second problem was a flat plate subjected to a sinusoidal freestream oscillation. The solution is:

$$\frac{u}{U_0} = \exp\left(\frac{y}{\ell_s}\right)\cos\left(\Omega t - \frac{y}{\ell_s}\right), \tag{3.2}$$

where the characteristic thickness, $\ell_s = (2\nu/\Omega)^{1/2}$, becomes very small at high frequencies.

Karlsson (1959) performed one of the first experimental studies of an unsteady turbulent boundary layer. He used a wind tunnel with a sinusoidally driven shutter system to produce a sinusoidal variation superimposed on a mean freestream velocity. He characterized the velocity response in terms of a sum of the mean, the first harmonic, and a residual containing higher harmonics and the chaotic portion of the turbulence. He observed no systematic variation of the mean velocity profiles with amplitude or frequency, even for amplitudes as high as 34%. In the inner portion of the boundary layer, the velocity led the freestream in phase by as much as 35°, while at low frequencies there was a lag in phase in the outer portion of the boundary layer.

18

Cousteix, Desopper, and Houdeville (1977) studied the structure and development of a turbulent boundary layer in an oscillatory flow. They measured the mean velocity, $\overline{u'^2}$, and $\overline{u'v'}$ for comparison with the prediction from two different turbulence models, a mixing-length model, and a transport equation model. While their tests were limited to low Strouhal numbers (0.0127 based on boundary layer thickness), they concluded that the general behavior of the boundary layer and the structure of the turbulence were not affected by the flow oscillations. Furthermore, they concluded that, within the limits of low Strouhal number flows, both the mixing-length model and the $k - \epsilon$ transport equation model did a good job of predicting the behavior of the turbulent boundary layer.

Cousteix, Javelle, and Houdeville (1981) extended the work described above to a broader range of Strouhal numbers. They studied a Strouhal range from 1.5 to 18, where the Strouhal number was based on the distance from the virtual origin. They observed a periodicity in the mean velocity that appeared to be the consequence of a travelling wave with a convective velocity of $0.75U_\infty$. A similar periodicity in the phase averaged turbulence intensity inferred a convective velocity of $0.85U_\infty$. The shear stress correlation coefficient maintained a constant value of 0.45 across the boundary layer, consistent with observations from steady flow. Across their range of Strouhal numbers, they concluded that the mean flow was not affected by the imposed unsteadiness. However, for Strouhal numbers greater than 5, the inner region law-of-the-wall did not hold and did not have a consistent logarithmic overlap area with the outer region of the boundary layer.

Simpson, Chew, and Shivaprasad (1981) characterized the nature of the unsteady separating turbulent boundary layer in a series of reports. (Also see Shiloh *et al*). Their experimental work was done in an air tunnel using a programmable rotating blade damper to create a periodic freestream unsteadiness. In a sequence of three reports, they documented all the mean velocities, all the Reynolds stresses, and the flatness and skewness factors for a separating boundary layer.

Jayaraman, Parikh and Reynolds (1982) studied the effects of a steady, uniform upstream velocity with a sinusoidally varying downstream velocity. They observed that while the mean flow was relatively unaffected by the unsteadiness, the periodic velocity field was strongly affected and the law of the wall could not be applied to phase-averaged profiles. They concluded that the Strouhal number, based on the streamwise distance in the unsteady region, was the dominant parameter in describing the effects of freestream oscillation. In general, at low Strouhal numbers, the phase of the boundary layer tended to lag the freestream, with the inner region of the boundary layer leading the outer region. At high Strouhal numbers, the phase variation was confined to a small "Stokes layer" near the surface, consistent with the classic solution to Stokes Second Problem. Finally, the integral parameters, displacement thickness and shape factor, showed periodic variations. While the amplitude of oscillation decreased with increasing frequency, at high frequencies the phase of the displacement thickness was nearly 180° out with respect to the free stream.

Simpson, Shivaprasad, and Chew (1983) continued their study of the separating turbulent boundary layer. They presented time-averaged and phase-conditioned profiles of the streamwise velocity, the back-flow velocity, and the Reynolds stress components $\overline{u'^2}$, $\overline{v'^2}$, and $\overline{-u'v'}$. They stressed the importance of characterizing the flow in terms of the intermittency of forward motion, $\widehat{\gamma_{pu}}$, and they presented a number of correlations between $\widehat{\gamma_{pu}}$ and the phase conditioned shape factor, $\hat{H}$. The same correlations held for unsteady flow as for steady flow except that the unsteady cycle produced a hysteresis loop which increased in size with increasing frequency. Finally, they observed that the near-wall velocity led the pressure gradient by as much as 135°.

Binder and Kueny (1981) and then Binder et al. (1985) studied large amplitude oscillations in the wall region of a turbulent channel flow. Their experiments in a water facility varied the Reynolds number by a factor of 2, the frequency by a factor of 15, and the amplitude from 5% to 70% of the centerline velocity. This included

20

flow regimes where reverse flow occurred at the surface for portions of each cycle. They concluded that as long as the frequency was sufficiently high such that the the Stokes layer was within the viscous sublayer, then the phase and magnitude of the velocity and wall stress followed the Stokes solution. This restraint required the Stokes thickness, ℓ_s, to be such that

$$\ell_s^+ := \frac{\ell_s u_\tau}{\nu} = \frac{2u_\tau^2}{\nu\Omega} \leq 10. \tag{3.3}$$

In this region, the near wall velocity fluctuations ranged from 0 to $\overline{u_\infty'^2}$ over the distance of the Stokes thickness, and the phase led the center line phase, approaching $45°$ at the wall. For intermediate values, $10 < \ell_s^+ < 20$, the behavior began to deviate from the Stokes solution, and for $\ell_s^+ > 20$, the behavior was more quasi-steady in nature. They also concluded that their data confirmed their criteria for predicting reverse flow (1981),

$$\frac{\hat{u}}{u_\tau} > \frac{\ell_s^+}{\sqrt{2}}. \tag{3.4}$$

Finally, even though in some cases the deterministic fluctuations, $\widetilde{u'^2}$, were 25 times larger than the mean fluctuations, $\overline{u'^2}$, there were no significant variations in the mean statistical quantities when compared to steady flow.

Most recently, Tardu, Binder, and Blackwelder (1987) reported their preliminary results of a study to understand the relationship between turbulent bursting and imposed unsteadiness. While they had seen some trends, their observations had not yet led to any clear quantitative conclusions.

Chehroudi and Simpson (1985) continued the study of Simpson *et al.* in separating turbulent boundary layers using a rapidly scanning laser anemometer. In this technique, the LDA measuring volume was rapidly scanned across the entire boundary layer by a steering mirror which oscillated at frequencies up to 59 Hz. In this manner they were able to obtain space-time correlation coefficients, from

21

which they could obtain an integral length scale. They also produced scatter plots of the velocity within a spatial interval to infer the percent of time that the velocity exceeded the mean value. They concluded that the structure of the flow in the backflow region was strongly related to the local outer region flow.

Brereton, Reynolds, and Carr (1985) studied the reponse of the turbulent boundary layer to abrupt changes in the free-stream velocity. While maintaining a steady upstream velocity in their water facility, they abruptly diverted a portion of the freestream flow, causing a streamwise linear decrease of the freestream velocity. Their results agreed well with the analytical solution to Stokes' first problem, where only a Stokes layer, of thickness $\ell_s^* = 2\sqrt{\nu t}$, followed the "motion" of the stationary plate, and the remainder of the flow acted as a slug with the freestream. This was true for both $\widetilde{\tilde{u}/\overline{U_\infty}}$ and $\widetilde{u'^2/\overline{U_\infty^2}}$ when scaled with y/ℓ_s^*. During the first-half second of the transient, the displacement thickness of the entire flow responded simultaneously. In contrast, during relaxation after the first half second, the displacement thickness responded on a time scale proportional to the "local freestream time of flight".

Cousteix and Houdeville (1985) continued their study of the evolution of turbulence and skin friction in an oscillating boundary layer. The entire flow was oscillated such that the amount of variation of the freestream velocity (12 to 15 percent) was maximum near the leading edge and then decreased linearly with streamwise position, x. While the time-averaged properties were not affected much by the unsteadiness, they observed a "quasi-periodic spatial oscillation" of the momentum thickness and displacement thickness. They related this effect to an interaction between the unsteadiness and the convection of turbulence at a celerity of $0.85U_\infty$. For y^+ values on the order of 10, and outside the boundary layer, $\widetilde{u'^2}$ was in phase with $\tilde{u}$, but in the middle region of the boundary layer the phase varied up to 180°. For high frequencies, these variations were confined to a thin Stokes layer on the order of $\ell_s = (2\nu/\Omega)^{1/2}$. While the time-averaged profiles exhibited a logarithmic

region over the entire frequency range, only at low frequencies was the friction velocity from the law-of-the-wall related to the actual skin friction measured. The amplitude and phase of the skin friction did not correlate well with $\Omega x / U_\infty$ but did correlate well with $\Omega \nu / (\overline{u_f^2})$. Finally, they saw no obvious correlation between the unsteadiness and any bursting phenomena.

Cook, Murphy, and Owen (1985) and then Cook (1986) reported on turbulent boundary layers in oscillating flows. The experimental work was performed in a low-speed air tunnel where the flow rate was controlled by a choked, variable-throat-area exit nozzle. They compared the experimental results to analytical results using two different turbulence models, one developed by Cebeci-Smith and the other by Glushko. While the results from neither model matched the experimental observations very well, in general, the results from the Cebeci-Smith model yielded results which were closer. In the experiments, the amplitude of oscillation and the phase difference of the freestream both increased with increasing frequency. While the amplitude variation was greatest for low values of x, the streamwise distance from the entrance, the phase variation was greatest at large values of x. Inside the boundary layer, the ratio of local velocity to freestream often exceeded unity. Meanwhile, the phase of the inner boundary layer region tended to lead the freestream while the phase of the outer region tended to lag the freestream. Both of these trends were most pronounced at larger values of x and for higher frequencies. Finally, the turbulence intensity, $\sqrt{\overline{(u')^2}}/U_\infty$, deviated from steady predictions in the outer region of the boundary layer, particularly at higher frequencies.

In their review paper, Reynolds and Carr (1985) proposed a simple control volume vorticity balance for a boundary layer subjected to an unsteady adverse pressure-gradient. The accumulation of spanwise vorticity is seen as the difference between the convective inflow of vorticity and the convective outflow of vorticity, plus the vorticity flux at the surface due to the pressure gradient. While the spanwise vorticity embedded in the boundary layer is convected downstream by the mean flow, there is a tendency for the vortices to travel upstream due to an image

effect from the surface. When the boundary layer is subjected to a sudden adverse pressure gradient, three things occur: (1) the image effect may now allow the spanwise vorticity to overcome convection and move upstream, (2) the larger flux of vorticity into the control volume than out causes an accumulation of vorticity, and (3) the adverse pressure gradient causes a flux of opposite sign vorticity into the control volume. Since the third effect tends to be small, the vorticity tends to "grow to the scale of the boundary layer and then is shed."

Cook and Murphy (1987) used the facility described previously to study in more detail the effect of amplitude and frequency of oscillation on the phase-averaged, streamwise normal stress, $\widetilde{u'^2}$. The amplitude of oscillation ranged from 6.5% to 16.9% and the frequency ranged from $3.85Hz$ to $21Hz$, resulting in local Strouhal numbers ranging from 0.54 to 4.05. While there was no effect of amplitude or frequency on the mean turbulence levels, they observed a phase shift between $\tilde{u}$ and $\widetilde{U_\infty}$ and a phase shift between $\widetilde{u'^2}$ and $\tilde{u}$. Both phase shift effects varied with frequency and amplitude of oscillation, and with streamwise position. The frequency where effects were seen was more than an order of magnitude below the estimated turbulent burst frequencies. Finally, their results indicated that the variation in the turbulence level was more than could be accounted for by the variation in boundary layer thickness alone, in disagreement with the suggestion by Cousteix et al. (1985).

Brereton and Reynolds (1987) expanded the work of Jayaraman et al. with two-component LDA measurements. They observed that most time-averaged quantities, including turbulent length scales and the dominant production term, were similar to their counterparts in steady flow and were invariant with frequency. The two time averaged terms that did vary with frequency were the $\partial \overline{(\tilde{u}_k \tilde{u}_i)}/\partial x_k$ tensor and the $\overline{u'v'}(\partial \tilde{u}/\partial y)$ production term. In contrast, most of the phase-conditioned quantities (except for $\tilde{v}$) were strongly dependent on frequency. The production of kinetic energy was very anisotropic in that $\widetilde{u'u'}$ was much greater than $\widetilde{v'v'}$ and that $\widetilde{u'u'}$ lead $\widetilde{v'v'}$ in phase angle. Finally, in all cases, they found that transfer of the

24

kinetic energy was from the organized unsteady component $\widetilde{\tilde{u}\tilde{u}}$ to the unorganized component $\widetilde{u'u'}$.

Gajdeczko and Ramaprian (1987) also studied a periodic turbulent boundary layer in an adverse pressure gradient. In their water tunnel, the wall opposite the test surface was contoured to create the desired adverse pressure gradient, and the periodic flow was caused by a rotating sleeve in the exit section of the channel. Their 2-component LDA provided mean and phase-averaged profiles. The time-averaged profiles showed the effects of unsteadiness in the strong pressure gradient case, in the regions where flow reversal occurred. In their phase-averaged profiles, the shape of the profiles changed substantially as the Strouhal number, based on streamwise position, increased from 1.89 to 28.43. They saw poor agreement with predictions from a computational model which was developed for unsteady flow with a zero pressure gradient. Thus they concluded that turbulent production occurs much further from the wall in flows with an adverse pressure gradient.

3.3 Vorticity in Unsteady, Separating, Turbulent Flows

The work presently published on vorticity in unsteady separating turbulent flows relates mostly to spanwise vortices which are formed during dynamic pitching operations and those that are shed when the boundary layer separates. Very little, if any, work has been done with skew-induced streamwise vorticity in an unsteady, turbulent boundary layer.

McCroskey, Carr, and McAlister (1976) studied dynamic stall on oscillating airfoils. They sought to understand the mechanism that led to the shedding of the strong "vortex-like" structure during dynamic stall. In all their study cases, they observed that the difference between dynamic and static stall is that in dynamic stall a "vortex-like disturbance develops and passes over the airfoil at a convection velocity on the order of $\frac{1}{3}$ to $\frac{1}{2}$ of U_∞." They concluded that dynamic stall originates with a breakdown of the turbulent boundary layer, not with bursting of a

25

laminar separation bubble. As the frequency was varied, the phase within each cycle changed for the different events associated with the formation and convection of the disturbance vortex, but the basic progression of events did not change. In a similar way, the reduced frequency affected both the strength and phase of the vortex shedding. In contrast to this, there was very little effect of Reynolds number on the nature of the dynamic stall.

Reisenthel, Koga, and Nagib (1985) looked at control of separated flows with a spanwise flap. The flap was actuated in a manner that generated a large, spanwise vortical structure which generally caused earlier reattachment and better pressure recovery. Measurements of the pressure coefficient, C_p, indicated a sharp, local drop in C_p at the flap with a much quicker recovery to a C_p of 0. This effect increased as the frequency increased from $2.5 Hz$ to $10 Hz$. It also increased as the flap deflection angle increased to $40°$, after which no further increase was seen for larger deflection angles. These various effects collapsed into a single curve when the reattachment length was plotted against the reduced frequency, fh/U_∞, where h was the height of the flap measured normal to the wall. In summary, the reattachment length decreased linearly with increasing reduced frequency until it reached a value of 0.4, after which no further improvement was seen.

Sigurdson and Roshko (1985) looked at unsteady excitation of the reattaching flow on a circular cylinder. A closed circular cylinder was placed in a wind tunnel with its axis aligned parallel with the freestream flow. Separation occured at the circular leading edge of the cylinder. The flow was excited through slits at the leading edge by an acoustic speaker placed inside the cylinder. The pressure coefficient, the reattachment length, and the drag were used as global evaluation parameters. All three parameters were reduced with forcing. The maximum effect was seen for frequencies that corresponded to a wavelength comparable to the separation bubble height. The optimum excitation frequency, when non-dimensionalized with the Cylinder diameter, $f_{ex}D/U_\infty$, was in the range of 2 to 3. Alternately, this same

frequency range, when scaled with the local velocity at separation and the bubble height, $f_{ex}h/U_s$, was 0.26 to 0.32.

Luttges, Robinson, and Kennedy (1985) looked at the control of unsteady, separated flow structures on airfoils using a spanwise vortex generator and a spanwise air jet. They first observed the structures that formed on a pitching airfoil with no control devices. During pitching, a vortex formed near the leading edge. It convected downstream and then elicited a trailing edge vortex of opposite sign which led to a "cataclysmic stall". As the mean angle of attack was increased, the leading edge vortex formed earlier and convected more slowly. In contrast, increasing the pitching amplitude or reduced frequency delayed the vortex formation and led to a faster convection velocity. Similar effects were seen on a stationary airfoil with a vortex initiated by either a vortex generator or an air jet. Since the air jet provided better flexibility and dynamic response, it was used for most of the experiments. Finally, the air pulses were combined with the pitching of the airfoil. The effect of the air pulses varied with reduced frequency and phasing, but for reduced frequencies greater than 1.0 (meaning there was always at least one vortex over the airfoil) flow adherence to the airfoil was improved. They concluded that careful programming of air pulses could eliminate flow conditions that lead to "cataclysmic stall".

Lutges (1987) continued his work with the formation and convection of leading edge and trailing edge vortices during unsteady flow. While part of the study concentrated on characterizing the vortices on a flat plate and a NACA 0015 airfoil, the other portion of the study concentrated on understanding the unsteady mechanisms that allow a dragonfly to produce lift coefficients on the order of 5. For his studies with the flat plate and airfoil, he looked at mean angles of attack ranging from 10° to 30°, at oscillating angles ranging from 2° to 9°, and at reduced frequencies ranging from 0.4 to 2.0. He concluded that while the reduced frequency was very significant in describing the results, the Reynolds number and surface geometry were relatively inconsequential.

Bhattacharjee, Scheelke, and Troutt (1985) looked at modification of vortex interactions in a reattaching separated flow. Forcing was provided by a loud speaker placed on the wind tunnel wall opposite the backward facing step that caused the separation. The forcing, as observed with hot-wire probe signals, appeared to cause pairing and a trend toward two-dimensional flow of spanwise vortical structures. Forcing modified primarily the outer portion of the boundary layer, moving higher velocity fluid closer to the surface. The forcing seemed to be optimum at a frequency corresponding to the passage frequency of a mixing layer of the width of the backward facing step. This corresponded to a Strouhal number range based on the step height of 0.2 to 0.4. The forcing reduced the reattachment length by about 10%.

In a similar program, Roos and Kegelman (1985) looked at control of coherent structures in reattaching laminar and turbulent shear layers. They used a flap which projected along the flow direction from the edge of a backward facing step. The flap was oscillated at very small amplitudes on the order of 1% of the unseparated boundary layer thickness, and at several frequencies in the range of $20Hz$. This corresponded to a Strouhal number, based on the backstep height, of 0.22. Gentle excitation of the shear layer at the separation point provided and strong "regularizing" process and reduced the reattachment length by nearly 20% in laminar flow and nearly 30% in turbulent flow. While the changes due to excitation were small in the mean velocity profile, there was a substantial increase in the Reynolds shear stress and pressure fluctuations, indicating intensified turbulence activity within and beneath the reattaching shear layer.

Walker, Helin, and Chou (1985) studied unsteady surface pressure measurements on a pitching airfoil. The pitch rates on the NACA 0015 airfoil ranged from $230°/sec$ to $1380°/sec$, while the angle of attack varied from $0°$ to $60°$. With a $6in$ chord and a range of freestream velocities from $20ft/sec$ to $80ft/sec$, the resulting range of dimensionless pitch rates was 0.05 to 0.6. Comparison of the pressure distribution and the integrated lift coefficients revealed parallel and consistent trends. For a

28

constant Reynolds number, increasing the pitch rate increased $C_{\ell_{max}}$, $\partial C_\ell / \partial \alpha$, and the angle of attack at $C_{\ell_{max}}$. Increasing the Reynolds Number at constant pitch rate produced the opposite effect. The characteristics of the curves were similar when plotted for constant non-dimensional pitch rate, $\alpha^+ = \dot\alpha c / U_\infty$.

In a computational study, McCoy and Sarpkaya (1986) looked at the stability of vortex motion in an oscillating flow. Their study was geared towards the understanding of cycle to cycle variations in the flow observed around a cylinder in unsteady flow. They traced the separate histories of either one or two vortices placed in the vicinity of a circular cylinder. Their conclusion was that observed variations in the vortex motions resulted mostly from chaotic motion caused by the advection of vortices in a time-dependent flow.

Gad-el-Hak and Ho (1986) studied the unsteady vortical flow around three-dimensional lifting surfaces. They used flow visualization with seven different lifting surfaces in a tow-tank to characterize the formation, convection, interaction, and shedding of spanwise vortices on a pitching lifting surface. The reduced frequency, the leading edge shape, and the planform of the lifting surface all had significant effects on the nature of the vortex interactions.

Gad-el-Hak and Blackwelder (1987) studied control of the discrete vortices from a delta wing, using oscillatory injection of fluid at the leading edge. They used both flow visualization and hot wire/film in both a water tow tank and a wind tunnel. The spanwise vortices associated with dynamic lift were significantly altered by the perturbation at the leading edge. The effect of the perturbation was the largest when the speed of the injected fluid was near the ambient velocity and when the excitation frequency was a subharmonic of the natural shedding frequency of the delta wing.

3.4 Unanswered Questions in the Literature.

One of the most obvious questions, which appears not to have been addressed in the literature, is addressed by this study. That is, how do vortex generators affect the nature of a boundary layer subjected to an unsteady adverse pressure gradient? To answer that question, one must address many more specific questions, several of which are posed here.

(1) The studies of unsteady flows have shown that there is a thin *Stokes layer* that follows the pressure gradient, while most of the flow acts as a slug flow with the freestream. In contrast, vortex generators tend to act in the wake region of the boundary layer. How much interaction will there be between these two processes, and over what portion of the boundary layer will this interaction occur?

(2) Studies of streamwise vortices in a steady adverse pressure gradient indicate that the pressure gradient accelerates vortex growth, which decrease the core vorticity. What will happen to the streamwise vorticity when subjected to an *unsteady* adverse pressure gradient? If the streamwise vorticity is rapidly diffused, can it still help delay boundary-layer separation?

(3) Many of the vortex studies emphasize that the mechanisms associated with vortex generators are dominated by convection effects. If this is the case, what role do the turbulent terms play in the mechanisms that enable a vortex generator to delay boundary-layer separation?

(4) Finally, what are the characteristic time scales associated with the response of the boundary layer, with and without vortex generators, to an unsteady adverse pressure gradient?

These are the questions that this study will seek to answer.

4. Experimental Facility

The Unsteady Flow Facility used for this program is a complex, unsteady, water channel that has evolved through the experimental research programs of Jayaraman, Parikh, and Reynolds (1982) and Brereton and Reynolds (1987). During the period from 1985 to 1987, major upgrades to the facility were designed and implemented as a cooperative effort among three graduate students and Professor Reynolds. Further details of the mechanical design of the test section and computer-controlled valves are described by Henk and Reynolds (1989). In a similar manner, Carlson and Reynolds (1989) document in more detail the computerized valve control system and data acquisition system.

As shown in figure 4.1, water is pumped from a sump tank at atmospheric pressure to a constant head tank overhead, where the water level is maintained by a weir at $2.7m$ above the elevation of the leading edge of the test surface. Water exits the constant head tank and enters the test section through a series of flow-straightening devices and a 20:1 contraction. A new boundary layer forms on the upper surface as the flow passes over an elliptical leading edge. For turbulent experiments, the boundary layer is then tripped at a streamwise postion of $12.8cm$. As the boundary layer develops along the upper surface, suction slots on the side-walls minimize the growth of the side boundary layers while manual valves on the lower surface draw off sufficient flow to maintain a steady, mean, zero pressure gradient. With this steady flow as a mean, unsteady conditions are imposed by computer-controlled valves which are also located on the lower surface. Since the valves are computer-controlled and can be placed at any location in the channel, nearly any arbitrary, oscillatory, pressure-gradient can be established.

Near the leading edge a stationary helium-neon LDA system monitors the upstream velocity, while in the test section a traversing multiple-component argon-ion LDA system measures two or three components of the velocity in the boundary

31

layer. An IBM PC performs valve control while an AST AT accomplishes the data acquisition.

The major subsystems of the facility in its present configuration are: (1) the test section, (2) the flow conditioning systems, (3) the velocity measurement systems, and (4) the computerized control and data acquisition systems. In the following sections, each subsystem will be described in greater detail.

4.1 The Test Section.

Basic Tunnel Construction. The test section of the water channel is a stainless-steel external structural frame with inset transparent panels on the sides and upper surface, and drain panels on the lower surface for either manual or computer-controlled valves. The channel was designed in this manner to allow ease of access to the interior of the channel, maximum flexibility for adapting to different experimental configurations, maximum optical access for flow visualization and laser measurement systems, and easy relocation of the position of drain valves on the lower surface. The channel is 35.6cm wide, 12.9cm high, and 3.65m long.

Sidewall Boundary Layer Control. The eight side windows on each side are constructed from lucite, are 39.4cm wide by 16.5cm high, and can be easily removed and replaced to allow access to all interior parts of the channel. The stainless steel frames surrounding each window interlock to form a side suction slot 0.25mm wide every 46cm along each side of the channel. A needle valve located at the base of each slot regulates the suction flow rate. The adjustment of each valve is based on a combination of LDA measurements, flow visualization, and the measurment of its discharge rate relative to the other valves.

The upper inset panels are functionally divided into three sections as (1) a 1.37m laminar test section with elliptical leading edge, (2) a 1.37m turbulent test section with two smaller drop-in test surfaces, and (3) a 0.91m exit section with a deflector plate to guide the exiting flow.

32

Laminar Test Section. The leading edge of the laminar test section is a stainless-steel semi-ellipse with a 16:1 ratio of major to minor axes. It was machined on a Matsuura N-C mill and then hand polished. Flow approaching above the stagnation streamline is bypassed to the sump tank through a honeycomb structure and four manual valves. These valves are carefully adjusted using a hydrogen bubble-wire in front of the leading edge and by observing the smooth release of dye at a slot which is located 14.9cm behind the leading edge. The slot is formed at the junction between the stainless-steel leading-edge structure and a sheet of 1.9cm thick float glass. Float glass was chosen for the laminar inset plate for optimum flow visualization since mechanical access through the test surface was not required. For turbulent experiments, this first 1.37m section serves as the development section for the turbulent boundary-layer, by tripping it at a streamwise location of 12.8cm. The trip is a crimped stainless-steel wire .13mm in diameter, which when rotated forward serves as a hydrogen bubble wire at the leading edge.

Turbulent Test Section. The turbulent test surface and the exit section were each fabricated from 1.9cm lucite with spanwise stiffening ribs every 23cm. The lucite construction allows for two smaller and easier to remove test surfaces in the turbulent test section, each 26.6cm by 11.4cm. The vortex generators used in this program were mounted on one of these smaller test surfaces located at a streamwise position of 1.49m. The configuration of the vortex generator test surface will be described in detail in Section 6.1. The exit section has a 1.3cm float-glass plate situated at a 15° angle to the axis of the water channel. This provides for a smooth exit of the flow at the end of the channel while also allowing optical axis directly upstream through the end of the channel.

Passive Pressure Gradient Control. The lower surface of the water channel (the surface opposite the test surface) is divided into 24 separate drain panel locations. At each location, either a manual or a computer-controlled valve is installed. The 1.9cm diameter manual valves maintain a mean, steady, zero pressure gradient while the 10cm diameter computer-controlled valves alter the streamwise

33

gradient of the freestream velocity. All the drain plates on the lower surface are constructed from 0.64cm PVC. The drain hole pattern over the manual drain valves is two rows of holes, 3mm in diameter staggered on 6mm centers (113 holes) with a total area of 8.95cm^2. In contrast, the plates over the computer-controlled valves have 9 rows of 6mm diameter holes staggered on 13mm centers (167 holes) for a total area of 52.9cm^2. Each drain plate configuration was designed for optimum spanwise uniformity while keeping the throat area of the valve as the controlling flow resistance.

Active Pressure Gradient Control. The computer-controlled valves regulate the flow by means of two adjacent disks with identical hole patterns as one disk rotates against the second stationary disk. As the rotating disk moves from closed to open position, the two hole patterns gradually align with each other so the flow area varies in a linear fashion with the angular position of the valve. At the full open postion, the flow area is 8.3cm^2 for the low flow valve and 29.9cm^2 for the high flow valve. Each high flow valve can pass about 0.8m^3/min of water at the design head of 2.7m. The linear variation of flow area yields a linear variation in the freestream velocity. Water exiting the channel through each drain plate is funneled through a lucite adapter for a smooth transition from the 14cm by 34cm rectangular exit to the 10cm diameter valve. After passing through the valve, water is directed back to the sump tank through a 10cm diameter PVC pipe in a manner that minimizes the air entrainment, while providing a free atmospheric pressure interface at the disk assembly of the valve. The valve is linked by sprocket and chain to a Motion Technologies Model 00-01203-002 Printed Circuit Motor which is capable of driving the valve at frequencies up to 10Hz. Henk and Reynolds (1989) describe the valve construction in more detail, and the valve control will be described more in section 4.4.

4.2 Flow Conditioning Systems

The water entering the test section from the nozzle is carefully conditioned to minimize freestream turbulence, to maintain temperature within $0.1°C$, to eliminate microscopic dissolved air bubbles, and to control the size of particles in the flow.

Flow Straightening. Straightening of the flow and minimization of free-stream turbulence begins in the constant head tank. A constant area stainless-steel adapter smoothly adjusts the flow geometry from round $15cm$ diameter pipe to rectangular. The flow then turns and decelerates through three honeycomb blocks as the flow area increases to $92cm$ by $92cm$ in the stilling chamber, as shown in figure 4.1. Each honeycomb section has a nominal cell size of $1cm$ and is $13cm$ thick. In the stilling chamber, the flow passes through three $22mesh$ screens spaced $10cm$ apart. The screen material is $0.1905mm$ stainless steel wire which results in 69% open area. The screens are stretched tightly over stainless steel frames, and can be removed from the stilling chamber periodically for cleaning. Finally, the flow passes through a 20:1 contraction into the entrance of the water channel. The resulting freestream turbulence level is approximately 0.5%.

Temperature Control. During operation of the water channel, the water temperature is stabilized and maintained at $16.7°C \pm 0.1°C$. A $2.24kW$ pump operates in parallel with the main $5.6kW$ pump, directing flow from the sump tank to a water/ethylene-glycol heat-exchanger which is chilled by a $35kW$ Trane refrigeration system. While the water-flow through the heat-exchanger runs continuously, the temperature control system enables or disables the refrigeration system in response to a thermistor located in a region of the sump tank where very high mixing occurs.

Deaeration. Air is removed during system start-up using a back-flow purge system, and then during operation dissolved air is continuously removed with a deaeration system. The purge system is necessary during start-up to ensure that no trapped air bubbles in any of the suction holes or slots alter the flow rate through

35

each valve. Once the system is running, microscopic air bubbles must be removed These bubbles come from air which was originally dissolved in the tap water and air that is entrained at the air/water interface in the sump tank. For this purpose, a deaeration system runs continuously. A portion of the water leaving the main pump is bypassed through a venturi which drops the pressure sufficiently for boiling to occur at room temperature. The water vapor tends to nucleate on the microscopic air bubbles which then combine and grow in size as they convect along a horizontal pipe $2m$ in length. A mechanical vacuum pump then draws off the air and water vapor in a settling chamber, while the water is returned to the main pump inlet through a smaller $1.1kW$ pump.

Particulate Control. The particle content in the flow is controlled both while the system is filling and during operation. Tap water entering the system passes through a $125micron$ and a $5micron$ filter in series so that the only particles entering the water channel are $5microns$ or smaller. This is the optimum particle size for light scattering with LDA systems in water. To prevent the build-up of any larger particles in the system while it is operating, all the tanks in the system are kept carefully covered, and a set of three parallel filters in the chiller loop removes any impurities that do get into the system.

4.3 Velocity Measurement Systems

Two LDA systems are used for velocity measurement. This enables a single-component system to monitor the steady upstream conditions while a multiple-component system measures velocities in the boundary-layer downstream. In addition, the two systems can be located side by side in a steady, freestream flow to verify the calibration of each system.

Single Component Upstream Monitoring. The single-component system uses a $5mW$ helium-neon laser with Dantec transmitting and receiving optics. A custom fixture secures the laser and Dantec optics on a platform that rests on the

water channel. Two turning mirrors mounted on the fixture direct the transmitted beams down and across the channel, and two additional turning mirrors on the fixture direct the scattered light back up to the receiving optics. This fixture allows easy placement and removal of the system anywhere on the channel, as necessary. The LDA signal is processed by a Dantec model 55N24 tracker, which gives a direct digital reading of the mean velocity and sends an analog signal to the data acquisition system.

Multicomponent Measurements. The multiple-component LDA system uses a $4W$ Lexel model 95 argon-ion laser with TSI transmitting and receiving optics. While many different optical arrangements were tried in the preliminary phases of this program, two arrangements evolved which were used for final data acquisition, depending on whether two or three velocity components were to be measured. Schematics of the two-component system are shown in figures 4.2 through 4.4, and schematics of the three-component system are shown in figures 4.5 and 4.6. In addition, tables 4.1 and 4.2 summarize the key optical components in the two LDA systems. In both configurations, the optics are located on a breadboard which allows automated simultaneous traverses of the transmitting and receiving optics in the direction normal to the test surface. In addition, linear bearings allow manual motion in the spanwise direction, and trolley wheels along two I-beams allow manual motion in the streamwise direction. Also, in both the three-component and the four-component systems, the standard TSI dichroic color separator was modified by removing two beam steering prisms. This enabled a single beam to enter the separator module on-axis and allowed the green beam to exit on-axis, while the blue beam was displaced $25mm$.

Two-Component LDA. The two-component LDA system uses a modified TSI dichroic color separator (see figure 4.4) to create a four-beam, forward scatter system. Two green beams ($514.5nm$) create a measuring volume along the z-axis for measuring the u-velocity component, while two blue beams ($488nm$) create a measuring volume for measuring the v-velocity component. One blue beam is offset

37

back to the center to allow measurements to be made very close to the test surface. Figure 4.7a shows the configuration of the four beams. This particular configuration was chosen because the green beams create a measuring volume that contains no contamination from v or w, which in some of the separating flows under investigation could be a significant percentage of u. The orientation of the v measuring volume accepts about $3°$ of w contamination in order to make measurements very near the test surface. One of the green beams is Bragg-shifted at $38MHz$ and one of the blue beams is shifted at $40MHz$. This allows measurement of reversing flows in both velocity components, and gives frequency separation in addition to color separation for processing the scattered light. The scattered light passes through a $50micron$ pinhole in the field stop system then is dichroically separated and processed by separate photo-multiplier tubes (PMT's). Each PMT signal is then downmixed to $200kHz$ by TSI model 9186A mixers, and routed to TSI model 1090 trackers through a Krone-Hite model 3202 low-pass filter set at $800kHz$. The filter has an attenuation of $3dB$ at the indicated frequency with a roll-off of $80dB/decade$.

Three-Component LDA. A new three-component LDA system collected all the primary data in this project. It also uses a modified TSI dichroic color separator (see figure 4.4) to yield three green beams in forward-scatter and two blue beams in side scatter. Figure 4.7b summarizes the configuration of the five beams.

Forward Scatter Measurement of u and v. The three-beam forward-scatter system meaures u and v, each with about $3°$ of w contamination. The forward shooting u beam is shifted at $40MHz$ and the upward shooting v beam is shifted at $38MHz$ so that reversing flows in both u and v can be measured and so that frequency separation can be used as the primary means to separate the u and v signals during processing of the scattered light. The doppler bursts from both green measuring volumes are detected by a single PMT after passing through the dichroic color separator and a narrow-band color filter. The PMT signal is split to enter two TSI 9186A mixers. Since one signal is down-mixed at $200kHz$ relative to $40MHz$ and one relative to $38MHz$, frequency separation occurs when each mixer output passes

38

through the effective low-pass filter of each tracker. The u and v signals coming out of the low-pass filters are then processed by TSI trackers in the same manner as the two-component system above.

Side Scatter Measurement of w. The two transmitted blue beams of the side-scatter system enter through the transparent upper test-surface of the water channel and are oriented so as to measure very nearly pure w. During the alignment procedure, the measurement volume is oriented at a 45° angle to the x and z axes rather than measuring pure w, because it is impossible to observe the beam crossing in the receiving optics when viewed "straight-on". After the optics are sufficiently aligned such that a doppler signal can be detected by a tracker or counter, the optics are carefully rotated back to a position where pure w is measured for final optimization of the signal. To ensure that the path length in air and water does not change as the system traverses in the direction normal to the surface, a water-tight air-tube traverses up and down in a miniature tank of water, which is also maintained at constant temperature. The side-scattered blue light passes through the same field-stop system as the green forward-scattered light. It is then separated from the green light by the dichroic color separator, and then passes through a narrow band-pass color filter into a PMT. Selection of the appropriate pinhole in the field-stop system is very critical to good turbulence measurements, and this selection becomes much more complex for a system using a combination of forward scatter and side scatter. This critical pinhole issue will be discussed at length in section 5.3

Side Scatter Signal Processing. Since the count rate is much lower in side scatter, the PMT output is processed by a TSI model 1980 Counter after being downmixed to $200kHz$. The low-pass filter in the counter has an attenuation of $100dB/decade$. In contrast to trackers which need nearly continuous doppler bursts to track properly, a counter works well with lower count rates. The analog output from the two trackers and the counter then feed into the analog-to-digital input of the data acquisition system, where the appropriate mathematical operations convert voltages into velocities.

To achieve reasonable count rates in side scatter, the flow had to be seeded. While several different seeding materials were tried, the seed that was least expensive yet gave good results was Titanium Oxide (TiO_2). Initially, about $4cm^3$ of seed was added to the $5.7m^3$ of water in the system. While the data validation rate for the forward scattered signals varied very little with the addition of seed, the count rate on the side scattered signal increased from about $50cps$ to $600cps$. Because the filters in the system tended to slowly remove seed, occasionally $1cm^3$ of seed was added to maintain the count rate in the freestream at about $600cps$.

One of the beams was shifted at $40MHz$ to allow measurement of reversing flows. Since both the green u signal and the blue w signal were shifted at $40MHz$, and since the dichroic color separation in the receiving optics is not 100 percent efficient, each signal was checked for contamination by the other signal. When the counter was adjusted to count bursts from the w signal at a rate of 400 to $800cps$, the w beams were blocked while the u beams were not. The counter was not able to validate any stray bursts from the u signal. A similar test confirmed that the trackers were unable to track stray w signals when the u beams were blocked. Therefore, cross-contamination was not a problem.

4.4 Computerized Control and Data Acquisition

Both the computer valve-control system and the data acquisition system operate on either IBM or IBM-compatible personal computers. Both of these systems run with menu-driven software developed at Stanford, and the valve-control system uses control boards which were also developed at Stanford. The details of these systems are described by Carlson and Reynolds (1989).

Valve Control. The valve-control system operates on an IBM PC, with custom-designed control boards, and a Sorensen DCR 40-125A Power Supply. The system allows the user, through a menu-driven system, to select the waveform and frequency for a set of up to eight valves. Waveforms presently programmed are a sine

40

wave, square wave, and triangular wave, but since the program generates its own look-up table, virtually any waveform could be generated. Once the user selects the waveform and frequency for the set of valves, the amplitude and phase of each of the eight valves can be set independently. Typically, upstream and downstream valves are operated out of phase but with balanced amplitudes so the flow downstream of the upstream valve oscillates while the flow upstream remains steady. The valve controller sends two pulses to the data-acquisition system. The first pulse is continuous for triggering phase-sampling at specified phases of the cycle, and the second pulse identifies the zero-phase point of each cycle.

Data Acquisition. The data acquisition system operates on a $10MHz$ AST AT with an $80MByte$ hard disk. Analog-to-digital processing of the LDA signals is accomplished by a Tecmar model TM-40-PGH board and the traverse is run through the computer digital-out. The menu-driven software allows the operator to specify all the parameters of sampling through a set of input control files. The system is presently capable of simultaneously collecting velocity data from three LDA systems. From the three input signals, the three velocity components are calculated, then individual phase ensembles are collected for the appropriate statistical quantities. When the LDA is operated with two components, two mean velocities and three Reynolds stress terms are collected at each phase point. When the LDA is operated with three velocity components, three mean velocities, six Reynolds stress terms, and ten triple-product terms are collected for each phase point. All three channels are sampled on command within a period of 70 microseconds. The equivalent correlation length associated with this time delay is $y^+ \leq 0.5$ (based on $U_\infty = 0.5m/sec$ and $u_\tau = 0.021m/sec$). This is much smaller than the effective measurement volume ($y^+ \simeq 10$), and thus does not degrade the data. The data-acquisition system can control the traverse system so that an entire set of profiles is taken of each of these quantities, at each phase, at each y-location in the boundary-layer.

Unsteady Flow Facility
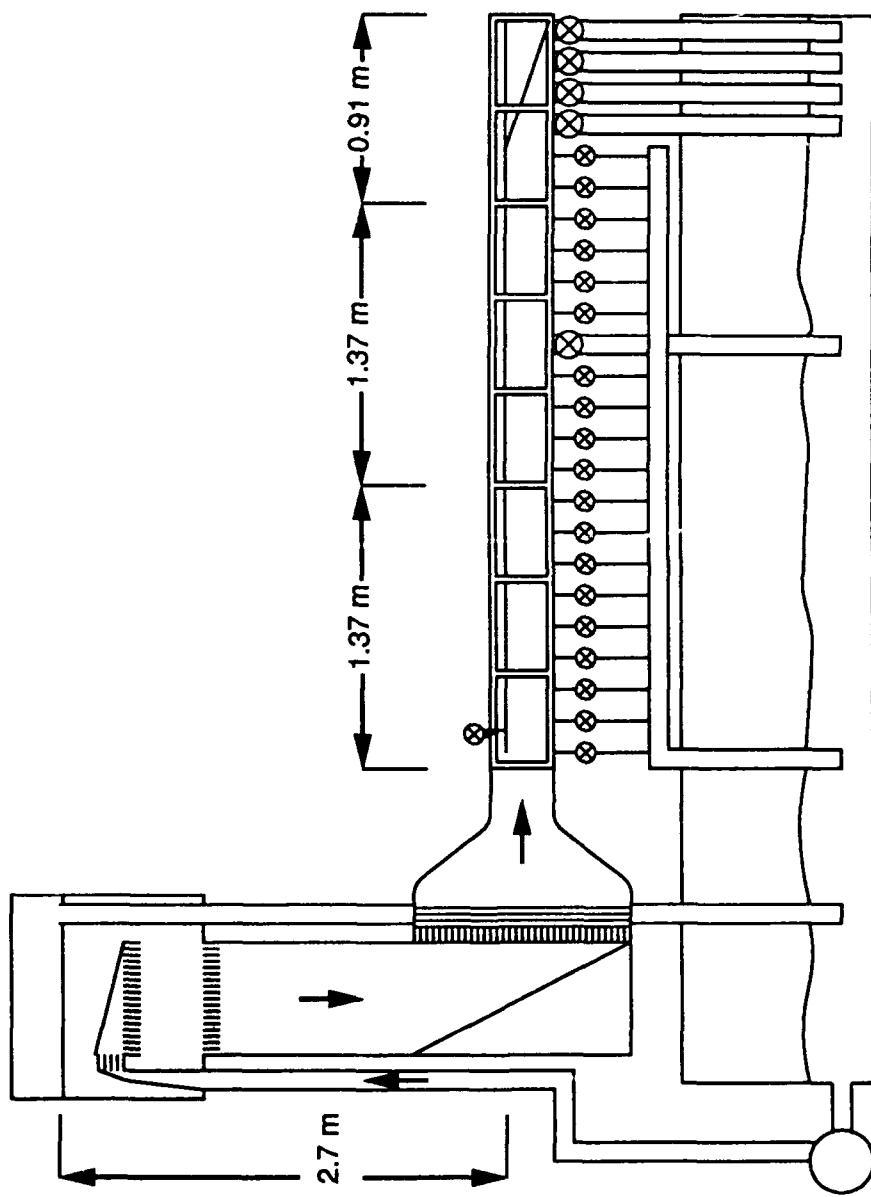
Figure 4.1 Schematic of unsteady flow facility
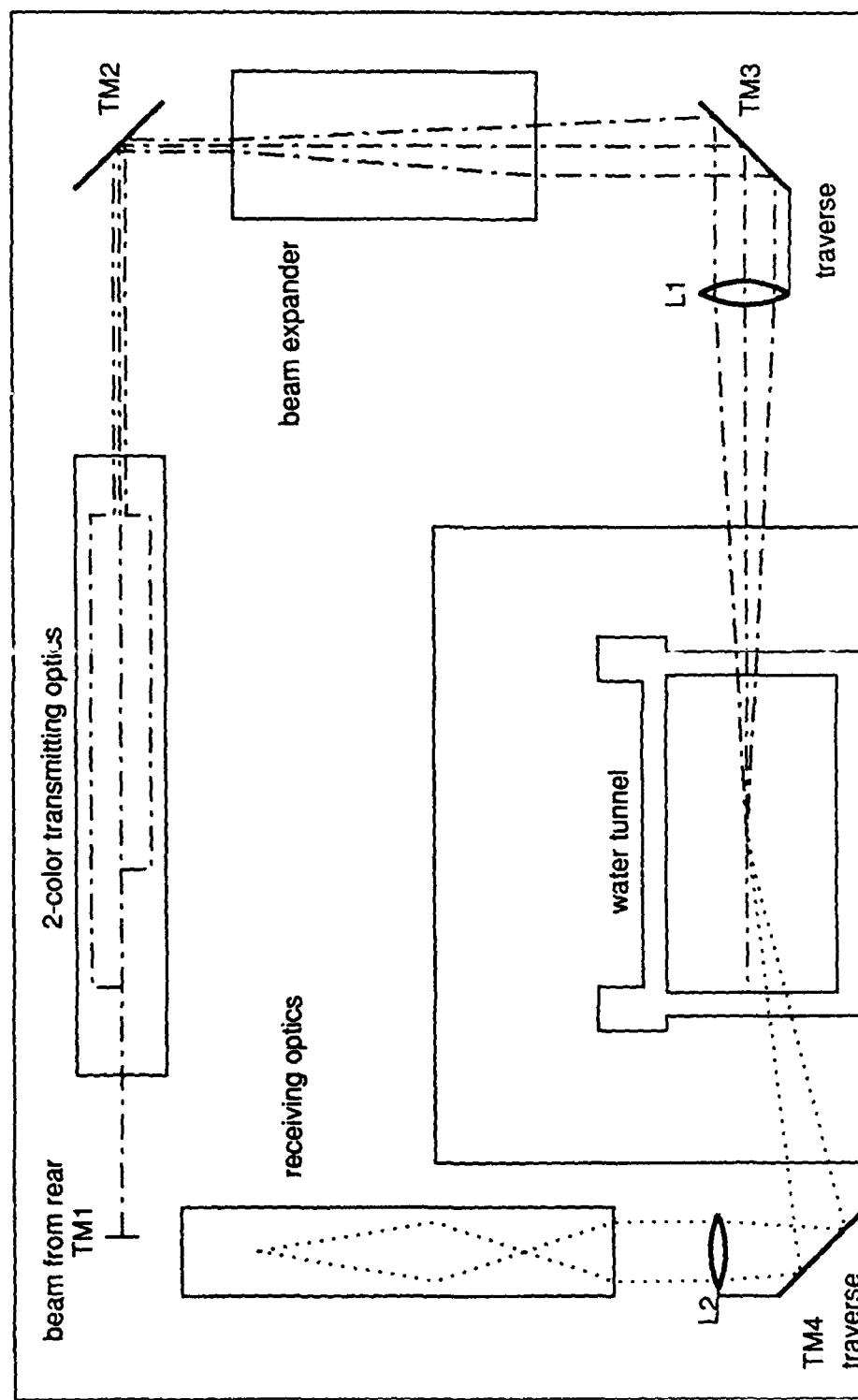
Figure 4.2 Two-component LDA system

2-Color Transmitting Optics

A   Rotating Mount, TSI 9178-1
B   Dichroic Color Separator, TSI 9112
C   Beam Splitter, TSI 9115-1
D   Beam Displacer, TSI 9174
E   Beam Splitter, TSI 9115-1X
F   Bragg Cell, 514.5 nm, TSI 9182-12
G   Bragg Cell, 488 nm, TSI 9182-11
H   Beam Steering Module, TSI 9175
J   Beam Displacer, TSI 9171
J   Beam Spacer, TSI 9114-22
K   Rotating Mount, TSI 9179
L   Field Stop System, TSI 9143
M   Ring Mount, TSI 9176
N   Color Separator (Scattered), TSI 9144A
O   PMT (2), TSI 9162

Receiving Optics

To PMTs (O)

Figure 4.3 Two-color transmitting and receiving optics

44

Standard Dichroic Color Separator (TSI 9112)


```
— · — · blue-green
—  —  green
· · · · · · · blue
```
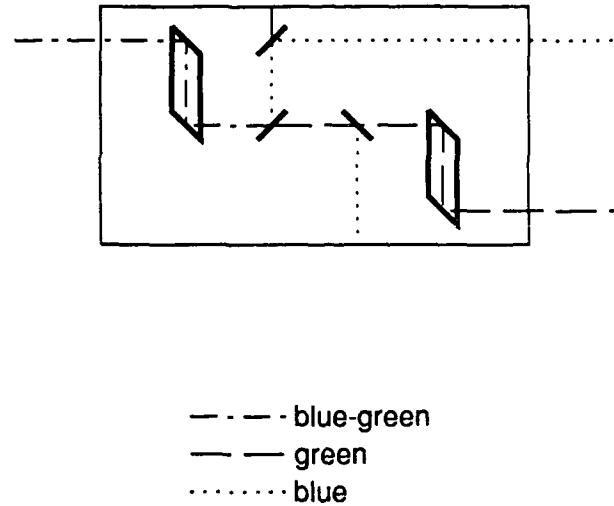
Modified Dichroic Color Separator (prisms removed)
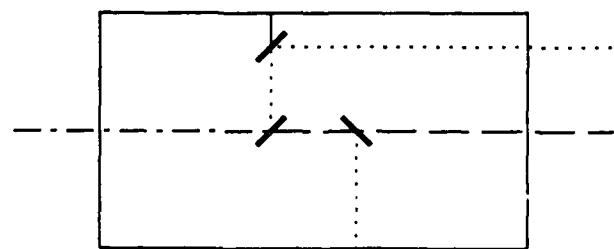
Figure 4.4 Dichroic color separator
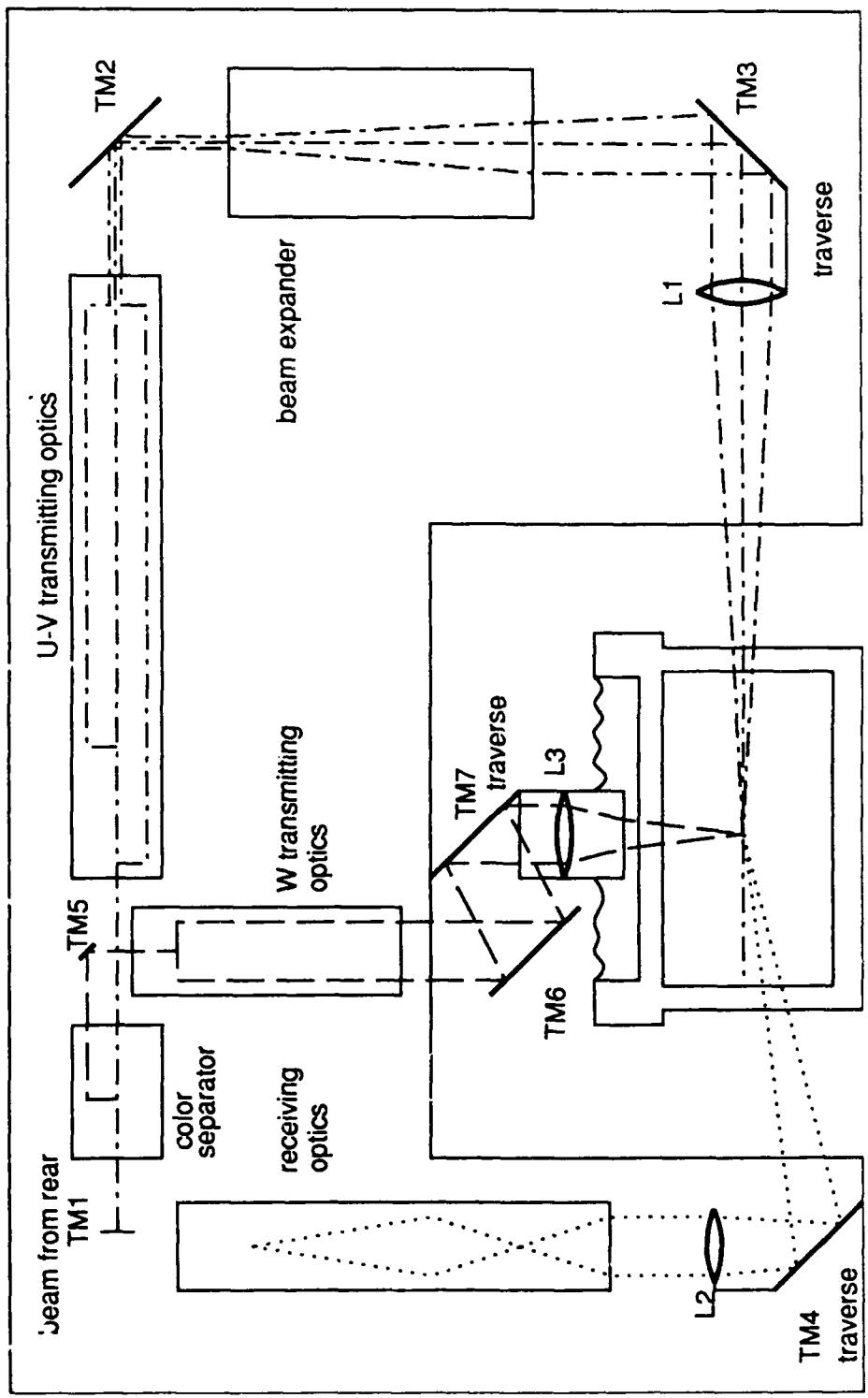
Figure 4.5 Three-component LDA system

46

U-V Transmitting Optics
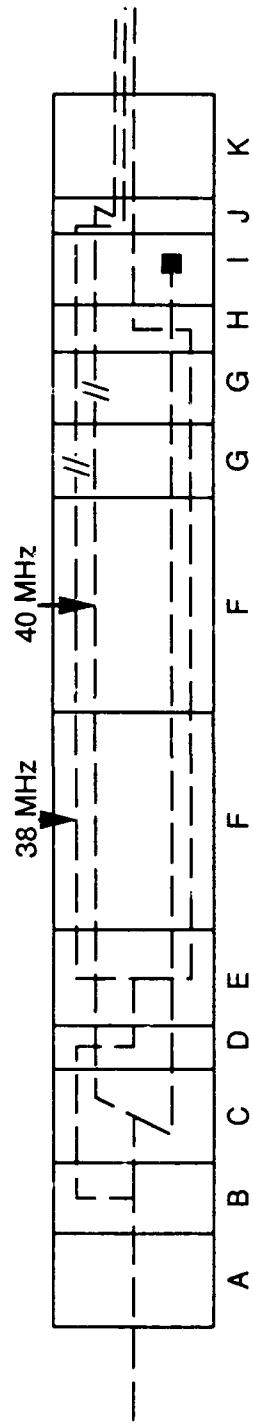
W Transmitting Optics
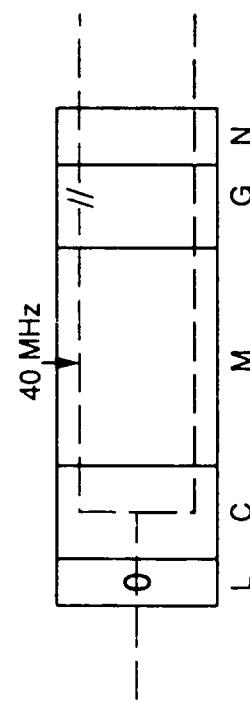
A — Rotating Mount, TSI 9178-1
B — Offset Beamsplitter, TSI 9116-1
C — Beam Splitter, TSI 9115-1
D — Beam Displacer, TSI 9174
E — Beam Splitter, TSI 9115-1X
F — Bragg Cell, 514.5 nm, TSI 9182-12
G — Beam Steering Module, TSI 9175
H — Beam Displacer, TSI 9171
I — Beam Stop, TSI 9181-2
J — Beam Spacer, TSI 9114-22
K — Rotating Mount, TSI 9179
L — Polarization Rotator, TSI 9102-11
M — Bragg Cell, 488 nm, TSI 9182-11
N — Ring Mount, TSI 9176

Figure 4.6 Three-component transmitting optics

47
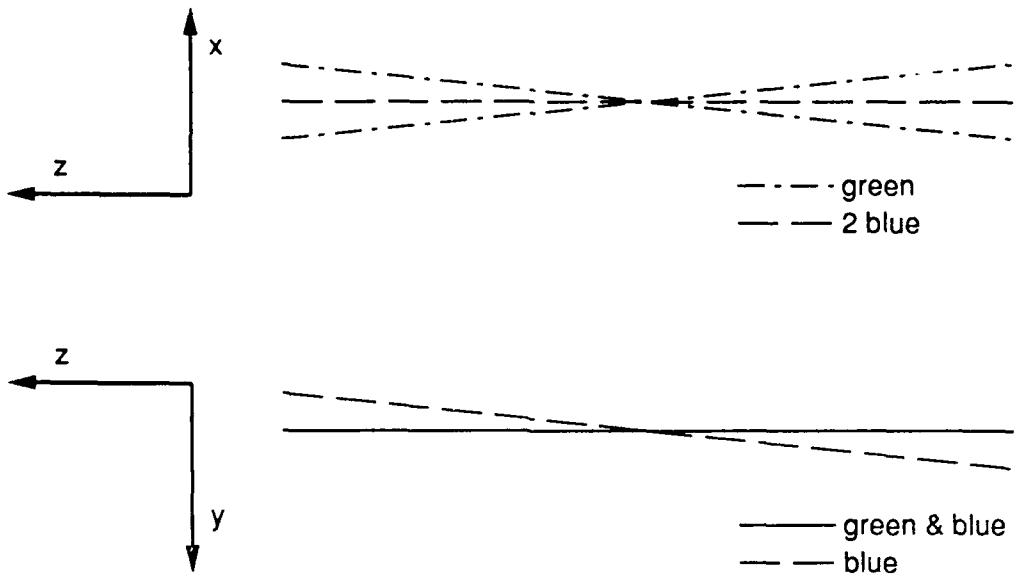
Figure 4.7a Beam configuration for two-component system
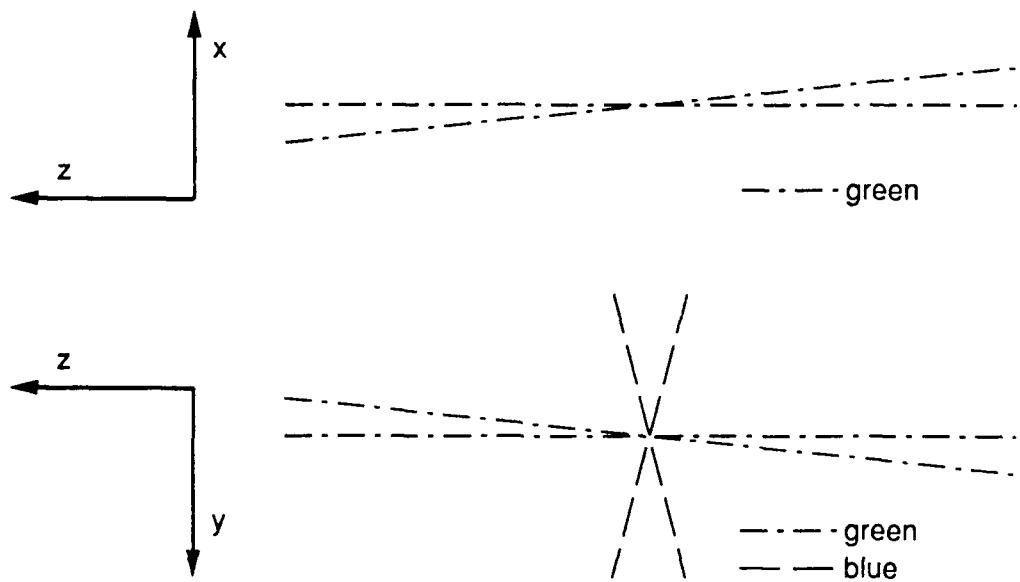
Figure 4.7b Beam configuration for three-component system

Table 4.1 Summary of Two-Component LDA Components

Component	Description	Part Number
TM1	1in dia. mirror, 45°	TSI 9109
TM2	4in dia. mirror	NRC 630A-4
TM3	6in dia. mirror	NRC 630A-6
TM4	4in dia. mirror	NRC 630A-4
L1	450mm lens/178mm dia.	TSI 9169-450
L2	500mm lens/83mm dia.	TSI 9167-500
Transmitting Optics	see figure 4.3	
Beam Expander	3.75X	TSI 9189
Receiving Optics	see figure 4.3	

Table 4.2 Summary of Additional Three-Component LDA Components

Component	Description	Part Number
TM5	1in dia. mirror, 45°	TSI 9109
TM6	4in dia. mirror	NRC 600A-4R
TM7	4in dia. mirror	NRC 600A-4R
L3	200mm lens/76mm dia.	NRC KPX229AR.14
Color Separator	see figure 4.4	
U-V Transmitting Optics	see figure 4.6	
W Transmitting Optics	see figure 4.6	
Receiving Optics	see figure 4.3	

What we have to learn to do we learn by doing.

— Aristotle, 325 B.C.

5. Facility Validation

Facility validation involves verification that the quality of the flow meets the basic requirements of the experiment and that the measurement techniques and instrumentation are yielding correct, consistent information. The key issues regarding quality of the flow are repeatability of the steady, mean flow; streamwise uniformity of the velocity for zero pressure gradient work; low freestream turbulence; spanwise uniformity in the flow; and the absence of any vortex-type flow structures that would detract from the two-dimensional nature of the boundary layer. Issues regarding the velocity measurements are the fundamental accuracy of the absolute magnitude of the mean velocity, the correctness of the RMS fluctuating quantities, and the proper spatial and temporal resolution when two fluctuating quantities are correlated. To verify the flow quality one would like to have a well-proven velocity measurement system, and conversely to verify the LDA system one would like to have a well known, well behaved flow. In this program, where both the water channel and the LDA optical configuration were new, a systematic validation program was required to verify both the quality of the flow and the credibility of LDA measurements.

5.1 Characterization of the Freestream Velocity

For initial validation of LDA measurements, the water channel simulated a nominally steady, two-dimensional flow over a flat plate. First, the flow bypass around the leading edge was adjusted by flow visualization for optimum stagnation conditions at the leading edge. Then the opposite wall suction was adjusted for a nominally uniform freestream velocity, using the LDA as an indicator of uniform relative velocity. With a relatively good flow along a single streamline, then, the measurement volumes of the TSI system and the Dantec system were moved within several centimeters of each other for comparison of absolute velocity measurements.

51

Although velocity measurement with an LDA system is fundamental in nature, (that is, the time to traverse between fringes in an interference pattern is measured rather than inferred from a secondary measurement such as heat transfer) careless determination of crossing angles can lead to errors as large as 10% in the absolute measurement of velocities. By projecting the transmitting beams of the LDA through the channel wall and across the width of the lab, lengths from $20cm$ to $1.7m$ could be used to determine the crossing angles, which typically are between $6°$ and $12°$, to a precision of about 1%. After this careful calibration, the measurements from the TSI and Dantec systems agreed with each other to within about 0.5%.

RMS Measurements. Since two very different LDA systems were able to independently verify the absolute magnitude of velocity measured by the other system, confidence in the mean value of LDA measurements is very high. The remaining question about fundamental LDA measurements was the RMS value of fluctuations in the u-component of velocity, $\overline{u'^2}$, and what it implied about the freestream turbulence intensity, $\sqrt{\overline{u'^2}}/U$. While some of the data presented in subsequent chapters indicate that the apparent turbulence intensity is about 1% to 1.5%, studies of various LDA configurations indicated that the actual turbulence intensity of the water channel is lower, about 0.5% to 0.7%. The difference appears to come from electronic noise introduced with the use of Bragg cells and the down-mixing circuitry. This was demonstrated by setting up the TSI optics in a simple two-beam system with no color separation and no Bragg cells. With careful adjustment of the collimator, the freestream turbulence level was measured to be 0.5% to 0.7% at a freestream velocity of $0.7m/sec$. Without changing any flow conditions, the optics were then modified to a simple two-beam system *with* a Bragg cell. The apparent freestream turbulence intensity then changed to between 1% to 1.5%, and no optimizing of the system seemed to improve that. Since the turbulence intensities inside the boundary-layer are much greater than this, this limitation in the LDA system was deemed to be acceptable.

Spanwise Uniformity of the Flow. Early in the testing of the new water channel, studies of the spanwise uniformity revealed several regions in the $-z$ portion of the channel where the boundary layer was thicker than over the rest of the span. The problem was traced to leakage from the leading edge bypass back into the dye slot near the leading edge. When this was corrected, the mean velocity showed no major spanwise variations. These results are shown in figure 5.1. The spanwise uniformity and symmetry of the flow behind the vortex generators under unsteady flow conditions will be presented in chapter 6, both for mean velocities and RMS measurements.

5.2 Mean Velocity Measurements in a Steady, Zero Pressure-Gradient Turbulent Flow

With the fundamental LDA issues resolved, the next logical step to validate was the behavior of the turbulent boundary-layer in a zero pressure-gradient flow, and the ability of the LDA system to measure the mean two-dimensional velocity components. Figure 5.2 shows the streamwise velocity history of the flow in the configuration used for the following validation data. The opposite wall suction was adjusted for a constant freestream velocity at about $0.5 m/sec$. Figure 5.2 shows that the variation from this mean value is less than 0.5% throughout the entire test section.

During data acquisition, a steady zero pressure-gradient profile is taken at each spanwise position in order to establish the apparent position of the LDA measuring volume and to determine the integral boundary-layer parameters. In figure 5.3, one such profile is shown in wall coordinates. The outer region is fit to Coles' Law,

$$u^+ = \frac{1}{0.41}\ln(y^+) + 5.0 + \frac{\Pi}{0.41}W\left(\frac{y}{\delta}\right), \tag{5.1}$$

where

$$W\left(\frac{y}{\delta}\right) = 2\sin^2\left(\frac{\pi}{2}\frac{y}{\delta}\right) \tag{5.2}$$

53

while the linear sublayer is fit to

$$u^+ = y^+. \tag{5.3}$$

In each profile that is analyzed, the apparent position of the measuring volume is first inferred from the best fit of a line to the inner points. Then, the outer region is fit by linear regression to equation (5.1), which determines the values of δ and u_τ. It is apparent from the figure that the data fits the equations very well. In addition, the value of Π from the linear regression for the case shown was 0.489. This value is relatively close to the value of 0.55 suggested by Coles (1956) for a zero pressure gradient turbulent boundary layer. Finally, figure 5.3 also shows very good agreement with predictions by Spalart (1986). Therefore, the mean values of the streamwise velocity component, u, appear to be very consistent with all predictions.

The v-component of the mean velocity is much more difficult to measure, since a very small u-contamination (less than $0.5°$) or a slight error in the value of the downshift frequency as read by the data acquisition system can completely obliterate the correct mean value of v. Figure 5.4 shows v profiles taken at several spanwise locations. These profiles are in general agreement with the profiles reported by Brereton and Reynolds (1987).

The w-component of the mean velocity is also difficult to validate, since it is not present in a two-dimensional flow. However, the LDA side-scatter measuring volume can be oriented to measure $u \cos \theta + w \sin \theta$, where $\theta \simeq 45°$. By orienting the w side-scatter optics at $45°$ in a two-dimensional flow, the u velocity component was measured simultaneously with the normal forward scatter u optics and with the $45°$ side-scatter w optics. The two values agreed within the 1% uncertainty of the velocity calibrations.

5.3 Measurement of Second Order Statistics

The most difficult measurements to make, and hence the most difficult to validate, are the fluctuating quantities and correlations in a turbulent flow. After

setting up an LDA system, one can easily obtain measurements that have a measureable fluctuation, but getting meaningful turbulent quantities takes some care. The key indicators of good turbulent measurements are the frequency distributions or power spectra, known values of correlations between u' and v' in shear layers, and published results for standard experiments such as steady flow over a flat plate.

Measurement of Normal Reynolds Stresses. The best "first test" of the goodness of fluctuating quantities is to look at the spectral content of the apparent turbulent kinetic energy. Figure 5.5a shows the energy spectrum of $\overline{u'^2}$ and $\overline{v'^2}$ under steady flow at a position, $y/\delta \simeq 0.4$, and figure 5.5b shows the same for $\overline{w'^2}$. The $\overline{u'^2}$ spectrum shows a roll-off at about $1 Hz$. Consistent with Hinze's (1981) discussion of homogeneous shear-flow turbulence, there is a region where the slope is -1 and a region where it is $-5/3$. The $\overline{v'^2}$ spectrum shows a roll-off at a somewhat higher frequency and thus, within the frequency limitations of the FFT taken, only the region with slope of -1 is seen.

Both the $\overline{u'^2}$ and the $\overline{v'^2}$ spectra and the relationship between the two are virtually identical to those reported by Brereton and Reynolds (1987). In addition, the spectra for $\overline{v'^2}$ and $\overline{w'^2}$ are very similar in magnitude and shape, and this is consistent with the calculations of Kim, Moin, and Moser (1987) in the outer portion of the boundary layer. Finally, for an unsteady driven flow, it is important to compare the spectra of the driven turbulent flow with that of the steady flow. Figure 5.6 shows the spectra of $\overline{u'^2}$ while the flow is driven at $0.5 Hz$. While the flow shows a clear, sharp peak at $0.5 Hz$, the roll-off location and characteristic slopes have not changed from the steady flow spectra.

One final evaluation of the normal stresses is comparison with published results for turbulent steady flow over a flat plate. These profiles are shown in figure 5.7a and 5.7b along with the flat plate simulation results of Spalart (1986) for a momentum thickness Reynolds number of 1410. Except for some wall interference with values of w'/u_τ, the two are in very good agreement. Note that figure 5.7a shows good near wall agreement. For comparison in the outer region of the boundary layer,

55

the results are replotted in figure 5.7b against y/δ, to accomodate the difference in Reynolds numbers ($\mathrm{Re}_\theta = 1840$ for this program). The values shown for u'/u_τ and v'/u_τ are also in very good agreement with the experimental results by Laufer (1950) and Brereton and Reynolds (1987).

Shear Stress Measurements. Measurement of the shear stresses adds another level of complexity. The *one-point correlations* will only correlate well if the corresponding measuring volumes are indeed located at nearly the *same point* in space. Blackwelder (1983) noted that the active length of a hot-wire probe needed to be on the order of $y^+ \leq 20$ to obtain good near-wall correlations. For a properly aligned LDA system, the diameter of the measuring volume is normally much less than this, but the length of the measuring volume is much greater, so a pinhole is used to limit this length. While an off-axis forward-scatter system places some rather severe constraints on the pinhole selection, a combination of side-scatter and forward scatter places additional conflicting constraints on the pinhole requirements.

Figure 5.8 demonstrates why there are conflicting requirements on selection of the optimum pinhole. The critical issue is the size of the *image* of the limiting aperature as it is projected onto the measuring volume. Figure 5.8 shows that the pinhole image is extended by the inverse of the cosine of 15° or a factor of 1.04 as it is projected on the side-scatter measuring volume, but it is extended by the inverse of the sine of 15° or a factor of 3.85 as it is projected on the forward-scatter measuring volume. Therefore, to obtain the same effective size of measuring volumes, different pinhole sizes are required. The following are the key factors and decisions that went into the selection of pinholes:

(1) There are three pinhole locations, the blue PMT, the green PMT, and the field-stop system. Also, the imaging optics of the PMTs magnify the pinhole image by a factor of 2.5, while the field stop system magnifies the pinhole image by a factor of 5.

56

(2) Correlations between u and v are the most difficult because the maximum $u'v'$ values occur in small eddies very close to the surface. This task is simplified somewhat in the three-component system because the same PMT is used for both u and v. Therefore, a 50 micron pinhole placed in the green PMT, with a magnification of 2.5 and a projection factor of 3.85, has an image length of $481 microns$. For the run conditions of this experiment, the measurement volume length in wall coordinates is therefore $\ell^+ = 9$, which should be satisfactory for good $\langle u'v' \rangle$ correlations. Observations of the doppler bursts on a dual-trace storage oscilloscope confirmed that the u and v trackers were both tracking the same bursts.

(3) In a similar fashion, a $200 micron$ pinhole placed in the blue PMT, with a magnification of 2.5 and a projection factor of 1.04, has an image of $520 microns$ which in wall coordinates is $\ell^+ = 10$.

(4) The field-stop system will control the spatial proximity of the w measuring volume to the u and v measuring volumes. Due to the difference in magnification factors, a $100 micron$ pinhole in the field-stop system also results in a $520 micron$ image on the side-scatter optics. The best compromise possible was to let the smaller image of the green PMT $50 micron$ pinhole *look through* the center of this larger pinhole. In practice, since traversing requires near perfect alignment of two sets of transmitting optics and one set of receiving optics, the $100 micron$ pinhole in the field-stop system would have required correction of the alignment during the traverse. Since the unsteady profiles each took 26 hours of continuous data acquisition, this was not acceptable, and a $200 micron$ pinhole had to be used in the field-stop system.

(5) The net result of the pinhole tradeoffs is that the u and v measuring volumes are co-located with an effective length of $\ell^+ = 9$. The w measuring volume has an effective length of $\ell^+ = 10$, but at worse case the u and v measuring volumes could be offset from the w measuring volume by as much as $\ell^+ = \pm 20$. This tradeoff was deemed to be acceptable since the correlations of u and v with w generally would result from larger scale structures in the outer boundary layer induced by the

57

vortex generators. Also, this measuring volume is still small compared to the X-wire probes used by Pauley and Eaton (1988) who still obtained very good correlations.

A key indicator of quality shear stress measurements as reported by both Barlow and Johnston (1985) and Brereton and Reynolds (1987), is the behavior of correlations between u' and v' very near the test surface. In figure 5.9, the correlation coefficient, $-\overline{u'v'}/\sqrt{\overline{u'^2}}\sqrt{\overline{v'^2}}$, is plotted along with the results from Spalart (1986). In figure 5.10, v'/u' is plotted in a similar manner, for values of y^+ near the wall. Barlow observed that, with properly aligned optics, the correlation coefficient reached a value of 0.4 by y^+ values of 10 to 20. In addition, he observed that the ratio of v'/u' remained linear as y decreases until y^+ values of about 7 to 10. In figure 5.9 the correlation coefficient reaches a value of 0.4 at a y^+ value of 40 and in figure 5.10 the ratio of v'/u' remains linear as y decreases until a y^+ value of about 20. While these values are about three times larger than the y^+ values reported by Barlow, the friction velocity for this flow is also about three times larger than Barlow's flow. Therefore, the two trends appear to occur at the same location in actual physical space. Since this distance is on the order of several beam diameters, the limitation may be physical interference between the test surface and the transmitted beams. Given this qualification or stipulation, the correlations between u' and v' shown in figures 5.9 and 5.10 indicate that the cross-terms and correlations are valid.

5.4 Measurement of Turbulent Triple Products

The new data acquisition system provided the capabilty of collecting the third-order statistics, even for phase-averaged unsteady conditions, without any penalties to the other data collection requirements. Since these measurements were available basically "free of charge", they were collected for whatever information they could provide. Klewicki and Falco have recently published results on the times required for statistical convergence of various turbulent quantities. In general, they indicate that the third order statistics take four times longer to converge than the second order

58

statistics. The steady triple product measurements of the terms normally found in a two-dimensional boundary layer appear to be nearly converged, and are in general agreement with results published by Murlis, Tsai, and Bradshaw (1982) and Pauley and Eaton (1988). These results, shown in figures 5.11 and 5.12, differ only in that they show peak values near the surface not shown in the other experiments. The location of these peak values, however, seems consistent with the fact that maximum production occurs very near the surface. Finally, for unsteady flows this program accepted a compromise on convergence of the second order statistics and had to do without the triple products because of the unacceptably long sampling times required for convergence.

5.5 Uncertainty Analysis

Estimates of the uncertainty in each of the measured and calculated quantities were made, and are summarized in Table 5.1. These estimates are given at the 95 percent confidence level according to the recommendations of Kline and McClintock (1953) and follow the recent procedural recommendations of Moffat (1988). The details of this process are shown in Appendix A. Because the uncertainty analysis requires insightful judgement, guidance was also sought from similar recent programs here at Stanford, in particular Brereton and Reynolds (1987), Pauley and Eaton (1988), and Eaton and Johnston (1980).

Table 5.1 Uncertainty Estimates for Measured Variables

| Variable	Typical Value	Uncertainty Interval	
		Absolute	Relative
$\langle U \rangle$	$1.0 \cdot 10^{-1}$	$6.3 \cdot 10^{-3}$	$6.3 \cdot 10^{-2}$
$\langle U \rangle$	$1.0 \cdot 10^{-0}$	$1.5 \cdot 10^{-2}$	$1.5 \cdot 10^{-2}$
$\langle V \rangle$	$3.0 \cdot 10^{-2}$	$1.2 \cdot 10^{-2}$	$3.9 \cdot 10^{-1}$
$\langle V \rangle$	$1.5 \cdot 10^{-1}$	$1.5 \cdot 10^{-2}$	$9.8 \cdot 10^{-2}$
$\langle W \rangle$	$3.0 \cdot 10^{-2}$	$1.2 \cdot 10^{-2}$	$3.9 \cdot 10^{-1}$
$\langle W \rangle$	$5.0 \cdot 10^{-2}$	$1.5 \cdot 10^{-2}$	$2.9 \cdot 10^{-1}$
$\langle u'u' \rangle$	$1.5 \cdot 10^{-2}$	$3.7 \cdot 10^{-3}$	$2.5 \cdot 10^{-1}$
$\langle v'v' \rangle$	$1.5 \cdot 10^{-2}$	$3.7 \cdot 10^{-3}$	$2.5 \cdot 10^{-1}$
$\langle w'w' \rangle$	$1.5 \cdot 10^{-2}$	$3.7 \cdot 10^{-3}$	$2.5 \cdot 10^{-1}$
$\langle u'v' \rangle$	$2.5 \cdot 10^{-3}$	$9.1 \cdot 10^{-4}$	$3.6 \cdot 10^{-1}$
$\langle u'w' \rangle$	$5.0 \cdot 10^{-3}$	$1.8 \cdot 10^{-3}$	$3.6 \cdot 10^{-1}$
$\langle v'w' \rangle$	$2.5 \cdot 10^{-3}$	$9.1 \cdot 10^{-4}$	$3.6 \cdot 10^{-1}$
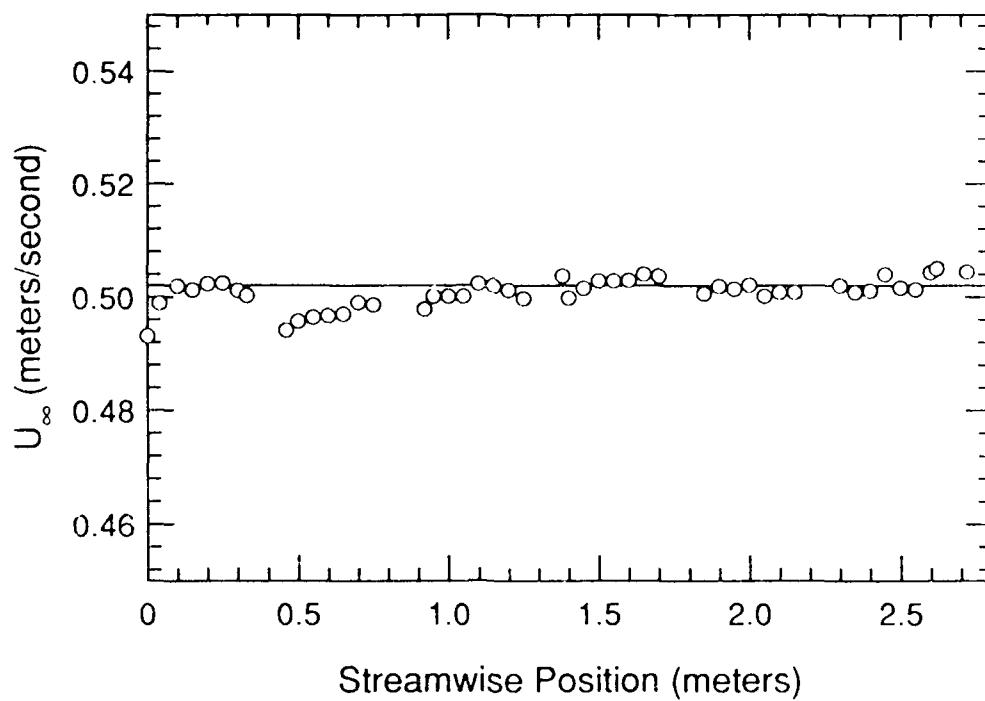
Figure 5.1 Streamwise velocity history
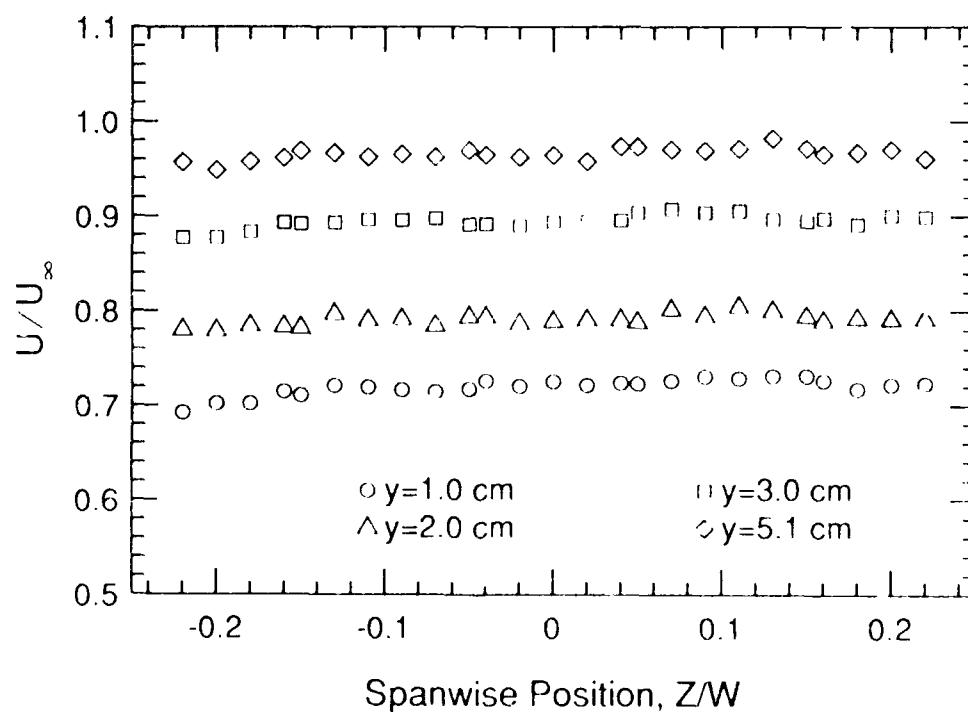
Figure 5.2 Spanwise uniformity of u

61
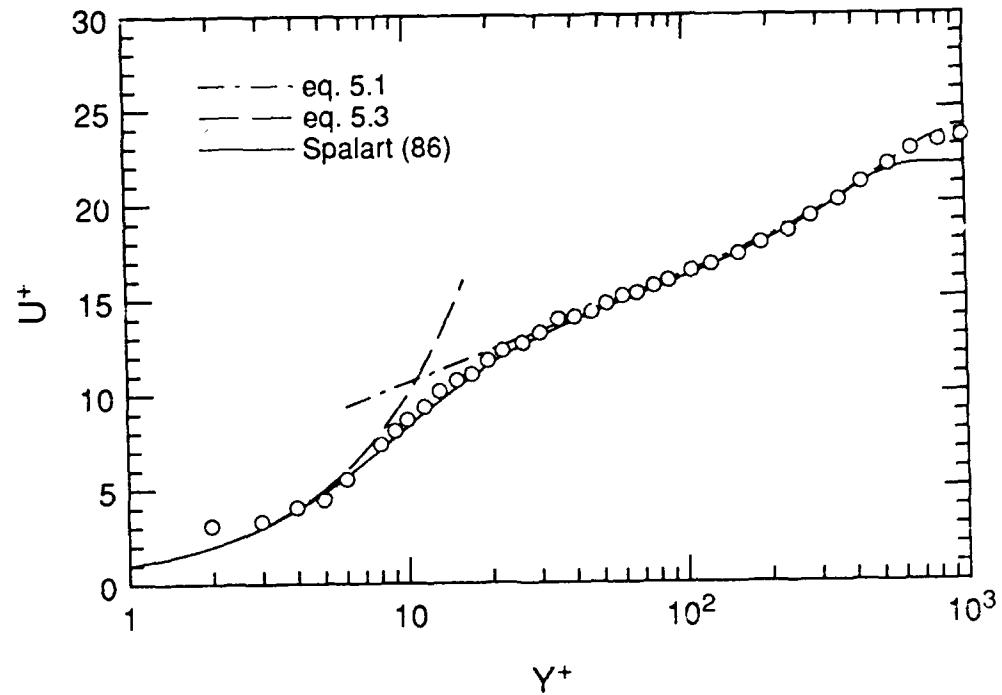
Figure 5.3 Mean profiles in wall coordinates at zero pressure gradient
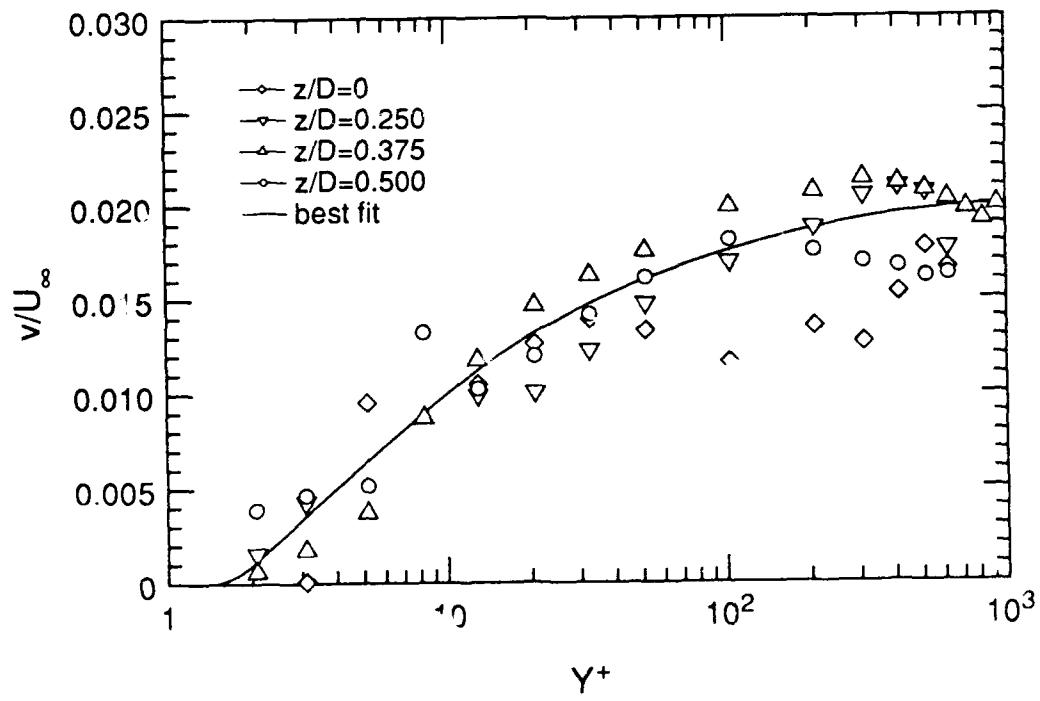
Figure 5.4 Mean profiles of v at zero pressure gradient
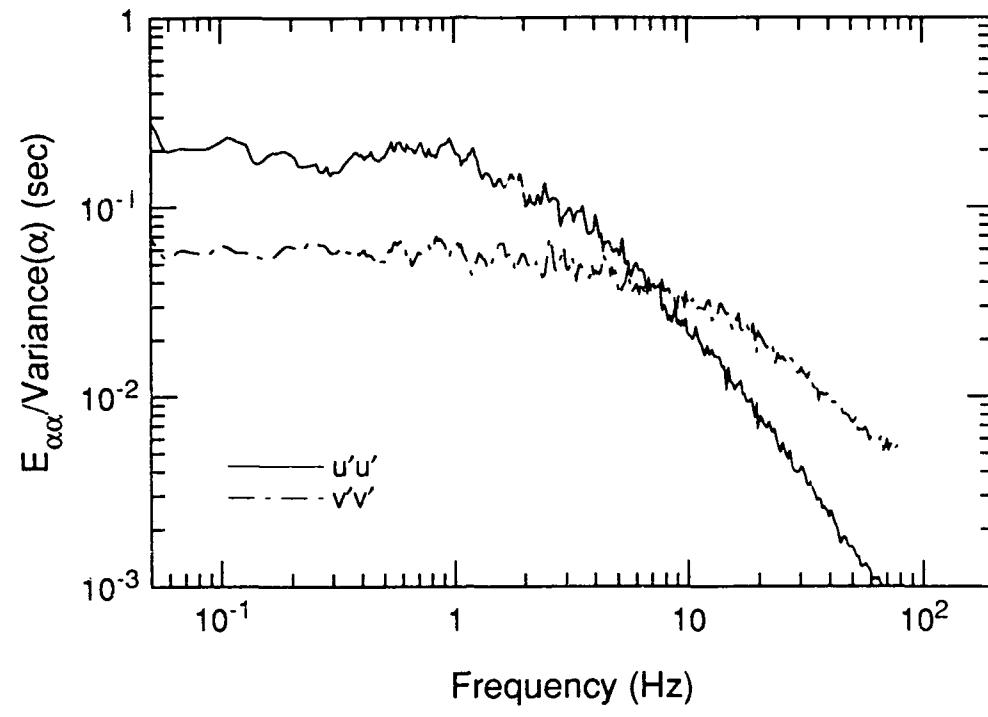
Figure 5.5a Energy spectra for $u'u'$ and $v'v'$
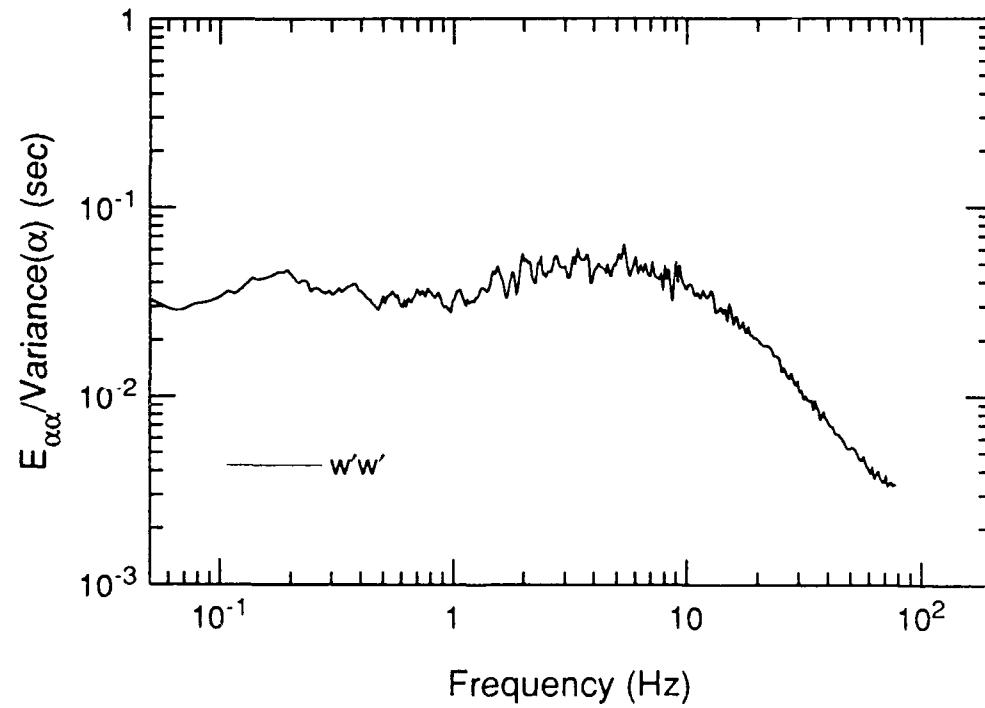

Figure 5.5b Energy spectra for $w'w'$
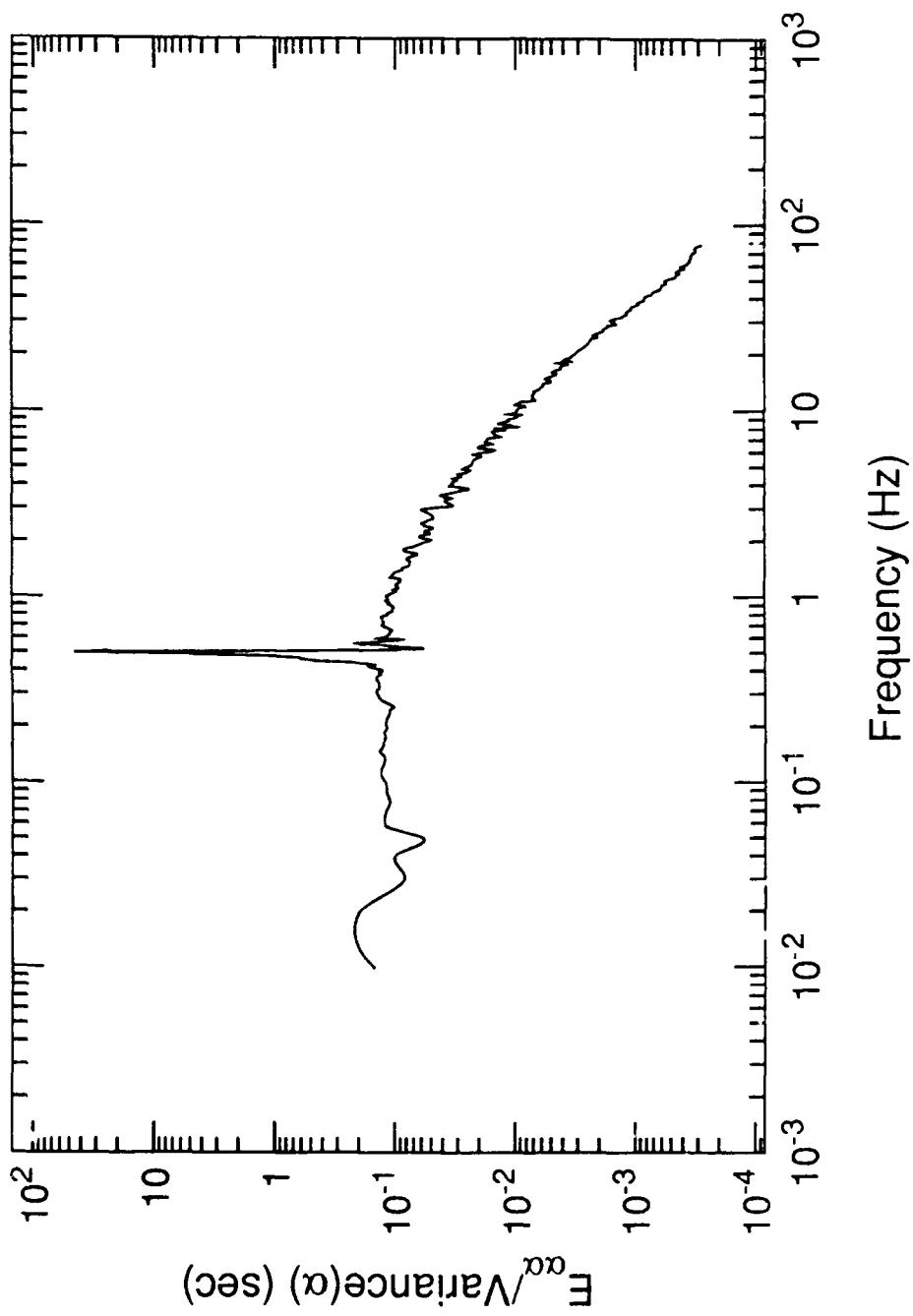
Figure 5.6 Energy spectra for $\overline{u'u'}$ with flow driven at $0.5Hz$
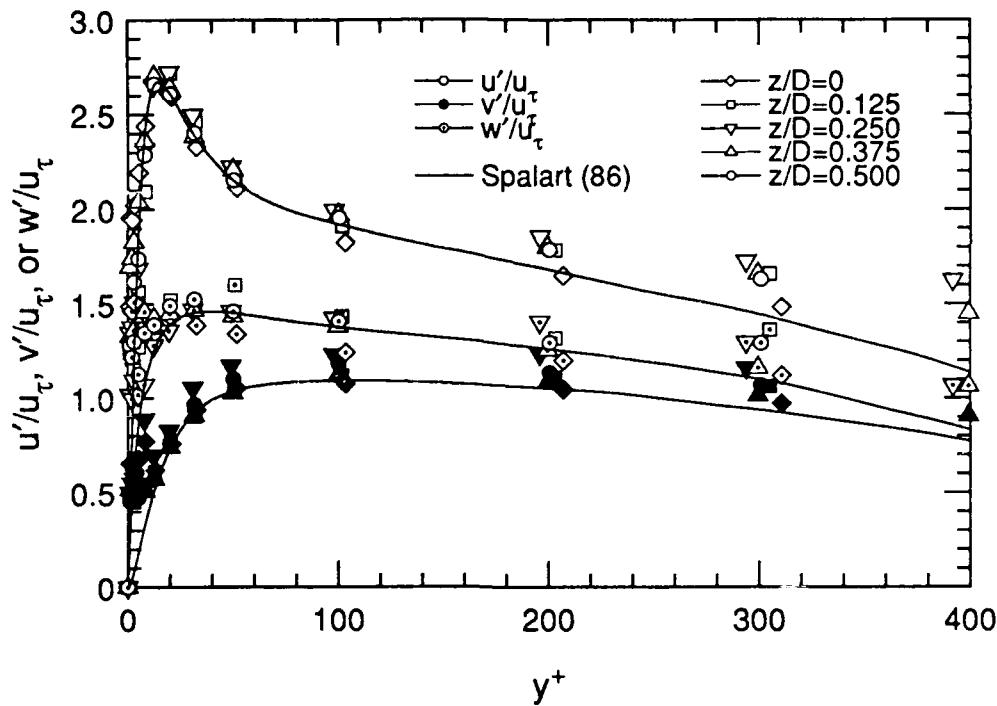
Figure 5.7a u'/u_τ, v'/u_τ, and w'/u_τ versus y^+

Figure 5.7b u'/u_τ, v'/u_τ, and w'/u_τ versus y/δ

65
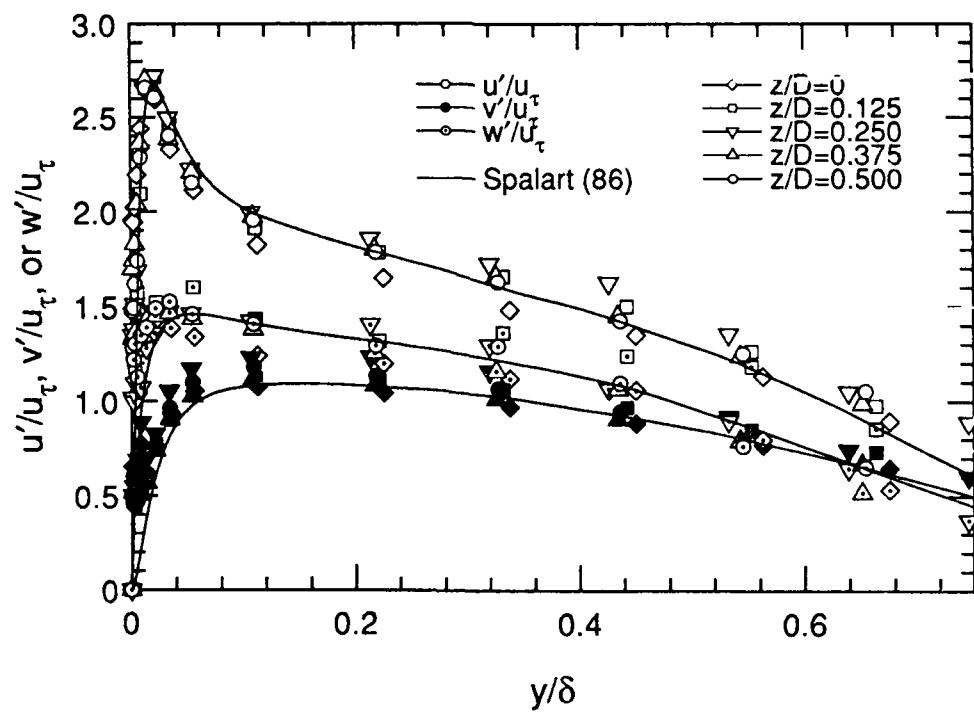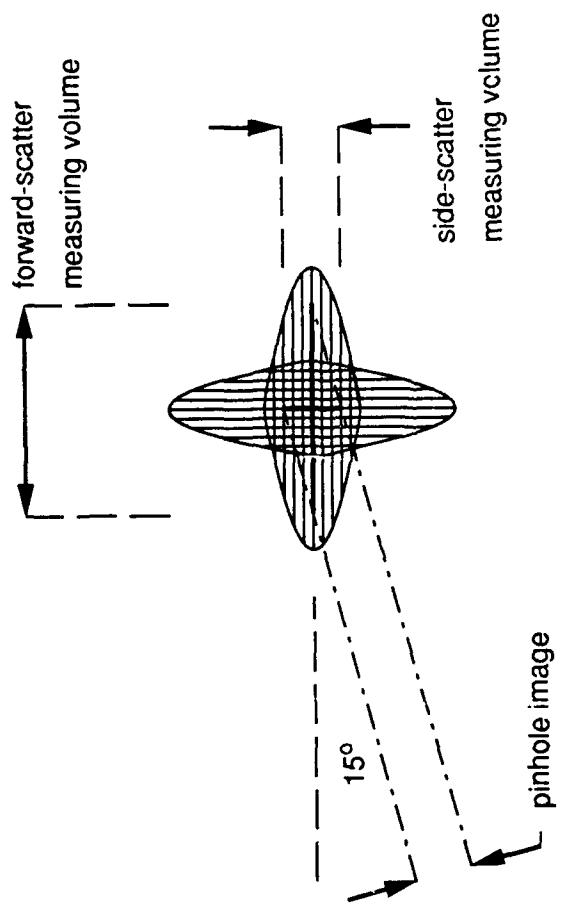
Figure 5.8 Pinhole requirements for forward scatter and side scatter
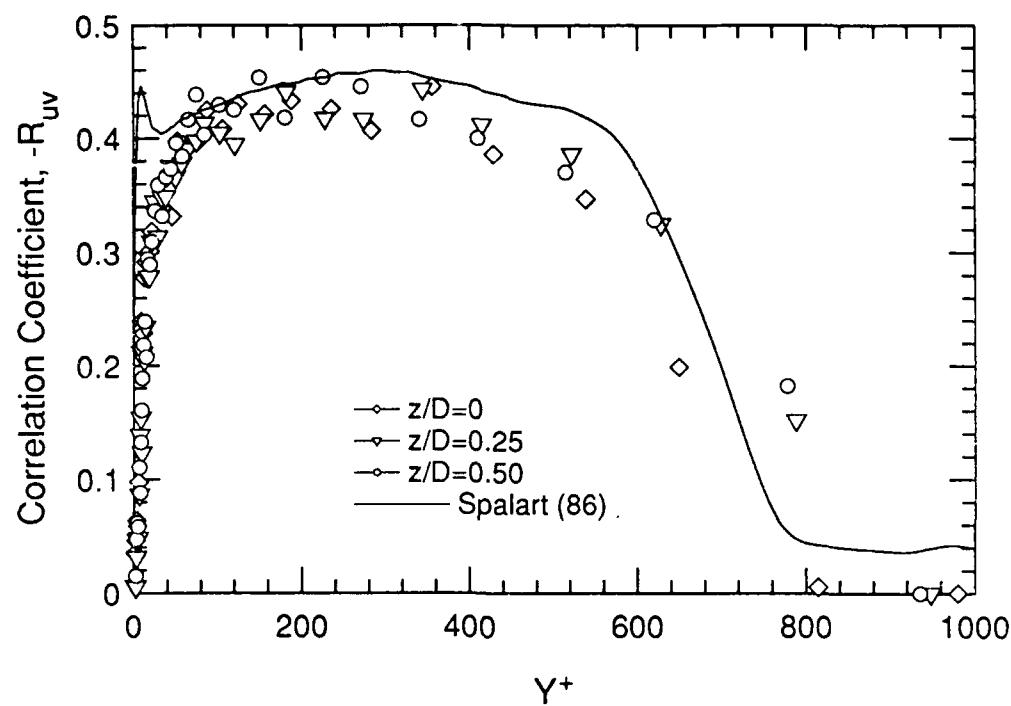
Figure 5.9 Correlation coefficient for $\overline{u'v'}$ at zero pressure gradient
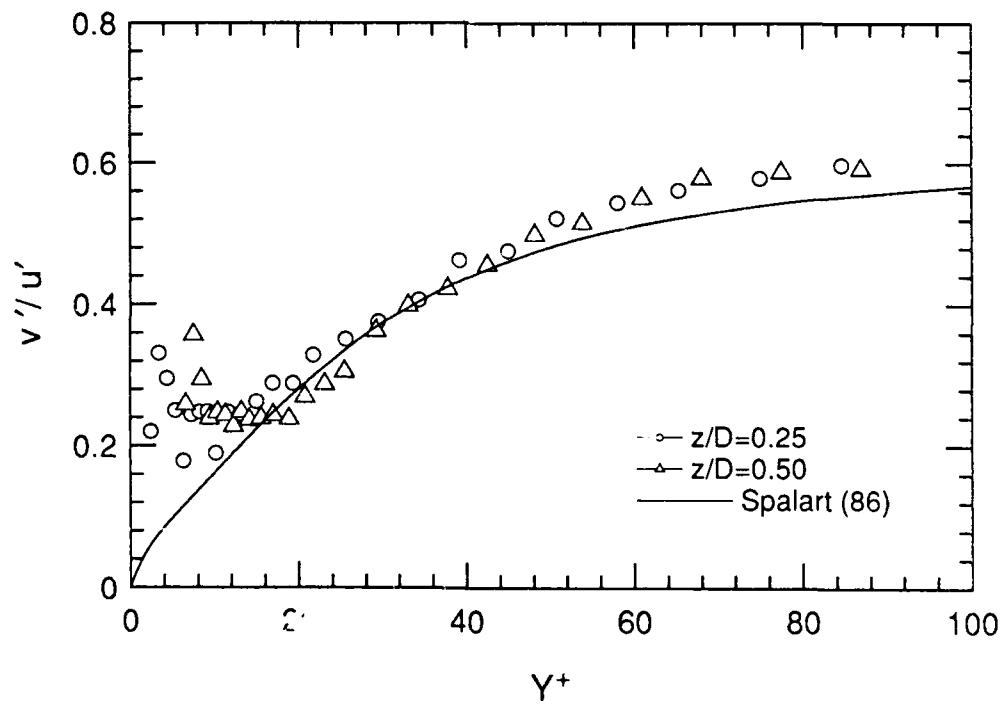

Figure 5.10 Ratio of v'/u' at zero pressure gradient

67
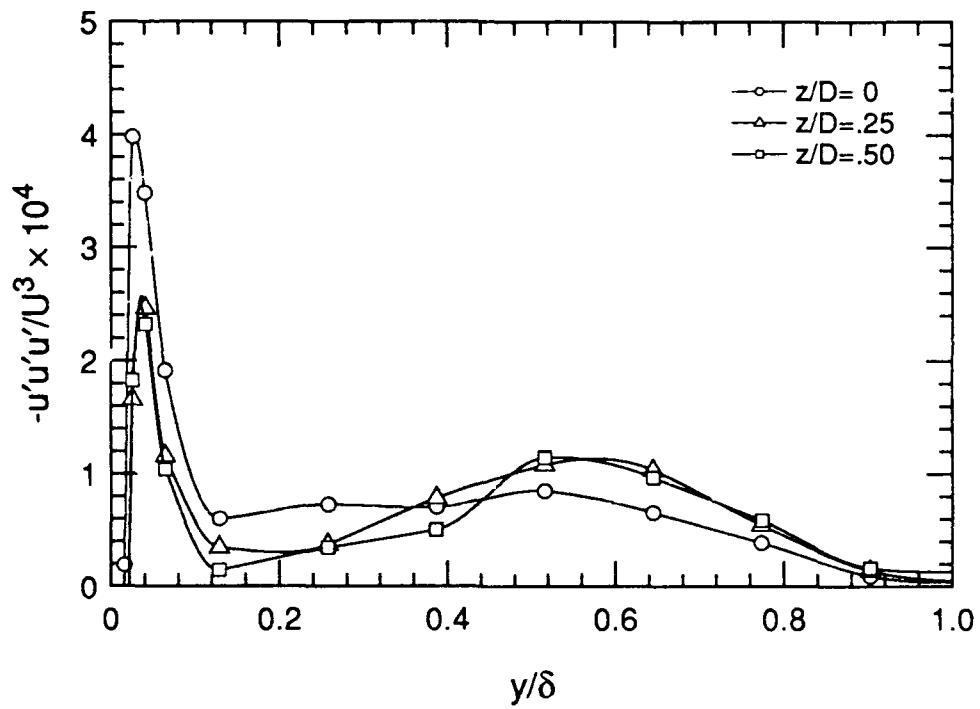
Figure 5.11 $\overline{u'u'u'}/U_\infty^3$ at zero pressure-gradient
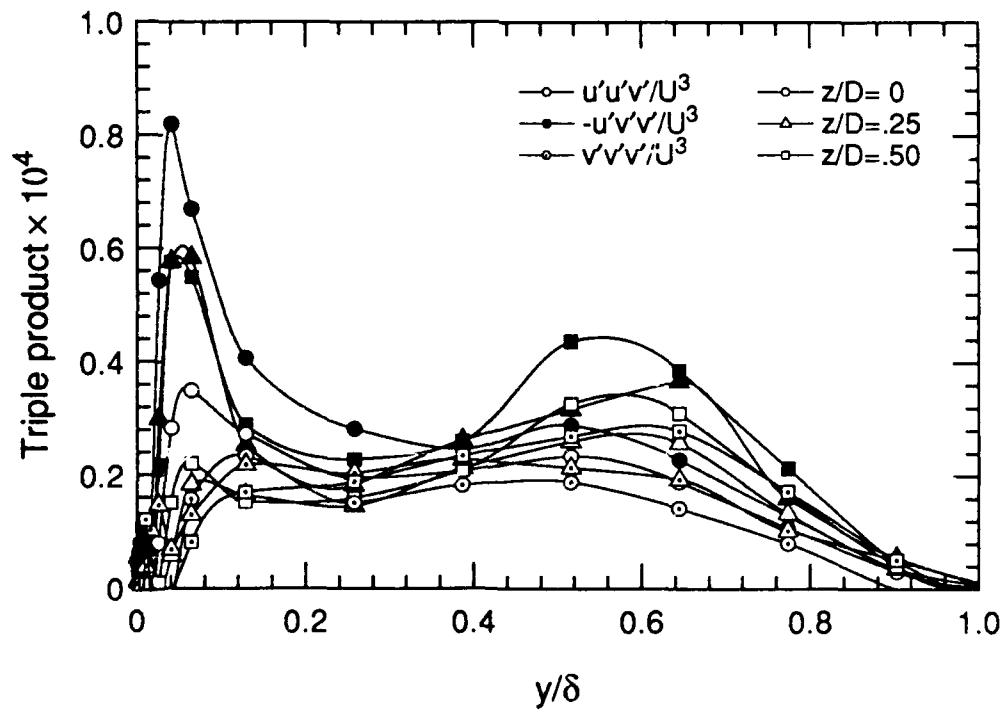
Figure 5.12 $\overline{u'u'v'}/U_\infty^3$, $\overline{u'v'v'}/U_\infty^3$, and $\overline{v'v'v'}/U_\infty^3$ at zero pressure-gradient

6. Experimental Plan

This chapter will describe the vortex generator test apparatus, the manipulation of the freestream velocity to create the desired unsteady pressure gradient, selection of a realistic parameter space for the experimental problem, and some of the procedures necessary to obtain a quality data set.

6.1 Vortex Generator Test Apparatus

The vortex generator test apparatus inserts into the forward portion of the turbulent test surface and supports an array of six half-delta-wing counter-rotating vortex generators. While the design scheme allowed for computer-controlled actuation of the vortex generators, in this program the surfaces were manually rotated as a set to the desired angle of attack. In addition, the test plate has dye slots for introducing dye into the boundary layer just ahead of the leading edge of the vortex generators.

Each vortex generator surface is a half-delta-wing with a chord length of $3cm$ and a height of $1.2cm$. Details of the vortex generator geometry are shown in figure 6.1 The half-delta-wing was chosen primarily because that shape has produced satisfactory results in other programs at Stanford. The dimensions were based on recommendations by Pearcey (1961) for an array of generators with the best combination of spacing and range:

$$D/d = 4$$
$$D/h = 10$$
$$\ell/h = 2.5. \tag{6.1}$$

While Pearcey's recommendations tend to favor a co-rotating array, the counter-rotating array was chosen because the vortices tend to convect straight along the

69

channel. In contrast, co-rotating arrays tend to "walk" sideways because of the effect of the image vortices.

Once a counter-rotating array was chosen, the number of pairs of generators was basically fixed by the size constraints of the water channel. The pairs were to be spaced so that the effect of image vortices would simulate an infinite array (see figure 6.2). In addition, an odd number of pairs was chosen so that one pair would be located on the channel center line for ease in LDA measurements. Since with five vortex generator pairs the size of each generator surface would have been too small relative to the boundary-layer thickness, the logical choice was three vortex generator pairs. With three pairs scaled according to equations 6.1, the 1.2cm height of each vortex generator compares favorably to a nominal momentum thickness of 0.4cm and a boundary-layer thickness of 4cm.

The basic mounting plate for the vortex generators is a 26.6cm by 11.4cm lucite insert which fits into the turbulent test surface. Figure 6.3 shows a photograph of the flow side of the insert plate with the vortex generators set at an angle of attack of about 18°, and figure 6.4 shows the opposite side of the test plate, revealing the control mechanism. Each generator blade fits into a slot in a 12.7mm stainless-steel shaft. A sprocket on the opposite end of the shaft rotates the assembly. Figure 6.5 shows a cross-section schematic of the shaft assembly. Pump seals are used to allow rotation while preventing leakage. Each shaft is supported by two nylon bearings, one in the lucite plate and one in the aluminum sprocket mount plate. This plate also is used to compress the pump seals by means of adjustable rings which allow each shaft to be individually positioned flush with the flow surface.

Figure 6.3 also reveals that there are four separate dye slots adjacent to each other, each with its own plenum. These allow introduction of dye onto all or just part of the surface, or the opportunity to use different color dyes to study the mixing between vortices.

Figure 6.4 shows the drive chain assembly used to rotate the generators to the desired angle of attack. A steel-reinforced polyurethane belt engages the sprocket on each shaft in a serpentine manner, resulting in the counter-rotation of each vortex pair. This particular approach was chosen over a variety of alternate designs because the chain and sprocket assembly ideally has no backlash, and because the same drive approach works very successfully on the computer-controlled valves described in chapter 4. In practice, the eccentric loads on each shaft result in too much friction for this design to work well for rapidly actuated vortex generators. Nevertheless, this design was quite satisfactory for manually setting the set of vortex generators to a desired angle of attack. Checks for repeatability indicated that the angle of attack of each generator can be set to within about one degree of the angle set for the array.

6.2 Tailoring the Freestream Flow and Pressure Gradient

Since the stated goal of this program was to study the effect of vortex generators placed in an unsteady, separating, turbulent boundary layer, the computer-controlled valves modify the freestream velocity such that the tr bulent boundary layer separates downstream of the vortex generators when they are at an angle of attack of 0°. A family of steady streamwise velocity gradients capable of creating this separation are shown in figure 6.6. This figure shows four different steady velocity gradients. The first shows constant velocity or a zero pressure gradient condition. In the subsequent three cases, a pair of valves are manipulated together to create the adverse pressure gradients. The upstream valve (located between $1.95m$ and $2.05m$) was opened while a downstream valve was closed a proportional amount such that the velocity at the leading edge remained constant at $0.5m/sec$. As this suction through the upstream valve is increased, the velocity and pressure gradients become steeper until, in the fourth case, the boundary layer separates at about $2.05m$.

For an unsteady, adverse pressure gradient, the two valves oscillate with the same waveform and frequency but 180° out of phase. By monitoring the upstream and downstream velocities on a dual-trace oscilloscope, the relative amplitudes and phases of the two valves can be adjusted and balanced for the exact flow conditions desired. While the facility has the capability of imposing the pressure-gradient in virtually any time waveform desired, a square wave was chosen for this experiment so that frequency was not a parameter. The corners of the square wave were slightly rounded over 0.2 seconds of the 10-second cycle (71% change in 0.05 seconds, 91% change in 0.1 seconds, 98% change in 0.15 seconds, and 100in 0.2 seconds). Figure 6.7 shows the resulting unsteady adverse pressure gradient. Note that at $tU_0/l = 0$, there is no pressure gradient. At $tU_0/l = 1$ the gradient is the strongest, and then as the tunnel adjusts to the blockage caused by the separation, the gradient relaxes a small amount.

The location of the adverse pressure gradient with respect to the location of the vortex generators was chosen for optimum interaction between the streamwise vortices and the separating boundary-layer. It was also important that the vortex generators were located in a region of *steady* flow such that the streamwise vortices convected *into* the region of *unsteady* flow. Laser sheet flow visualization in steady flow gave a good indication of the size and strength of the vortex structures that are formed by the vortex generators. Figure 6.8 shows spanwise cross-sections of the structures behind the vortex generators at various streamwise positions and for three blade positions: 18° (common flow up), 0°, and 18° (common flow down). The common flow down case at a location 60*cm* downstream of the vortex generators appears to be optimum in terms of a vortex that is not too diffuse but has grown to where the structures fill most of the boundary layer. Therefore, the location of the adverse pressure gradient was chosen so that separation tends to occur about 60*cm* downstream of the vortex generators. Figure 6.9 summarizes the relationships between the locations on the test surface of the vortex generators and the imposed pressure gradient.

6.3 Upstream Conditions.

This experiment was designed such that the velocities varied in a near linear fashion along the pressure gradient ramp, and such that they were steady in time upstream of the ramp. To verify this, and to document the upstream conditions for computational purposes, unsteady profiles were taken at the streamwise positions $x = 1.88m$ and $x = 2.00m$. The resulting profiles for the separation portion of the cycle are shown in figures 6.10 and 6.11.

6.4 Spanwise Uniformity

Chapter 5 demonstrated that the spanwise uniformity of the flow was very good under steady conditions. Unsteady flow acts as an amplifier and greatly exaggerates any inconsistencies in the flow. The same can be said of an adverse pressure gradient. Therefore, one would expect that it is far more difficult to maintain good spanwise uniformity under unsteady adverse pressure gradient conditions. Figure 6.12 shows the spanwise uniformity of the streamwise velocity component, $\langle u \rangle$, with vortex generators set at $\alpha = 0°$, and figure 6.13 shows similar results for $\alpha = 18°$. In both cases, at $tU_0/l = 0$ the velocity is quite uniform across the span. Also, at $tU_0/l = 1$, the initial response to the suction is quite uniform in both cases. However, as the flow adjusts to the separation and to the resulting blockage in the tunnel, some non-uniformity does develop. Figure 6.12 indicates the pressure gradient relaxes more on the positive z axis, resulting in a spanwise gradient in the $-z$ direction. This effect is even stronger with the vortex generators set to $\alpha = 18°$. While the reason for this effect was not determined, the spanwise flow caused by this spanwise gradient is seen very clearly in the secondary flow vectors presented in chapter 7. Finally, figures 6.14 through 6.16 show the unsteady spanwise uniformity of $\langle v \rangle$, $\langle u'u' \rangle$, and $\langle v'v' \rangle$ respectively. Note that while $\langle u'u' \rangle$ and $\langle v'v' \rangle$ do show larger fluctuations on the $-z$ side, which is consistent with a stronger adverse pressure gradient, that $\langle v \rangle$ does not show much non-uniformity. This suggests that

73

the suction created by the automated valve is very uniform, and that the valves are not the cause of the spanwise variation.

6.5 Experimental Approach

This chapter has already identified most of the experimental parameters of the experiment. The dimensions of the vortex generators have been defined and the characteristics of the unsteady adverse pressure-gradient have been explained. The question that remains is where to take data. The basic experimental objective was to completely map out a symmetrical spanwise section of the unsteady flow field at a single streamwise position, so that mean and turbulent transport terms could be estimated.

Streamwise Location. The streamwise location selected for the data plane was simply determined by how close the three-component optics could be located on the downstream side of the point of separation. Because of a support rib on the top of the test section, and because of the water tank required for optical path length compensation on the top of the tunnel, the closest location was $x = 2.08m$. The most significant length for the experiment is the distance downstream of the pressure ramp, which commences at $x = 1.95m$. Therefore $\ell = 13cm$, as indicated in figure 6.9. Also, this defines a useful time scaling parameter, the convection time based on the initial freestream velocity. For convenience in scaling time only, since $U_0 = 0.5m/sec$, the length will be taken as $12.5cm$ so that

$$\frac{\ell}{U_0} = \frac{0.125m}{0.50m/sec} = 0.25sec \tag{6.2}$$

Time Period of Unsteady Cycle. The factor that most directly affected how many spatial data points to take was the time required for each unsteady phase-average. This, of course, depended on the time period of each cycle and the number of cycles required for reasonable convergence of the turbulence quantities. Preliminary tests at various locations in the flow indicated that most of the "mean"

74

velocity change occurred in about $0.5sec$, and most of the change in the turbulence quantities occured in about $2sec$, but some adjustment occurred over the next several seconds. Therefore, in order for the flow to not have the characteristics of the driving frequency, a ten second cycle was chosen. Since the valve control software had not been set-up to accommodate different times for the separation and recovery phases, this meant there was a five-second separation phase followed by a five-second recovery phase.

Convergence Requirements. Convergence requirements were discussed briefly in chapter 5, but the study referenced there by Klewicki and Falco (1988) did not address the added complication of phase-conditioned sampling. Using the ten-second cycle discussed above, preliminary data sets were taken at selected locations in the boundary layer, for phase-conditioned averages based on 200, 500, 1000, and 3000 cycles. The 200-sample averages showed reasonably good convergence of the "mean" velocities, but very poor convergence of the Reynolds stress terms. The 500-sample averages showed very good convergence of the "mean" velocities and reasonable convergence of the turbulence quantities. As would be expected, the 1000-sample and 3000-sample averages showed proportionately better convergence. The minimum acceptable number of cycles, therefore, was 500. While more cycles would have been desired, a compromise was made because of the time constraints discussed in the following section. This compromise was possible because time history information was used to make up for the incomplete convergence of the turbulence quantities using *phase smoothing* of the data, a concept which will be presented in section 7.2.

Data Grid Selection. The sampling requirements defined in the previous two paragraphs result in a sampling time requirement of 5000 seconds, or one hour and 23 minutes at each individual point in space, and two vortex generator postions were to be run at each point. Faced with these unpleasant realities and the awareness that equipment malfunctions do occur in any complex facility, a less dense data grid was selected than would have been selected for a steady experiment. The

minimum spanwise requirements were to map between the center line and the line of symmetry between vortex generator pairs. (In terms of the vortex generator parameters defined in figure 6.1, $0 \leq z/D \leq 0.5$.) Across the span, five spanwise locations were selected as the minimum realistic number that could capture the key features of the flow. In the y direction, 6 logarithmically spaced points were selected to map the inner region of the boundary layer, and 12 evenly spaced points were selected to map out the outer region. Once again, this seemed to be a minimum reasonable number that could capture most of the structure of the flow field. Table 6.1 summarizes the basic data grid for this experiment.

The data grid of Table 6.1 was followed in a manner that provided the greatest breadth of information as early as possible in the data acquisition process. Each spanwise position required a major realignment of the w optics, so a complete data set was taken at each spanwise position. At each position, a sequence of one or more *quick* steady profiles was taken to verify that the u and v optics were properly aligned, paying special attention to the $u'v'$ correlation coefficient as a sensitive indicator of good alignment. Next the w optics were aligned to the u and v optics. Then, a documentation set of steady profiles were taken at $\alpha = 0°$ and $\alpha = 18°$. Finally, if all the steady data looked good, the unsteady profiles were taken. Allowing for automated traverse time, each unsteady profile took about 26 hours. The data acquisition process was checked every several hours, and could be stopped and restarted as necessary.

Table 6.1 Primary Data Grid

					Spanwise position, z/D			
	alpha	$-1/2$	$-1/4$	0	1/8	1/4	3/8	1/2
Steady	0°	21	21	21	21	21	21	21
Steady	18°	21	21	21	21	21	21	21
Unsteady	0°	6	6	18	18	18	18	18
Unsteady	18°	6	6	18	18	18	18	18

Note: The number in each column indicates the number of points in that particular profile

D = 12 cm
d = 3 cm
h = 1.2 cm
l_{vg} = 3 cm
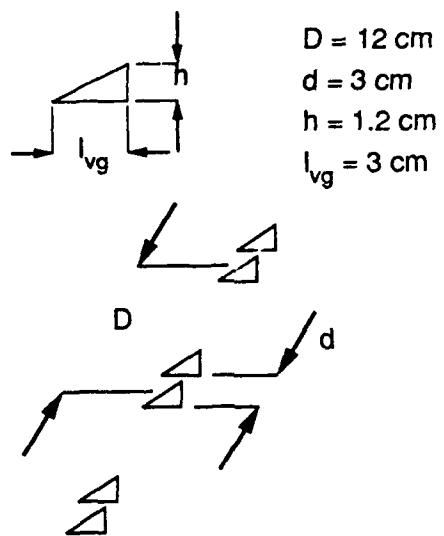
Figure 6.1 Dimensions of vortex generator assembly

Vortex Generator Configuration

in Water Channel

D = 12 cm

image vortex pair

13 cm
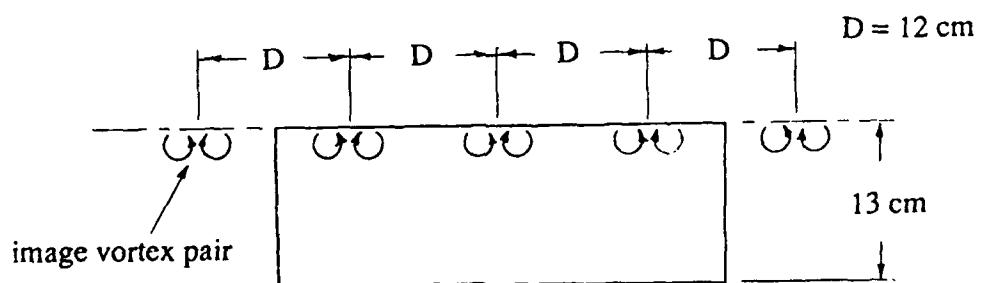
Figure 6.2 Effect of image vortices
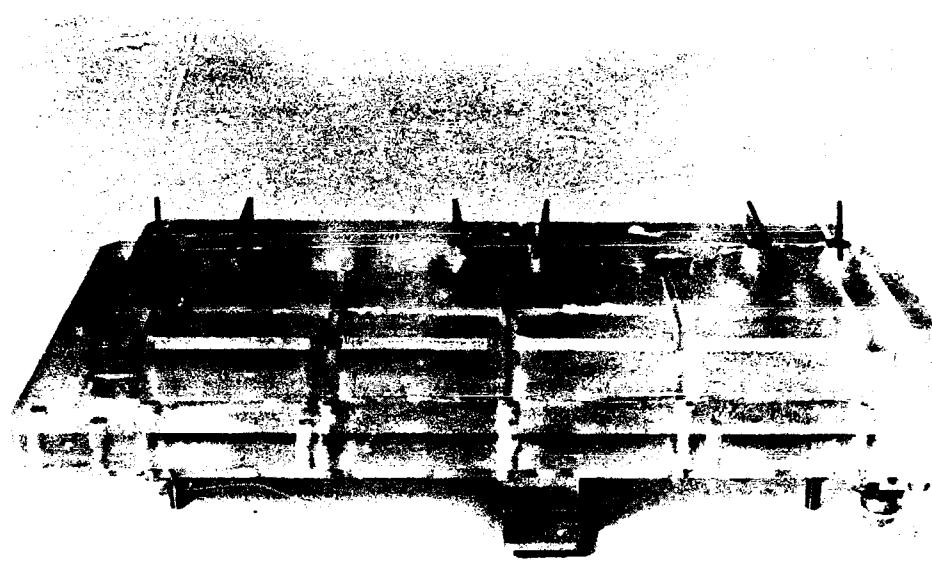
Figure 6.3 Flow-side of vortex generator test plate
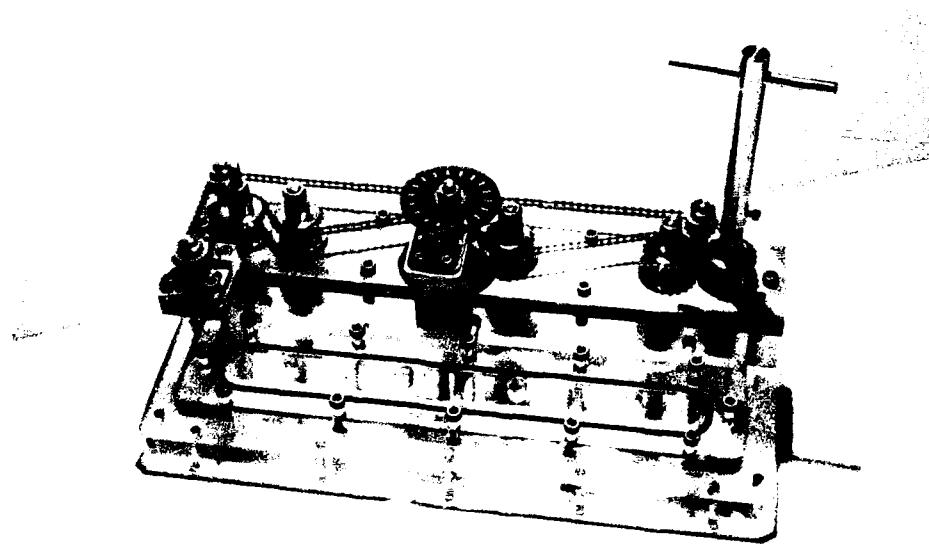
Figure 6.4 Control mechanism for vortex generator test plate

Figure 6.5 Cross-section of vortex generator assembly
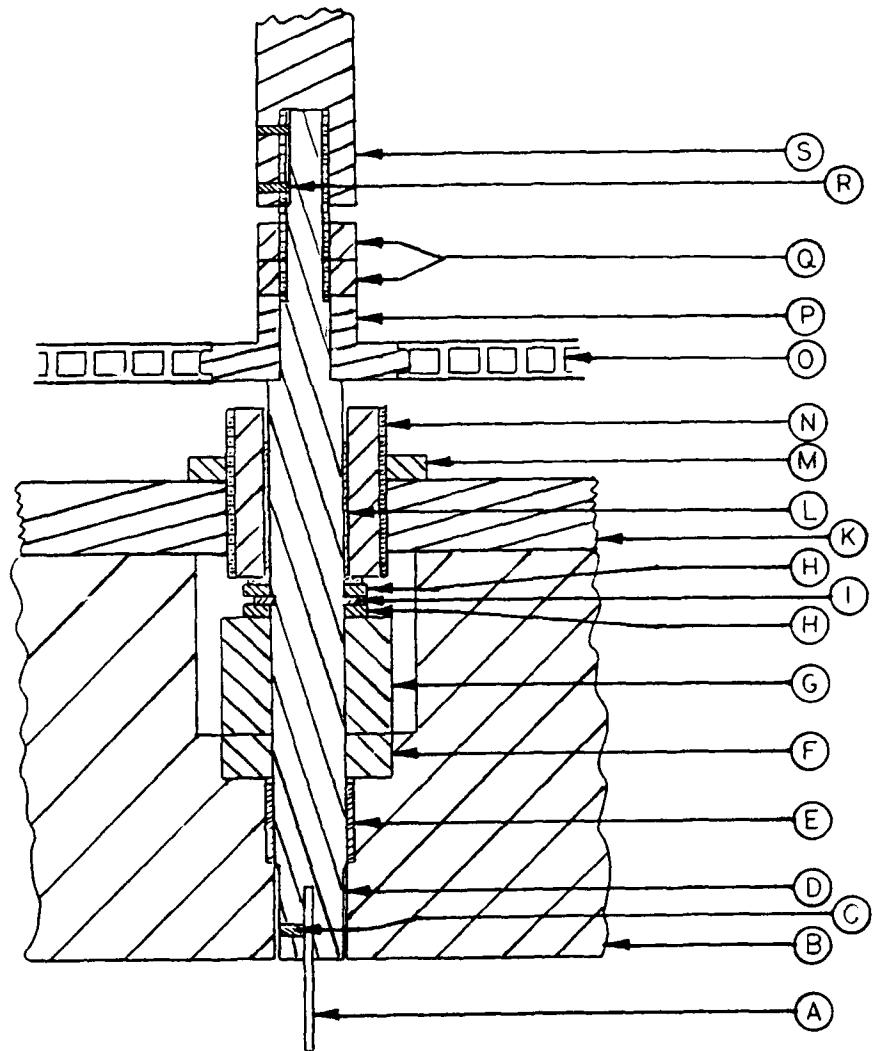
A - vortex generator blade   K - sprocket mount plate
B - drop-in test surface   L - nylon bearing
C - set screw   M - lock ring
D - sprocket shaft   N - adjustment ring
E - nylon bearing   O - cable chain
F - pump seal seat   P - chain sprocket
G - pump seal head   Q - stainless-steel nut
H - stainless-steel washer   R - set screw
I - retaining ring   S - shaft coupling
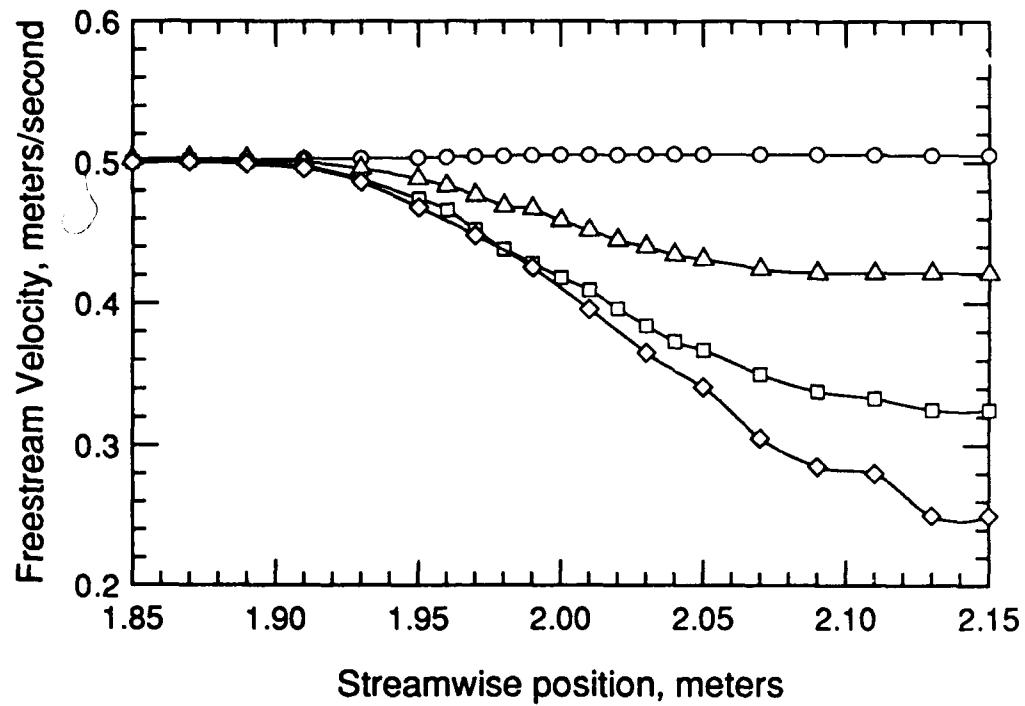
Figure 6.6 Steady streamwise veloctiy gradients
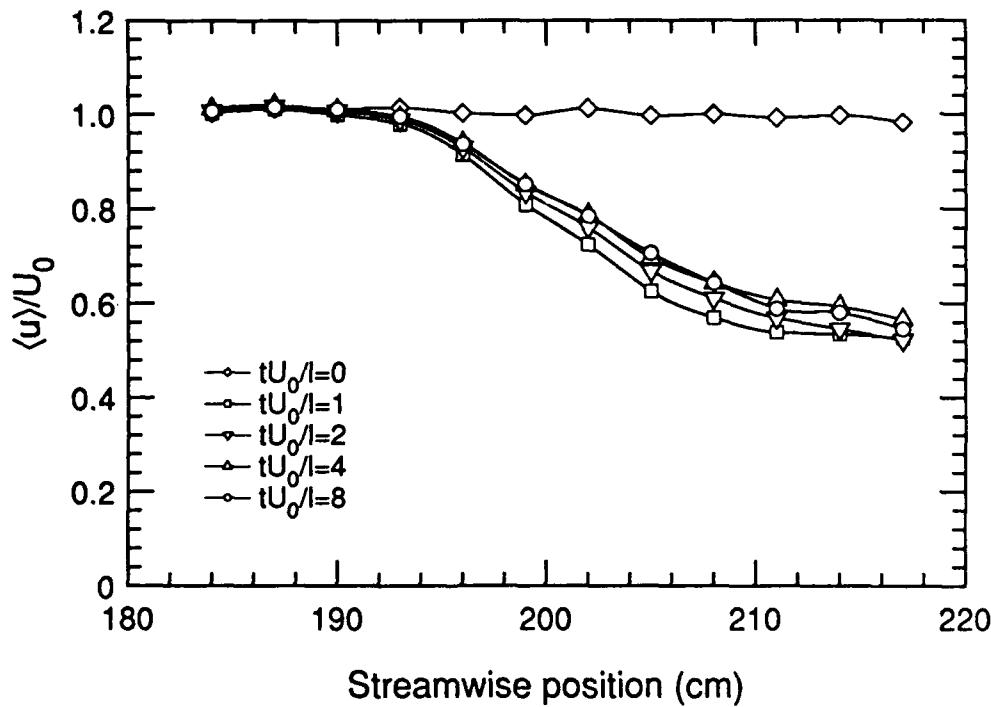
Figure 6.7 Unsteady streamwise velocity gradients

81
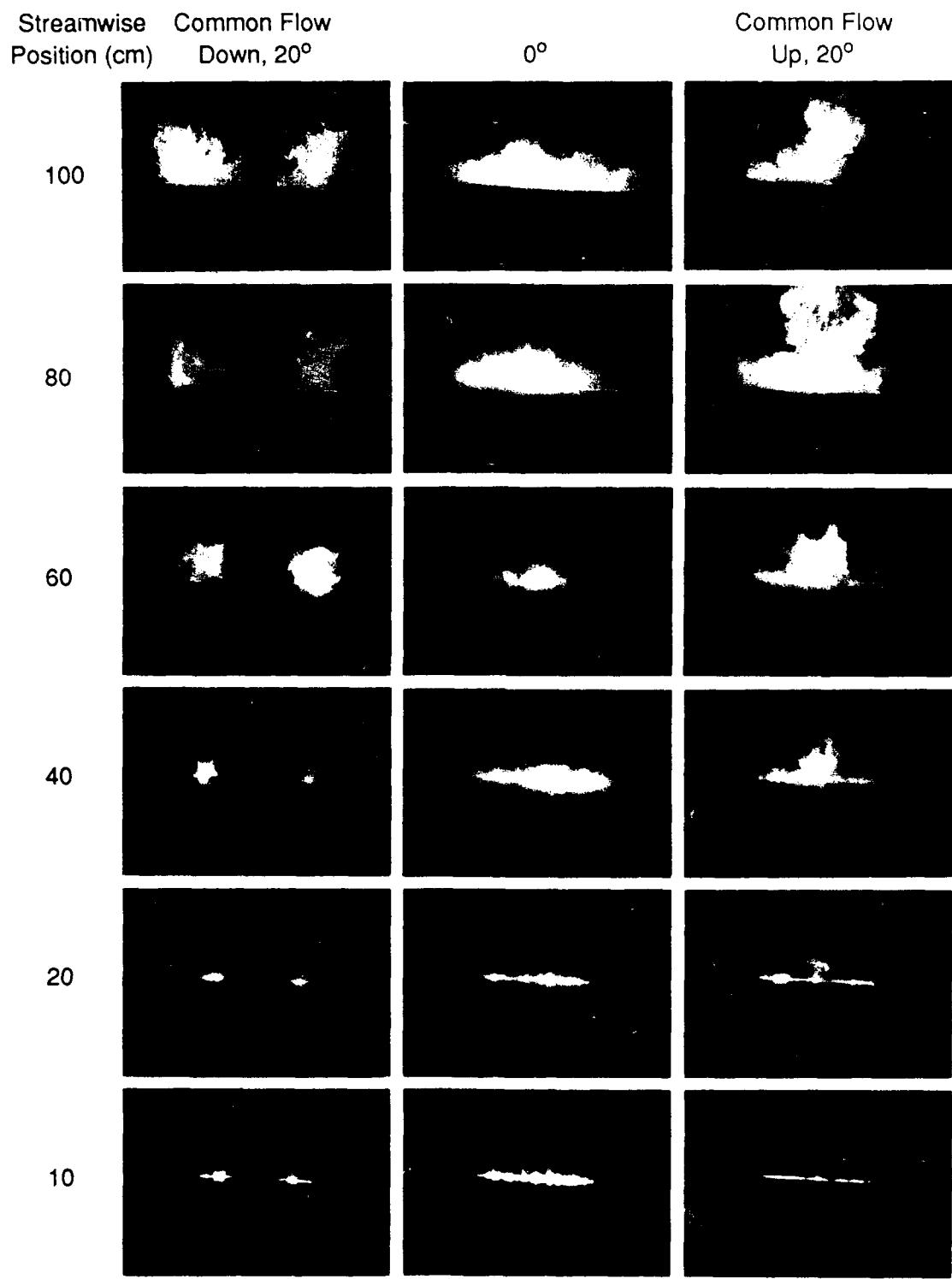
Figure 6.8 Streamwise development of embedded streamwise vorticity
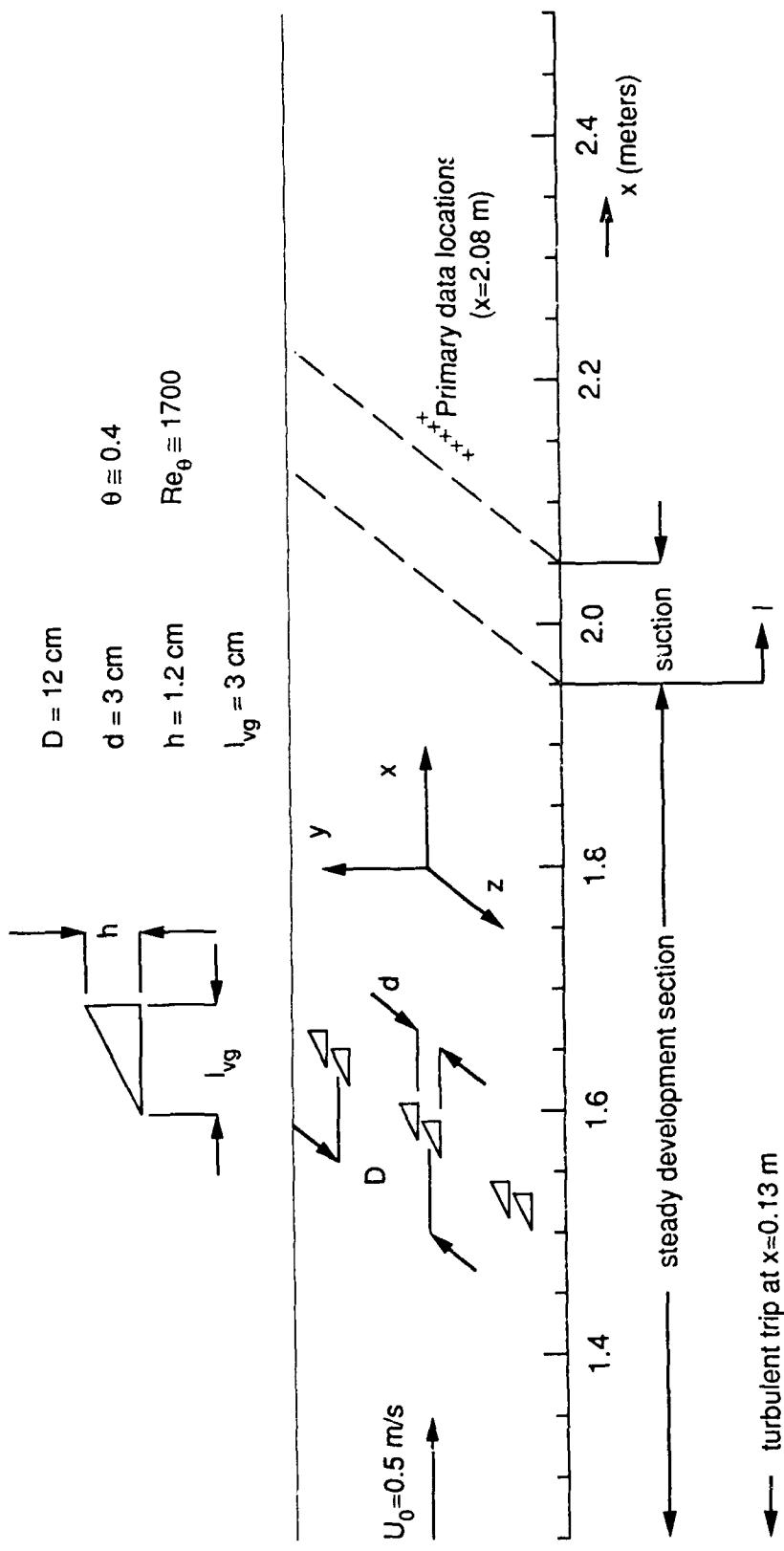
Figure 6.9 Location of vortex generators and adverse pressure-gradient
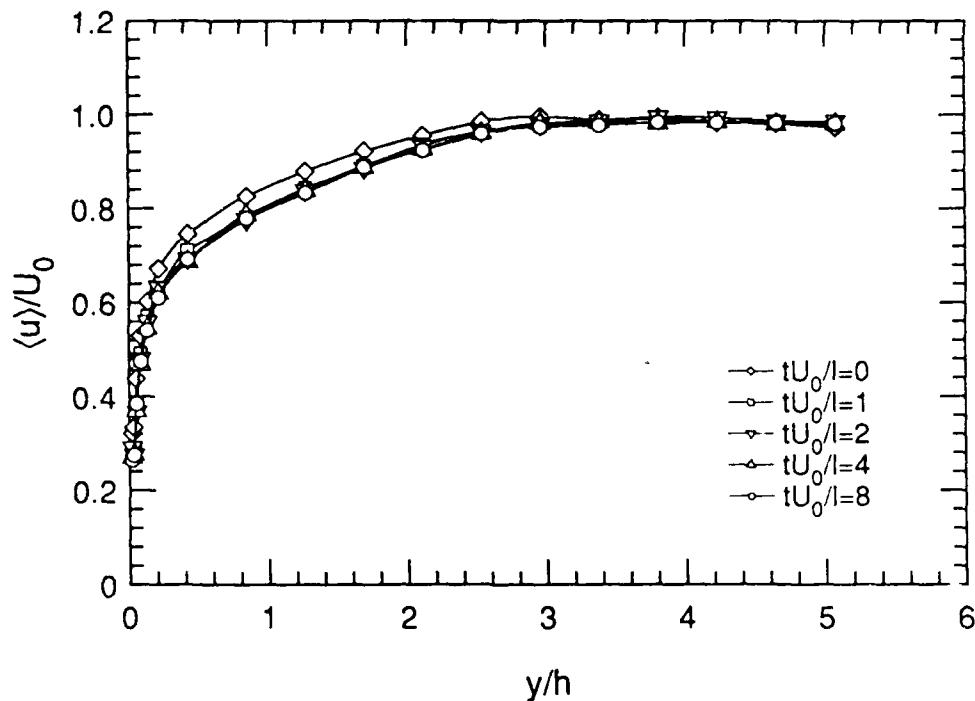
Figure 6.10 Unsteady upstream profile at $x = 1.88m$
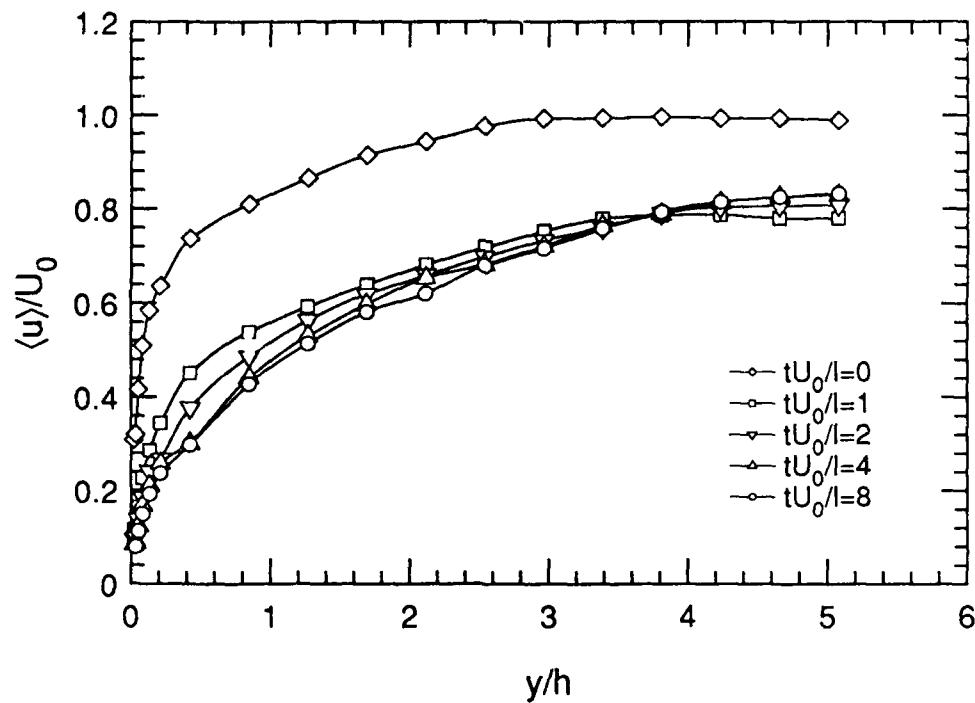
Figure 6.11 Unsteady upstream profile at $x = 2.00m$
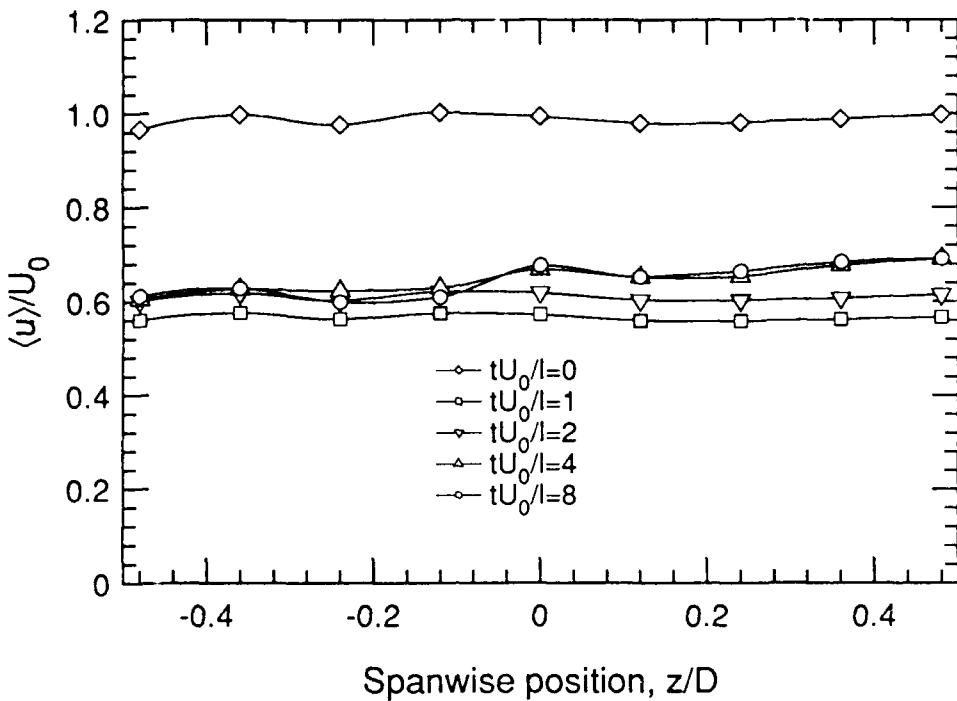
Figure 6.12 Spanwise uniformity of unsteady $\langle u \rangle$ at $\alpha = 0°$
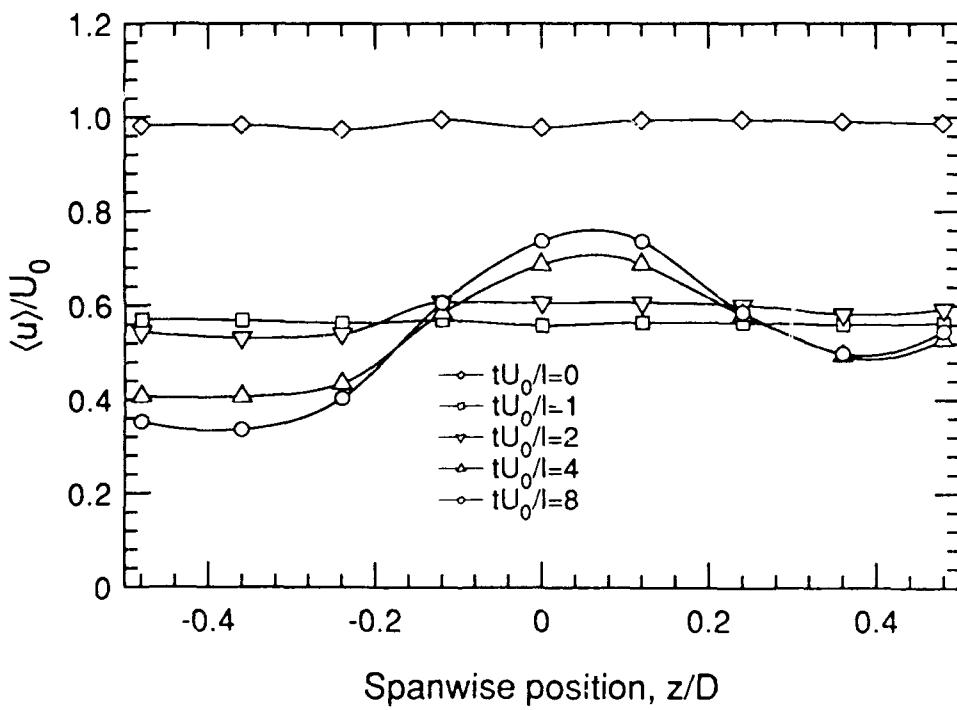
Figure 6.13 Spanwise uniformity of unsteady $\langle u \rangle$ at $\alpha = 18°$

85
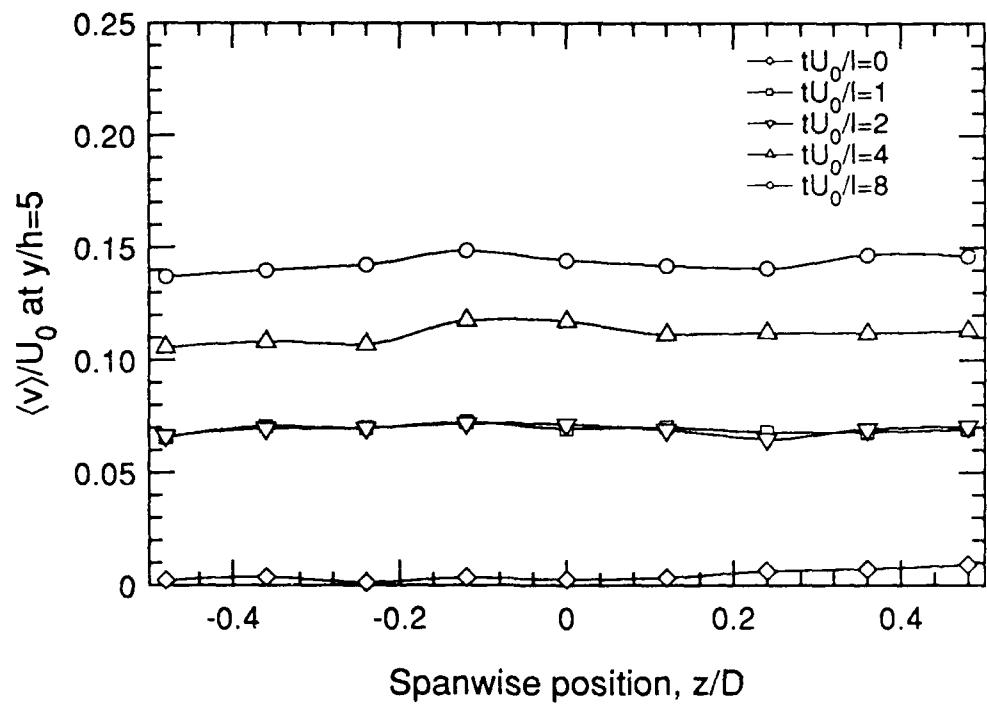
Figure 6.14 Spanwise uniformity of unsteady $\langle v \rangle$ at $\alpha = 0°$
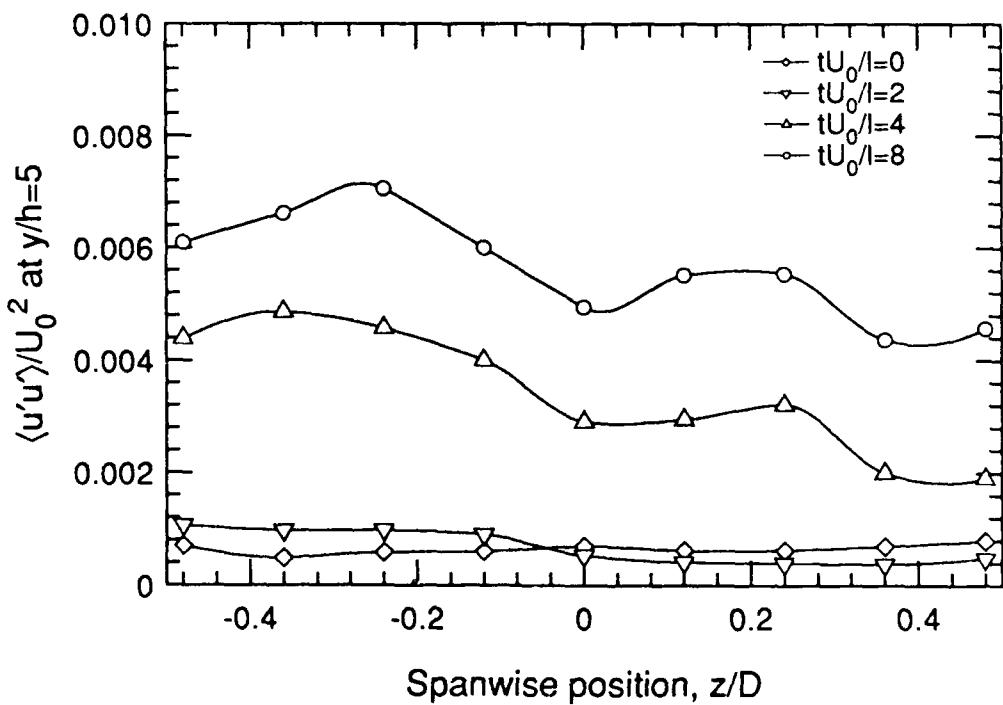
Figure 6.15 Spanwise uniformity of unsteady $\langle u'u' \rangle$ at $\alpha = 0°$
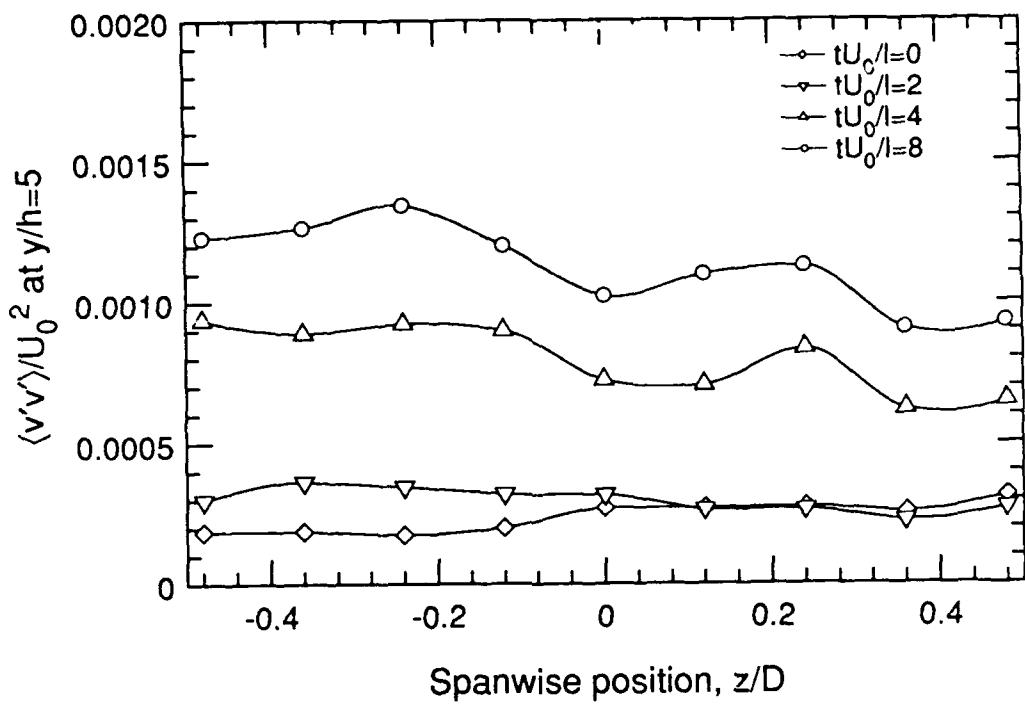
Figure 6.16 Spanwise uniformity of unsteady $\langle v'v' \rangle$ at $\alpha = 0°$

One can get a proper insight into the practice

of flying only by actual flying experiments

— Otto Lilienthal

7. Results I: Unsteady Measurements

This chapter will present the basic phase-averaged measurements of velocity and Reynolds stresses. The major analysis and evaluation of the results, however, will be reserved for chapter 8. While steady, zero pressure-gradient profiles were taken as part of the set-up validation process at each spanwise location, these results are usually redundant with the unsteady results obtained at $t = 0^-$. Therefore, steady-flow data will not be shown in this chapter. However, some steady results will be discussed in chapter 8 as a point of departure from other steady experiments with streamwise vorticity.

The key features of the experimental plan described in chapter six were that the primary unsteady data for this experiment consists of two 5 by 18 grids at a single streamwise location, one grid for the vortex generators at an angle of attack of $0°$ and one at an angle of attack of $18°$. The grid consisted of 5 spanwise positions and 18 positions normal to the surface. Each unsteady cycle consisted of a (1) step change from zero pressure gradient to adverse pressure gradient, (2) 5 seconds of constant adverse pressure gradient, (3) a step change back to zero pressure gradient, and, finally, (4) a 5-second recovery period at zero pressure gradient. During each cycle, the data acquisition system maintained phase averages at 400 separate phases, that is, every $0.025sec$. While the second half of the cycle produced information on the boundary layer recovery, all the results discussed in this report pertain only to the separation half of the cycle.

It is a challenge to know just how to display adequately both time development and spatial relationships in the data. Since the data was measured at one point in space at a time, it seems most natural to begin with the time histories of the various quantities at selected spatial locations. This then leads logically to an explanation of how data at a given point in time was assembled over an entire spatial plane.

89

Finally, the chapter will conclude with limited flow visualization results to reinforce the information conveyed by the data.

7.1 Time History of Single Point Measurements

Figures 7.1 through 7.5 present the time history of the phase-averaged quantities $\langle u \rangle$, $\langle v \rangle$, $\langle u'u' \rangle$, $\langle v'v' \rangle$, and $-\langle u'v' \rangle$ for the first two seconds of the separation cycle. Consistent with the non-dimensionalization described in chapter six, one second is equivalent to 4 convection times, tU_0/l. The two-second time length was chosen for display since most of the significant changes in the flow have occurred by this time. In each figure, three locations of y/h are shown, one which is fairly representative of the inner region of the boundary layer, one representative of the inner portion of the wake, and one representative of the outer portion of the wake.

The time history curves were created by joining all the phase-averaged data points collected between $t = -0.25sec$ to $t = 2.0sec$. Since the sampling program maintained a separate phase-averaged bin every 0.025 seconds, there are actually 90 separate phase-averaged data points represented in each trace. Data symbols were eliminated from these plots for clarity. These time histories are included to demonstrate the relative magnitude of change in each quantity as well as the relative time over which the changes occurred.

In general, the mean velocities respond much more quickly than the turbulent stresses. With respect to $\langle u \rangle$, there is a fast response which occurs in the same time frame as the opening of the control valve, followed by a slower adjustment period. In general, the velocity continues to decrease during the adjustment period, but in certain regions of the downwash, it actually increases during this adjustment period. The normal velocity component, $\langle v \rangle$, responds very little in the inner region of the boundary layer. In addition to responding much more slowly than the mean velocities, the turbulent stresses decrease in the inner boundary layer as the separation develops, but *increase substantially in the outer region of the boundary*

90

layer. The time response of $\langle u \rangle$, $\langle v \rangle$, and $\langle u'u' \rangle$ will be characterized in considerable detail in chapter 8.

7.2 Phase-Smoothing of the Data

The time histories shown in figures 7.1 through 7.5 also convey information about the degree of convergence obtained for each quantity during the 500 cycles over which phase averages were taken. The quantity $\langle u \rangle$ seems to be fully converged and $\langle v \rangle$ seems to be almost converged. In contrast, the three turbulence quantities shown are not fully converged. As discussed in chapter 6, the number of spatial points and number of averaging cycles chosen required some compromises in order to obtain a reasonable data set in a reasonable time period. However, to overcome this lack of convergence, one can take advantage of the fact that the phase-averaged quantities should evolve "smoothly" in time.

For this experiment, a piece-wise parabolic least-squares fit was used to approximate the expected "smooth" behavior of each variable. In general, 9 or 11 adjacent phases were fit using a NAPL Singular Value Decomposition (SVD) subroutine, which produced a least-squares parabolic fit. (NAPL is the Numerical Analysis Package Library developed by Argonne National Laboratory.) The central time value of the phases being smoothed was then substituted into the least-squares fit. The value obtained from that fit was then used as a "phase-smoothed" value for most of the remaining data presentation and analysis. While this process is a data smoothing process, in many respects it is simply an intelligent extension of the averaging process used in all turbulence studies.

To demonstrate the validity of this technique, figure 7.6 shows time histories of $\langle u \rangle$ and $-\langle u'v' \rangle$ with the values obtained by phase-smoothing shown as symbols plotted over the time traces. Figure 7.6a demonstrates that the phase-smoothing process yields values that are consistent with the well-converged values of $\langle u \rangle$. In a similar fashion, figure 7.6b shows that the phase-smoothed values are also representative of

91

what one would expect for the converged $-\langle u'v' \rangle$ observations. Since this process yields credible values for both converged and non-converged data, it was applied to all the remaining data in this chapter, and will be referred to as "phase-smoothed" data.

7.3 Spanwise presentations of the data

While the time history data just presented were useful in seeing how the velocities and Reynolds stresses at a point evolve in time, one is usually also interested in how these quantities vary in profile format, both in the direction normal to the surface and in the spanwise direction. Therefore, using phase-smoothing to improve the convergence of the data, the velocities and Reynolds stresses were reassembled into complete spanwise planes of data for a single instant in time and for a specific position of the vortex generator.

Frequently, spanwise sets of data are presented as contour plots. Contour plots work best for dense data grids, but several disadvantages of contour plots are: (1) the actual data points are not shown, (2) splining through data before contour plotting can produce some bizarre and anomalous features on the contours, and (3) data smoothing effects are concealed from the reader (and from the data analyst if he is not careful). Since time requirements dictated a rather coarse data grid, the results from this experiment seemed particularly vulnerable to the weaknesses of contour plotting. Therefore, in this report, contour plotting will be minimized. An alternative display, which will be used in all the remaining figures in this chapter, is a three-dimensional perspective view of the profiles from each of the five primary spanwise locations.

In each of the figures, from figures 7.7 through figure 7.32, four complete spanwise data sets are presented. The upper two data sets represent cases with the vortex generators at an angle of attack of 0° and the lower two data sets represent cases with the vortex generators at an angle of attack of 18°. Also, the two data sets on

the left represent a single phase in time, and the two sets on the right represent a later single phase in time. In this way, each figure provides the reader with a comparison to a different phase of the cycle and a comparitive view of the effect of the vortex generators. In most cases, the curve drawn is a 5-point piecewise parabolic least-squares fit to the data. For simplicity in reading, all the figures from 7.7 to 7.32 follow this identical pattern.

Streamwise velocity component. Figures 7.7 through 7.10 present the development of the streamwise velocity component, $\langle u \rangle$. At $tU_0/l = 0$, the profiles are quite full both with and without vortex generators. In contrast to the stronger vortices studied by Pauley and Eaton (1988), these profiles do not show a large velocity deficit in the vortex core. A closer evaluation of the boundary layer integral parameters in chapter 8 will highlight other differences in these profiles. In succeeding figures, the profiles are seen to react erratically to the intial change in the pressure gradient. Without the vortex generators, the boundary layer begins to separate at $tU_0/l = 6$. Since this experiment was intentionally designed to create a very mild separation, the boundary layer remains slightly attached at $z/D = 0$ and at $z/D = 0.5$, but reverse flow occurs at the other three locations. With vortex generators on, the flow remains attached in the downwash regions, $z/D = 0$, $z/D = 0.125$, and $z/D = 0.25$, but the boundary layer separates very quickly in the upwash regions of the vortex, $z/D = 0.375$ and $z/D = 0.5$. Reverse flow first begins at $z/D = 0.5$ at $tU_0/l = 3$, and by $tU_0/l = 8$ the separated region extends three generator heights away from the surface. Additional turbulent profiles in wall coordinates (u^+ vs. y^+), will be presented in chapter 8, along with discussions regarding the skin friction and friction velocity.

Secondary velocities. Figures 7.11 through 7.14 show the analogous behavior of the secondary flow, which is best seen as the combined vector sum of $\langle \vec{v} \rangle$ and $\langle \vec{w} \rangle$. Because the zero-velocity offset voltage is very hard to get precisely correct. small errors in $\langle v \rangle$ and $\langle w \rangle$ show up as large variations in the secondary flow. For this reason, at each location the values of $\langle u \rangle$ and $\langle w \rangle$ at $tU_0/l = 0$ and $\alpha = 0°$

were subtracted as the offset error. The small uniform vectors shown in figure 7.11 at this reference state are intended to communicate that the secondary flow there is *assumed* to be small and uniform. At $tU_0/l = 0$ and $\alpha = 18°$, the secondary flow associated with the vortex pair is clearly seen. The downwash and upwash regions are both evident, and the vortex core appears to be at about $z/D = 0.32$ and $y/h = 1.2$. Also, the vortex is quite weak in comparison to the vortex strength used in most studies in the literature. The maximum secondary velocity is about only five percent of the streamwise velocity. At $\alpha = 0°$, as the separation develops, $\langle v \rangle$ increases dramatically as the boundary layer separates. A small component of $-\langle w \rangle$ is also seen at $\alpha = 0°$ as the separation develops. This is consistent with the observations in chapter 6 that the tunnel tends to pull in the $-z$ direction during the adverse pressure gradient portion of the cycle. At $\alpha = 18°$, the circular secondary flow associated with the vortex can be seen until $tU_0/l = 3$. After this, the vortex seems to lose its identity and some large spanwise flows are seen in conjunction with the separation. The significance of these latter observations will be dealt with at the end of chapter 8.

Reynolds stresses. Figures 7.15 through 7.32 show the development of each of the components of the Reynolds stress tensor. The normal stresses, $\langle u'u' \rangle$, $\langle v'v' \rangle$, $\langle w'w' \rangle$, and the primary shear stress $-\langle u'v' \rangle$, all behave in the the same general manner. The trends are qualitatively similar to those seen by Pauley and Eaton (1988). At $\alpha = 0°$, the peak concentration of each stress tends to spread outward away from the surface as the boundary layer separates. Also, the magnitude of each stress increases during the adverse pressure gradient. At $\alpha = 18°$, the concentration of each stress is pushed inwards in the downwash region and redistributed outwards in the upwash region. This was described well by Mehta and Bradshaw (1988) as "convection of pre-existing boundary-layer turbulence by the vortices." As the separation develops, the magnitude of each stress increases even more at $\alpha = 18°$ than the increase seen at $\alpha = 0°$. This is particularly true of $\langle u'u' \rangle$ and $\langle v'v' \rangle$. Note that during the separation at $\alpha = 18°$ the shear stress, $-\langle u'v' \rangle$, even develops

regions of negative stress in the region of $z/D = 0.5$. With regard to the secondary shear stresses, $\langle u'w' \rangle$ and $\langle v'w' \rangle$, very little if any should be seen at $\alpha = 0°$, and very little is seen. There is a significant concentration of $\langle u'w' \rangle$ in the cross-flow region of the vortex, as would be expected. This stress is greatly amplified during the adverse pressure gradient. In addition, the small concentration of $\langle v'w' \rangle$ at $\alpha = 18°$ is also amplified significantly during the separation.

7.4 Flow Visualization

To add some additional insight into the behavior of the streamwise vortices, movies were taken of the vortices during an unsteady cycle, using laser sheet fluorescence. Water containing fluoroscein sodium salt ($C_{20}H_{10}Na_2O_5$) was introduced through the dye slots just upstream of the vortex generators. The fluid containing this dye tended to wrap around the vortex generator and mark the region of concentrated vorticity. A sequence of four photos from this movie is shown in figures 7.33 through 7.36. In all the photos the bright line is the laser sheet illuminating the surface and the "bar" seen is a support rib on the outer side of the channel. Figure 7.33 shows the fluid marked by the dye during the zero pressure gradient phase. These structures should resemble those shown in figure 6.8. Figure 7.34 shows the initial response to the applied suction. While for the moment the structures generally have not changed, one streak of fluid marked by the dye is being pulled out of the boundary layer. Figure 7.35 shows the fluid in the structures now being pulled away from the boundary layer until finally in figure 7.36, the marked fluid now extends about four times its original distance from the surface.
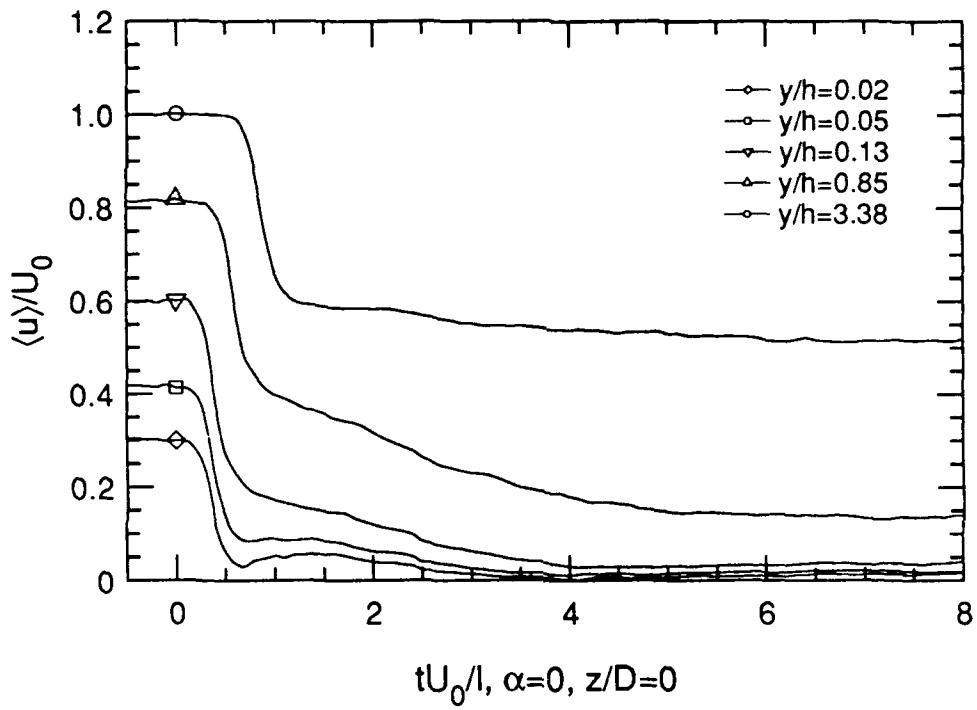
Figure 7.1a History of $\langle u \rangle$ at $z/d = 0$ for $\alpha = 0°$
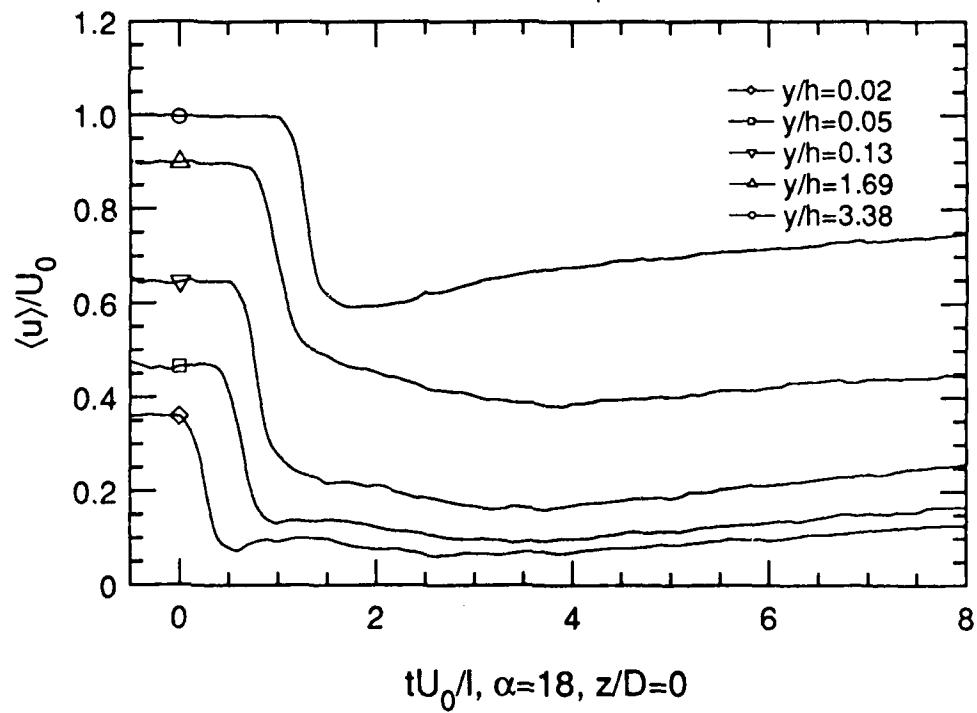
Figure 7.1b History of $\langle u \rangle$ at $z/d = 0$ for $\alpha = 18°$

96
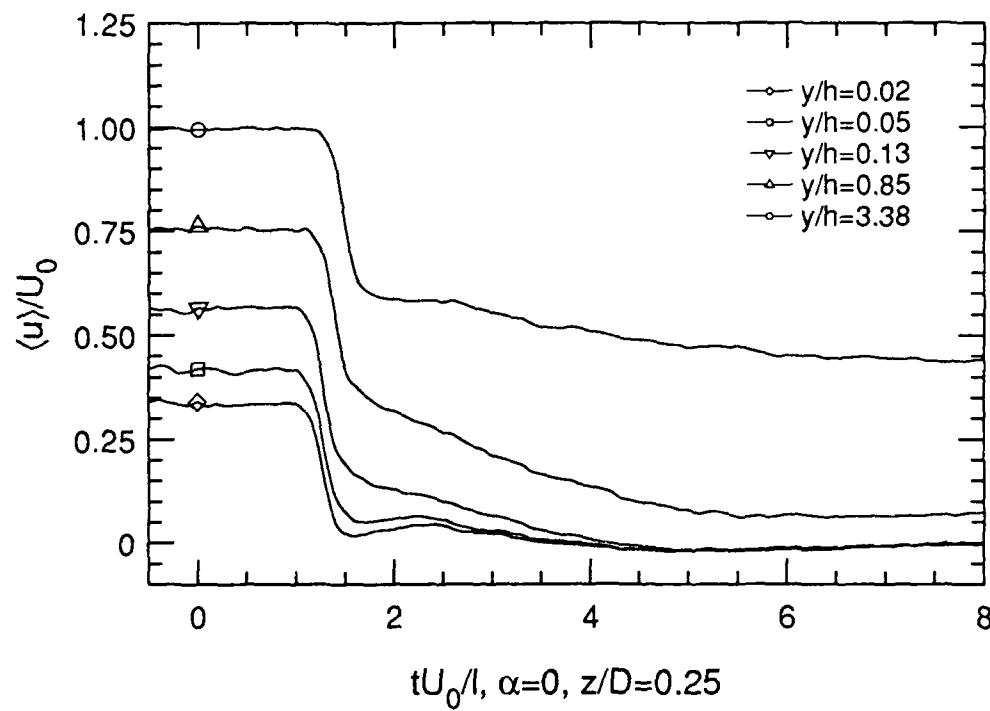
Figure 7.1c History of $\langle u \rangle$ at $z/d = 0.25$ for $\alpha = 0°$
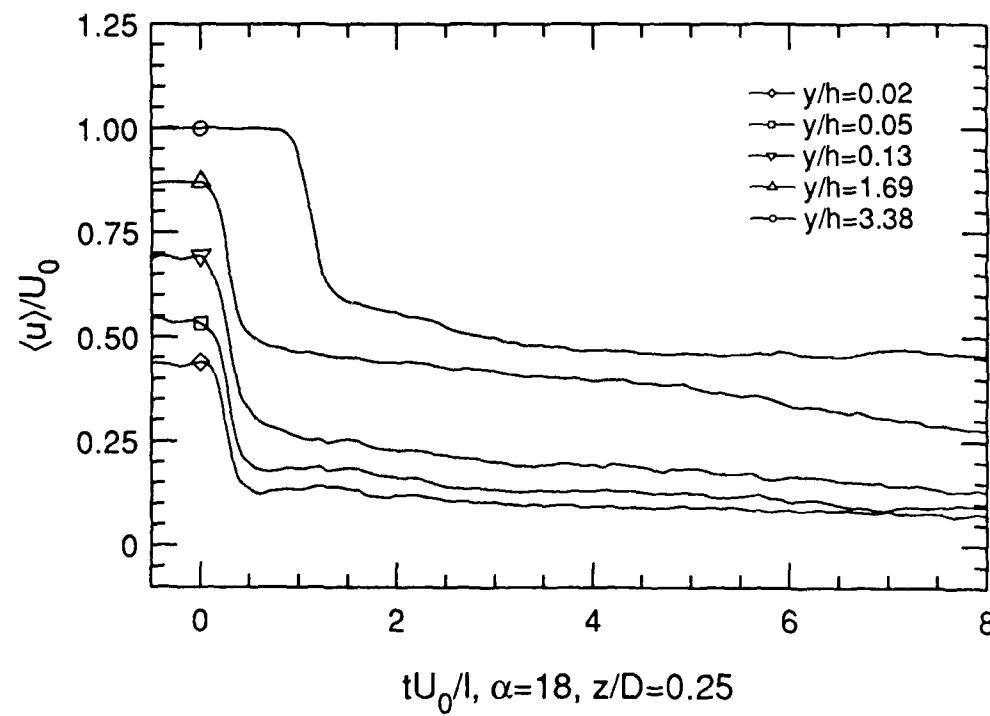
Figure 7.1d History of $\langle u \rangle$ at $z/d = 0.25$ for $\alpha = 18°$
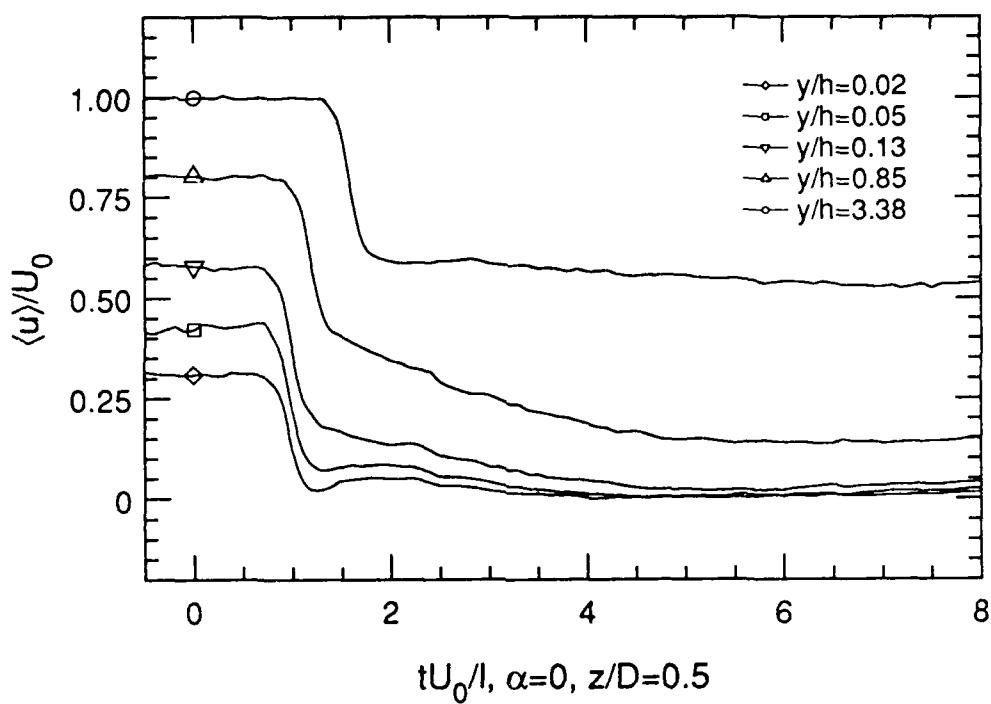
Figure 7.1e History of $\langle u \rangle$ at $z/d = 0.50$ for $\alpha = 0°$
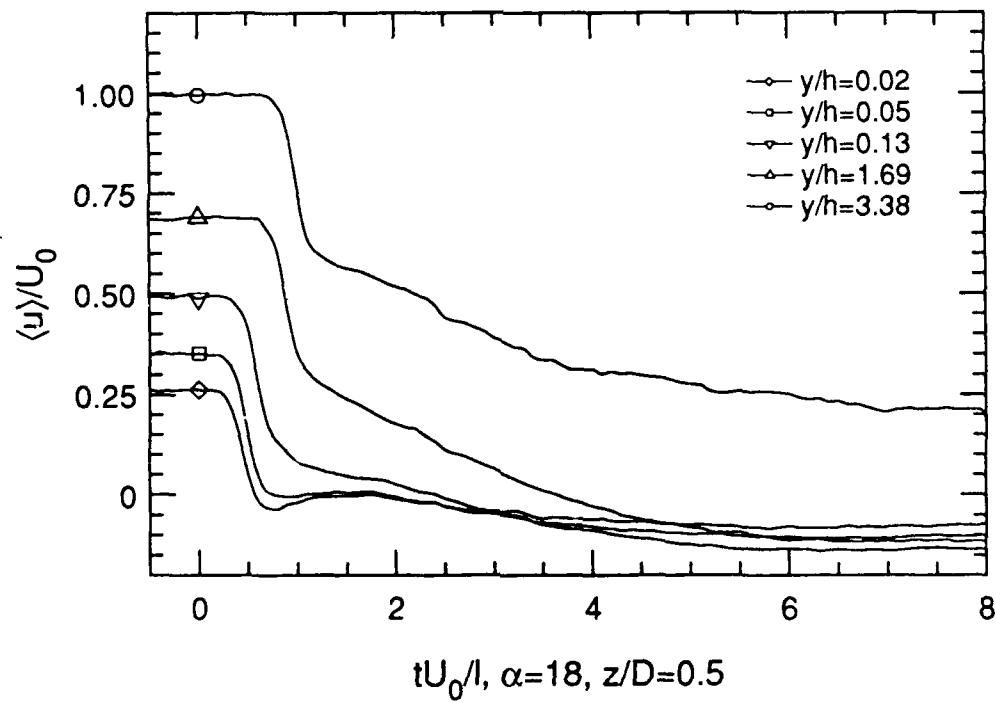
Figure 7.1f History of $\langle u \rangle$ at $z/d = 0.50$ for $\alpha = 18°$
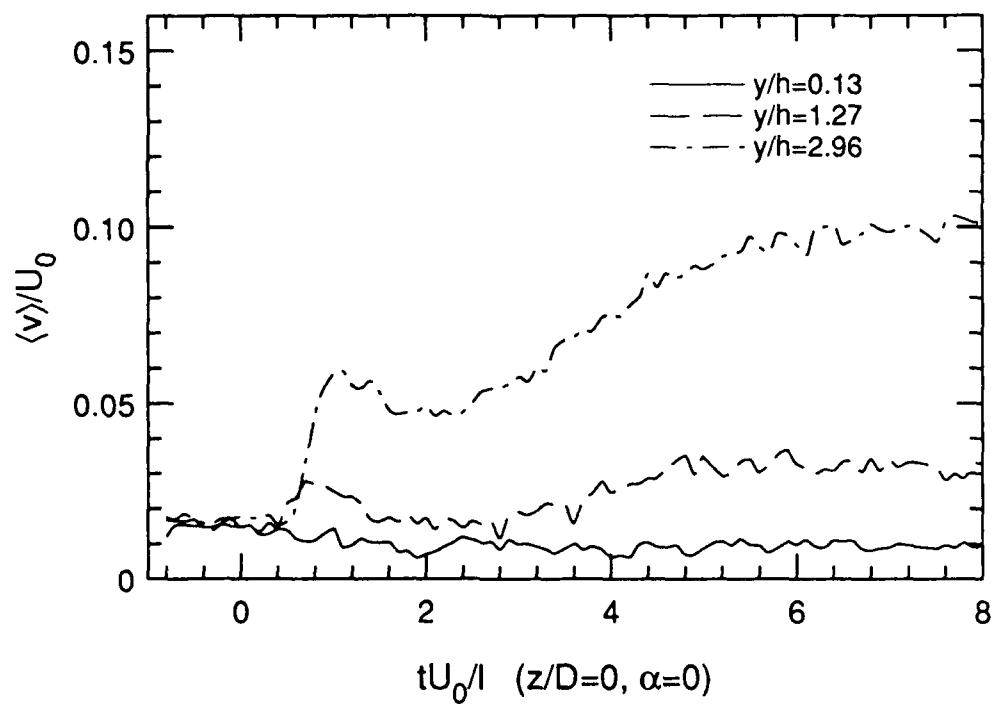
Figure 7.2a History of $\langle v \rangle$ at $z/d = 0$ for $\alpha = 0°$
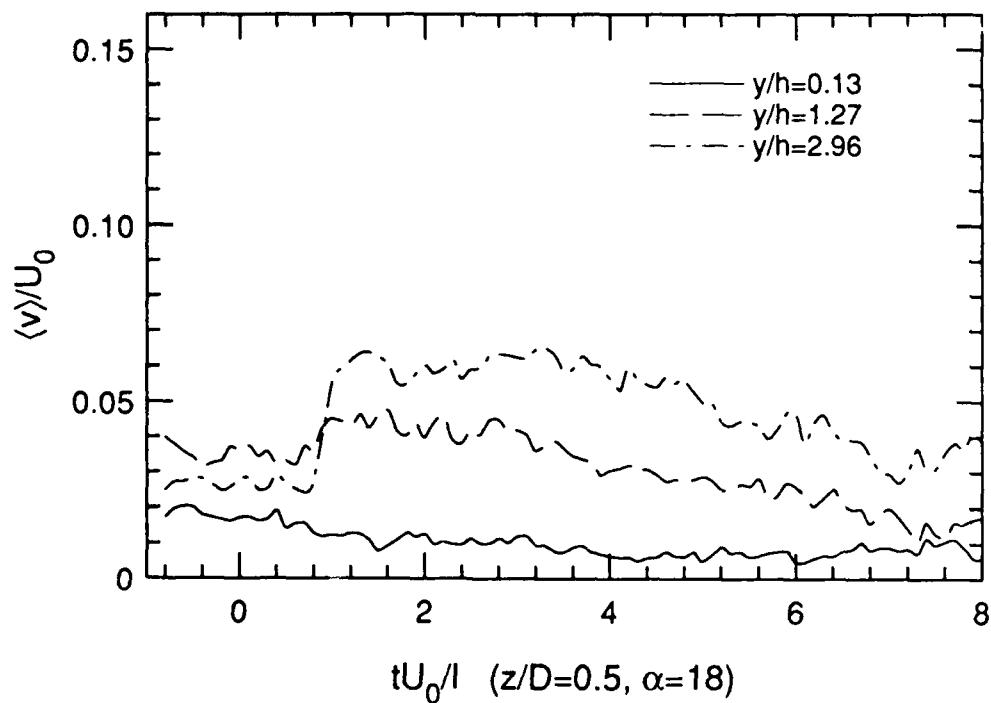
Figure 7.2b History of $\langle v \rangle$ at $z/d = 0.5$ for $\alpha = 18°$

99
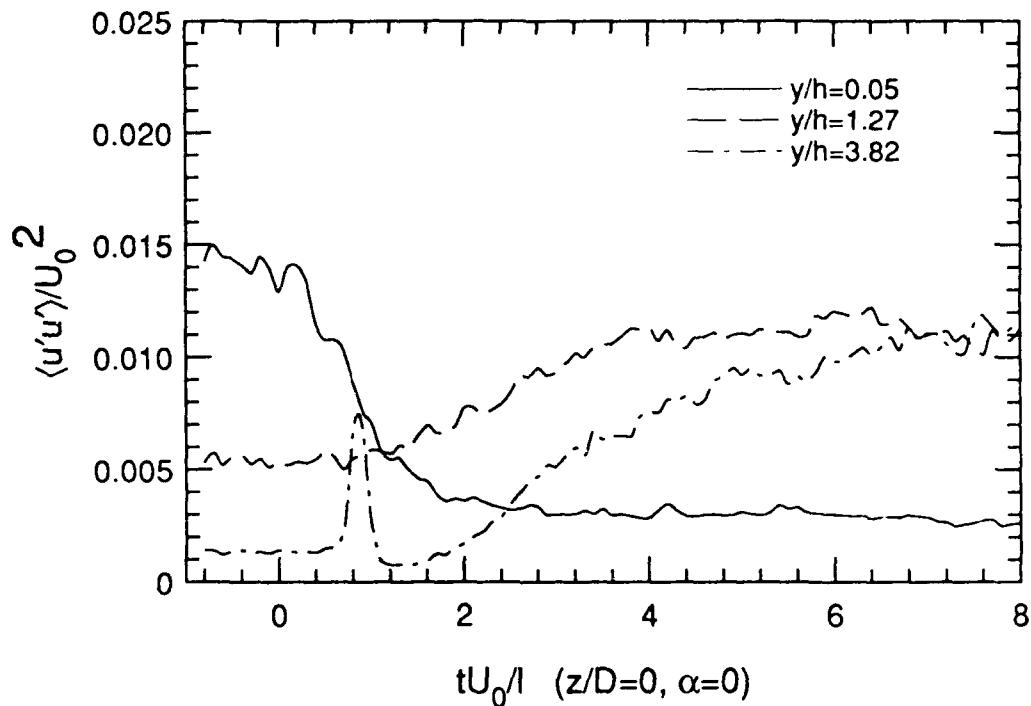
Figure 7.3a History of $\langle u'u' \rangle$ at $z/d = 0$ for $\alpha = 0°$
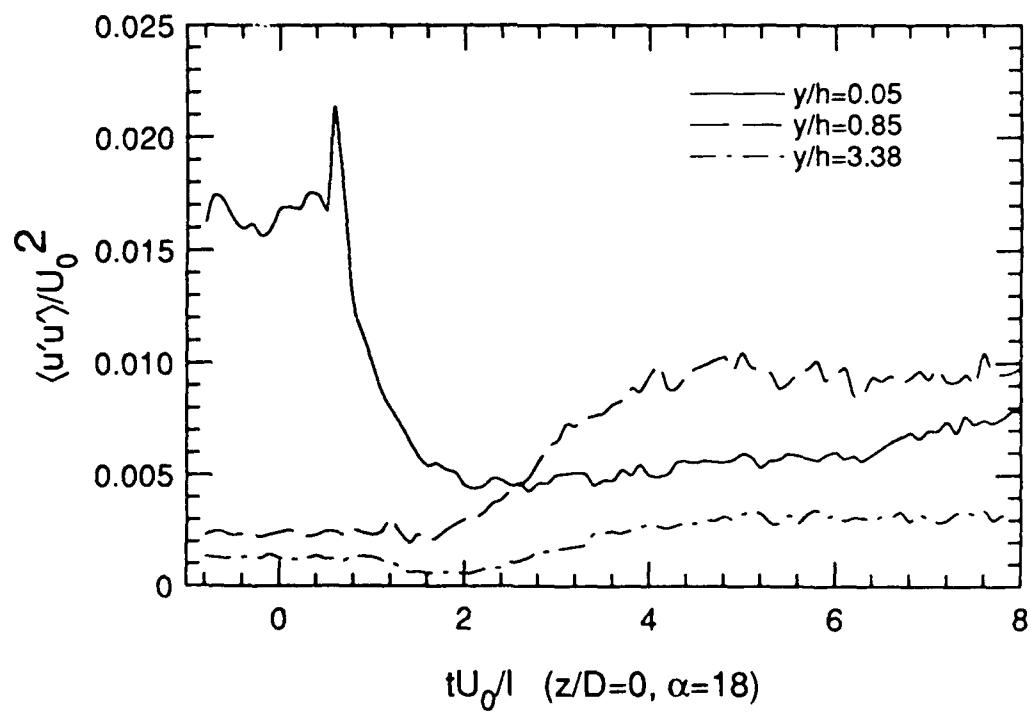
Figure 7.3b History of $\langle u'u' \rangle$ at $z/d = 0$ for $\alpha = 18°$

100
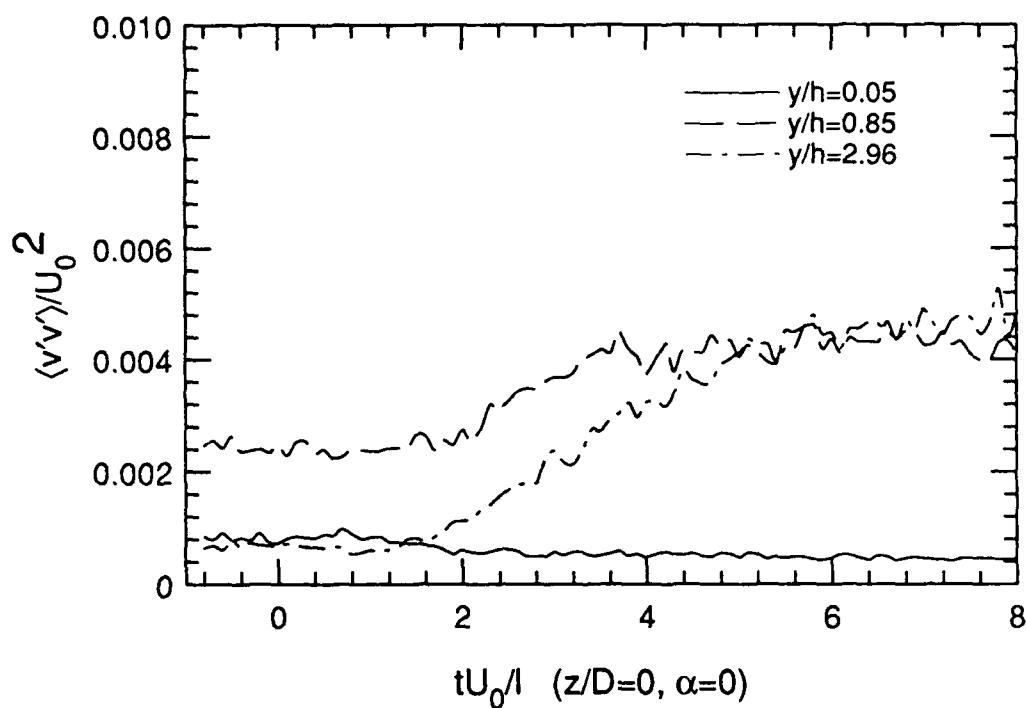
Figure 7.4a History of $\langle v'v' \rangle$ at $z/d = 0$ for $\alpha = 0°$
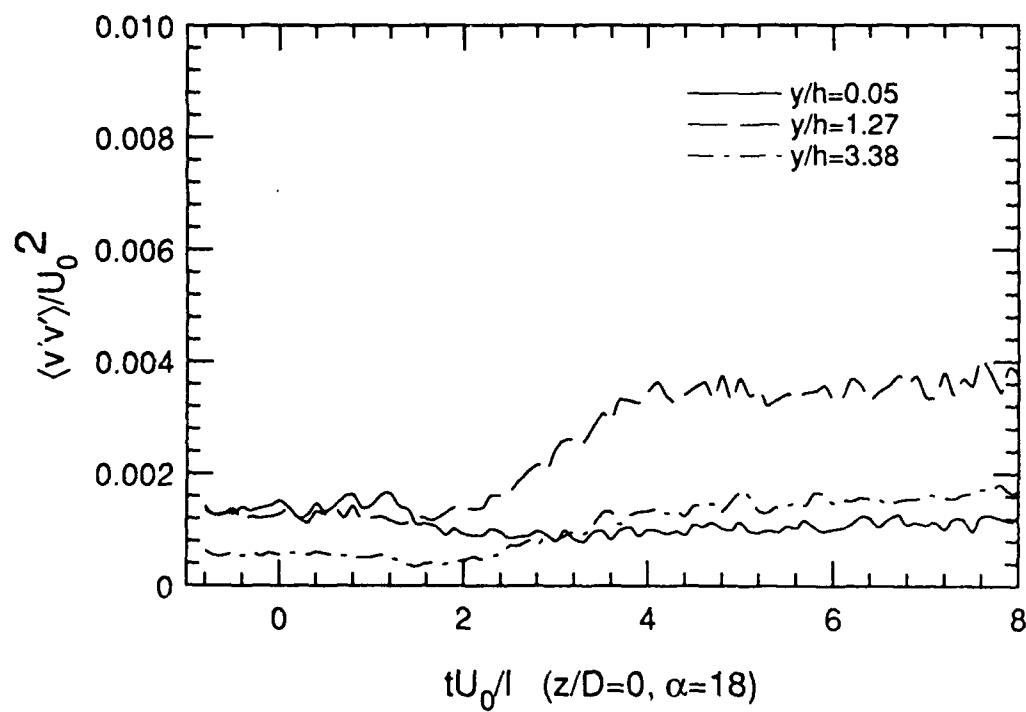
Figure 7.4b History of $\langle v'v' \rangle$ at $z/d = 0$ for $\alpha = 18°$

101
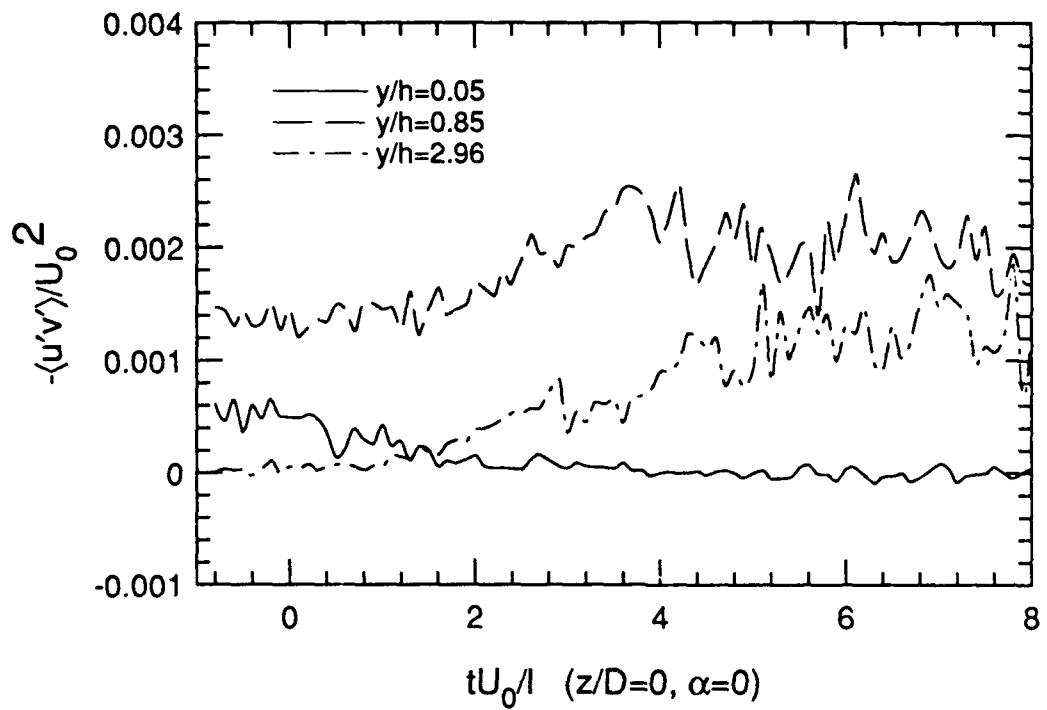
Figure 7.5a History of $-\langle u'v' \rangle$ at $z/d = 0$ for $\alpha = 0°$
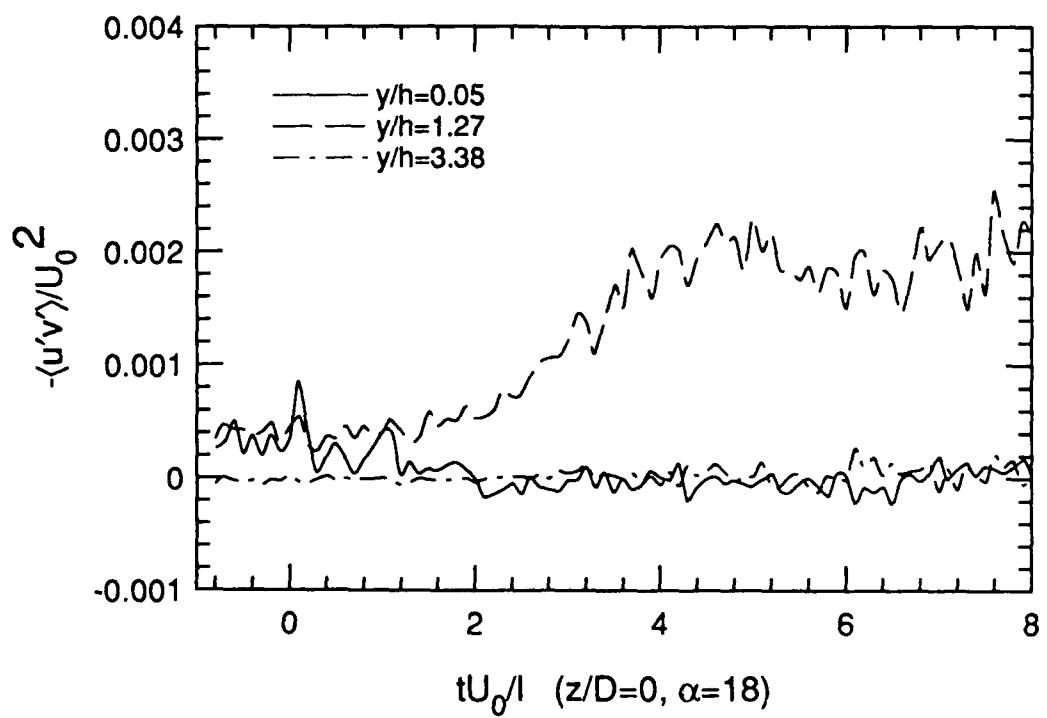
Figure 7.5b History of $-\langle u'v' \rangle$ at $z/d = 0$ for $\alpha = 18°$

102
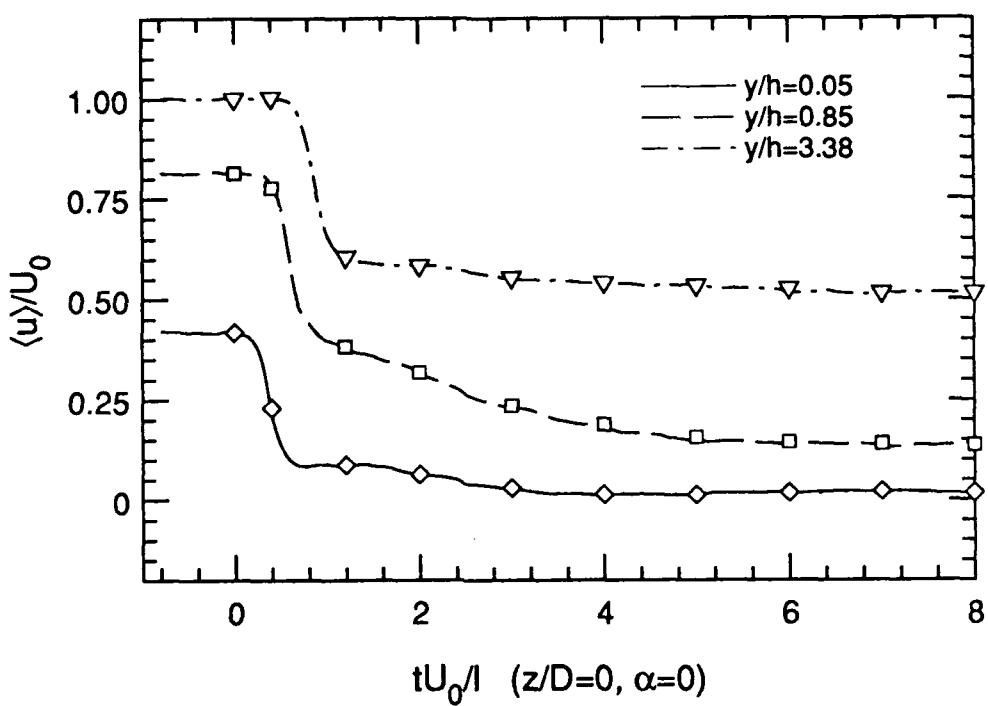
Figure 7.6a History of $\langle u \rangle$ with symbols showing piecewise fit to data
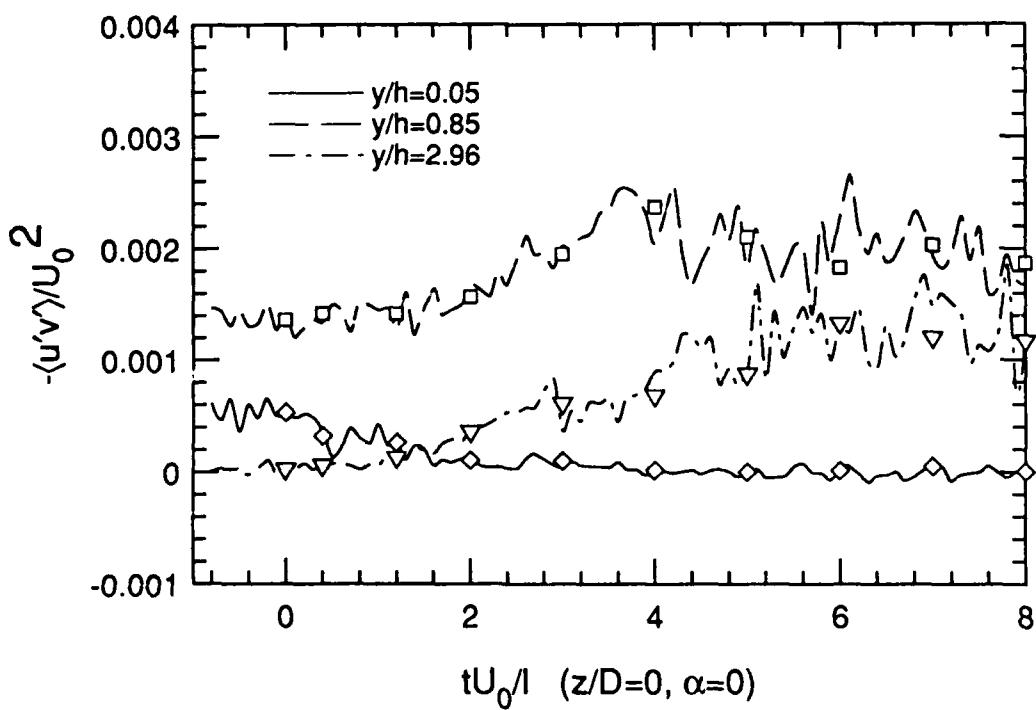
Figure 7.6b History of $-\langle u'v' \rangle$ with symbols showing piecewise fit to data

103
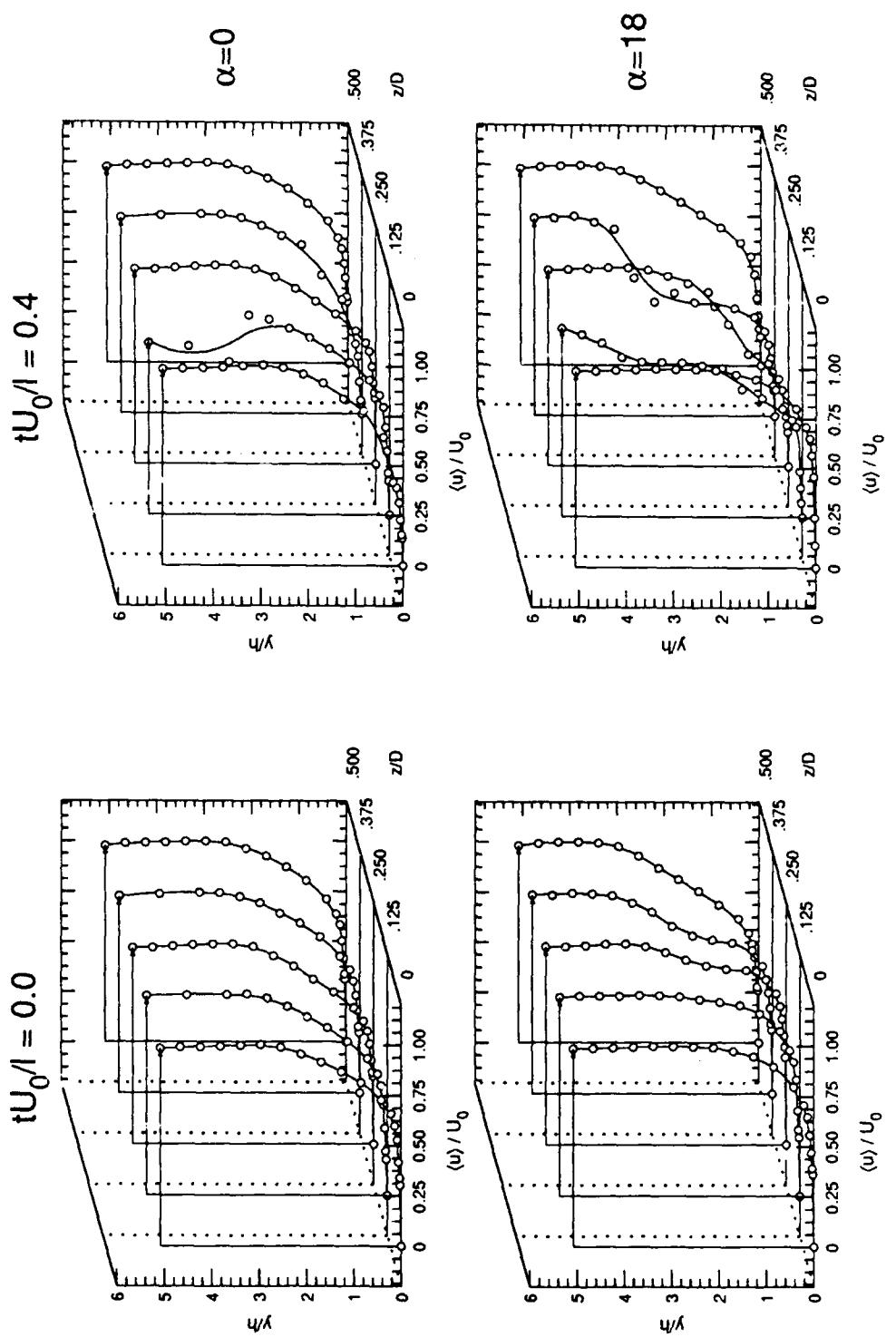
Figure 7.7 Profiles of $\langle u \rangle$ at $tU_0/l = 0$ and $tU_0/l = 0.4$
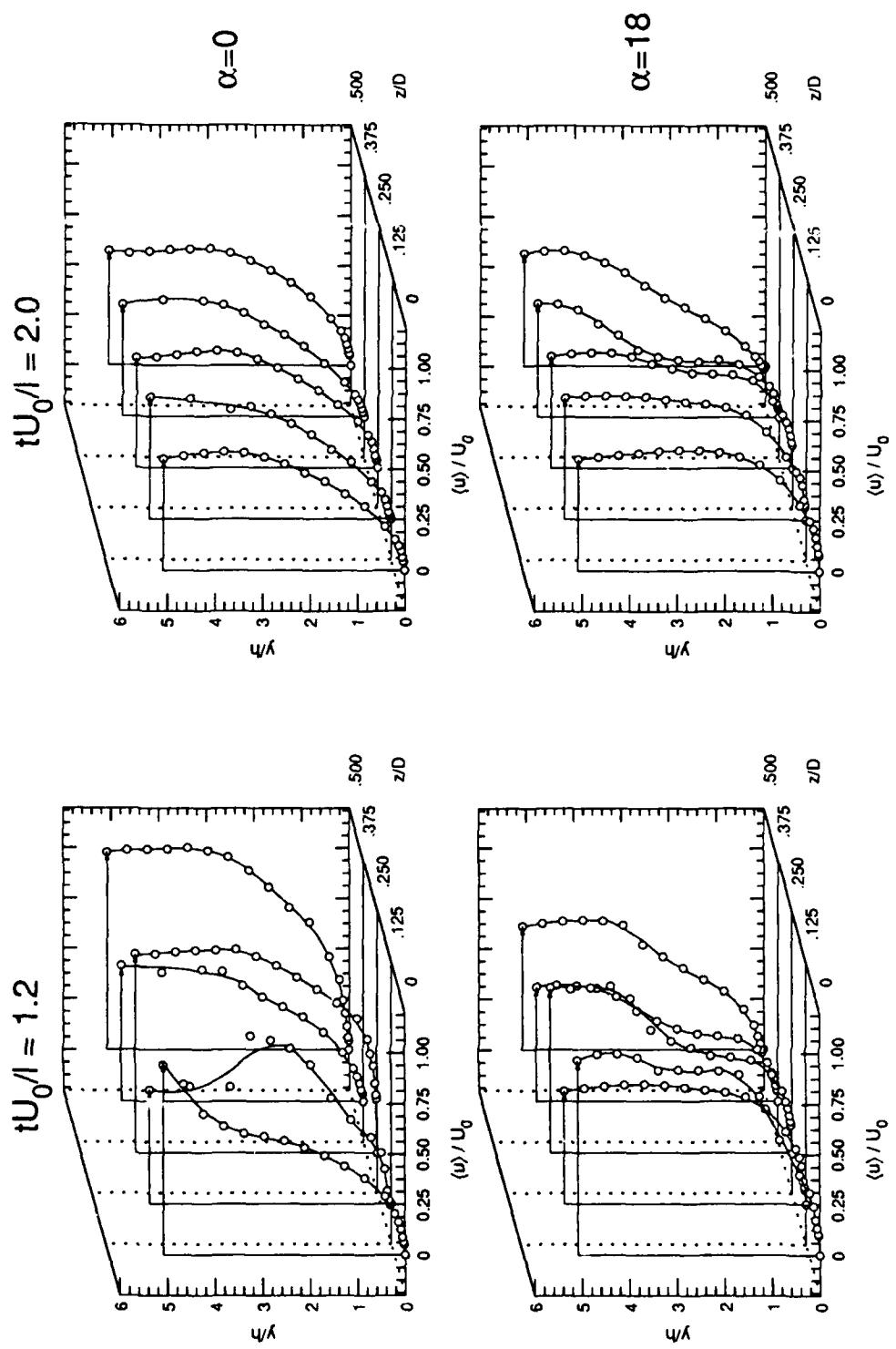
Figure 7.8 Profiles of $\langle u \rangle$ at $tU_0/l = 1.2$ and $tU_0/l = 2$
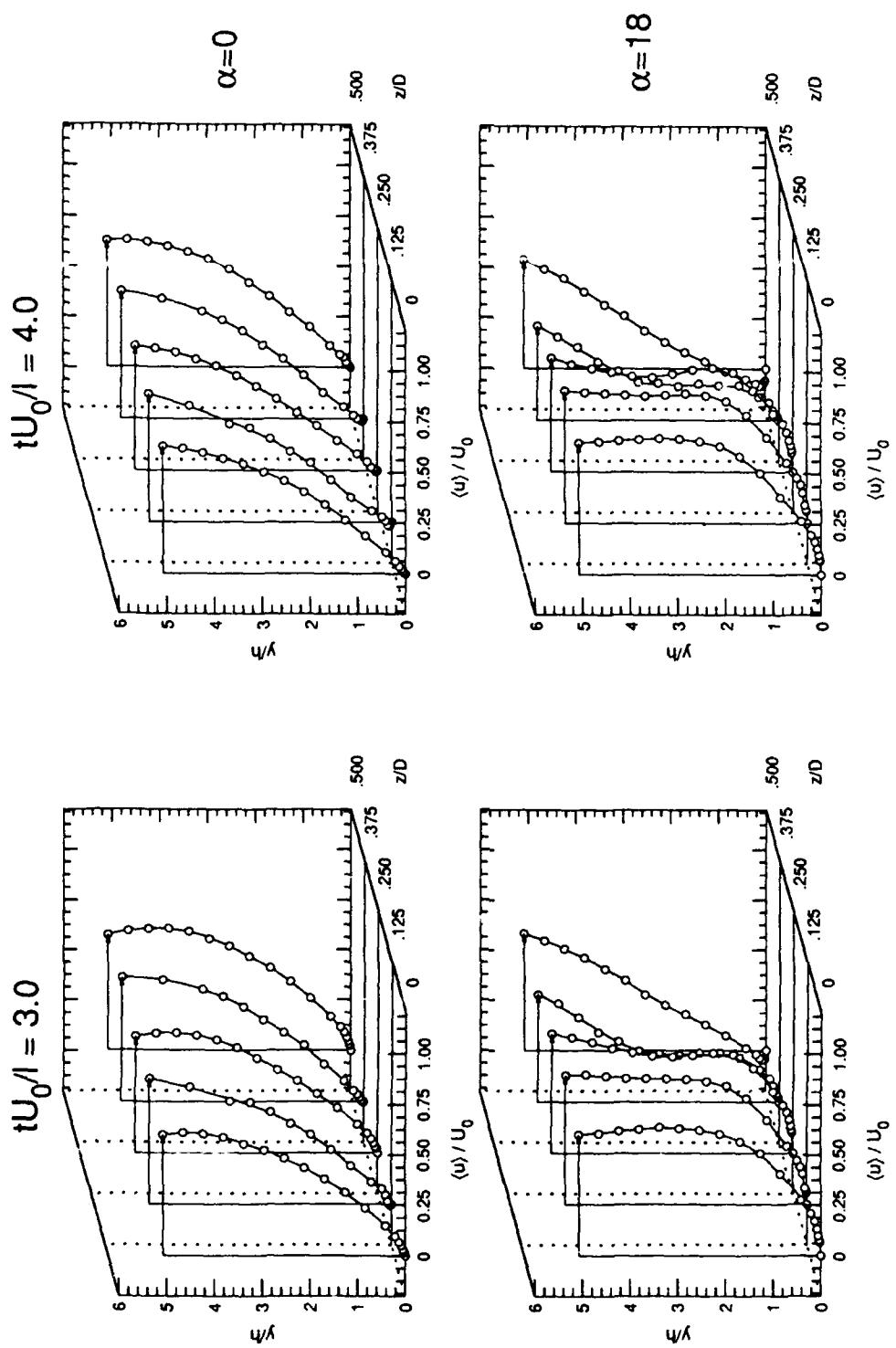
Figure 7.9 Profiles of $\langle u \rangle$ at $tU_0/l = 3$ and $tU_0/l = 4$
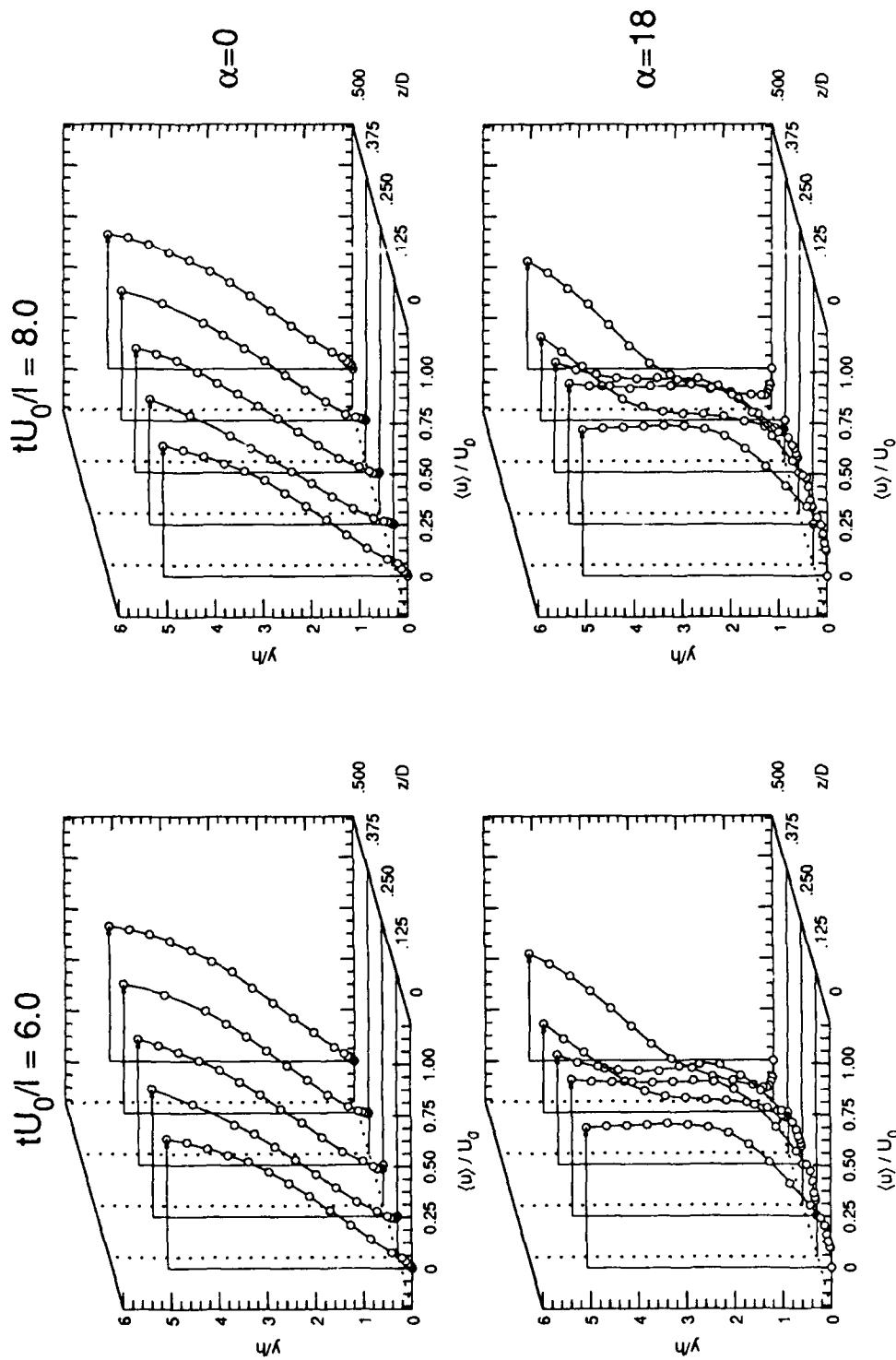
Figure 7.10 Profiles of $\langle u \rangle$ at $tU_0/l = 6$ and $tU_0/l = 8$
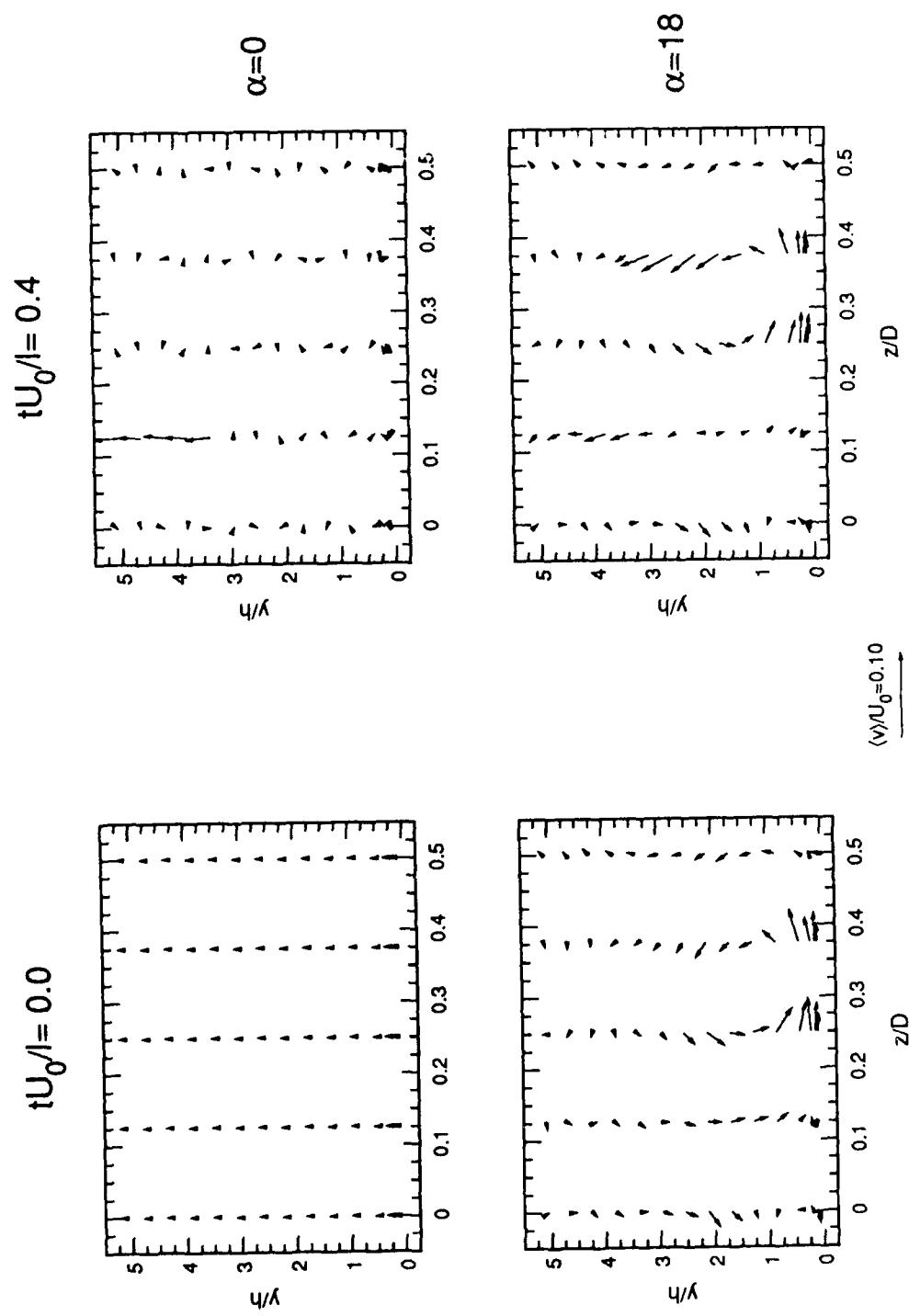
Figure 7.11 Secondary velocity vectors at $tU_0/l = 0$ and $tU_0/l = 0.4$
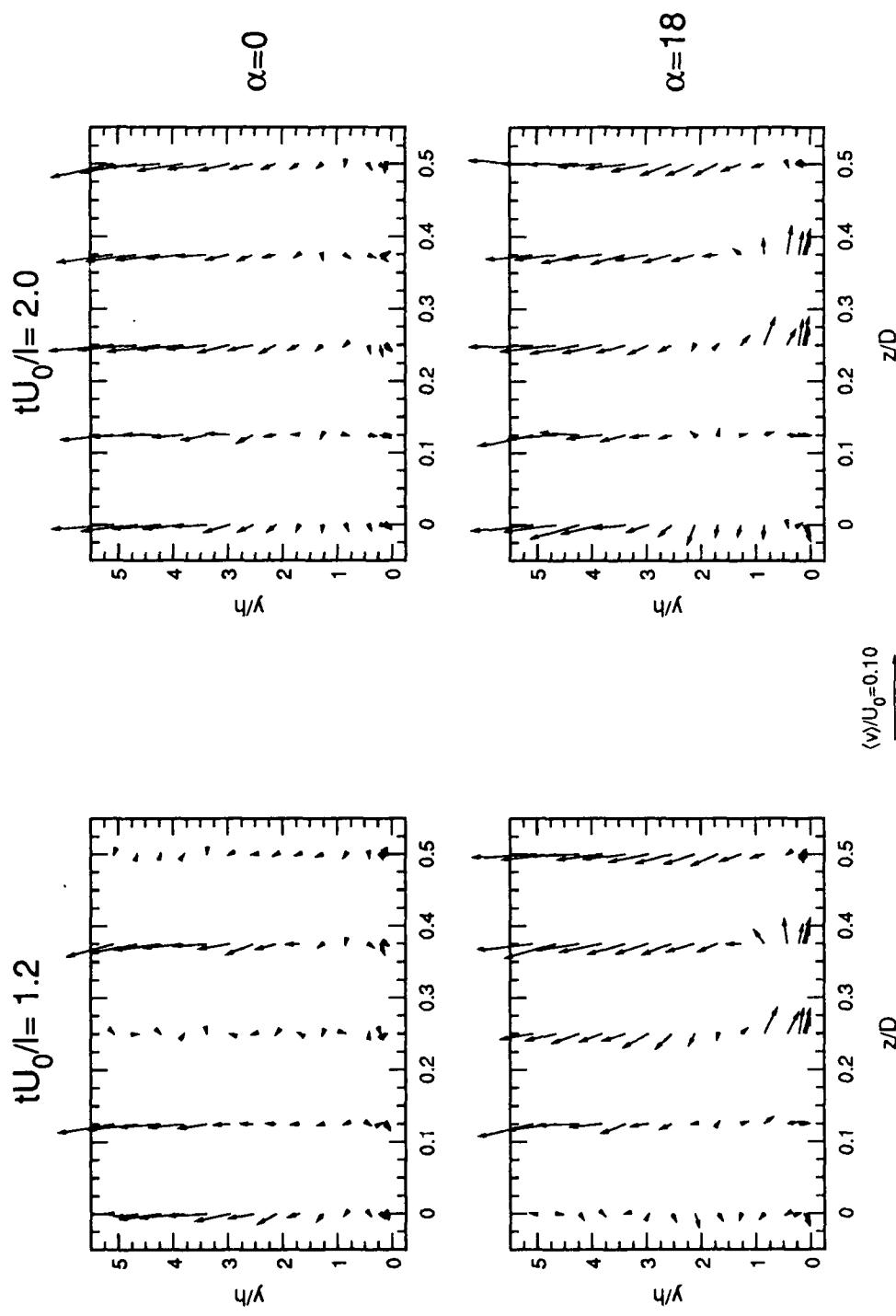
Figure 7.12 Secondary velocity vectors at $tU_0/l = 1.2$ and $tU_0/l = 2$
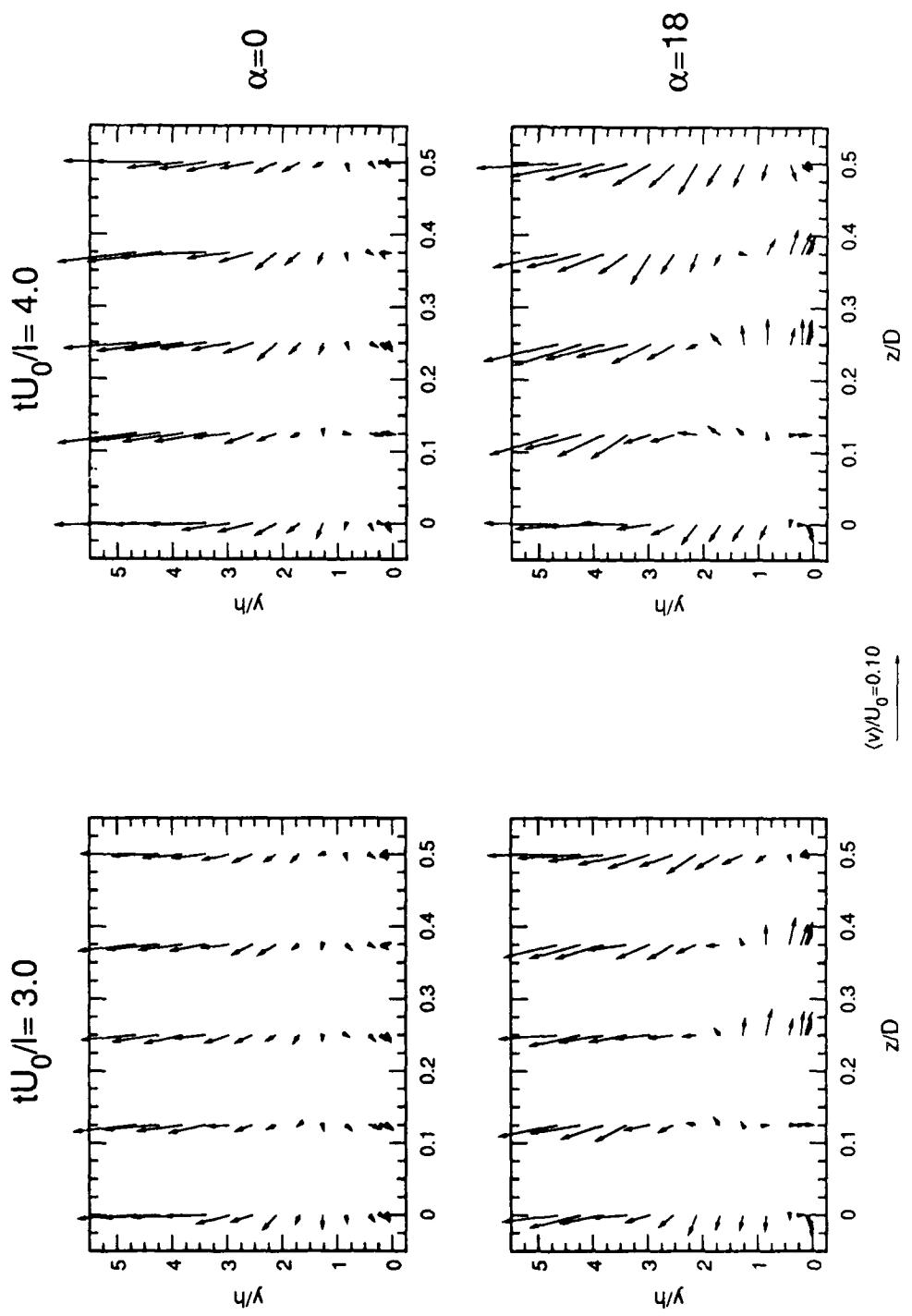
Figure 7.13 Secondary velocity vectors at $tU_0/l = 3$ and $tU_0/l = 4$
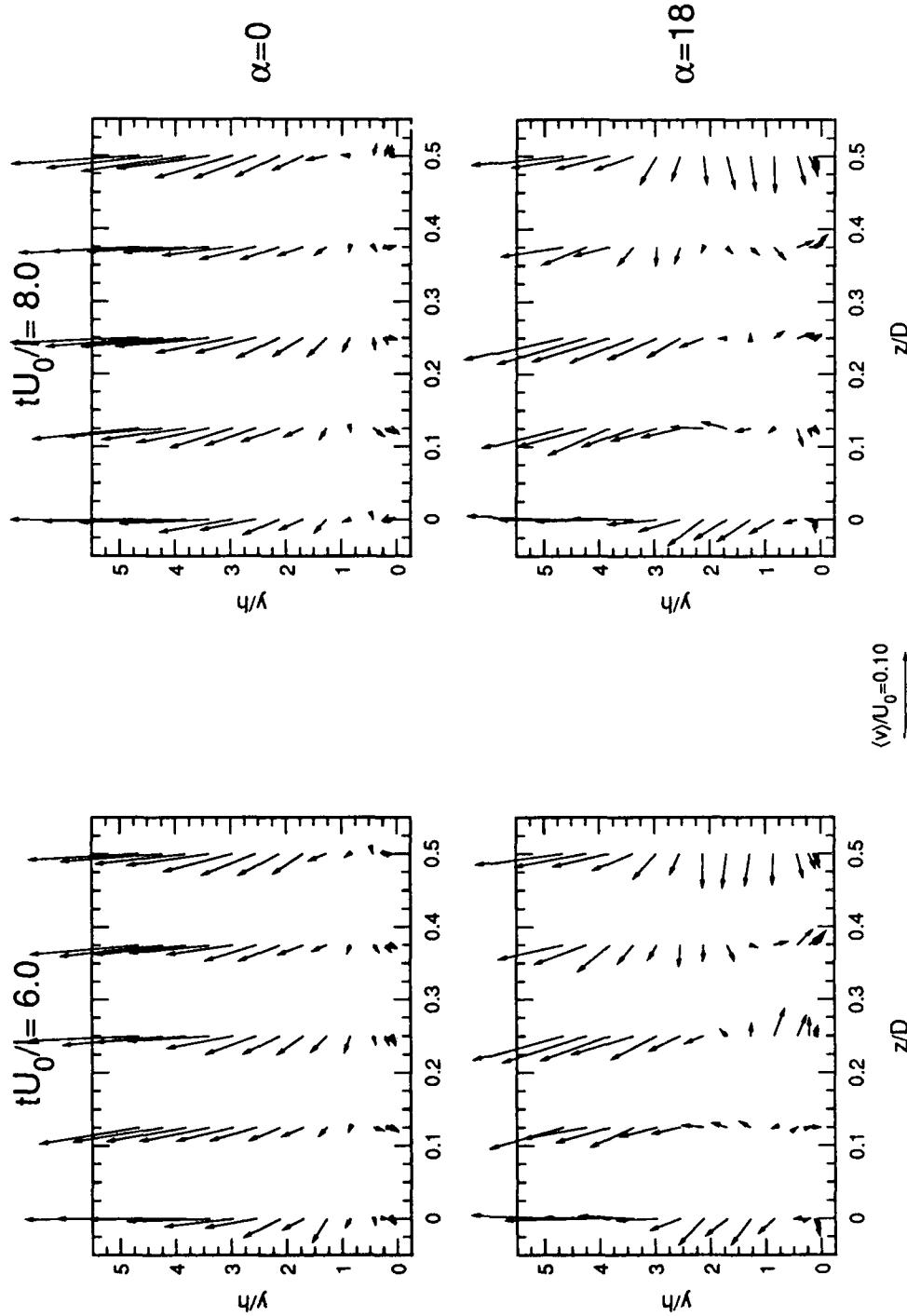
Figure 7.14 Secondary velocity vectors at $tU_0/l = 6$ and $tU_0/l = 8$
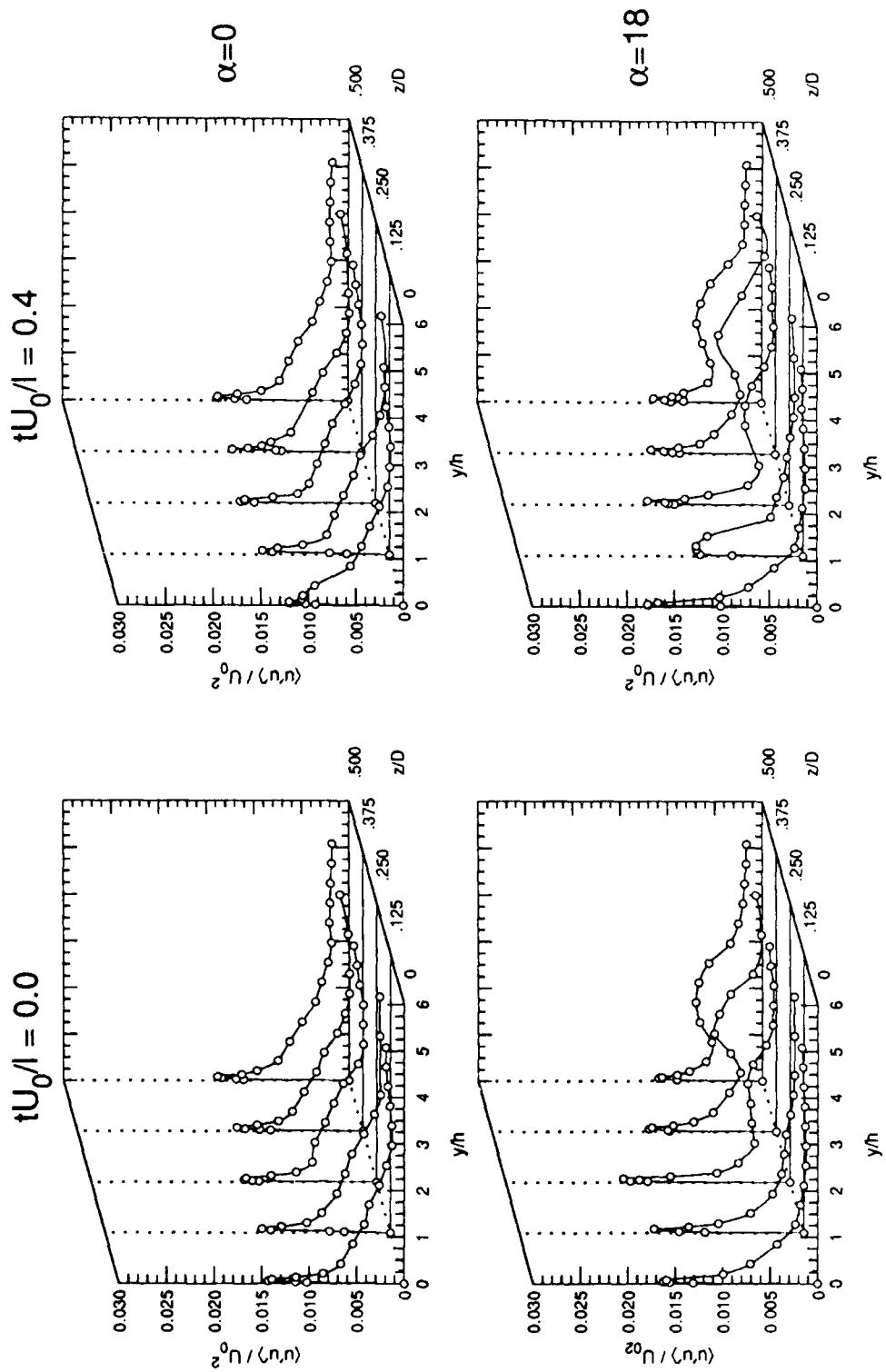
Figure 7.15 Profiles of $\langle u'u' \rangle$ at $tU_0/l = 0$ and $tU_0/l = 0.4$

112
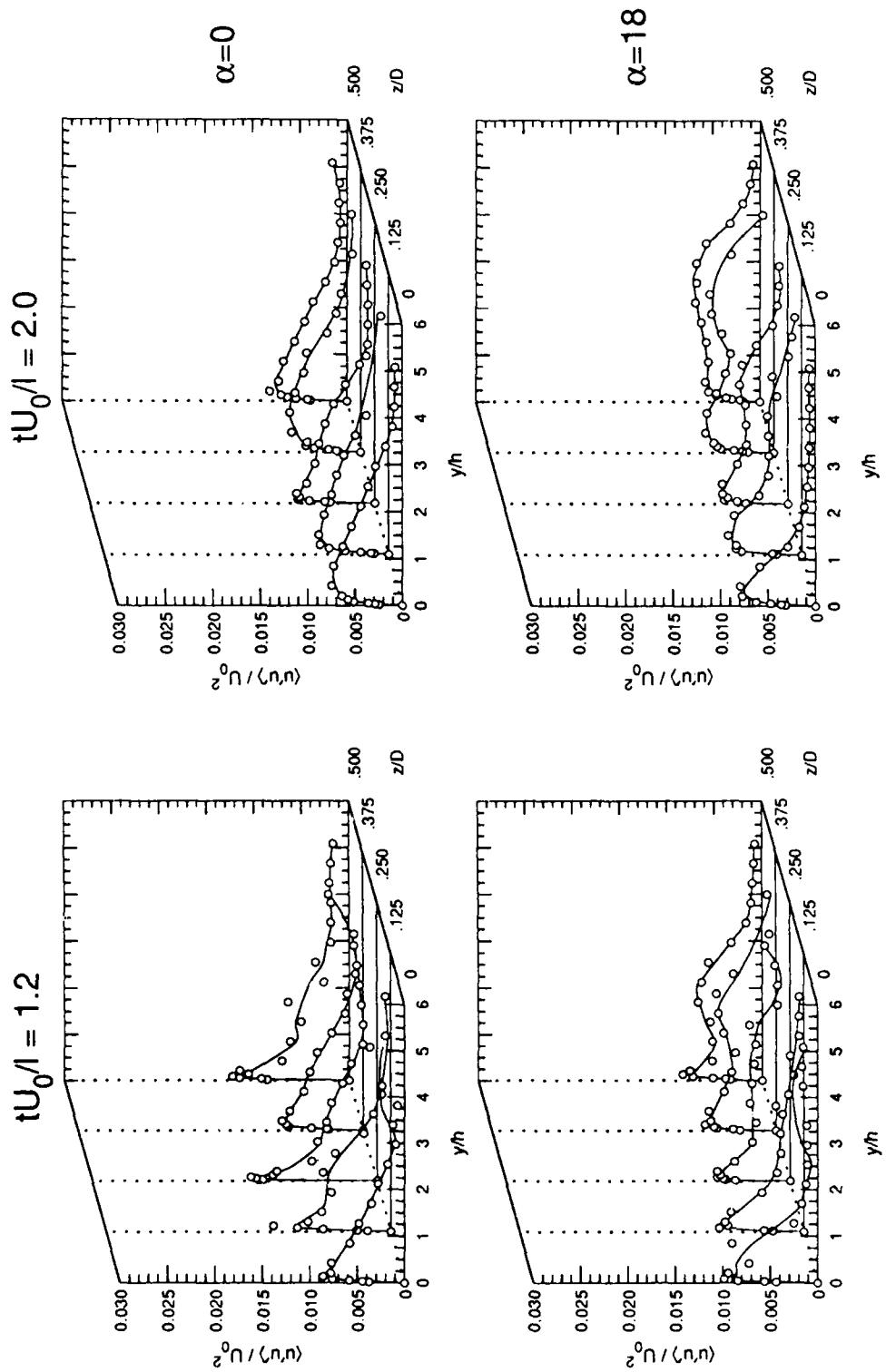
Figure 7.16 Profiles of $\langle u'u' \rangle$ at $tU_0/l = 1.2$ and $tU_0/l = 2$

113
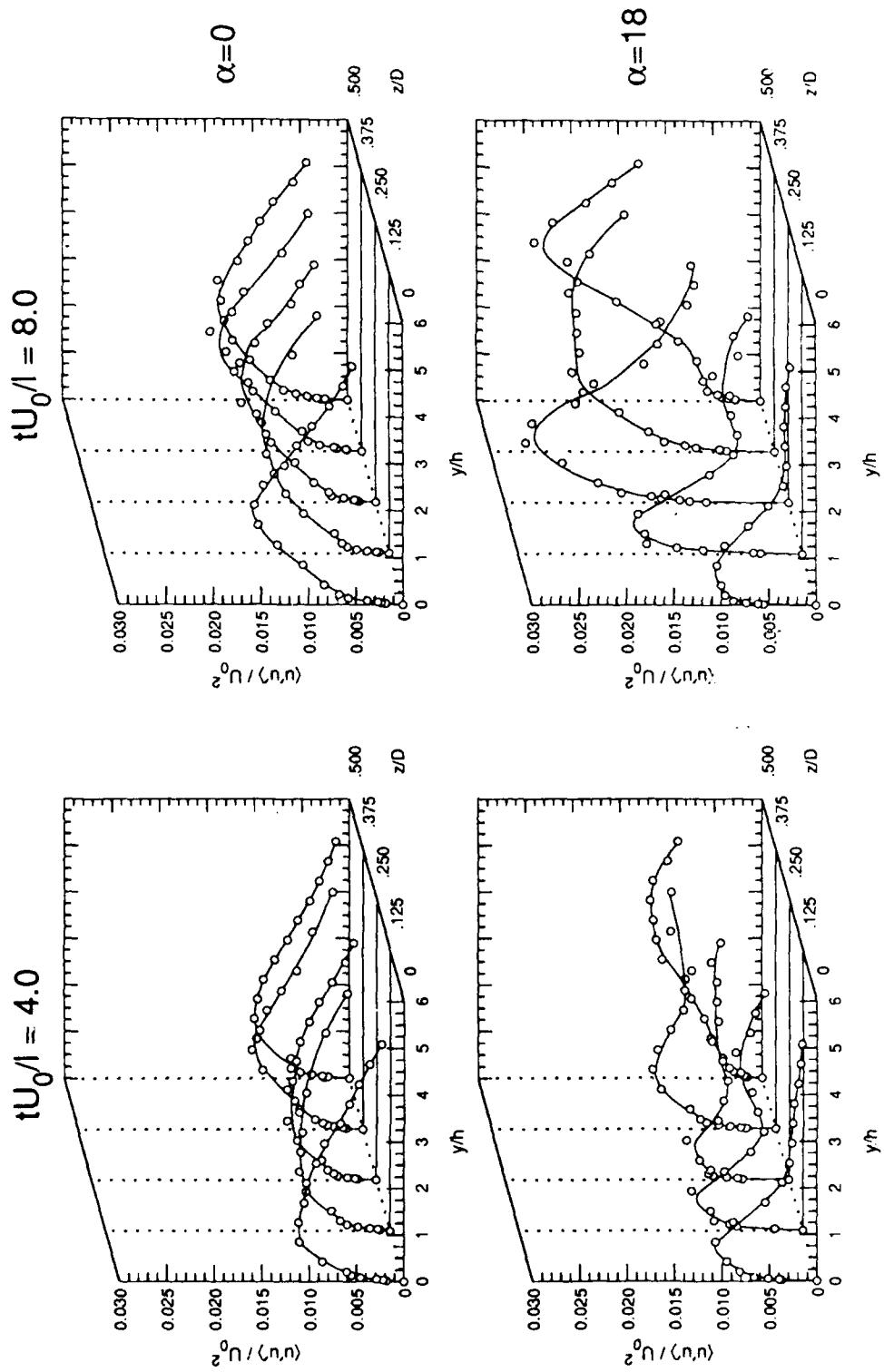
Figure 7.17 Profiles of $\langle u'u' \rangle$ at $tU_0/l = 4$ and $tU_0/l = 8$

114
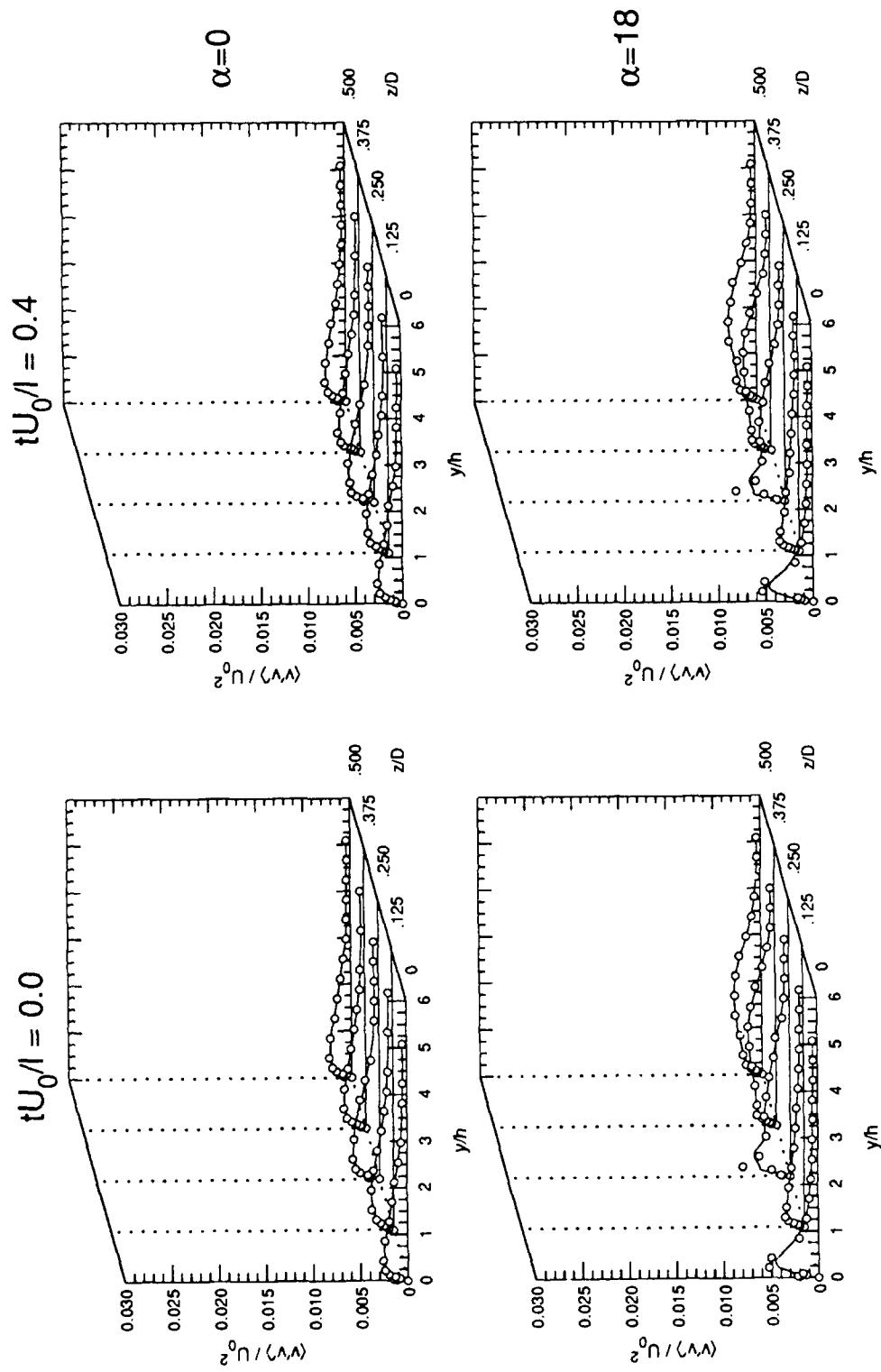
Figure 7.18 Profiles of $\langle v'v' \rangle$ at $tU_0/l = 0$ and $tU_0/l = 0.4$

115
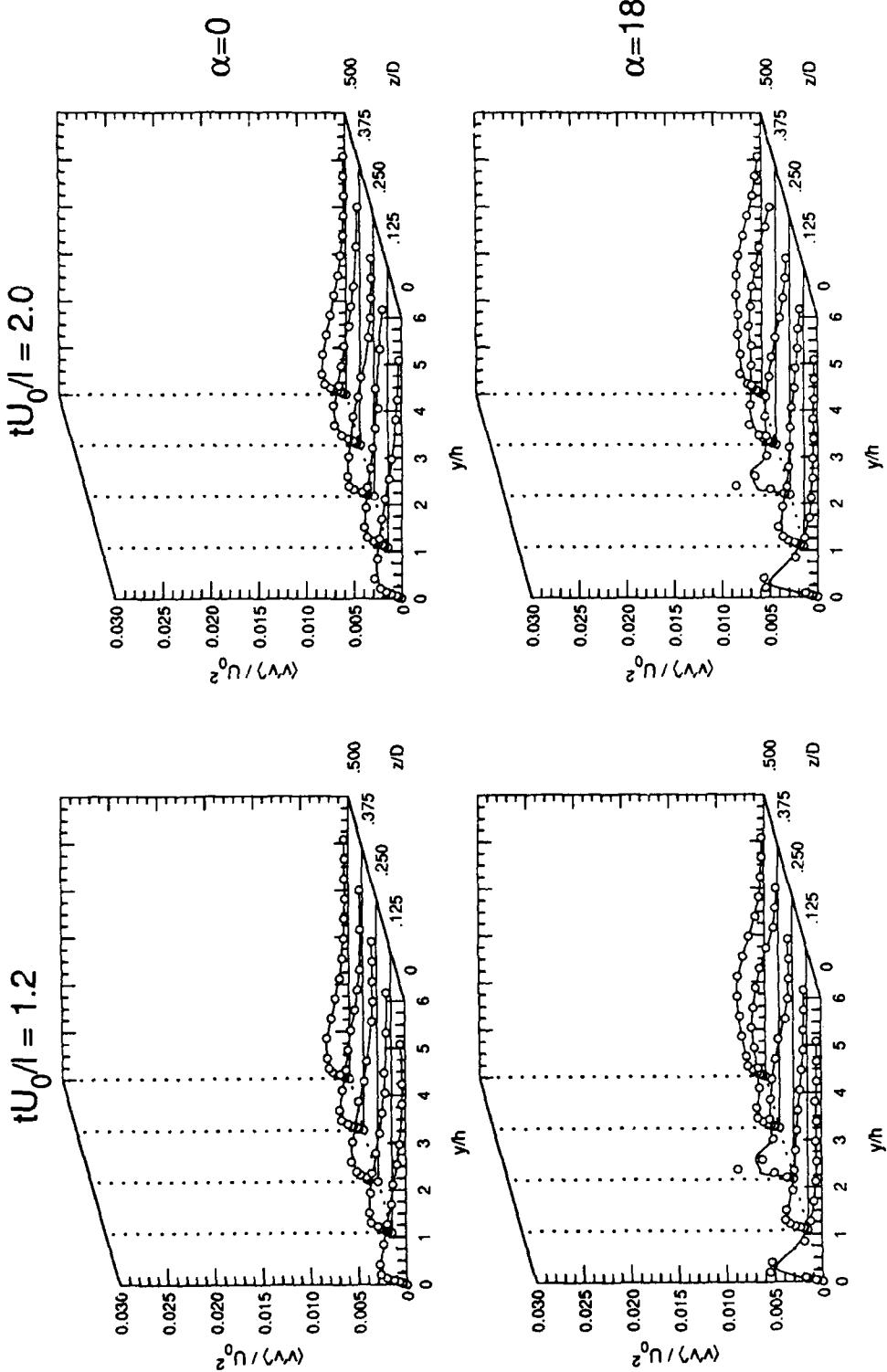
Figure 7.19 Profiles of $\langle v'v' \rangle$ at $tU_0/l = 1.2$ and $tU_0/l = 2$
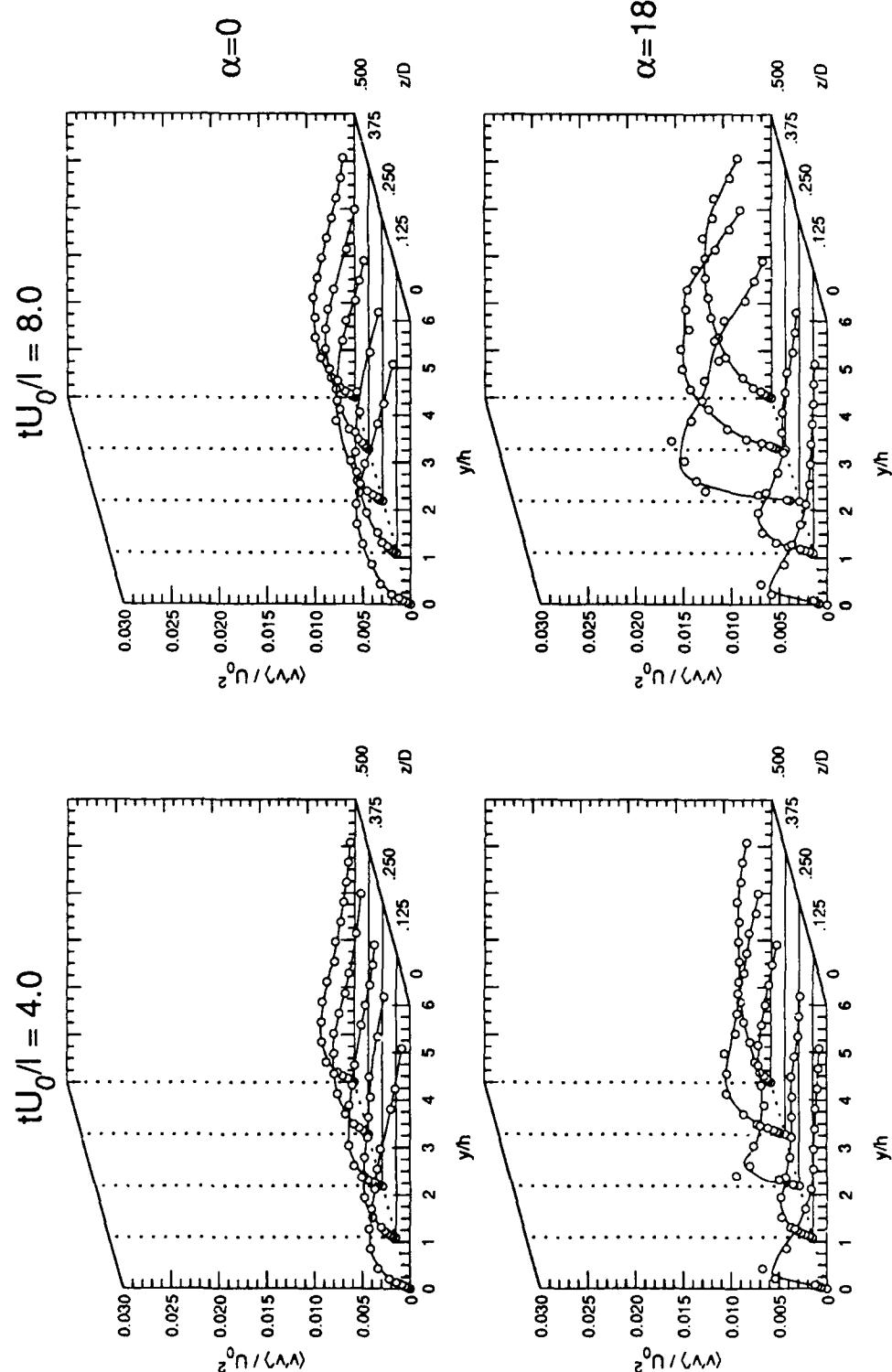
Figure 7.20 Profiles of $\langle v'v' \rangle$ at $tU_0/l = 4$ and $tU_0/l = 8$

117
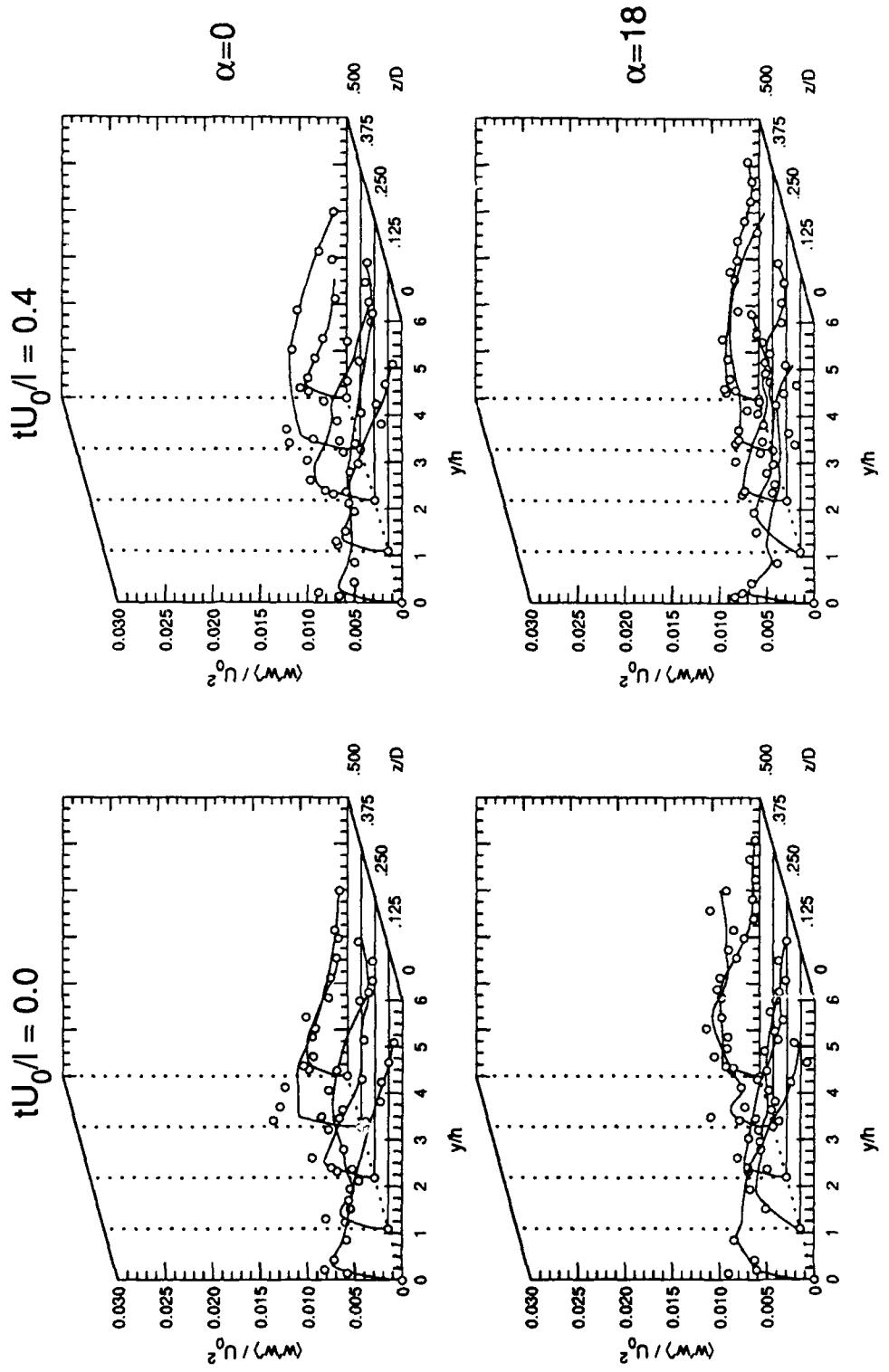
Figure 7.21 Profiles of $\langle w'w' \rangle$ at $tU_0/l = 0$ and $tU_0/l = 0.4$

118
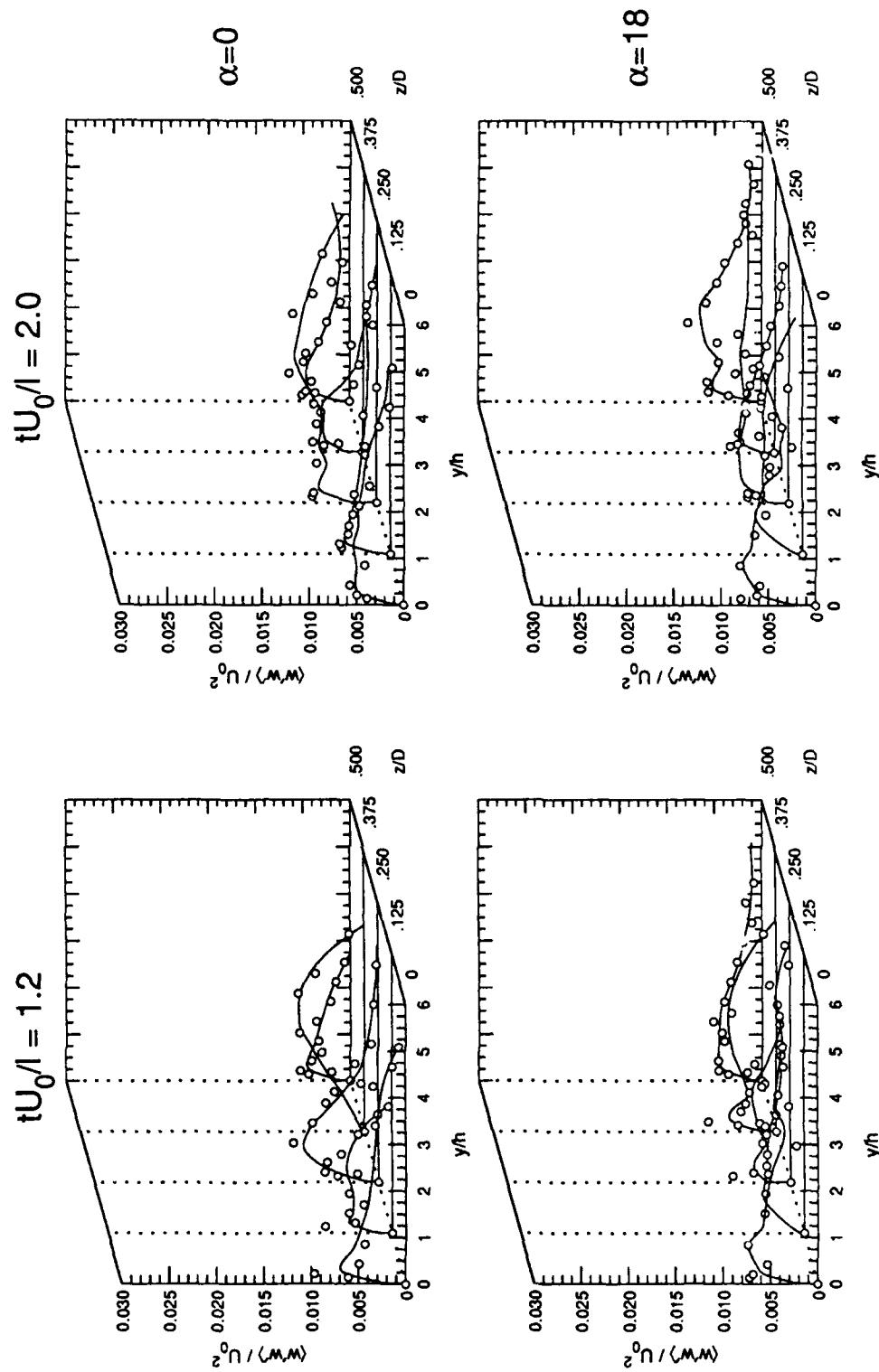
Figure 7.22 Profiles of $\langle w'w' \rangle$ at $tU_0/l = 1.2$ and $tU_0/l = 2$

119
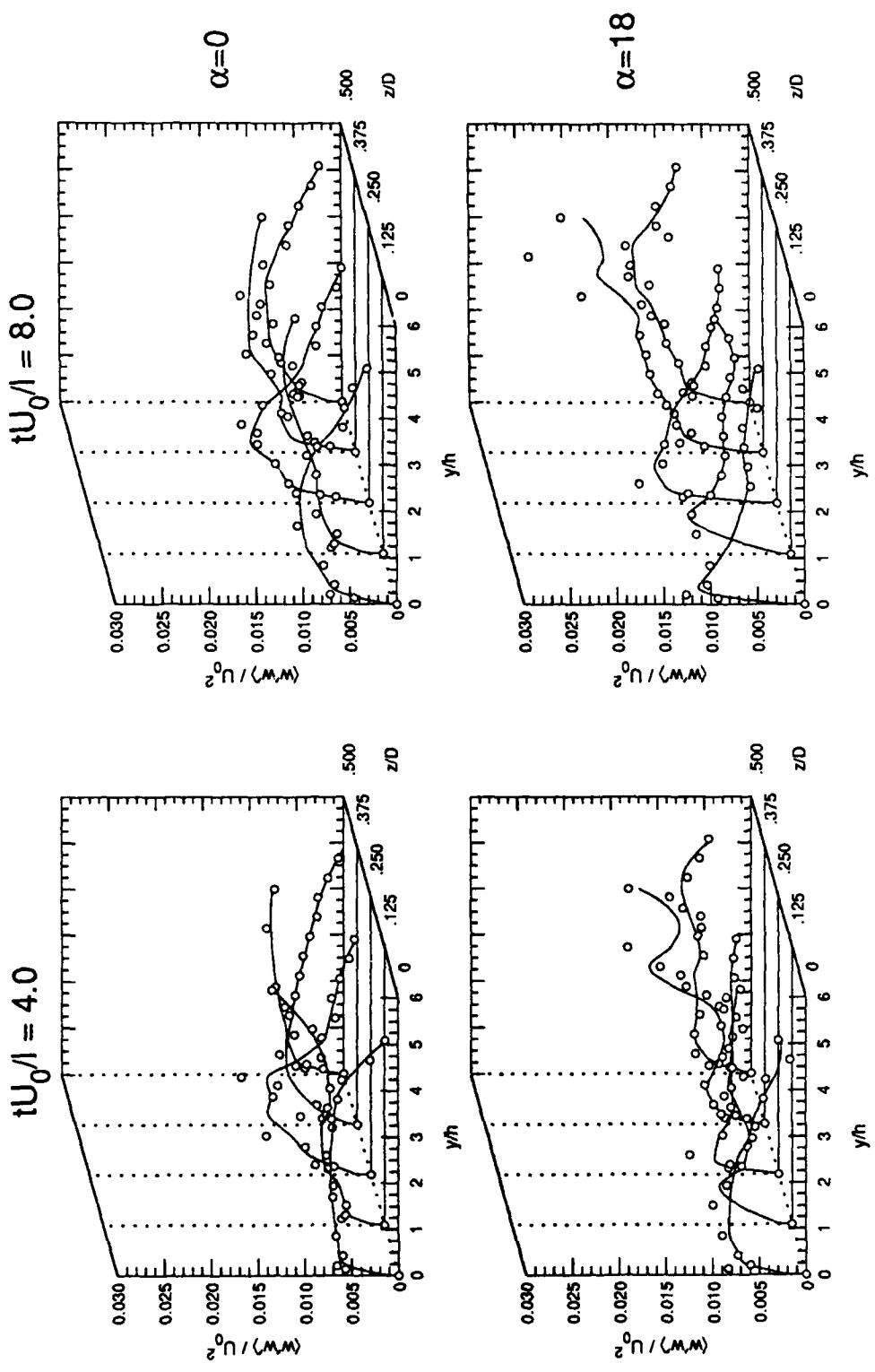
Figure 7.23 Profiles of $\langle w'w' \rangle$ at $tU_0/l = 4$ and $tU_0/l = 8$

120
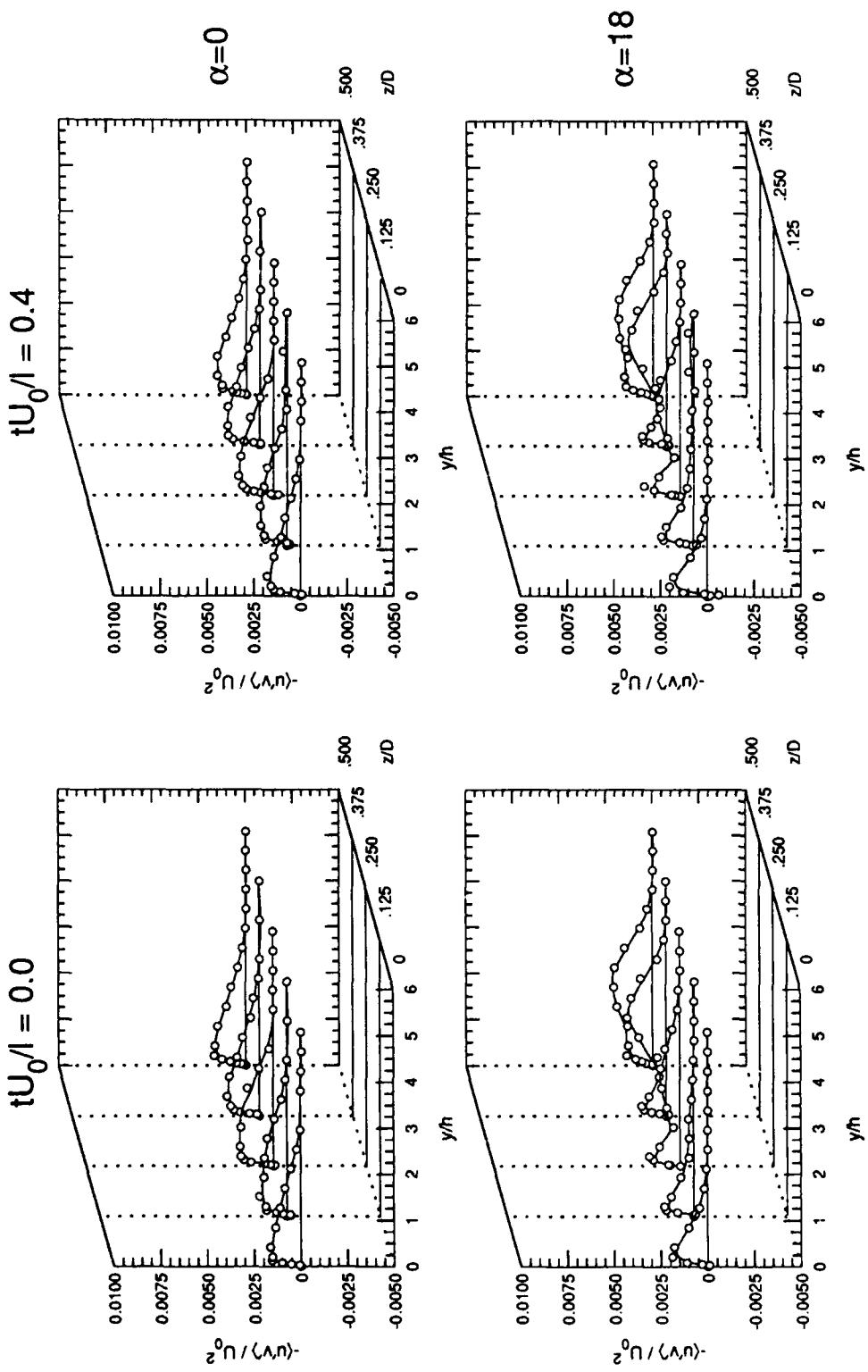
Figure 7.24 Profiles of $-\langle u'v' \rangle$ at $tU_0/l = 0$ and $tU_0/l = 0.4$

121
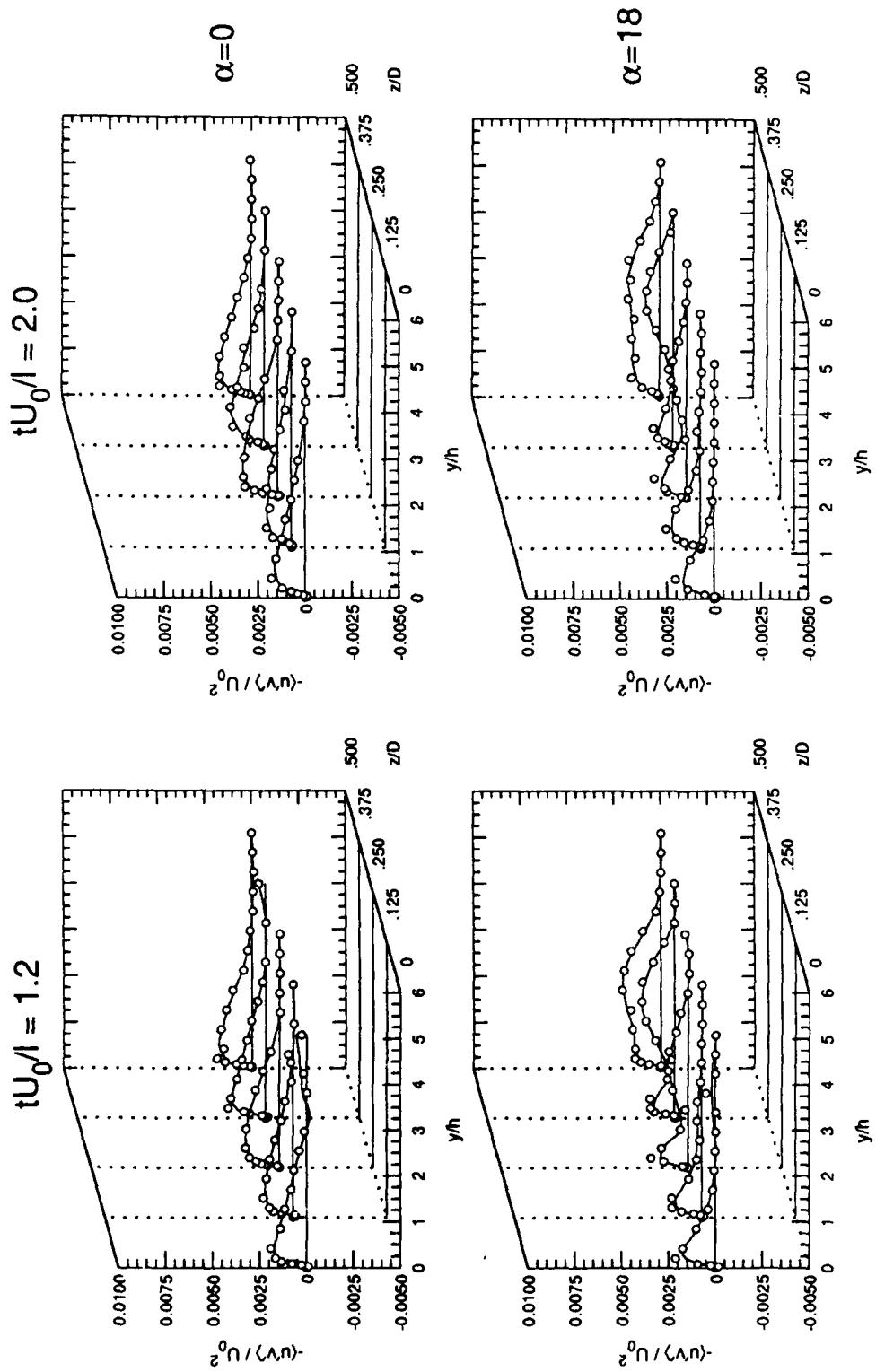
Figure 7.25 Profiles of $-\langle u'v' \rangle$ at $tU_0/l = 1.2$ and $tU_0/l = 2$

122
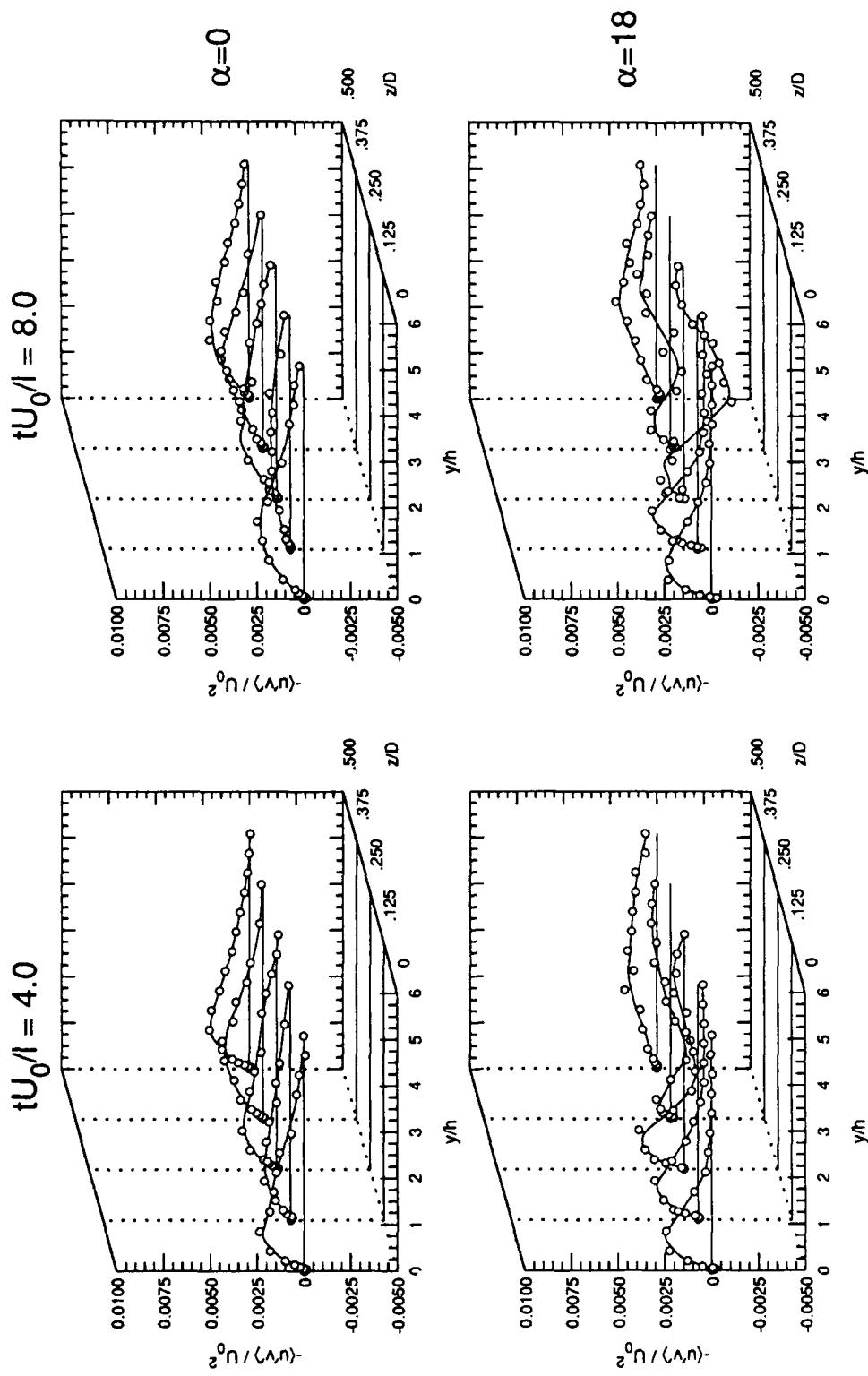
Figure 7.26 Profiles of $-\langle u'v' \rangle$ at $tU_0/l = 4$ and $tU_0/l = 8$

123
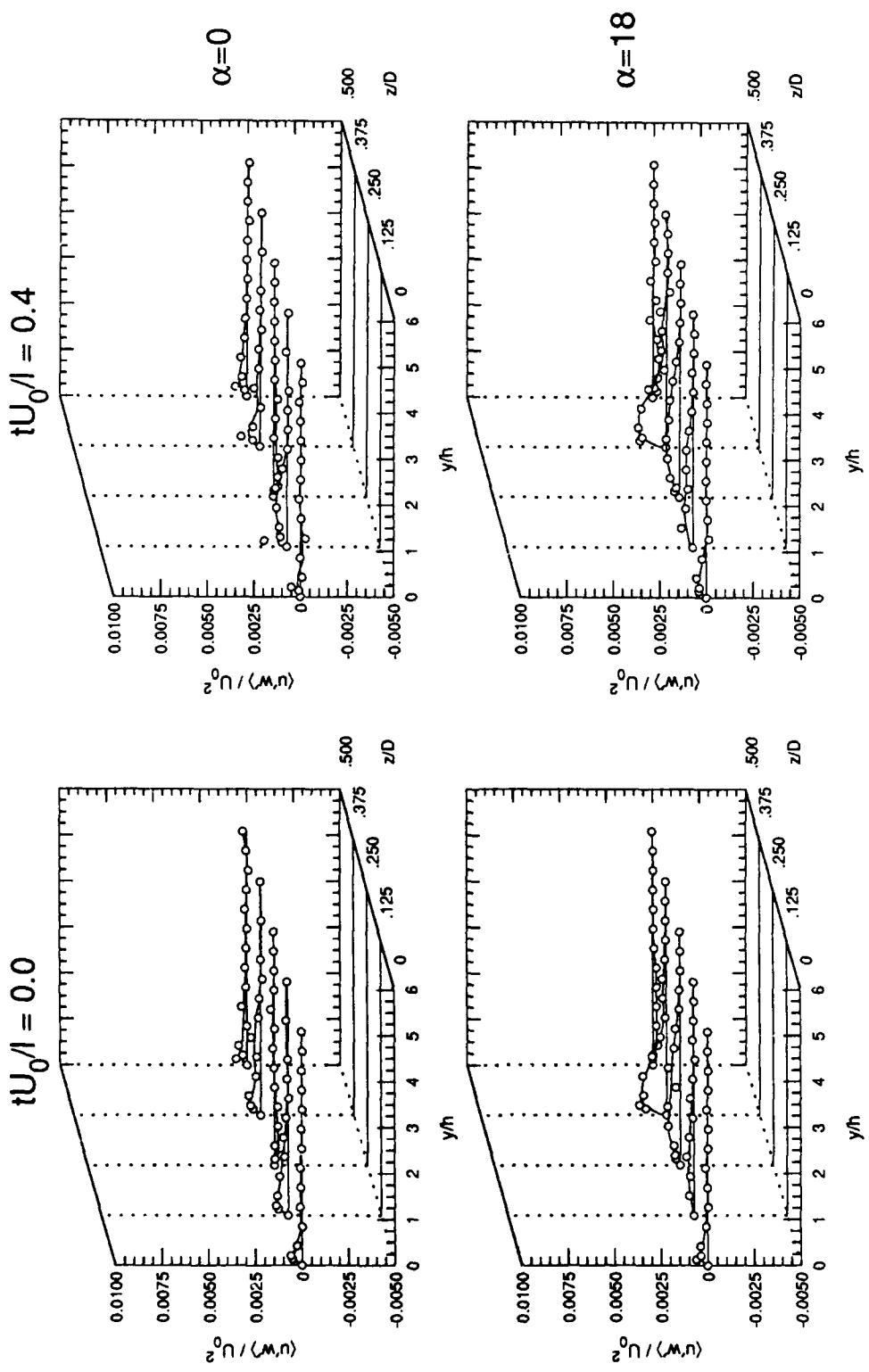
Figure 7.27 Profiles of $\langle u'w'\rangle$ at $tU_0/l = 0$ and $tU_0/l = 0.4$

124
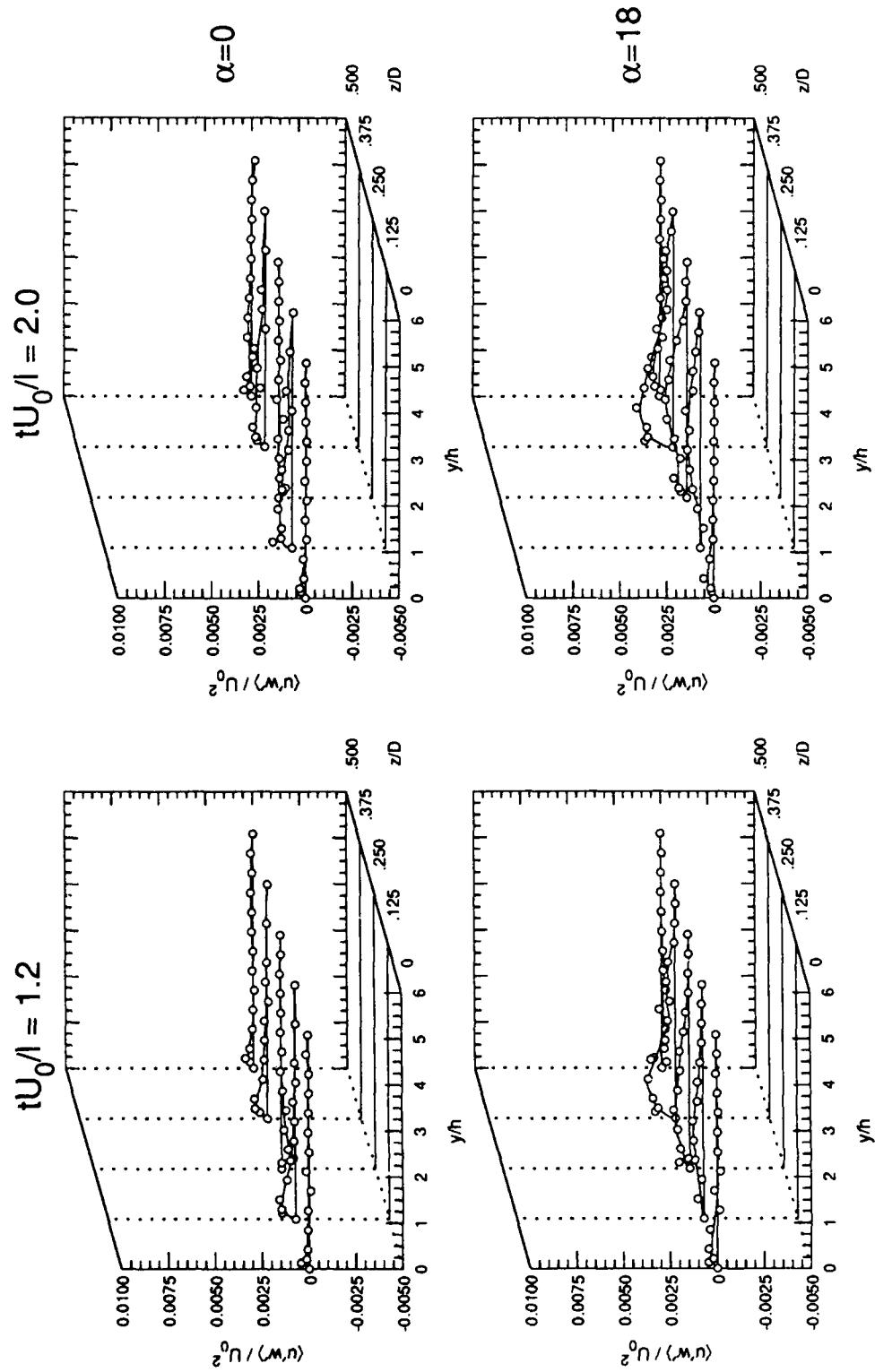
Figure 7.28 Profiles of $\langle u'w' \rangle$ at $tU_0/l = 1.2$ and $tU_0/l = 2$
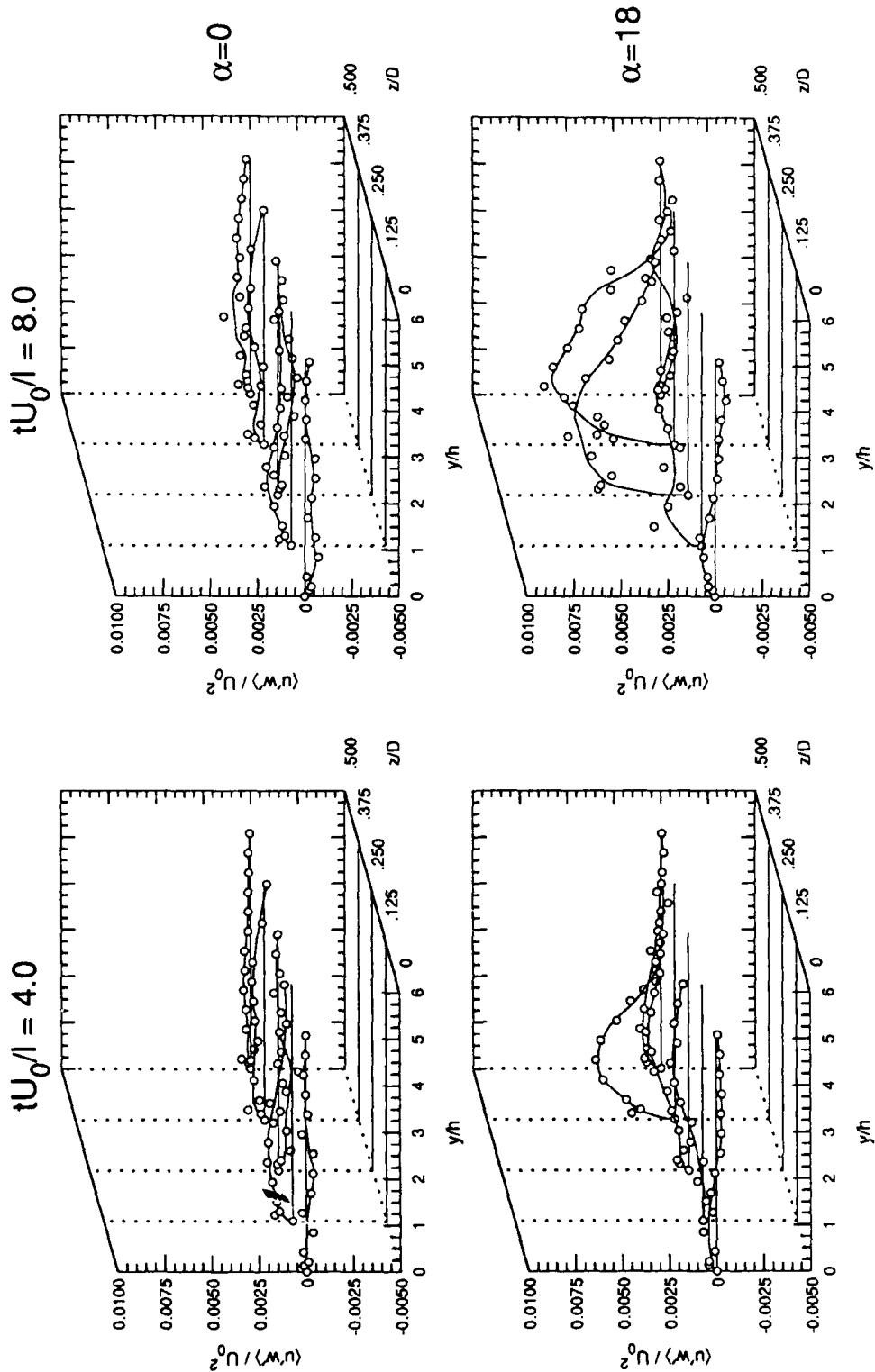
Figure 7.29 Profiles of $\langle u'w' \rangle$ at $tU_0/l = 4$ and $tU_0/l = 8$

126
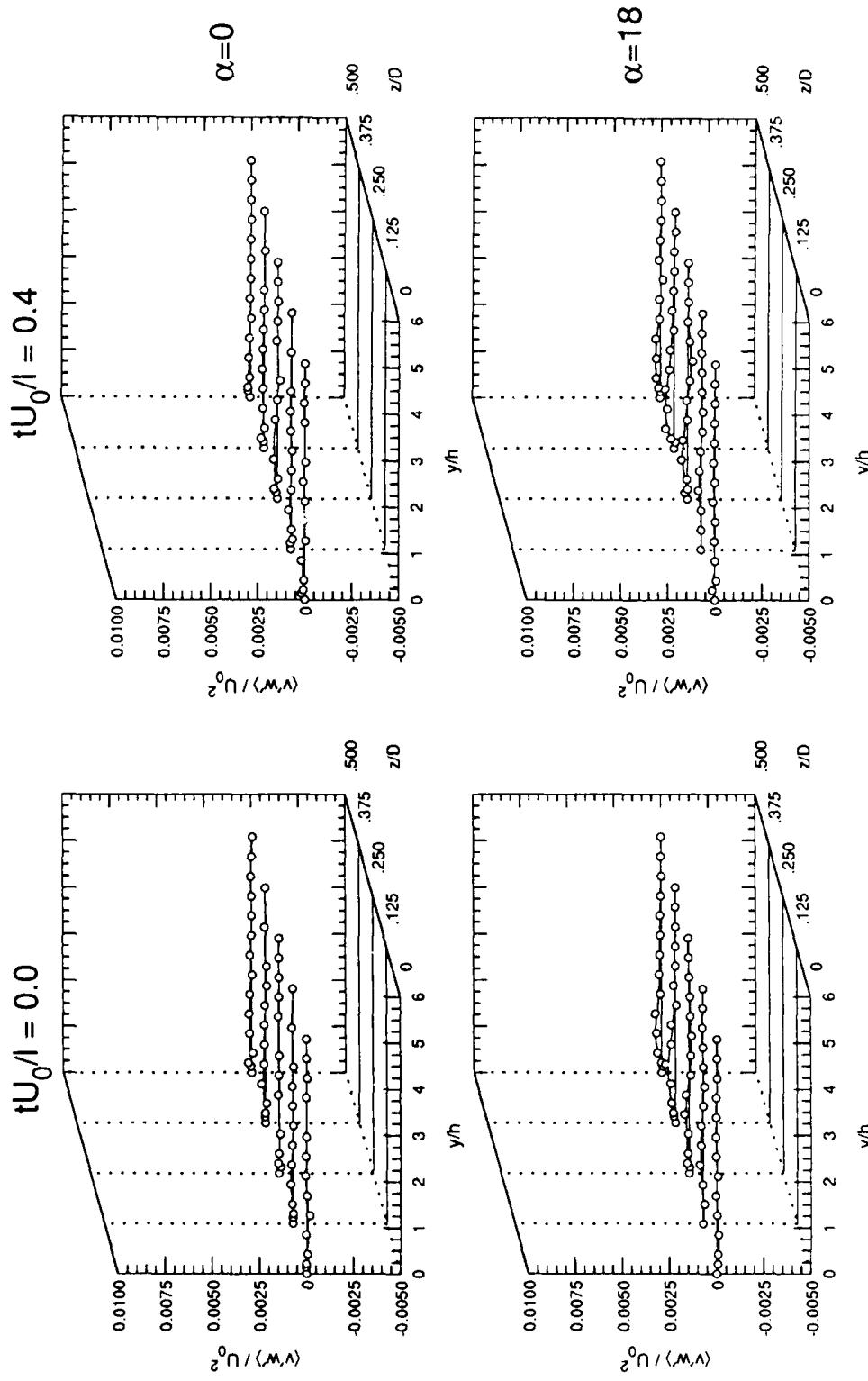
Figure 7.30 Profiles of $\langle v'w' \rangle$ at $tU_0/l = 0$ and $tU_0/l = 0.4$
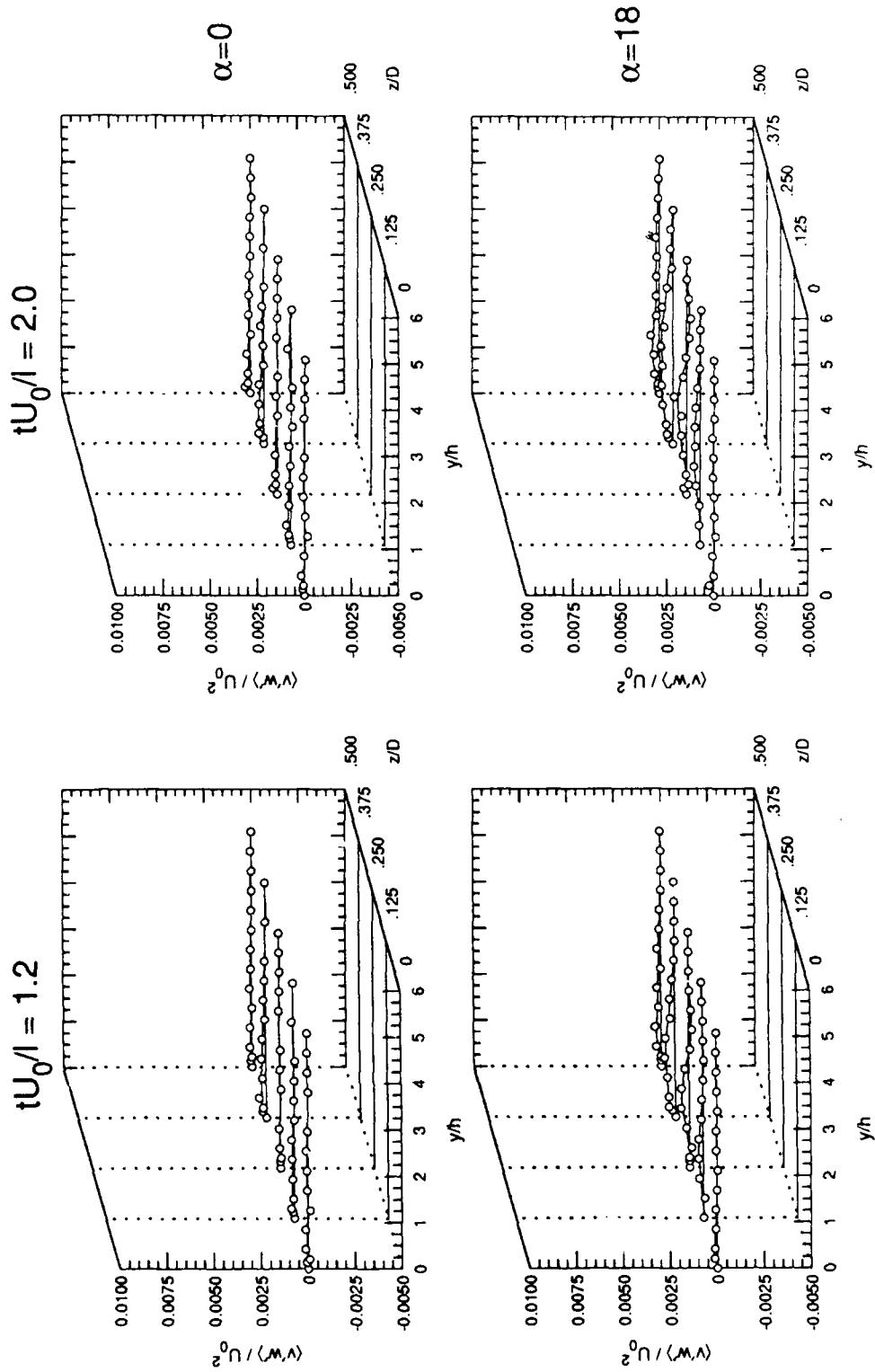
Figure 7.31 Profiles of $\langle v'w' \rangle$ at $tU_0/l = 1.2$ and $tU_0/l = 2$

128
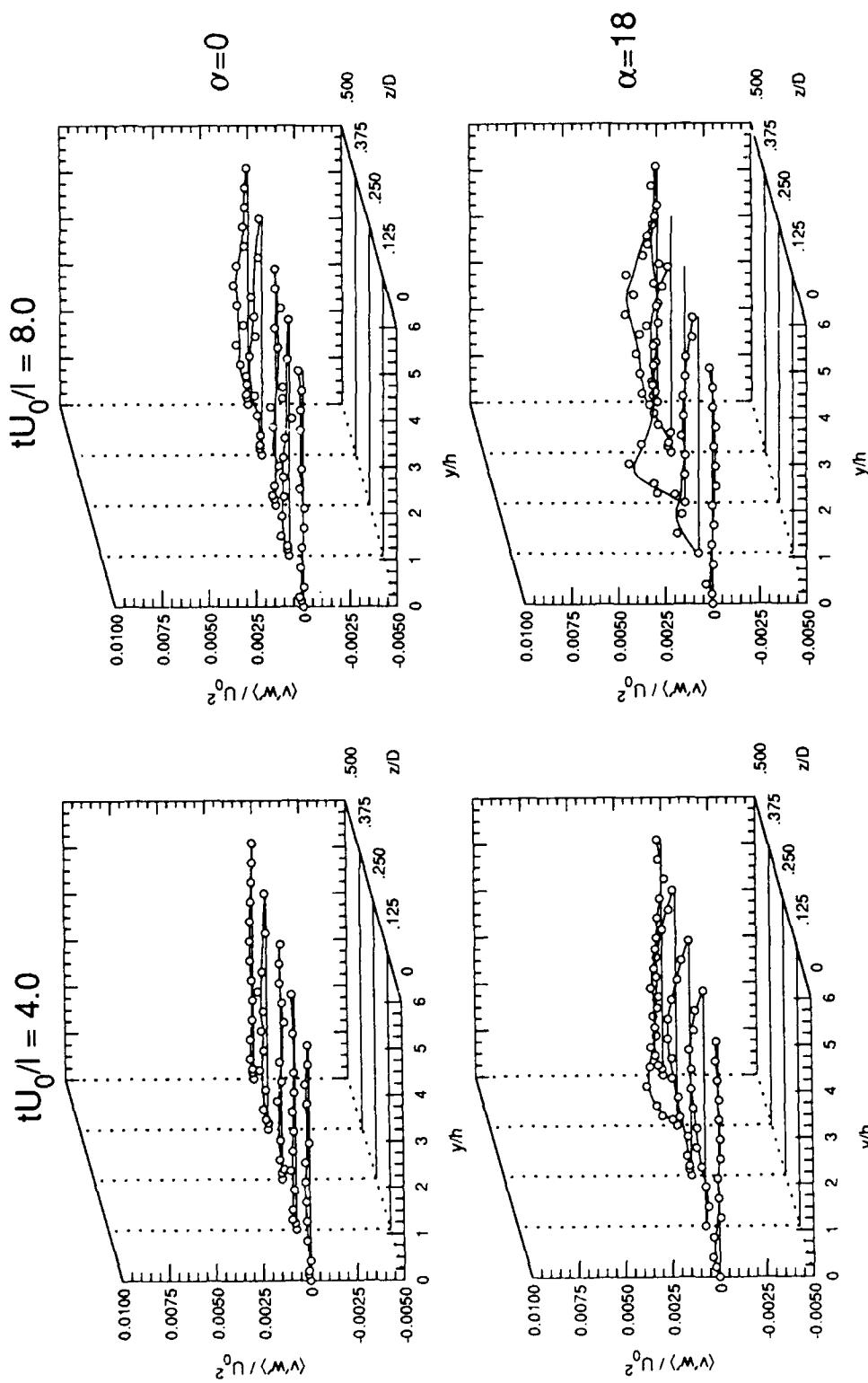
Figure 7.32 Profiles of $\langle v'w' \rangle$ at $tU_0/l = 4$ and $tU_0/l = 8$

129
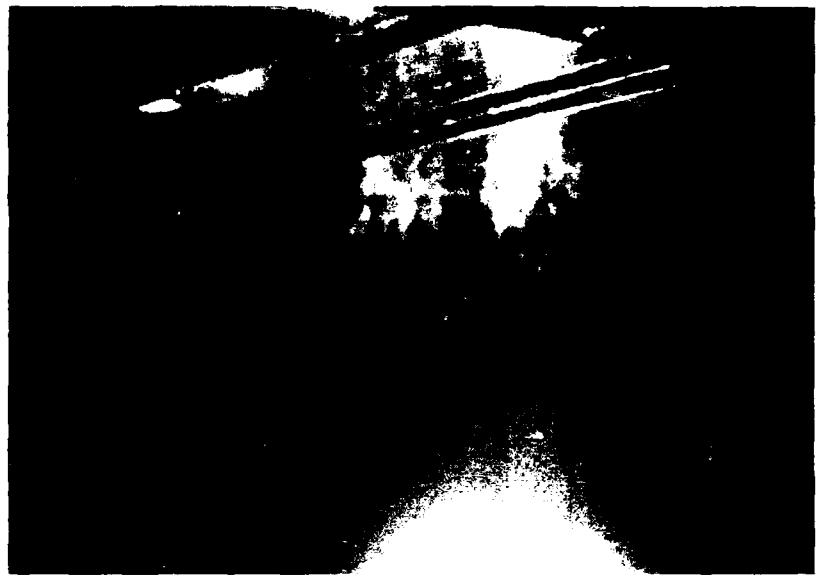
Figure 7.33 Flow visualization at $tU_0/l = 0^-$

Figure 7.34 Flow visualization at $tU_0/l = 0^+$

Figure 7.35 Flow visualization at $tU_0/l = 1$
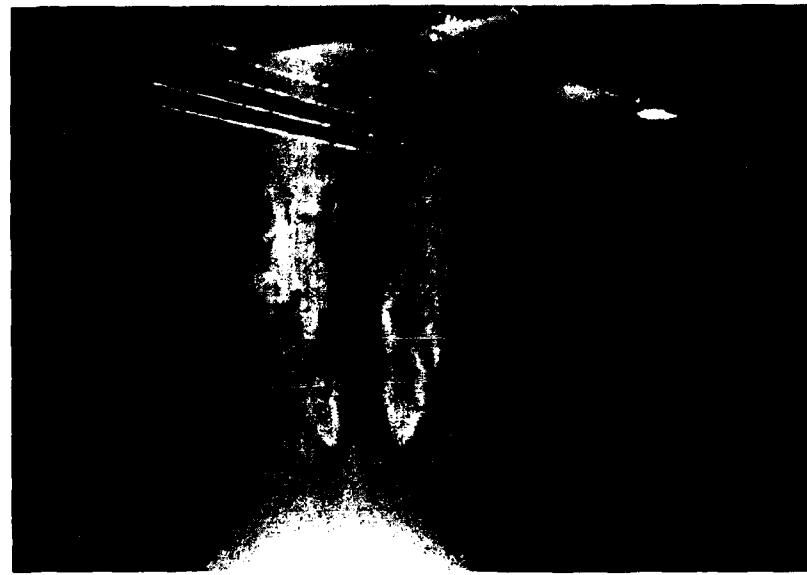
Figure 7.36 Flow visualization at $tU_0/l = 3$

Remember, when discoursing about water,
to induce first experience, then reason.
— Leonardo da Vinci

8. Results II: Analysis and Discussion

Chapter 7 fulfilled one program objective, which was to document profiles of the velocities and Reynolds stresses. This chapter will address the remaining objectives, which are to characterize the time response of the boundary layer and to understand the mechanisms by which vortex generators modify its response. The time response characteristics that will be presented offer useful information for the design of a flow control system and provide insight into the mechanisms of flow modification.

As a starting point for the analysis, some results at steady, zero pressure gradient conditions will be compared to similar results from other steady experiments. Then the time response characteristics of the integral parameters and of $\langle u \rangle$, $\langle v \rangle$, and $\langle u'u' \rangle$ will be discussed. The variation in skin friction coefficient and behavior of the mean velocity in wall coordinates are then presented for documentation purposes. Next, evaluation of the transport of streamwise vorticity, spanwise vorticity, and momentum provide additional insight into the mechanisms that make vortex generators work. Finally, a look at turbulent kinetic energy production and the anisotropy of the Reynolds stress tensor provides some insight into the response of the turbulence.

8.1 Steady Flow: Comparison to previous experiments

Skin Friction and Mean Turbulent Profiles. Use of the universal law of the wall lends insight into the two-dimensionality of the boundary layer and provides a means to estimate the spanwise skin friction variation with and without vortex generators. Eibeck and Eaton (1985) concluded that their weak vortices only affected the wake region of the boundary layer, whereas Pauley and Eaton (1988) in addition saw significant deviation in the logarithmic region. Steady zero pressure gradient profiles were taken as part of the initial validation at each spanwise position. These profiles are presented in wall coordinates in figures 8.1a and 8.1b.

133

For all the analysis in this chapter, steady and unsteady, the skin friction at the surface was estimated using a best fit of the near-wall data to the universal law of the wall. To accomplish this, several different approaches were evaluated: (1) a fit to the "inner law", $u^+ = y^+$, (2) a fit to the outer region following the recommendations of Coles (1968), and (3) a fit to the entire region covered by the universal law of the wall using interactive graphics and an approximate expression for the law of the wall. Of the three approaches, the third gave the most consistent and satisfactory results. Use of the "inner law" was unsuccessful because not enough data points were taken in the linear region. The Coles method, using computer codes developed by Jayaraman and Brereton, gave good results for the attached boundary layer without vortex generators. However, the vortex generators sufficiently distorted the boundary layer that the least-squares fit totally misinterpreted the location of the logarithmic region and wake. Fortunately, interactive graphics enable one to make a very good visual determination of a best fit.

For this experiment, the interactive graphics package *Quattro* was used. (*Quattro* is a registered trademark of Borland International, Inc.) The universal law of the wall was expressed in analytical form using an approximate implicit expression developed by Spalding (1961),

$$y^+ = u^+ + e^{-kc}\left\{e^{ku^+} - 1 - ku^+ - \frac{1}{2}(ku^+)^2 - \frac{1}{6}(ku^+)^3 - \frac{1}{24}(ku^+)^4\right\}, \quad (8.1)$$

where $k = 0.41$ and $c = 5.0$. Then, allowing for a small correction in the location of the wall (on the order of 1 y^+ unit) a best fit of the inner wall data is obtained visually by varying the skin friction (or friction velocity) and the offset from the wall. For boundary layers with no embedded streamwise vorticity, this method was compared to the Coles method using the computer codes by Jayaraman and Brereton. The comparison showed that the visual method is very sensitive and repeatable, yielding friction velocities consistent with the Coles method to about 2 percent. The visual "universal law" method also works, however, for boundary layers with highly distorted wake regions, where the Coles method does not. (Note:

A more useful expression than equation 8.1 is given by Liakopoulos (1984). This was discovered after completing the analysis described above.)

The resulting values for steady flow of the skin friction coefficient and the friction velocity are shown in figures 8.2a and 8.2b. The skin friction coefficient, C_f, and the friction velocity, u_τ, are each related to the wall shear stress, τ_w, by their definitions,

$$C_f = \frac{\tau_w}{\frac{1}{2}\rho u_\infty^2} \qquad u_\tau = \sqrt{\frac{\tau_w}{\rho}}. \tag{8.2}$$

Relative to a value of C_f of 0.004 without vortex generators, C_f varies from about 0.0047 at the centerline to about 0.0052 in the strongest downwash, and to about 0.003 in the upwash region. These values are similar in magnitude and in the degree of variation to the "common flow down" study of Pauley and Eaton (1988) and the "common flow up" study of Mehta and Bradshaw (1988). In general, the variation in C_f was less in this experiment than in the other experiments referenced. This is consistent with all observations that indicate the induced vortex in this experiment was quite weak relative to other experiments. Of the cases shown by Pauley, the variation in C_f is more similar to his downstream case where the variation from minimum to maximum values is a little less than a factor of 2. It is also important to note that in the other experiments which were all in air, the skin friction was actually *measured*, whereas in this experiment it was only *inferred* from the velocity profiles.

The velocity profiles in figure 8.1a indicate a nearly uniform wake region with the vortex generators at an angle of attack of 0°, whereas major variations are seen in the wakes of figure 8.1b with the vortex generators at an angle of attack of 18°. The spanwise variations seen in figure 8.1a are greater than spanwise variations seen before the vortex generator assembly was installed in the tunnel, and are attributed to the streamwise vorticity and total pressure wake that is formed around the vortex generators even at an angle of attack of 0°. With the vortex generators at 18°, however, the entire wake region is severely distorted. As would be expected, the

135

upwash region has a large amount of sluggish fluid and manifests a large wake. Conversely, the downwash and cross-flow regions have more energetic fluid near the surface and show very little evidence of any wake. Since the linear spacing of data points resulted in very few points in the logarithmic region, it is hard to be dogmatic about how much this region is distorted by the vortex generators. The evidence, though, seems to indicate that even with these weak vortex pairs, the inner portion of the boundary layer is not altogether two-dimensional, consistent with the observations of Pauley and Eaton.

The Integral Parameters. The integral parameters displacement thickness, δ^*, momentum thickness, θ, and shape factor, H, are useful since they summarize in a single number the condition of the entire boundary layer. Standard definitions of these quantities were used, but are restated below for clarity.

$$\delta^* = \int_0^\delta \left(1 - \frac{u}{u_\infty}\right) dy \qquad (8.3)$$

$$\theta = \int_0^\delta \frac{u}{u_\infty}\left(1 - \frac{u}{u_\infty}\right) dy \qquad (8.4)$$

$$H = \frac{\delta^*}{\theta}. \qquad (8.5)$$

The spanwise variation of the displacement thickness and momentum thickness is shown in figure 8.3a and the spanwise variation of the shape factor is shown in figure 8.3b. In all cases where integration was performed in this program, the integrands were first plotted to ensure that they were smooth, continuous functions with no anomalies at the origin or boundary-layer edge. Then, a parabolic numerical integration scheme was used, which allowed for the uneven spacing of data points near the wall.

136

The momentum thickness, with vortex generators at an angle of attack of $0°$, varies across the span from $3.8mm$ to $4.2mm$. As with the variation in C_f, this variation is presumed to be caused by vorticity generated by the vortex generators at $\alpha = 0°$. Using an average value for θ of $4mm$, along with the freestream velocity of $0.5m/sec$, and the kinematic viscosity of water at $16.7°C$, the momentum thickness Reynolds number, Re_θ, is determined to be 1840 ± 90. This number will be used to characterize the state of the boundary layer at the start of the adverse pressure gradient cycle. The variation in the integral parameters with the vortex generators at an angle of attack of $18°$ is very much as would be expected. In the downwash and crossflow regions the shape factor is about 1.2, which is well below the typical values of 1.4 to 1.5 for this range of Reynolds numbers. This is indicative of an energetic boundary layer with very little sluggish flow. In contrast, in the upwash region the momentum thickness, displacement thickness, and shape factor all increase, indicating that sluggish fluid from near the surface has been moved into the outer portion of the boundary layer.

Transport of Turbulent Kinetic Energy. As part of the validation of the data acquisition systems, chapter 5 presented the triple product measurements for a two-dimensional boundary layer. Shabaka, Mehta, and Bradshaw (1985) presented their triple product data in terms of transport velocities of normal and shear stresses. Pauley and Eaton (1988) presented their results in a similar fashion. In general, data collection times during this experiment were not long enough for good convergence of the triple products. This was particularly true for $w'w'$ statistics. Also, the coarser data grid selected for this study does not provide good resolution on a vector map. Nevertheless, secondary transport velocities of the quantity $u'u' + v'v'$ were computed and are presented in figure 8.4, to demonstrate that a similar transport phenonenon was observed with this experiment. The secondary transport velocities were computed from the following:

$$V = \frac{\langle u'u'v' \rangle + \langle v'v'v' \rangle}{\langle u'u' \rangle + \langle v'v' \rangle} \tag{8.6}$$

$$W = \frac{\langle u'u'w' \rangle + \langle v'v'w' \rangle}{\langle u'u' \rangle + \langle v'v' \rangle}. \qquad (8.7)$$

Figure 8.4 shows the same general qualitative trend as reported by Pauley and Eaton (1988) for their "common flow down" vortex pair. It also reveals the limitations of the triple product data taken as part of this experiment. Therefore, no further data analysis or interpretations will be based on triple product results.

8.2 Time Response of the Boundary Layer

Chapter 7 presented the characteristic time history of the mean velocities and the Reynolds stresses. This section will now characterize the nature of the boundary-layer response to the step change in pressure gradient. The analysis will show that there is an *immediate response* to the pressure gradient throughout the boundary layer which is characteristic of the elliptical nature of the governing equations, followed by a slow or *convective* response characteristic of the hyperbolic nature of the governing equations. This section will begin with contour plots of the streamwise velocity followed by the time development of the *integral parameters*, then will present the parameters which describe the step response in $\langle u \rangle$, $\langle v \rangle$, and $\langle u'u' \rangle$.

Contours of Streamwise Velocity. Contour plots of the streamwise velocity component provide a good visualization of the changes in the boundary layer. Figures 8.5 through 8.9 show contours of $\langle u \rangle$, with vortex generators at $0°$ and $18°$, as the boundary layer responds to the impulsively started adverse pressure gradient. The "jagged corners" on the contour plots result from the coarse data grid, and no attempt was made to conceal this. Figure 8.5 shows the nature of the boundary layer with zero pressure gradient. While it is thinned in the downwash region and thickened in the upwash region, there is not a large velocity deficit apparent in the core of the embedded vortex, as was seen in the experiments of Pauley and Eaton (1988). In this respect, this vortex more resembles the experiments of Bradshaw *et al.*, where the vortex generators were placed before the converging nozzle of their

138

wind tunnel. Succeeding figures show the growth of the boundary layer as the adverse pressure gradient is introduced. In figure 8.6, a small region of reverse flow is already apparent in the upwash region. In figure 8.7, reverse flow occurs across most of the span without vortex generators in addition to the upwash region with vortex generators. This trend then continues in figures 8.8 and 8.9. This sequence of figures follows the development of the boundary layer through $tU_0/l = 8$. Since all of the salient features of the flow adjustment process occur in that time frame, most of the analysis and discussion that follows will cover this same time period.

Response of the Integral Parameters. The integral parameters are one means of summarizing the condition of the entire boundary layer. It was impossible to compare the time responses of the integral parameters across the entire span because the boundary layer grew in the upwash region beyond the traverse capabilities of the three-component LDA system. The integrals in equations 8.3 and 8.4 only have meaning if the integrand goes to zero on the outer edge of the boundary layer. Since this was not the case across most of the span, the time response of the integral parameters is shown only for the center line position. Figure 8.10a shows the response of the displacement thickness and the momentum thickness, while figure 8.10b shows the response of the shape factor.

If a simple time constant for these integral parameters is defined as the length of time required for 63% of the change to occur, then the time constant of the momentum thickness, in both cases, is on the order of $1.5l/U_0$. The same is true for the displacement thickness when the vortex generators are at an angle of attack of $18°$, except there is a secondary adjustment which occurs over a longer time period but is small in magnitude. Since the freestream velocity is decelerating from U_0 to $0.6U_0$, this value of the time constant of $1.5l/U_0$ is approximately equal to the *time of flight* of fluid in the freestream. In contrast to this, the time constant for the displacement thickness when the vortex generators are at an angle of attack of $0°$ is approximately $3l/U_0$. The behavior of the shape factor in figure 8.10b represents the combined effect of the changes in the displacement thickness and

139

momentum thickness, which are occurring on different time scales. The analysis of the streamwise velocity time response, will provide more information into the nature of the boundary-layer response.

Time Response of the Streamwise Velocity. Figures 7.1a through 7.1f showed the time history of the streamwise velocity. In each case, there is an initial response during which the velocity decreases quite rapidly, followed by a slow adjustment period during which the velocity continues to change. While in most cases the velocity continues to decrease, it actually increases in portions of the downwash region. The response of $\langle u \rangle$ will be modelled, therefore, in a two-step fashion as depicted by figure 8.11.

The Mathematical Model. There are various ways that the velocity change can be normalized. After experimenting with several different schemes, the following was chosen.

$$\Phi = \frac{u_0 - u}{A_\infty}, \qquad A_\infty = U_0 - U_f. \tag{8.8}$$

In equation 8.8, A_∞ represents the amplitude of the freestream disturbance, which for this experiment was 0.4. This suggests that the linearized system response could be represented as

$$\Phi = 1 - e^{\beta(t-\tau_0)}, \tag{8.9a}$$

or equivalently,

$$u_0 - u = A_\infty \left(1 - e^{\beta(t-\tau_0)} \right). \tag{8.9b}$$

The justifications for this normalization scheme are: (1) this follows the general form of the solution to Stokes' first problem (except the actual solution is a complimentary error function), (2) the freestream disturbance, A_∞, can be viewed as a system input, (3) this scheme avoids ambiguities that arise when the change is

140

normalized on the total local change because the change is not always monotonic in time, and finally (4) this scheme in general provided a very good collapse of the data.

To demonstrate the actual behavior of Φ relative to the mathematical model shown in figure 8.11, representative values of Φ have been plotted in figure 8.12a and 8.12b for the centerline position, $z/D = 0$. Note that these figure show the same key features as the mathematical model. These features are: (1) a region where the response is very quick, characterized by an exponential rate, β, and a time delay, τ_0; (2) an initial roll-off where the slope decreases drastically, characterized by the time of the roll-off, τ_2, and the corresponding value, Φ_r; and (3) a slow adjustment period where the value of Φ may increase or decrease, characterized by the final value, Φ_f, and a time constant, τ_3, which is the time to reach $0.63(\Phi_f - \Phi_r)$.

Determination of the Time Response Parameters. Due to the smooth, well-converged nature of the streamwise velocity data, a straight-forward computerized scheme was used to identify the time response parameters at each y and z location. A segment of the curves from figures 8.12a and 8.12b are shown again in figures 8.13a and 8.13b with data symbols to demonstrate that there are sufficient data points along the quick rise portion of each curve to properly determine β. Basically, the computer scheme marched along the data until Φ changed by 5%. The program then computed the slope between each pair of points and identified the steepest slope. This steepest slope was then fit to an exponential expression from which β and τ_0 were determined. An alternate routine was also tested, which used a 3-point least-squares fit. It gave similar results, but actually had more scatter than the first scheme which simply used the two points with the steepest slope. To determine the location of the roll-off point, τ_2, the computer scheme computed predicted values based on a linear fit through the two points with the steepest slope. The value of τ_2 was defined, after some experimentation, as the point where this predicted value exceeded the actual value of the data by 0.2. Finally, the computer program marched through the remainder of the data and determined the maximum value of

141

the quantity $(\Phi_f - \Phi_r)$, then went back and located the time, r_3, where the value was $0.63(\Phi_f - \Phi_r)$.

The resulting values of these parameters are plotted in figures 8.14a through 8.14f. Figure 8.14a presents the roll-off value, Φ_r. Note that all the data sets, for all spanwise positions and both angles of attack, collapse onto the same curve. The vortex generators do not appear to affect this feature of the response. Due to the normalization scheme chosen, the outer portion of the boundary layer rolls off at a value of Φ_r of 1, while close to the surface the roll-off value is proportionately smaller. In contrast to Φ_r, which was not affected by the vortex generators, the values of the quantity $(\Phi_f - \Phi_r)$ as shown in figure 8.14b, are very clearly affected by the vortex generators. While the value of this quantity is quite consistent for the three spanwise positions at an angle of attack of $0°$, it is substantially reduced in the downwash region and substantially increased in the upwash region. These trends, in conjunction with the time scales that follow, provide insight into the mechanisms that make vortex generators work.

Figures 8.14c through 8.14f present the time scales for the step response of $\langle u \rangle$. Figure 8.14c shows that the value of the exponential rate for the initial response, β, is about the same for all data sets, and varies from a value of about -4.5 near the surface to about -7 in the outer portions of the boundary layer. Due to the finite rise-time of the control valve, the freestream response should have a value of β of -8.81. Within experimental uncertainty, it appears that the values of β computed from the data are approaching this value at the edge of the boundary layer. Once again, this feature of the response does not apear to be affected by vortex generators. On the other hand, the value of the initial phase delay, τ_0, does vary significantly between data sets, but the trends are not well defined. Figure 8.14d shows that the phase delay is greater in the outer portion of the boundary layer. The variation in the phase delay at an angle of attack of $0°$ is probably due to the opening characteristics of the flow control valve. There may be a subtle trend

142

indicating that the vortex generators reduce the magnitude of the phase delay but more data would be required to substantiate this.

Figure 8.14e shows that the value of $(\tau_2 - \tau_0)$ is constant at a value of about $0.35l/U_0$ through the boundary layer for all data sets. This indicates that the *duration* of the initial response is the same throughout the boundary layer and is unaffected by the presence of vortex generators. Since 90% of the change in the control valve position occurs in $0.4l/U_0$, it appears that the waveform introduced by the control valve propagates quite uniformly through the boundary layer. This trend is consistent with the observations from figure 8.14a and 8.14c. That is, because the *rate* of change is less in the inner region while the duration of the change is the same throughout the boundary layer, a lower roll-off value is seen in the inner region. Finally, figure 8.14f shows that the the time constant of the convective response, τ_3, generally has a value of about $3l/U_0$, except in the outer portion of the boundary layer where the vortex generators do cause some variations. Note that the large variations in the value of τ_0 in the inner regions of the boundary layer, shown in figure 8.14d, do not appear to affect τ_3. This is additional evidence to suggest that the time scale of the convective or hyperbolic response is independent of the time scale of the initial or elliptical response.

Conclusions regarding $\langle u \rangle$. (1) Vortex generators do not affect the basic response *rates* of the boundary layer. They only affect the *magnitude* of the *convective* portion of the response. (2) There is an initial response throughout the boundary layer typical of the *elliptical* nature of the governing equations, which is unaffected by the presence of vortex generators. The duration of this initial response reflects the waveform of the control valve and is uniform throughout the boundary layer, but because the rate of change is somewhat less in the inner region, the magnitude of the initial change is also proportionately less in the inner region. (3) There is also a slow or convective response throughout the boundary layer, typical of the *hyperbolic* nature of the governing equations, during which the magnitude is substantially modified by the presence of vortex generators. (4) Because the magnitude of the

convective response is substantially reduced in the downwash region, a far greater *percentage* of its response occurs during the initial response. The apparent effect of vortex generators in the downwash region, therefore, is that they substantially decrease the time required for the boundary layer to adjust to the step change to an adverse pressure gradient.

Time Response of $\langle v \rangle$. The mathematical model described in the previous paragraphs and summarized in figure 8.11 was also applied to the step response of $\langle v \rangle$, with several small changes. These changes were: (1) the convective response was more complex for $\langle v \rangle$ than for $\langle u \rangle$, so only the initial response has been modelled, (2) due to less convergence in the data, a 3-point least-squares fit was necessary, and (3) based on figure 7.2, a value of 0.06 was used for the disturbance almplitude, A_∞. Only three points could be used in the least-squares fit because the initial response occurs over a period which is spanned by only three or four phase points.

Figures 8.15a and 8.15b show the initial response rate and phase delay for the step response of $\langle v \rangle$. Once again, all the data sets show the same trend, so vortex generators do not appear to affect the initial response of $\langle v \rangle$. Due to the effect of the wall, the magnitude of the response in $\langle v \rangle$ is very small, thus the response rate, β, approaches 0 near the surface. In the outer region, however, β approaches the rise time of the control valve, as was observed for $\langle u \rangle$. The phase delay, τ_0, is relatively constant across the boundary layer. The larger values near the surface are probably not significant because of the near-zero slope of the response curve. Therefore, it appears that the initial response in $\langle v \rangle$ is governed by the same mechanisms that govern the initial response of $\langle u \rangle$.

Time Response of $\langle u'u' \rangle$. From the time histories shown in chapter 7, the step response characteristics of $\langle u'u' \rangle$ appear to be representative of all the turbulent quantities. The turbulent quantities show only a single response which occurs at a slow rate relative the initial response of the streamwise velocity. For comparitive purposes, this response was modelled in the same manner as the initial response of $\langle u \rangle$ and $\langle v \rangle$, except for the following modifications: (1) the initial response actually

144

describes the total response, (2) due to less convergence and a slower response, a 9-point least-squares fit was used, (3) based on the maximum change that occurs, a value of 0.015 was used for the disturbance amplitude, A_∞, and (4) the absolute value of Φ was used because $\langle u'u' \rangle$ decreases in the inner region of the boundary layer but increases in the outer region of the boundary layer.

Figures 8.16a and 8.16b show the response rate and phase delay of $\langle u'u' \rangle$. In general, the response rate is an order of magnitude smaller than the initial response rate of the streamwise velocity. In the outer region of the boundary layer, the inverse of β would correspond to a time constant in the range $2.5l/U_0$ to $4l/U_0$, which is about the order of magnitude of the convective response of $\langle u \rangle$. The turbulence does respond more quickly, however, in the innermost portion of the boundary layer. Also, this rate may be slightly increased in the downwash portions of the embedded vorticity. Finally, figure 8.16b shows the same typical values for the phase delay in the inner region as were seen for the initial phase delay of the streamwise velocity, but somewhat larger values in the outer region. It appears, therefore, that the turbulence in the inner region of the boundary layer begins to respond at the same time as the initial response of $\langle u \rangle$, except at a much slower rate. In contrast, the turbulence in the outer portion of the boundary layer responds to the growth of the boundary layer, which occurs on the slower convective time scales of the freestream velocity.

8.3 Time Development of C_f and Turbulent Mean Profiles

This section presents the variation in the skin friction coefficient and the turbulent mean profiles in wall coordinates, analogous to the results presented in section 8.1 for steady flow. In response to the adverse pressure gradient, the shape of the each profile changes drastically. Precisely the same methodology was used to determine the friction velocity for unsteady flow, up to the time where reverse flow begins. After that time no value of C_f could be inferred from the universal law of

145

the wall so no turbulent profiles are presented. The values obtained for C_f, without and with vortex generators, are shown in figures 8.17a and 8.17b. The same information is presented in figures 8.18a and 8.18b in terms of the friction velocity, u_τ.

Variations in the skin friction. In figure 8.17a for $\alpha = 0°$, the skin friction is initially quite uniform at $tU_0/l = 0$. At $tU_0/l = 2$, reverse flow appears to be imminent and has already begun near the spanwise location, $z/D = 0.125$. The initial "pull-away" at this location was seen very clearly in the velocity profiles of figure 7.8. After $tU_0/l = 2$, reverse flow occurs across most of the span. While there is no reverse flow at $z/D = 0$ and $z/D = 0.5$, C_f drops from a value of 0.004 to about 0.0001. Figure 8.17b reveals that the boundary layer with embedded streamwise vorticity responds much differently. In the upwash region, reverse flow occurs very rapidly at $z/D = 0.5$, and eventually occurs after $tU_0/l = 4$ at $z/D = 0.375$. At the remaining three spanwise positions, there is no tendency towards reverse flow. A spanwise average of these three positions would show that C_f drops from an initial value of 0.0048 to about 0.001 at $tU_0/l = 2$, and then holds quite steady at that value. The spanwise variations in time at these three locations are quite likely secondary effects due to the blockage effect in the tunnel from the upwash regions.

Variations in the Mean Turbulent Profiles. Using the friction velocities determined above, the phase-averaged "mean" turbulent profiles are presented for four dimensionless times in figures 8.19 through 8.22. The observations for figures 8.19a and 8.19b, for $tU_0/l = 0$, would be virtually the same as the observations made for the steady profiles at zero pressure gradient. As the adverse pressure gradient affects the velocity profiles at subsequent time intervals, the corresponding velocity profiles show several general trends. (1) At $\alpha = 0°$, the profiles deviate markedly from the universal law of the wall, and have no discernible overlap region. This is consistent with the observations of Jayaraman, Parikh, and Reynolds (1982) and with White's (1974) characterization of a reversing flow. Even near reverse flow, the profiles at different spanwise positions are quite consistent with each other, except in

146

the outermost portion of the boundary layer. (2) At $\alpha = 18°$, the profiles are similar on the inner portion, but once again do not have an overlap region consistent with the universal law of the wall. There is substantial spanwise variation in the profile shape past $y^+ = 60$, until at $tU_0/l = 8$, where the three profiles in the downwash region are surprisingly similar. Therefore, while the effect of the vortex generators may leave the inner portion of the boundary layer two-dimensional at zero pressure gradient, as observed by Eibeck and Eaton (1985), this is most certainly not the case in the presence of a strong adverse pressure gradient.

8.4 Evolution of Streamwise Vorticity

The analysis will now turn to the transport equations for additional insight into the mechanisms by which vortex generators modify the response of the boundary layer. Previous studies with vortex generators have explored in depth the streamwise vorticity equation, as originally formulated by Perkins (1970), so this seems to be a logical place to start. The results will show that after the step change occurs in the pressure gradient, the core of the embedded vortex diffuses very rapidly.

The Governing Equation. The streamwise turbulent vorticity equation is obtained by expanding the terms of equation 2.11 or 2.12, for the $i = 1$ component of vorticity. This yields

$$\langle \dot{\omega_x} \rangle + \langle u \rangle \langle \omega_x \rangle_{,x} + \langle v \rangle \langle \omega_x \rangle_{,y} + \langle w \rangle \langle \omega_x \rangle_{,z} = \langle \omega_x \rangle \langle u \rangle_{,x} + \langle \omega_y \rangle \langle u \rangle_{,y}$$

$$+ \langle \omega_z \rangle \langle u \rangle_{,z} + \nu \left(\langle \omega_x \rangle_{,xx} + \langle \omega_x \rangle_{,yy} + \langle \omega_x \rangle_{,zz} \right) + \langle u'v' \rangle_{,xz}$$

$$- \langle u'w' \rangle_{,xy} + \langle v'v' \rangle_{,yz} - \langle v'w' \rangle_{,yy} + \langle u'w' \rangle_{,zz} - \langle w'w' \rangle_{,yz} . \qquad (8.10)$$

The three components of the vorticity are

$$\langle \omega_x \rangle = \langle w \rangle_{,y} - \langle v \rangle_{,z} \qquad (8.11)$$

$$\langle \omega_y \rangle = \langle u \rangle_{,z} - \langle w \rangle_{,x} \qquad (8.12)$$

$$\langle \omega_z \rangle = \langle v \rangle_{,x} - \langle u \rangle_{,y} . \qquad (8.13)$$

In equation 8.10, the left-hand side represents the rate of change of streamwise vorticity plus the convection of vorticity out of the fluid element by the three phase-averaged velocity components. On the right-hand side, the first three terms represent vortex stretching and bending and the next three terms represent viscous diffusion into the fluid element. The last six terms represent turbulent transport of vorticity. They are the turbulent counterparts to the convection and stretching terms, and can be grouped in several different ways. In equation 8.10 they are grouped in pairs as the turbulent flux in the x, y, and z directions. Alternately, Perkins (1970) grouped them as

$$P_2 = (\langle u'v'\rangle_{,z} - \langle u'w'\rangle_{,y})_{,x} \tag{8.14}$$

$$P_3 = (\langle v'v'\rangle - \langle w'w'\rangle)_{,yz} \tag{8.15}$$

$$P_4 = \langle v'w'\rangle_{,zz} - \langle v'w'\rangle_{,yy}. \tag{8.16}$$

In a zero pressure gradient flow, Pauley and Eaton (1988) found that the terms P_3 and P_4 were dominant in changing the structure of embedded vorticity. For this flow, where there *are* significant gradients in the streamwise direction, any of the terms can act to create or alter the streamwise vorticity. Since this experiment was not configured so as to provide estimates of changes in the streamwise direction, the emphasis in the analysis that follows will be on *what* happens to the streamwise vorticity rather than a detailed analysis of the individual transport terms.

Differentiating Data. A major hazard associated with vorticity estimates in an experimental program is that differentiation of data is required. To estimate the vorticity, a single derivative is required, and to estimate terms in the equations above, up to three derivatives or the product of two derivative terms are required. The following considerations apply to each of the derivative terms that will be discussed in this section and the following sections. (1) A method was selected that found the slope of the *expected behavior* (that is a *fit* to the data) rather than finding slopes of the inconsistencies in the data. For the data in this program, the scheme that appeared to be most satisfactory, was to first make a 5-point piecewise

parabolic least-squares fit to the data, and then use a cubic spline through the resulting curve to estimate the derivative. (2) The fit of the splines through the smoothed data points was checked at each stage of the differentiation to ensure that the *expected behavior* was indeed represented. (3) Wherever possible, the *expected behavior* was compared to analytically predicted curves and baseline experimental curves. This was particularly important for second derivatives, where the the shapes of the curves, degree of curvature, and location of inflection points are all key features of the final results.

Determination of ω_x. Figures 8.23 and 8.24 show splines in the y direction through the smoothed values of $\langle w \rangle$, and figures 8.25 and 8.26 show splines in the z direction through the smoothed values of $\langle v \rangle$. Since the splines are reasonably well-behaved, the derivatives from these splines were used to calculate the streamwise vorticity, ω_x. These figures also demonstrate several important features about the embedded streamwise vorticity. (1) First, figure 8.25a is plotted on the same scale as figures 8.23 and 8.24. Notice that in general the y gradients of $\langle w \rangle$ and the z gradients of $\langle v \rangle$ are of the same general magnitude. This is characteristic of embedded vorticity generated by vortex generators and in contrast to the spanwise vorticity embedded in a boundary layer, where one of the two gradients is much larger than the other. (2) The exception to this trend is very near the surface where the $\langle w \rangle$ component is larger and then must decrease rapidly to meet the "no-slip" condition at the surface. This large gradient of opposite sign in $\langle w \rangle$ will be seen as a strong vorticity of opposite sign near the surface. (3) The scale on subsequent plots of $\langle v \rangle$ was necessarily changed to accomodate the growing value of this component as the boundary layer grows rapidly due to the adverse pressure gradient. (4) Figure 8.25a clearly identifies the location of the core of the embedded vortex, as the magnitude of the velocity component passes through zero at a spanwise position of $z/D \simeq 0.32$. (Note, since all derivatives were non-dimensionalized with respect to the vortex generator height, z is scaled here as z/h. Since the spacing between vortex pairs, D, is equal to $10h$, the conversion back to z/D is quite simple.)

149

The streamwise vorticity calculated from the splined data shown above is presented in figures 8.27 throught 8.31. In this case, contour plotting was the most practical graphical means to present the results. The contour plotting interpolation was done from the original data grid, since splining to create a denser grid also seemed to create fictitious regions of vorticity. The contour information was also checked against tabulations of the vorticity to confirm that the contours shown were realistic and consistent. Figures 8.27 through 8.31 show the progression in time of the streamwise vorticity, for the case $\alpha = 18°$ only. At dimensionless times of $tU_0/l = 0$, 0.4, 1.2, and 2, the embedded vortex (with negative vorticity) is clearly seen. The induced vorticity of opposite sign, due to the "no-slip" condition on $\langle w \rangle$, is also seen very clearly. The concentration of positive vorticity centered at $z/h = 5$ is generally accepted to result from the convection of the wall-generated vorticity by the primary vortex.

After several convection times, the primary embedded vortex suddenly loses its strength. At $tU_0/l = 3$ and 4, the primary vortex appears to be diffused and weakened in strength. Past this time, the negative vorticity appears to be "wrapped-around" a vortex of opposite sign that appears from the outer portion of the boundary layer. The weakening of the vorticity is the expected consequence of the adverse pressure-gradient, shown by the first term on the right-hand side of equation 8.10, $\langle \omega_x \rangle \langle u \rangle_{,x}$. The adverse pressure-gradient, caused by a negative value of $\langle u \rangle_{,x}$, "compresses" the vortex tube, making it "fatter" and weaker. While this same effect was seen by Westphal *et al.* (1987), they concluded that the core diffused more rapidly than could be accounted for by the streamwise velocity gradient term. Their analysis indicated that the anisotropy between the secondary normal stresses, $\overline{v'v'}$ and $\overline{w'w'}$, was responsible for the increased diffusion of vorticity. Since, under unsteady conditions, the turbulence responds quite slowly (as shown in section 8.2), its role in this diffusion process is less clear than in the case of steady flow.

To characterize the change in vortex strength, the vorticity of the primary vortex was integrated to estimate the total circulation. First, the data was splined to

150

create a denser grid, then following the practice of Westphal *et al.* the limits of numerical integration were defined by where the vorticity dropped to less than 10 percent of the peak value. The results shown in figure 8.32 indicate that, while the vorticity spreads out, the circulation stays relatively constant until the vortex loses its identity and integration becomes impractical.

The source of the positive vorticity that becomes more prominent at $tU_0/l = 6$ is not totally clear. Since there are gradients in all three directions, nearly all the terms in equation 8.10 could participate. Since figures 8.7 through 8.9 show that there is a strong spanwise gradient of $\langle u \rangle$, a likely source of positive vorticity appears to be the bending of the spanwise vorticity into positive streamwise vorticity by this strain-rate. This is described by the third term on the right-hand side of equation 8.10, $\langle \omega_z \rangle \langle u \rangle_{,z}$. However, after closer inspection one observes that part of this strain-rate appears with opposite sign in the second term of equation 8.10. Expanding the two terms together yields:

$$
\begin{aligned}
\langle \omega_y \rangle \langle u \rangle_{,y} + \langle \omega_z \rangle \langle u \rangle_{,z} &= \langle u_{,z} - w_{,x} \rangle \langle u \rangle_{,y} + \langle v_{,x} - u_{,y} \rangle \langle u \rangle_{,z} \\
&= \langle u_{,z}\, u_{,y} - w_{,x}\, u_{,y} + v_{,x}\, u_{,z} - u_{,y}\, u_{,z} \rangle \\
&= \langle -w_{,x}\, u_{,y} + v_{,x}\, u_{,z} \rangle .
\end{aligned}
$$

Therefore, it is very difficult to identify which term is the source of the apparent vorticity of opposite sign.

8.5 Evolution of Spanwise Vorticity

In their review paper, Reynolds and Carr (1985) stressed the importance of spanwise vorticity in understanding the mechanisms of a boundary layer separating due to an adverse pressure gradient. The accumulation of spanwise vorticity was seen as the difference between the convective inflow and outflow of vorticity plus the vorticity flux at the surface due to the pressure gradient. This section will attempt to identify the key transport terms and how they are modified by the embedded

151

streamwise vorticity. The results will show that diffusion and turbulent transport in the y direction are the dominant terms, and that the majority of vorticity transport occurs in the viscous inner region of the boundary layer.

Following the procedures for differentiating data that were outlined in section 8.4, the spanwise vorticity was estimated from the term $-\langle u \rangle_{,y}$. That is

$$\langle \omega_z \rangle = \langle v \rangle_{,x} - \langle u \rangle_{,y}$$
$$\simeq -\langle u \rangle_{,y}.$$

The time development of the spanwise vorticity, thus determined, is shown in figures 8.33 and 8.34. These figures vividly show that a healthy attached boundary layer is characterized by a very high concentration of spanwise vorticity at the surface. The scale on these figures was chosen to magnify the vorticity in the outer portion of the boundary layer at the expense of "chopping" the value near the wall. At zero pressure gradient, the vorticity at the surface peaks at about $10h/U_0$. This is consistent, as it should be, with the slope inferred by the fit to the law of the wall, u_τ^2/ν. In contrast, in the case where reverse flow is occurring, the vorticity is very nearly uniformly distributed throughout the entire boundary layer. Of course, part of the negative vorticity has inevitably diffused into the surface due to the adverse pressure gradient. The task for the vortex generators if they are to preclude separation, therefore, is to force a concentration of vorticity back into the surface against the natural processes that are occurring. Evaluation of the terms in the equation for transport of spanwise vorticity will lend insight into the mechanisms involved in this process.

The Governing Equation. The spanwise vorticity equation is obtained by expanding equation 2.12 for $i = 3$. For convenience in the analysis that follows, each term will be given a *name* that also serves to emphasize the nature of that term. With that preface, the spanwise vorticity equation is

$$\langle \dot{\omega}_z \rangle + C_1 + C_2 + C_3 = S_1 + S_2 + S_3 + D_1 + D_2 + D_3 + T_1 + T_2 + T_3. \quad (8.17)$$

In equation 8.17, the convection terms are

$$C_1 = \langle u \rangle \langle \omega_z \rangle_{,x}$$
$$C_2 = \langle v \rangle \langle \omega_z \rangle_{,y}$$
$$C_3 = \langle w \rangle \langle \omega_z \rangle_{,z} .$$

The vortex stretching and straining terms are

$$S_1 = \langle \omega_x \rangle \langle w \rangle_{,x}$$
$$S_2 = \langle \omega_y \rangle \langle w \rangle_{,y}$$
$$S_3 = \langle \omega_z \rangle \langle w \rangle_{,z} .$$

The viscous diffusion terms are

$$D_1 = \nu \langle \omega_z \rangle_{,xx}$$
$$D_2 = \nu \langle \omega_z \rangle_{,yy}$$
$$D_3 = \nu \langle \omega_z \rangle_{,zz} .$$

And the turbulent transport terms are

$$T_1 = \langle u'u' \rangle_{,xy} - \langle u'v' \rangle_{,xx}$$
$$T_2 = \langle u'v' \rangle_{,yy} - \langle v'v' \rangle_{,xy}$$
$$T_3 = \langle u'w' \rangle_{,yz} - \langle v'w' \rangle_{,xz} .$$

Following the procedures outlined in section 8.4 for taking derivatives of the data, all the terms except those requiring x derivatives were estimated. The three terms that appeared dominant and of the same order of magnitude were C_2, D_2, and T_2. Note that in T_2, $\langle v'v' \rangle_{,xy}$ could not be estimated, so only $\langle u'v' \rangle_{,yy}$ was used to estimate T_2. Since, from the arguments made by Reynolds and Carr, C_1 should

also be significant, this suggests that a simplified model for transport of spanwise vorticity might be

$$\langle \dot{\omega_z} \rangle + C_1 + C_2 = D_2 + T_2. \tag{8.18}$$

While in general, data was taken at only one streamwise position, an unsteady validation profile was taken at a location upstream of the primary data location, but half-way down the adverse pressure gradient ramp (see figure 6.11). By differencing data between these two locations, crude estimates of C_1 for $\alpha = 0°$ could be made. These estimates indicate that for $tU_0/l \leq 4$, the unsteady term tends to dominate the left-hand side of the equation 8.18, while for $tU_0/l > 4$, C_1 tends to dominate the left-hand side of the equation.

Estimates of Transport Terms. For comparison, figures 8.35 through 8.38 show the time evolution of D_2, figures 8.39 through 8.42 show the evolution of T_2, and figures 8.43 through 8.46 show the evolution of C_2. In reviewing these graphs, one should remember that the uncertainty in these terms requiring several derivatives of the data is on the order of 100 percent. However, for trends between families of curves, the *relative* uncertainty between them is probably less. Also, in figure 8.43a, C_2 is zero by the arbitrary decision explained in chapter 7, to correct for offset errors by using the values of $\langle v \rangle$ and $\langle w \rangle$ at $tU_0/l = 0$ and $\alpha = 0°$ as zero reference values. Finally, some of the trends shown by the spanwise data set at $z/D = 0.125$ seem to be inconsistent with the trends of the other four spanwise data sets. This was the last data set taken, and it was taken with a replacement laser after the primary laser was returned to the manufacturer for warranty repairs. While all procedures were followed to preclude potential inconsistencies, some trends shown at $z/D = 0.125$ may not be valid.

In making observations about the transport terms, it will be useful to think of terms being beneficial when they make the left-hand side of equation 8.18 more negative near the surface, since this indicates an increase in *negative vorticity* near the surface. The major observations regarding the transport of spanwise vorticity

154

are: (1) All three of these terms are *large* only in a region that is very near the surface. Note that for this reason y/h is on a logarithmic scale. Also, recall that at zero pressure-gradient, $h^+ = 230$, so this region where the terms are significant corresponds to $y^+ \leq 20$. This means that the significant transport of spanwise vorticity is occurring primarily in the viscous layer adjacent to the surface. (2) In general, diffusion and turbulent transport seem to be the two terms that maintain the vorticity equilibrium at zero pressure gradient. The term D_2 tends to increase the negative vorticity near the surface while T_2 tends to spread out the vorticity away from the surface. (3) At $\alpha = 18°$, the diffusion term is increased in the down-wash and crossflow regions. This effect is even more pronounced once the adverse pressure gradient begins. Figures 8.36a through 8.38a show that the diffusion term decreases substantially under the influence of the adverse pressure gradient. In contrast, figures 8.36b through 8.38b show that the diffusion is increasing the negative vorticity in the downwash and crossflow regions. This enhanced viscous diffusion of vorticity deep within the boundary layer may be the primary mechanism by which the vortex generators modify the transport of spanwise vorticity. (4) While T_2 is positive for $0.06 < y/h < 1.0$ at zero pressure gradient, T_2 becomes nearly zero or negative for the entire inner region, in response to the adverse pressure gradient. This indicates that while T_2 tends to spread out vorticity in opposition to the viscous diffusion during zero pressure gradient, T_2 actually assists in keeping vorticity near the surface during a separating flow. While the vortex generators may modify T_2, the effect is quite small. (5) Finally, the convection term is insignificant at $\alpha = 0°$ and smaller than the other terms at $\alpha = 18°$. Figures 8.43b through 8.46b show consistent trends. In the downwash and crossflow regions, and negative value of C_2 indicates *positive vorticity* is being convected *into* the surface. This, therefore, must be a detrimental secondary effect of the vortex generators, and not the primary mechanism.

8.6 Transport of Momentum

The transport equations for streamwise and spanwise vorticity have been examined to increase an understanding of the mechanisms by which vortex generators modify the behavior of a separating boundary layer. The last transport equation that will be examined for this purpose is the momentum equation. One explanation that is often given to explain how vortex generators work is that they enhance mixing and energize the sluggish flow at the surface with energetic fluid from the freestream. In terms of the momentum equation, this states that vortex generators increase the convection of u momentum in the $-y$ direction. The results that follow will demonstrate that this is true.

The Governing Equation. The momentum equation was stated in general form as equation 2.8. When applied to the u component of momentum with normal boundary layer assumptions, it can be expressed as follows:

$$\langle \dot{u} \rangle + \langle uu \rangle_{,x} + \langle uv \rangle_{,y} = \frac{1}{\rho} \langle p \rangle_{,x} + \nu \langle u \rangle_{,yy} - \langle u'v' \rangle_{,y} \,. \tag{8.19}$$

The intent here is to explore only the second convection term, $\langle uv \rangle_{,y}$. Often, if continuity has been subtracted from the momentum equation, this term appears as $\langle v \rangle \langle u \rangle_{,y}$. Following procedures outlined previously for taking derivatives, this convection term was calculated in both forms. The latter form tended more to map out the velocity gradient than the actual net convection, so it is not presented. The first representation of the momentum convection is presented without and with vortex generators, for four different phases, in figures 8.47 through 8.50. To further clarify some aspects of the convection term, the local convection of momentum was normalized by the local value of momentum. The analagous information is shown in this form in figures 8.51 through 8.54.

Observations. Figures 8.47 through 8.54 do verify that vortex generators help to energize the inner regions of the boundary layer, and to suppress the loss of momentum from the outer regions of the boundary layer. Before making more

156

specific observations, it is worth emphasizing that this term indicates the *loss* of momentum *from* a fluid element in the boundary layer, thus a positive number represents a detrimental effect and a negative number represents a positive effect. Also, as in other cases, figures 8.47a and 8.51a indicate zero convection because these values of $\langle v \rangle$ were used as reference values. Now, some specific observations are: (1) Figure 8.51b shows that at $tU_0/l = 0$ there is a net convection of momentum *into* the boundary layer in the downwash and crossflow regions, and there is a net convection *out of* the boundary layer in the upwash regions. The only trend that is at all surprising is the small region of momentum loss on the center line. This is perhaps due to a stagnation-type effect as the downwash parts along the center line. (2) In figures 8.52a through 8.54a there is loss of momentum from the entire boundary layer which is quite consistent across the entire span. The convection term is negative very near the surface because there must be a continual flux of momentum into the wall to overcome the wall shear stress. The negative convection term appears quite large because it is normalized by the very small amount of momentum that remains near the surface as separation occurs. (3) Figure 8.52b shows a region of momentum flux into the boundary layer at $z/D = 0.125$ and $z/D = 0.25$. This region, which has been shaded for emphasis, represents the overlap region of the boundary layer ($40 < y^+ < 200$) and may be the key region that is energized by the vortex generators. Note also that there is no net flux on the center line, where the downwash is not nearly as strong (reference for comparison figure 7.11). Also, as expected, there is a flux of momentum out of the boundary layer in the upwash regions of the vortex. (4) Figures 8.53b and 8.54b show that as the adverse pressure gradient continues, there is momentum loss across the entire span, but the average value is considerably less at $0 < z/D < 0.25$ than the average momentum loss shown in figures 8.53a and 8.54a.

8.7 Changes in the Structure of the Turbulent Boundary Layer

As the final discussion in this chapter, this section will address how the structure of the turbulence is modified by the combination of vortex generators and an unsteady adverse pressure gradient. The numerous studies of streamwise vortices embedded in a steady zero pressure gradient turbulent boundary layer, which were summarized in section 3.1, generally all indicated that the turbulence structure was modified significantly, and that complex models will be required to predict realistic values of the Reynolds stresses. In a similar manner, the unsteady experiments described in section 3.2 generally found significant effects of the unsteadiness on the turbulence structure. The results of this section will show that the production of turbulent kinetic energy which was complicated by the embedded vorticity, becomes even more confused in the presence of the unsteady adverse pressure gradient.

Chapter 7 already presented and discussed the distribution of Reynolds stresses in the boundary layer, and how they are modified by the vortex generators and an unsteady adverse pressure gradient. Due to the cruder data grid required because of the long sampling times associated with the unsteady cycle, this discussion cannot attempt to map out the spanwise variation in structural parameters in a manner analogous to Shabaka, Mehta, and Bradshaw (1985) or the recent work of Pauley and Eaton (1988). This section will address, however, the nature of the production of turbulent kinetic energy and nature of the anisotropy of the Reynolds stress tensor.

Production of Turbulent Kinetic Energy. Turbulent kinetic energy is defined as one-half the sum of the three normal Reynolds stresses. In this discussion k will denote the turbulent kinetic energy. That is

$$k = \frac{1}{2}\Big(\langle u'u'\rangle + \langle v'v'\rangle + \langle w'w'\rangle\Big) = \frac{1}{2}q^2. \tag{8.20}$$

Equation 2.9 defined the production of turbulent kinetic energy as

$$P_k = -\langle u_i' u_j'\rangle \langle u_{i,j}\rangle.$$

When this term is summed over i and j, there are nine terms that contribute to production:

$$P_k = -\langle u'u' \rangle \langle u,_x \rangle - \langle u'v' \rangle \langle u,_y \rangle - \langle u'w' \rangle \langle u,_z \rangle$$
$$-\langle u'v' \rangle \langle v,_x \rangle - \langle v'v' \rangle \langle v,_y \rangle - \langle v'w' \rangle \langle v,_z \rangle$$
$$-\langle u'w' \rangle \langle w,_x \rangle - \langle v'w' \rangle \langle w,_y \rangle - \langle w'w' \rangle \langle w,_z \rangle. \tag{8.21}$$

Six of the nine terms in equation 8.21 could be estimated by taking a product of the appropriate stress and a y or z derivative of the appropriate velocity. As stated previously, no data was taken that would provide a good estimate of x derivatives. In addition, due to higher apparent scatter in the $\langle w'w' \rangle$ measurements, the last term was also excluded from the estimate of turbulent kinetic energy production. Estimates of production based on the five remaining terms are presented in figures 8.55 through 8.57, for both $\alpha = 0°$ and $\alpha = 18°$, for six discrete points in time. In the production calculation the second term, $-\langle u'v' \rangle \langle u,_y \rangle$, was the dominant term over most of the region in most of the cases. This is consistent with the observations of Brereton and Reynolds (1987) for unsteady flows without vortex generators.

In figures 8.55 through 8.57, for the cases where $\alpha = 0°$, the magnitude and location of most of the production are consistent with the observations of Brereton and Reynolds. For comparative production terms scaled by u_τ and y^+, the appropriate scaling factor is roughly 60. This means that the peak production scaled by ν/u_τ^4 is between 0.15 and 0.2. This is slightly less than, but of the same rough magnitude as the peak production value of 0.25 seen by Laufer (1954) for his pipe flow experiments. Across the span, as the adverse pressure gradient evolves, the peak production descreases substantially. After $tU_0/l = 2$, when there is wall region reverse flow over most of the span, there is a small distribution of production across the shear layer, but no concentration of production near the surface. Since the adverse pressure gradient has significantly reduced the velocity gradients, or strain rates, that are responsible for production, the consequence has been a substantial drop in the total production in the boundary layer.

159

With vortex generators on, Pauley and Eaton observed "a complex interaction between the secondary flow field induced by the embedded vortices and the turbulence structure of the boundary layer." The same would appear to be true of the Reynolds stress distributions shown in figures 7.15 through 7.32 and of the turbulent kinetic energy production shown in figures 8.55 through 8.57. Pauley and Eaton saw a high concentration of turbulent kinetic energy in the core region of their upstream case, and associated this with the velocity deficit in the core. While this experiment did not show much velocity deficit in the vortex core (reference figure 8.5), figure 7.15 does indicate a large concentration of $\langle u'u' \rangle$ in the core region. In contrast, figure 7.18 indicates there is not a large concentration of $\langle v'v' \rangle$ in the core. With respect to production of turbulent kinetic energy, Pauley and Eaton saw an increase in the vortex core region, and an even larger increase in the upwash region. Figure 8.55 seems to indicate an increase of about the same magnitude in both the vortex core region and in the upwash region. After the adverse pressure gradient is initiated, production decreases in the downwash region, but since the boundary layer remains attached and a reasonable strain rate is maintained, there is more production here than in the separating boundary layer. In the upwash region, there is an apparent large production, despite relatively weak velocity gradients, because of the large magnitude of the normal stresses in the chaotic region of the separated upwash.

To summarize this discussion about turbulent kinetic production, vortex generators definitely alter the distribution of kinetic energy and the locations of maximum production. In an unsteady adverse pressure gradient, the modifications observed for steady flow are greatly amplified. In general, turbulent kinetic energy production appears to *respond to* changes that occur in the boundary layer, rather than be a *controlling factor* in the changes that occur.

Anisotropy of the Reynolds Stress Tensor. While the coarse data grid and time contraints on sampling unsteady events made a detailed investigation of the turbulence structure difficult for this experiment, it was possible to characterize

the general nature of the turbulence. The *general nature* of a boundary layer is two-component turbulence. As an adverse pressure gradient is introduced, does the structure remain two-component, or does it tend towards one-component, or isotropy? This section will briefly address this question, after an overview of essential definitions.

First, the Reynolds stress anisotropy tensor is a useful means to express the variation from isotropic turbulence. It is defined as

$$b_{ij} = \frac{R_{ij} - \frac{1}{3}q^2\delta_{ij}}{q^2}. \tag{8.22}$$

In general, one can find the principle axes for this tensor, along which only the diagonal terms are non-zero. If the turbulence is isotropic, then all the terms of the b_{ij} tensor are zero. The manner in which the terms of b_{ij} deviate from zero indicates the nature of the turbulence structure.

A compact means to characterize the anisotropy of the turbulence structure is to map b_{ij} onto an *anisotropy invariant map*. While the foundation for this technique lies in linear algebra, the essence of the technique is as follows. In its principle coordinates, the entire b_{ij} tensor can be expressed in terms of two independent parameters, which will be named *II* and *III*. (*II* and *III* are the *invariants* of the b_{ij} tensor.) Therefore, a particular state of turbulence, characterized by a particular set of values of the b_{ij} tensor, corresponds to a specific location on the plane formed by *II* and *III*. Furthermore, there is a limited region or space on this plane that is physically *realizable*. The limits of realizability are shown in figure 8.58. They are defined by isotropic turbulence at the origin, a straight line that defines two-component turbulence, a single point that defines one-component turbulence, the limiting trajectory from isotropy to two-component turbulence (axisymmetric contraction), and the limiting trajectory from isotropy to one-component turbulence (axisymmetric expansion).

The b_{ij} tensor was computed from the measured values of R_{ij} at the center line position, $z/D = 0$. Of the various spanwise positions, this one was chosen for investigation because it is a region where the vortex generators clearly have a beneficial effect in preventing separation. While the $\langle w'w' \rangle$ data had some unrealistic scatter, a careful review of the data at $z/d = 0$ revealed three y/h locations in the middle portion of the profile where something had apparently malfunctioned. After these several points were removed, the piecewise least-squares fit of $\langle w'w' \rangle$ looked very reasonable. The resulting values of b_{ij} were then used to map each point onto the invariant maps shown in figures 8.59a and 8.59b. In these two figures, the different symbols indicate different points in *time*. Two observations can be made from this figure. (1) The state of turbulence seems to tend from two-component turbulence towards isotropy. To see this tendency more clearly, trajectories at individual y/h locations are required. (2) There is no major difference in the appearance of the two maps at $\alpha = 0°$ and $\alpha = 18°$.

Figures 8.60 through 8.62 were prepared in an attempt to visualize the trajectories through time of individual points in the boundary layer. To keep the trajectories uncluttered, a representative but limited number of y/h positions were selected. Generally, successive arrowheads correspond to the dimensionless times $tU_0/l = 0.4$, $tU_0/l = 2$, $tU_0/l = 4$, and $tU_0/l = 8$. Occasionally intermediate arrowheads were removed when they obscured some aspect of the trajectories. Figure 8.60 shows the innermost region of the boundary layer where there was a very pronounced trajectory. These points very near the surface, where the turbulence is originally two-component, move very strongly to the left in the general direction of isotropy. The same trend, but less dramatic, is seen for the inner region with $\alpha = 18°$. The trend may be less dramatic because the vortex generators bring some more isotropic turbulent eddies closer to the surface. Figure 8.61 shows trajectories for points in the outer portion of the boundary layer. These points originate near isotropy and tend to be driven to the left, but not nearly as strongly. Finally, figure 8.62 shows points on the outer edge of the boundary layer. At $\alpha = 0°$ these points start

162

near isotropy and remain there, but at $\alpha = 18°$, some of the points tend to be less isotropic and their trajectories are more chaotic. This may be because the enhanced mixing from the vortex generators brings out some packets of fluid from the surface that are less isotropic.

To conclude, the invariant maps indicate several things about the turbulent structure. First, at this spanwise location where the vortex generators clearly delay separation, there is no major change in the anisotropy of the turbulent structure as a result of the embedded vortices. Second, under the influence of a strong adverse pressure gradient, points near the surface are driven from a state of two-component turbulence to a state much nearer isotropy.

8.8 Closure

This chapter has used many different analytical tools to investigate the nature of embedded streamwise vortices in an unsteady adverse pressure gradient. By far, the tool that yielded the most information was the time response analysis of secion 8.2. The results presented in figures 8.11 through 8.16 should be of use to engineers in the design of flow control systems. In addition, these results showed that the vortex generators do not modify the *immediate response* of the boundary layer, but they do modify the magnitude of the slower *convective response*. The results presented in the other sections are useful for comparisons to other studies in steady flow, and they add additional insight into the basic conclusions drawn in section 8.2.
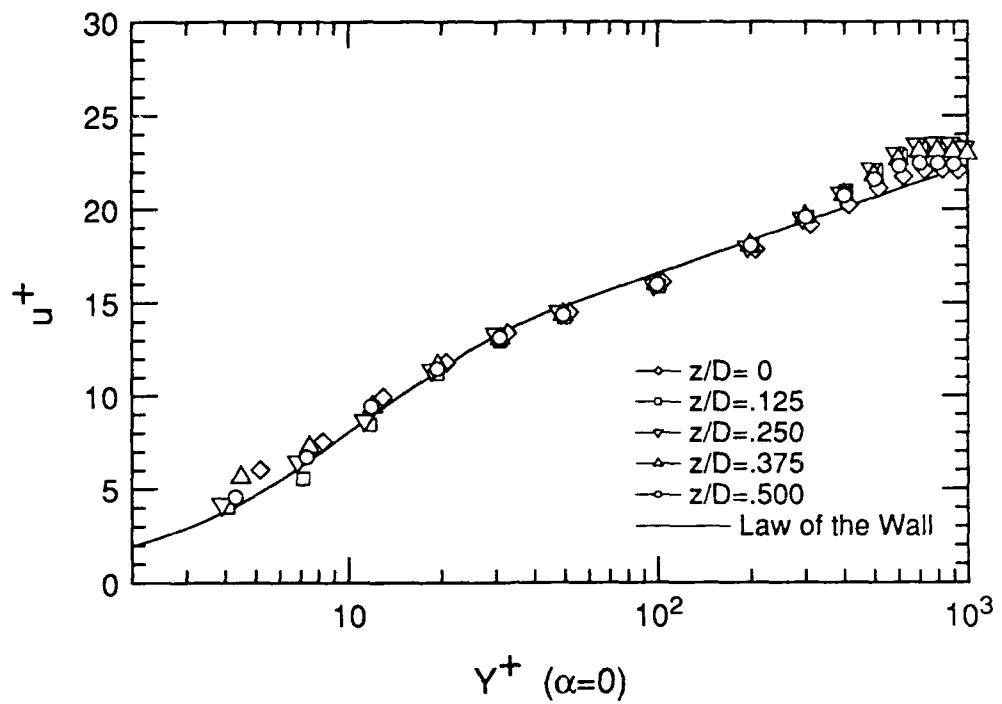
Figure 8.1a Steady mean profiles in wall coordinates for $\alpha = 0°$
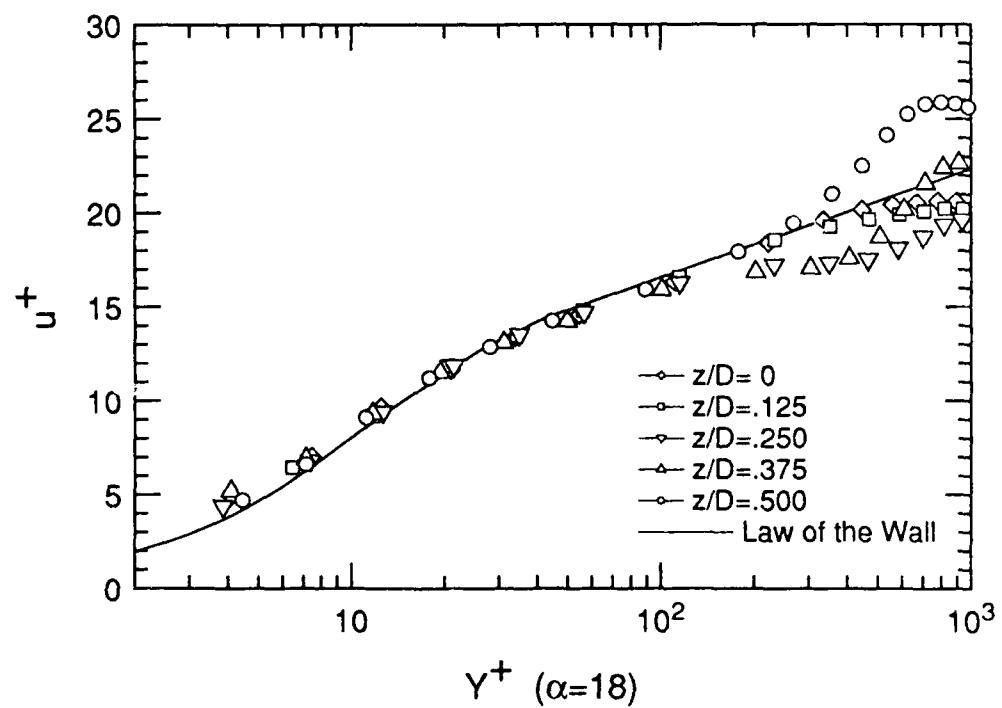
Figure 8.1b Steady mean profiles in wall coordinates for $\alpha = 18°$

164
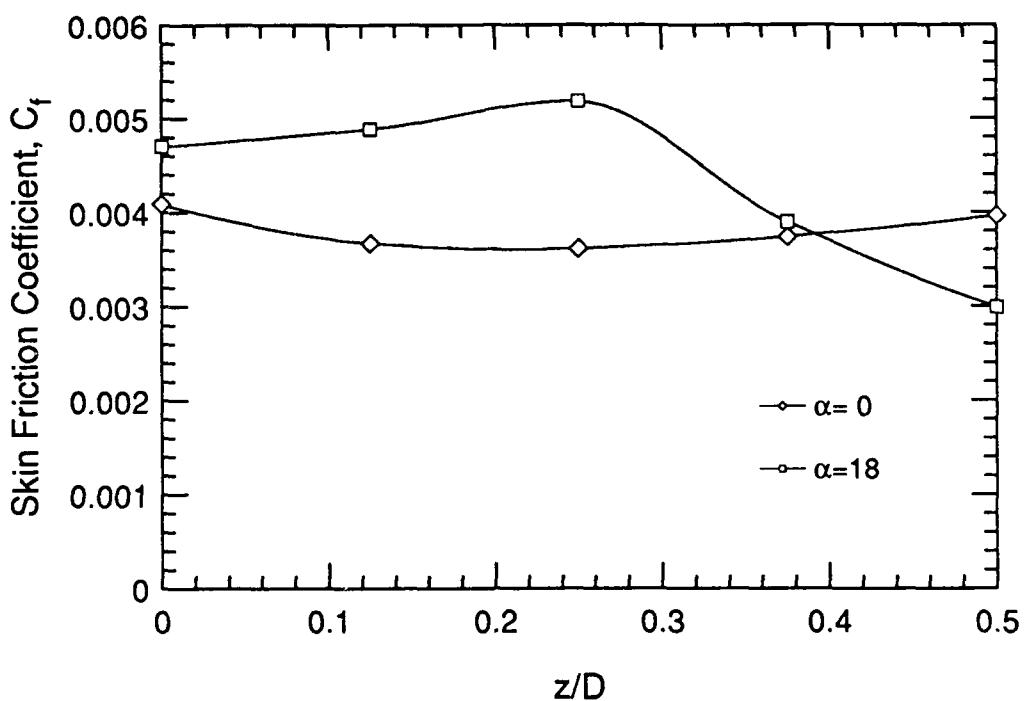
Figure 8.2a Spanwise variation in C_f for steady flow
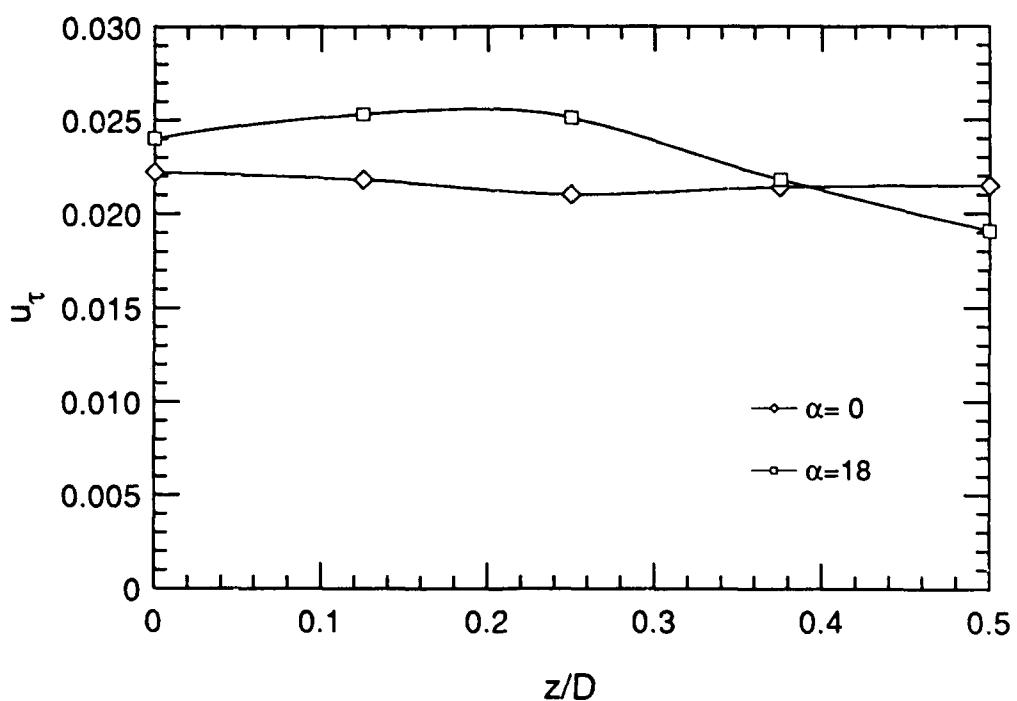
Figure 8.2b Spanwise variation in u_τ for steady flow
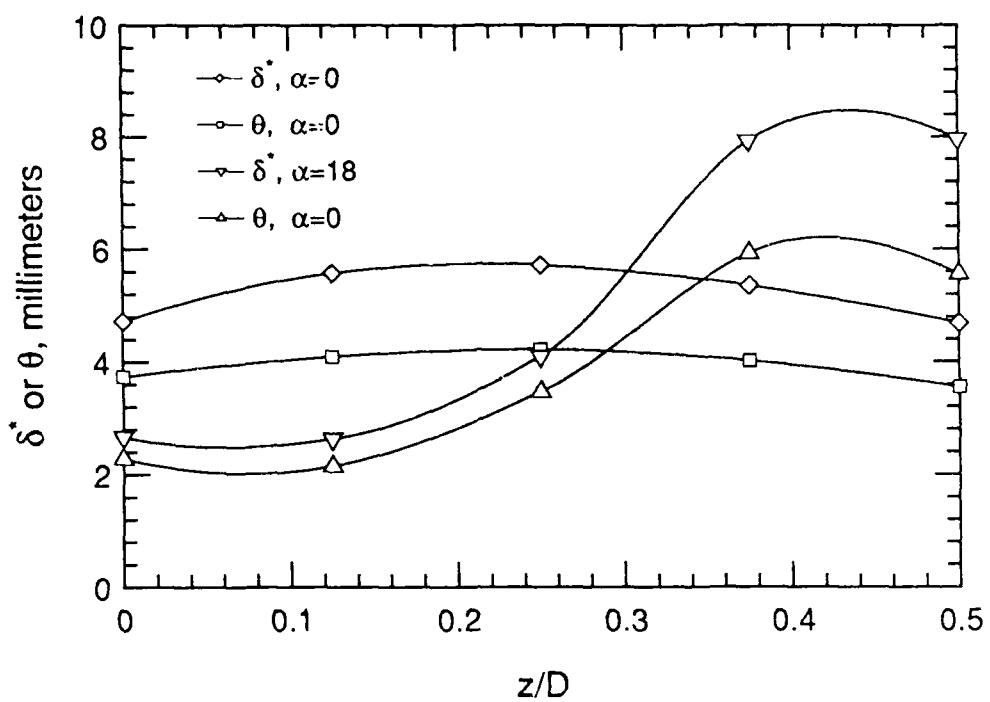
Figure 8.3a Spanwise variation of integral parameters for steady flow
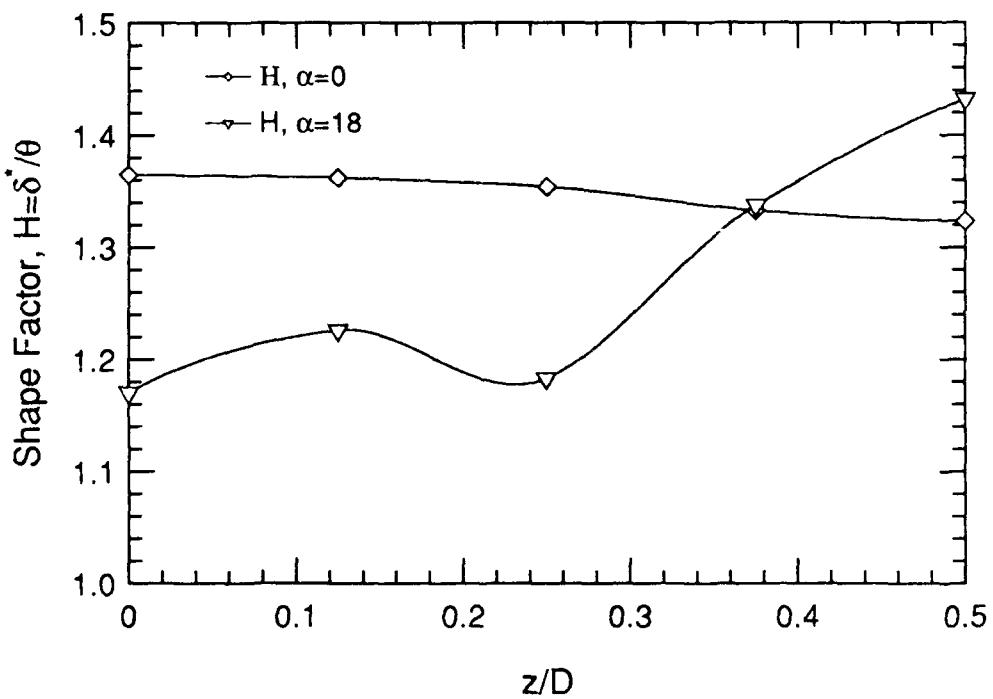
Figure 8.3b Spanwise variation of shape factor for steady flow

Figure 8.4 Transport velocities of $\langle u'u' \rangle + \langle v'v' \rangle$

167
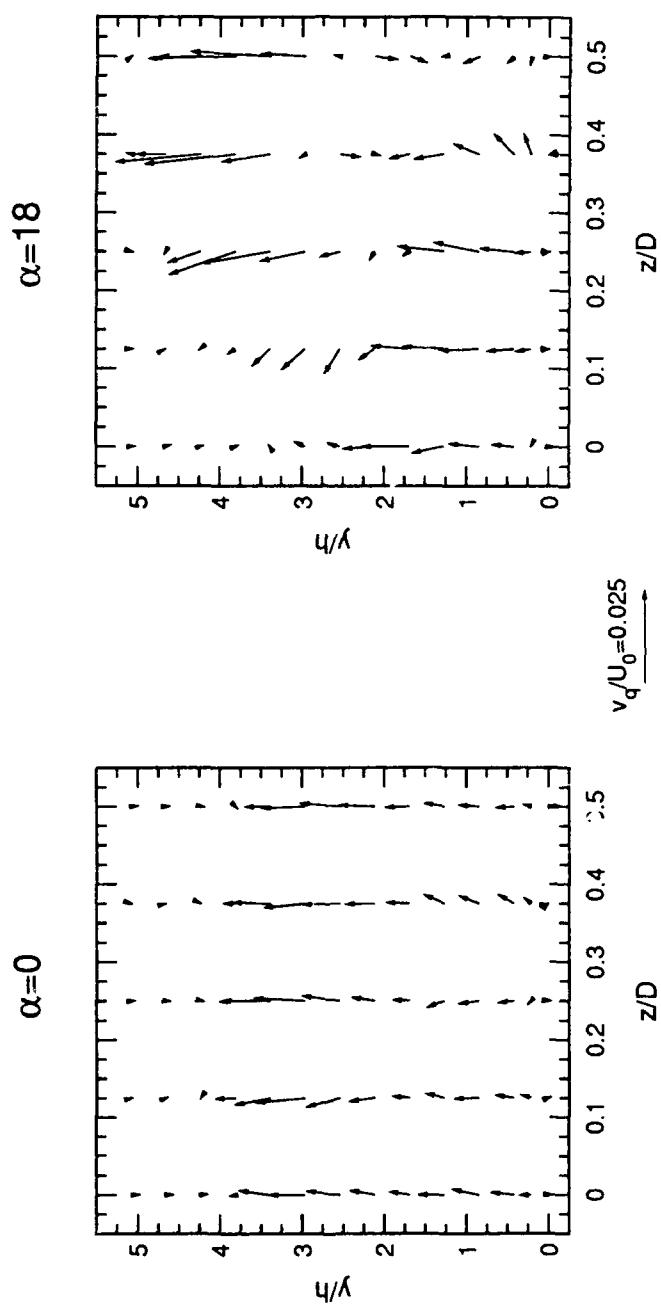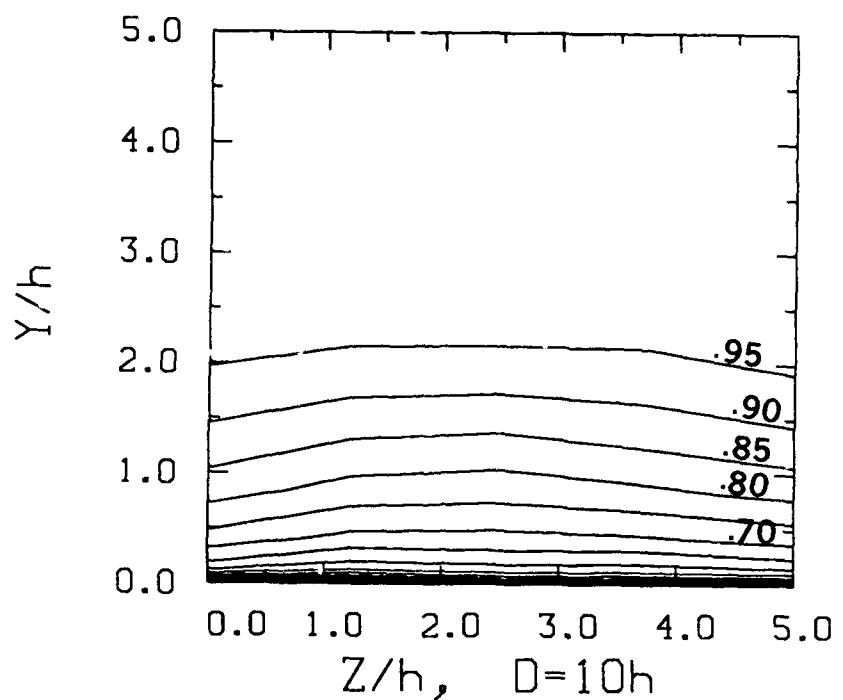
Figure 8.5a Contours of $\langle u \rangle / U_0$ at $tU_0/l = 0$ for $\alpha = 0°$
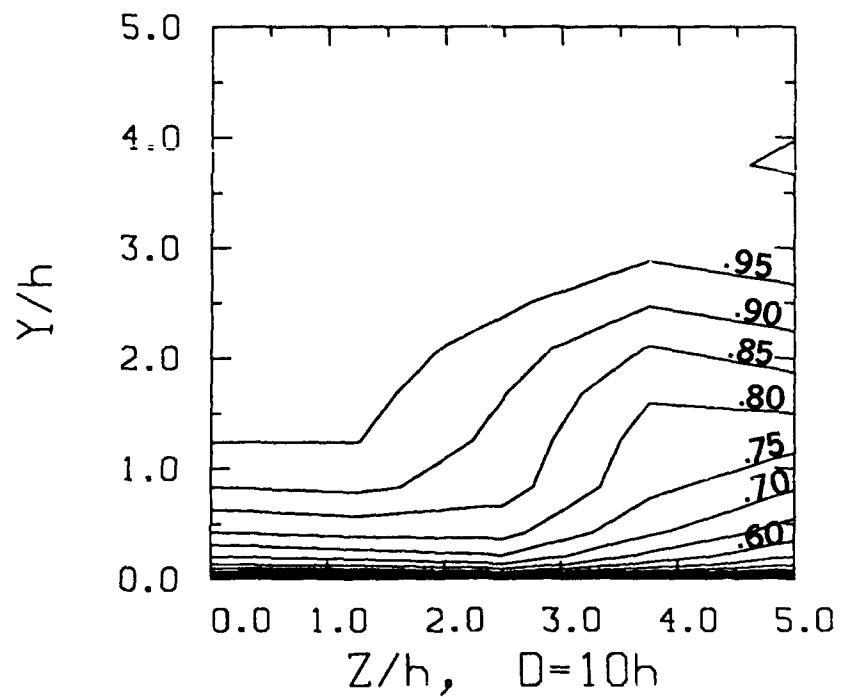
Figure 8.5b Contours of $\langle u \rangle / U_0$ at $tU_0/l = 0$ for $\alpha = 18°$
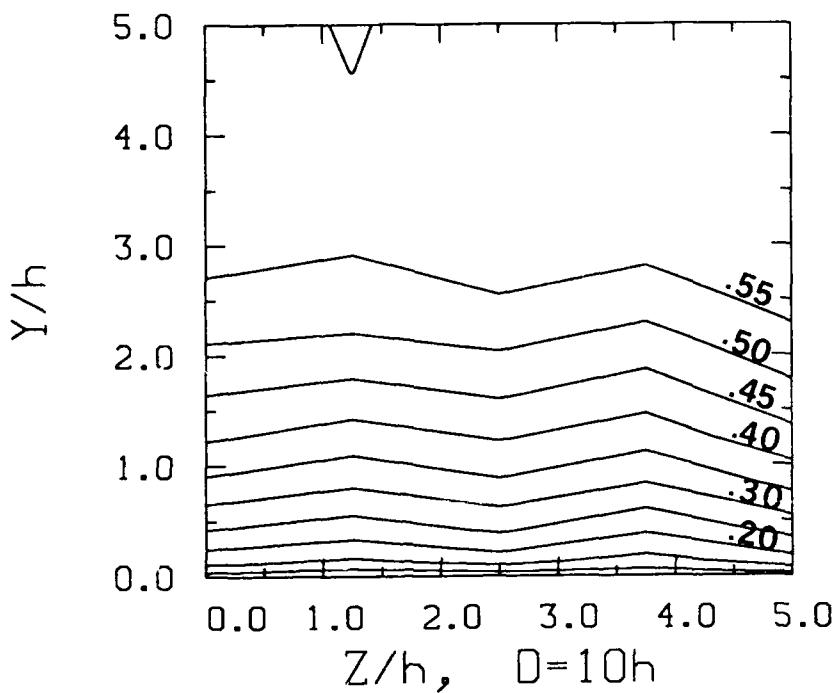
Figure 8.6a Contours of $\langle u \rangle / U_0$ at $tU_0/l = 2$ for $\alpha = 0°$
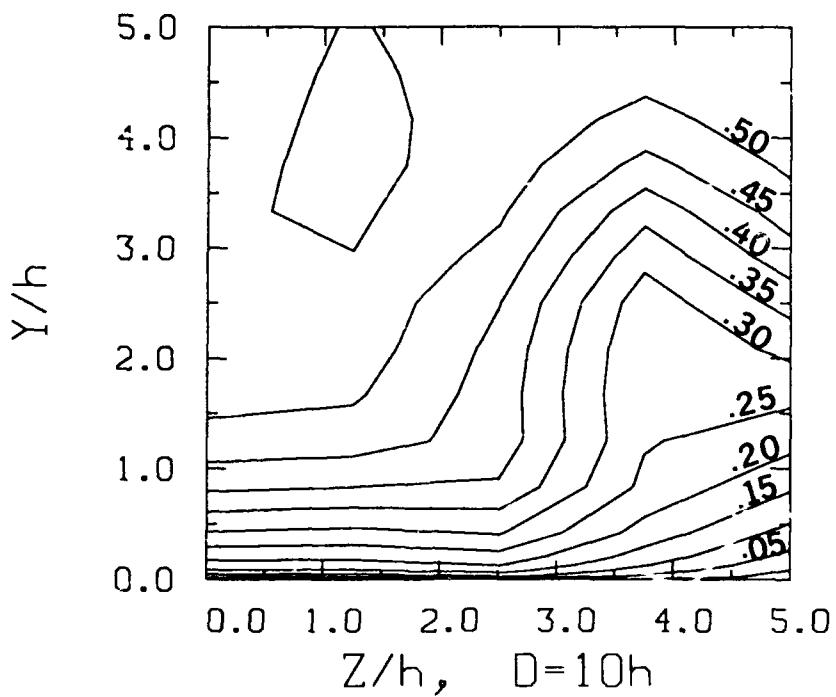
Figure 8.6b Contours of $\langle u \rangle / U_0$ at $tU_0/l = 2$ for $\alpha = 18°$

169
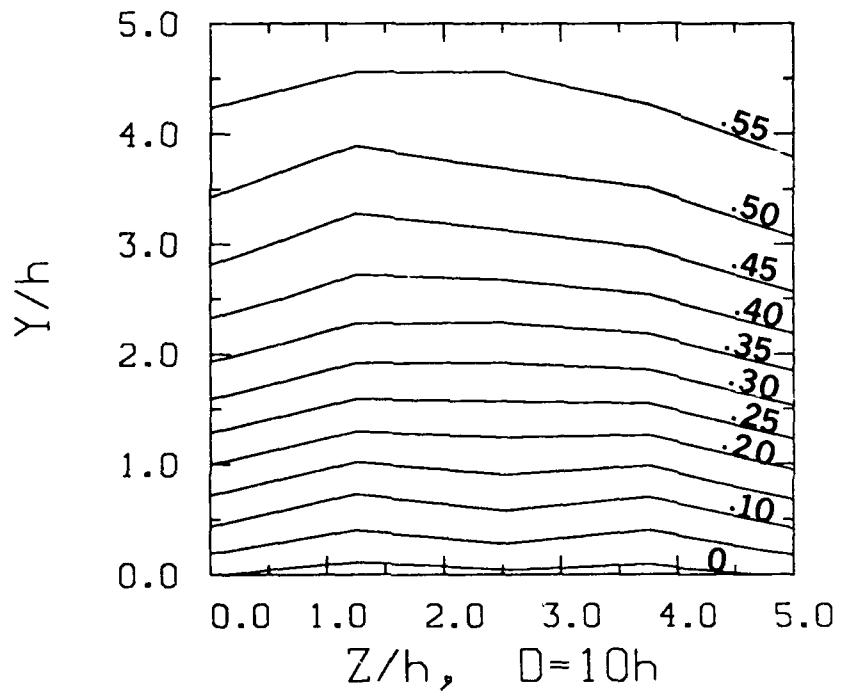
Figure 8.7a Contours of $\langle u \rangle / U_0$ at $tU_0/l = 4$ for $\alpha = 0°$
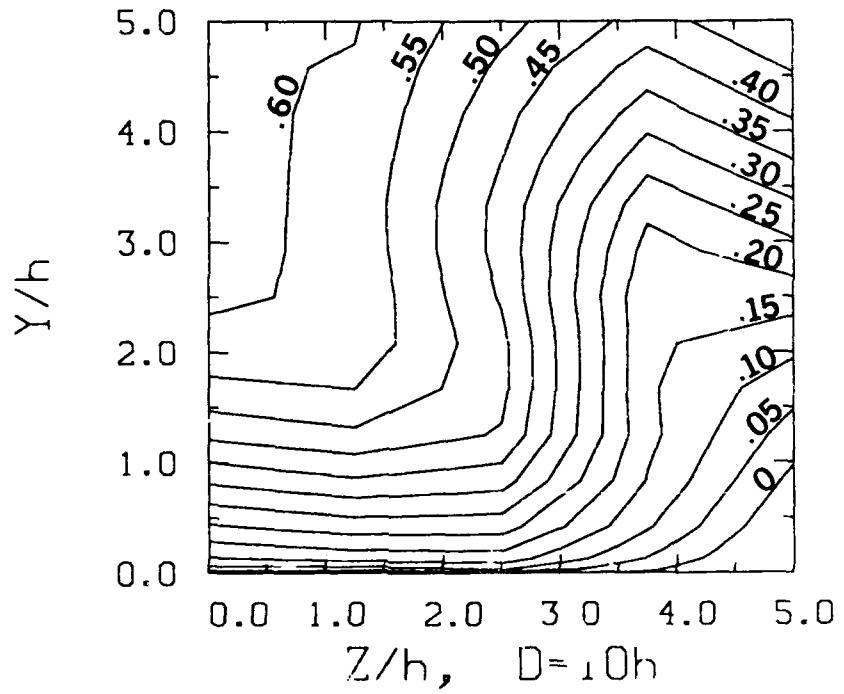
Figure 8.7b Contours of $\langle u \rangle / U_0$ at $tU_0/l = 4$ for $\alpha = 18°$

170
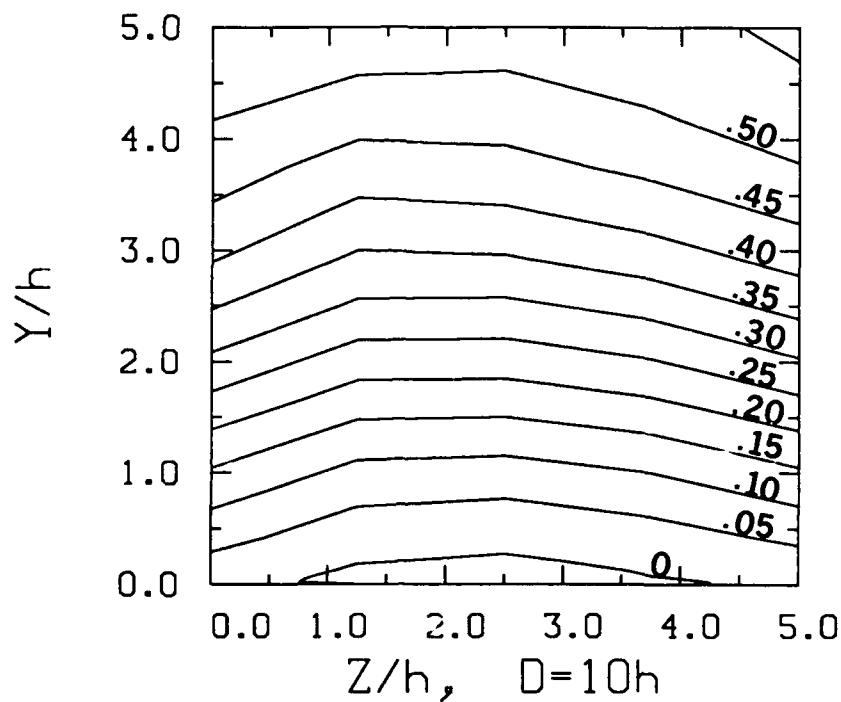
Figure 8.8a Contours of $\langle u \rangle / U_0$ at $tU_0/l = 6$ for $\alpha = 0°$
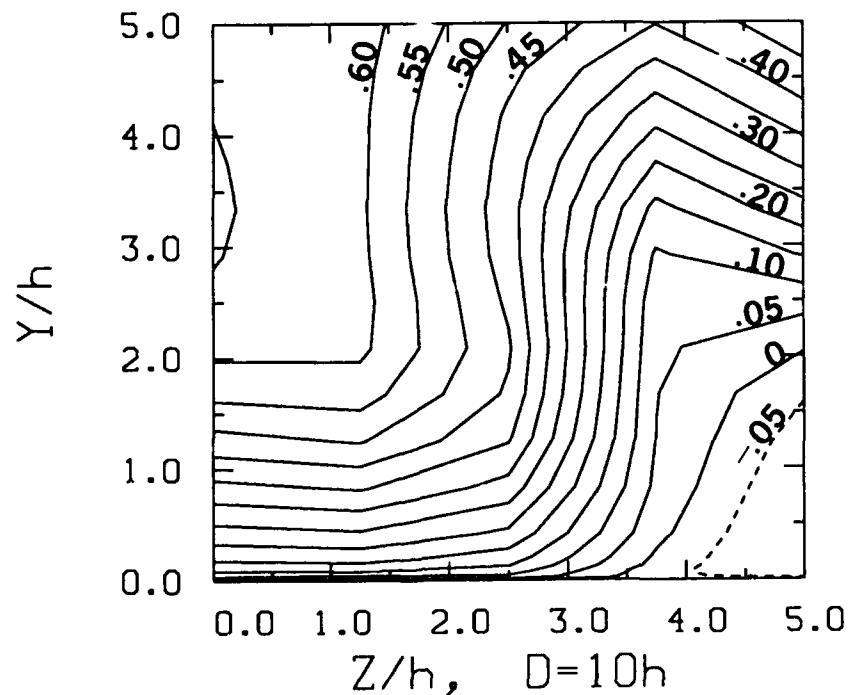
Figure 8.8b Contours of $\langle u \rangle / U_0$ at $tU_0/l = 6$ for $\alpha = 18°$

171
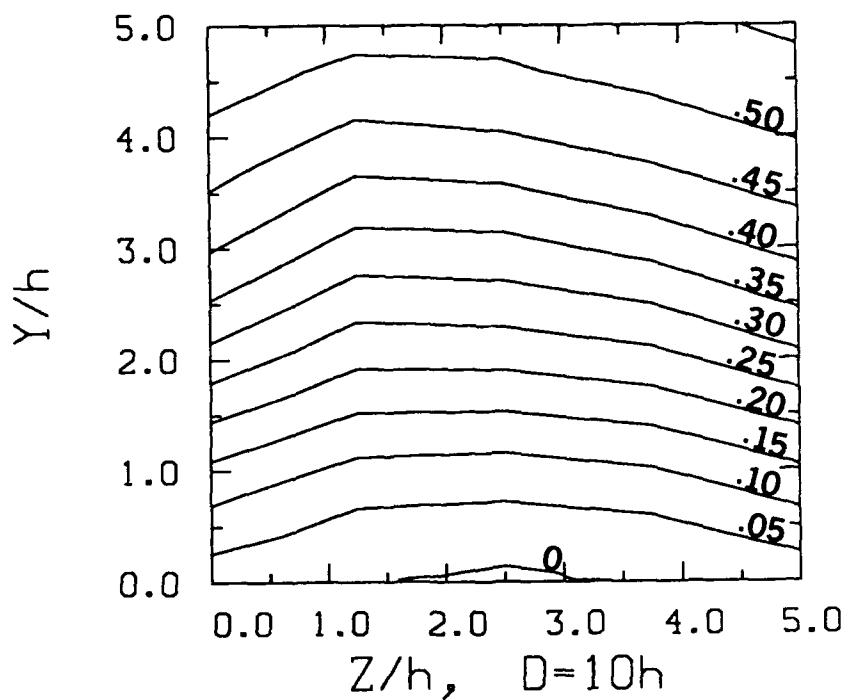
Figure 8.9a Contours of $\langle u \rangle / U_0$ at $tU_0/l = 8$ for $\alpha = 0°$
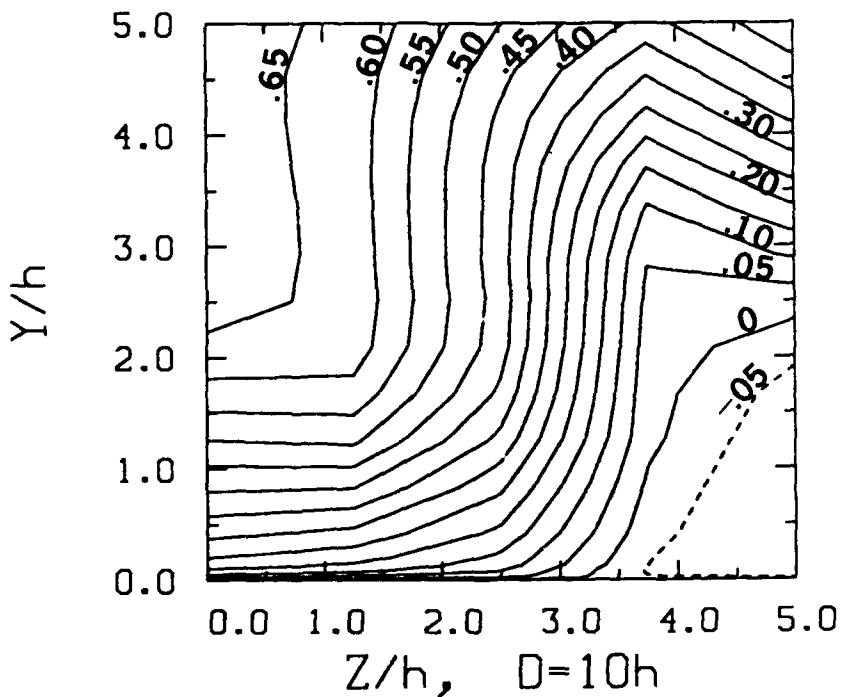
Figure 8.9b Contours of $\langle u \rangle / U_0$ at $tU_0/l = 8$ for $\alpha = 18°$

172
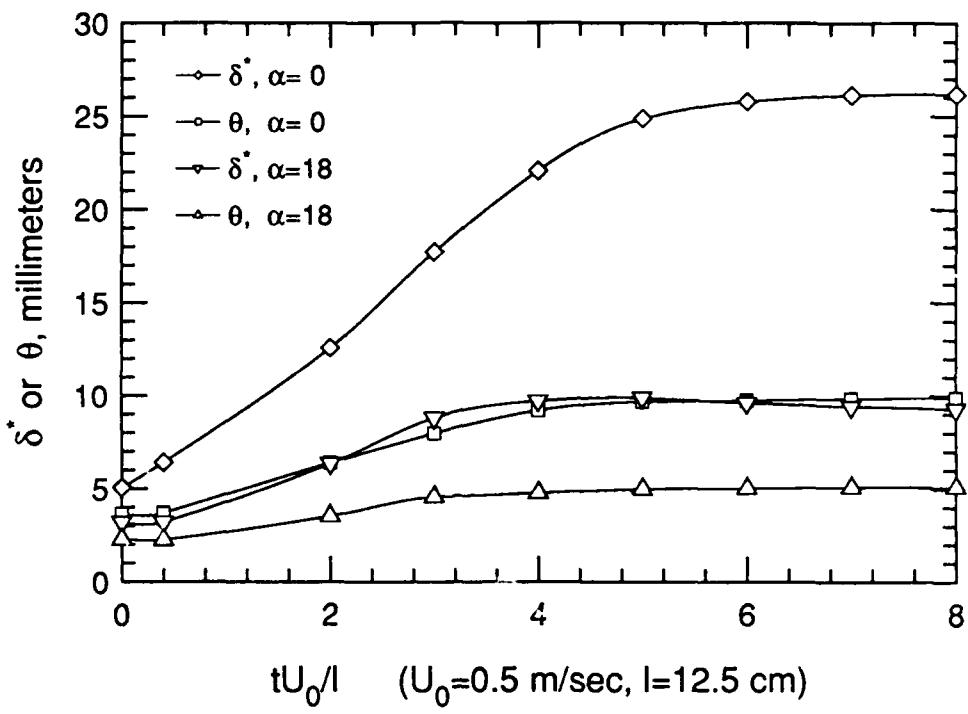
Figure 8.10a Time response of integral parameters at $z/D = 0$
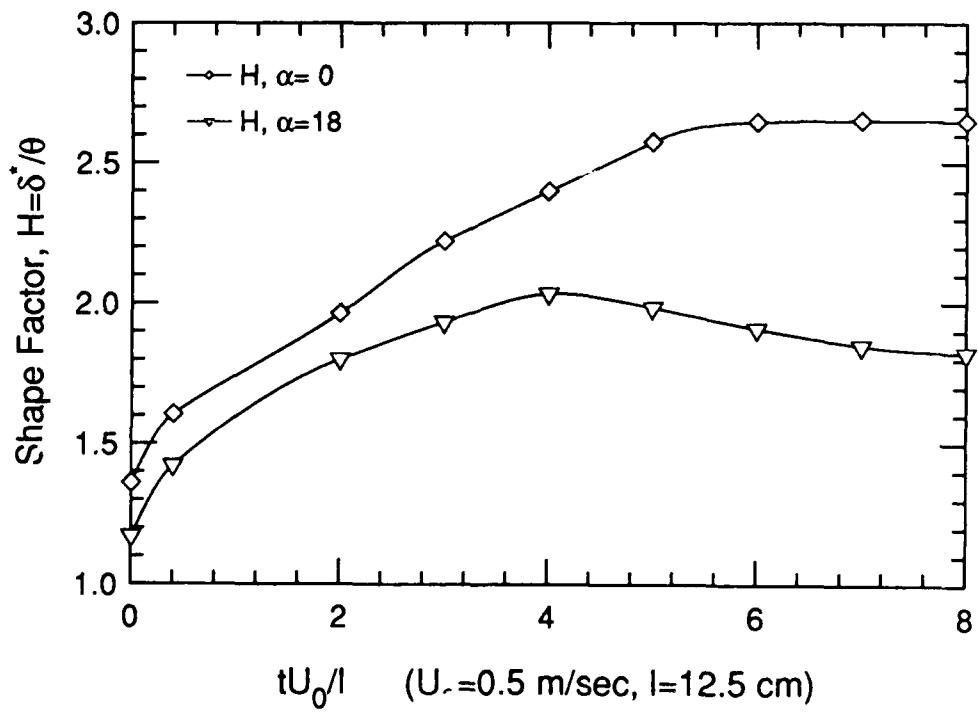
Figure 8.10b Time response of shape factor at $z/D = 0$

173
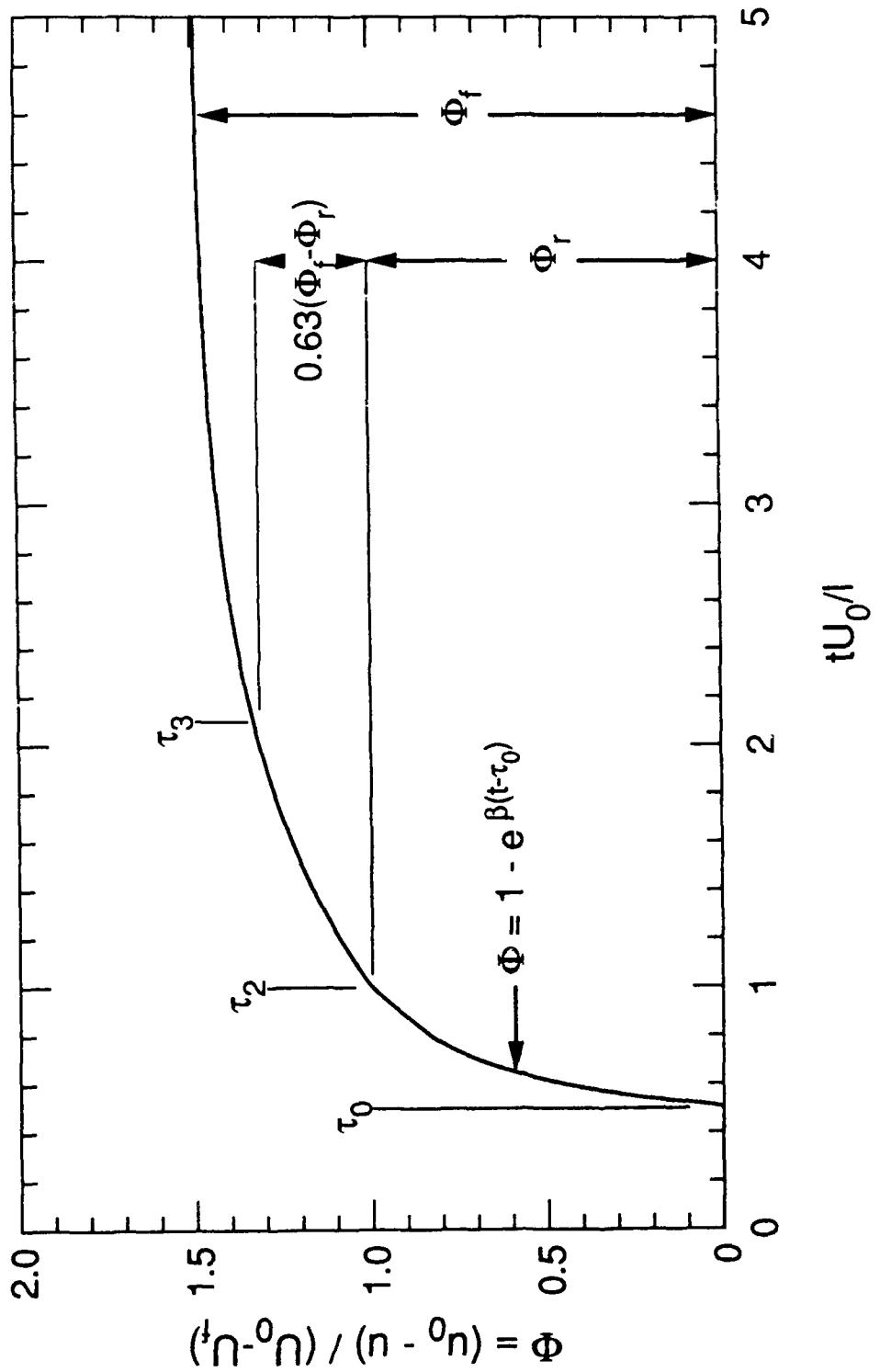
Figure 8.11 Mathematical model for time response of velocity

174
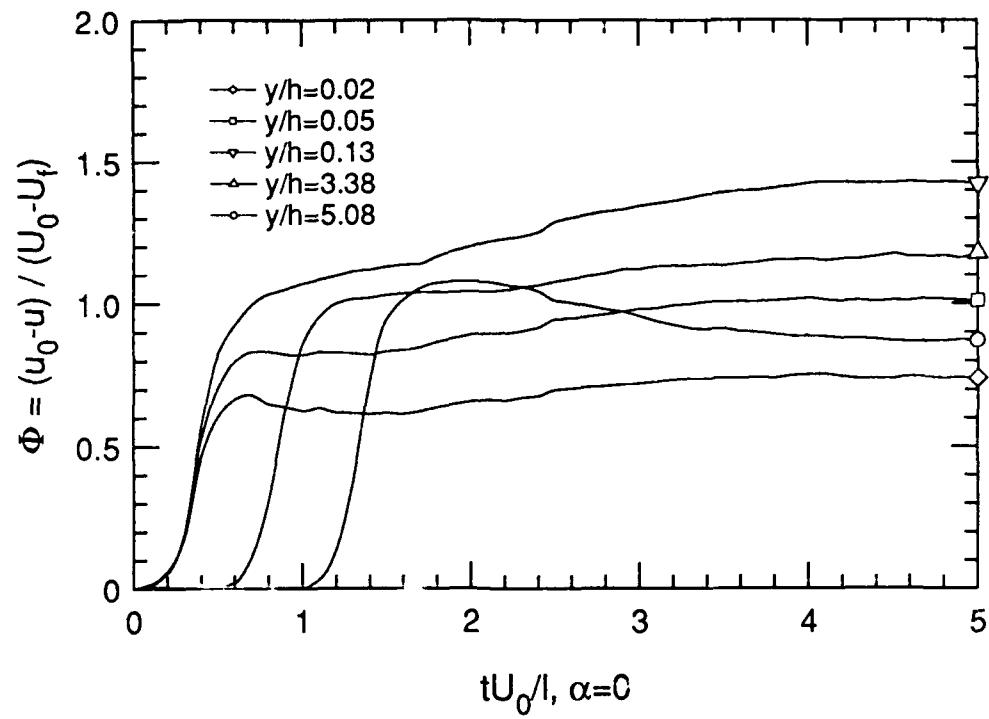
Figure 8.12a History of Φ for $\alpha = 0°$ at $z/D = 0$
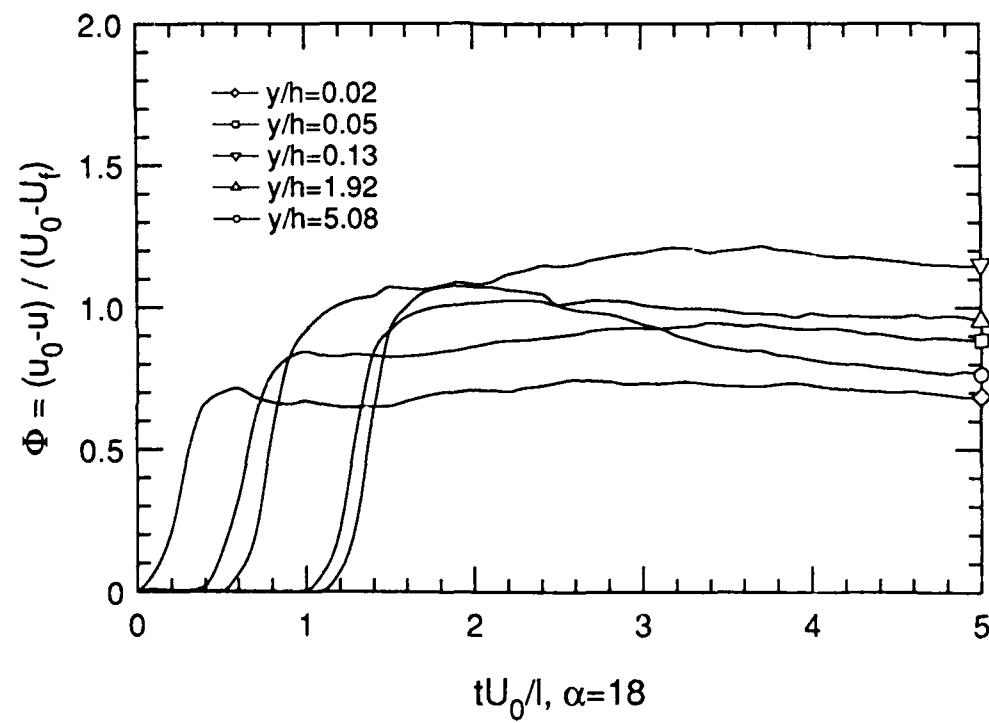
Figure 8.12b History of Φ for $\alpha = 18°$ at $z/D = 0$

175
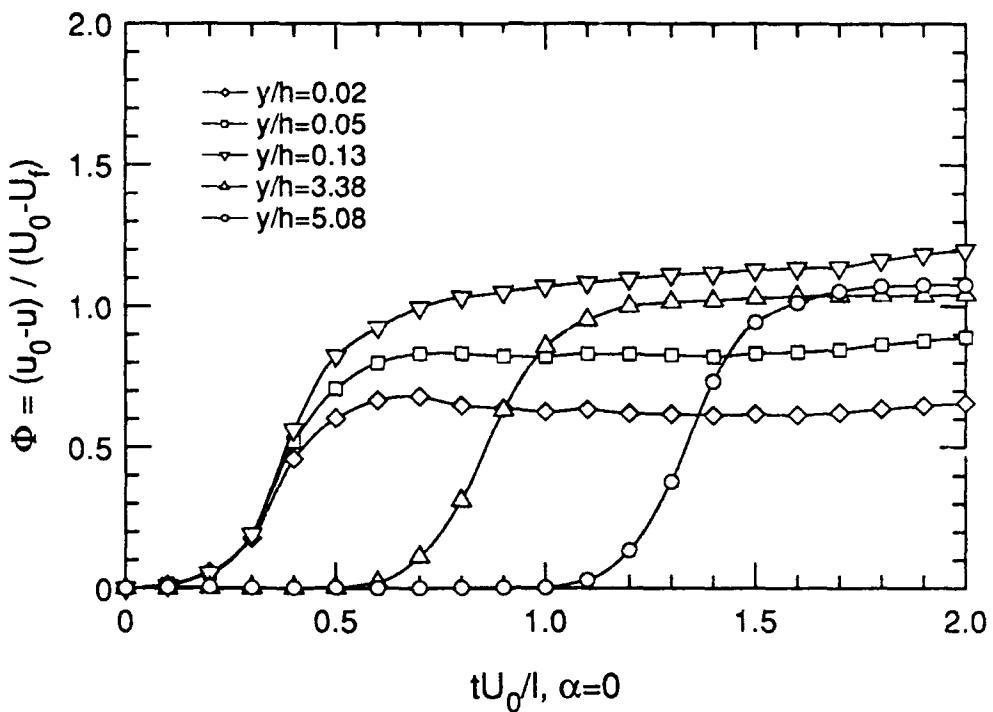
Figure 8.13a History of Φ for $\alpha = 0°$ showing data
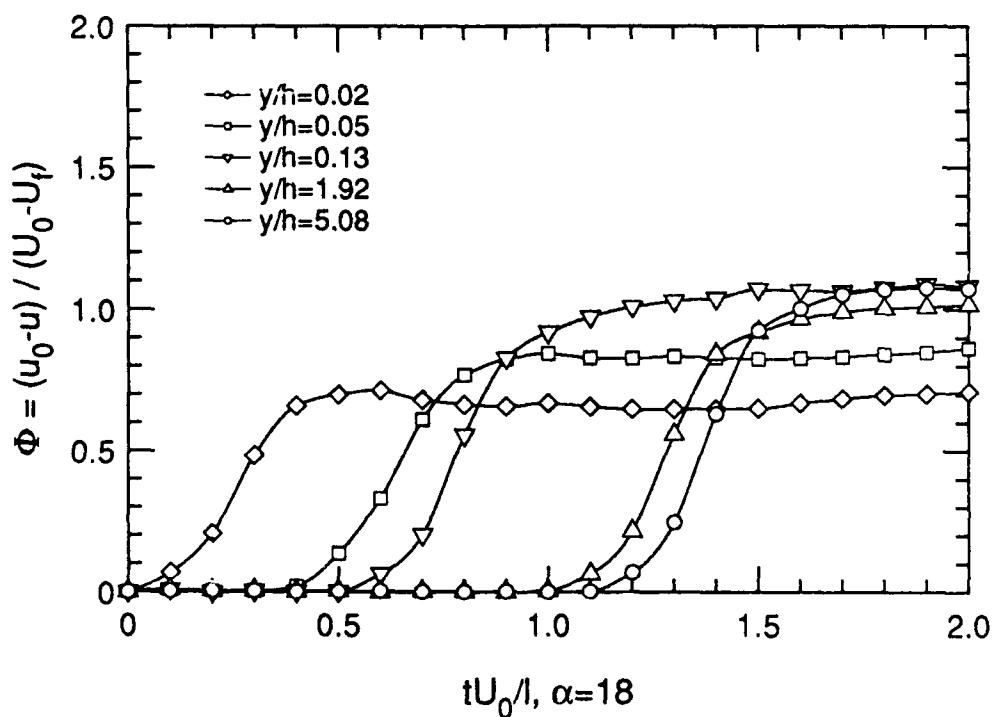
Figure 8.13b History of Φ for $\alpha = 18°$ showing data

176
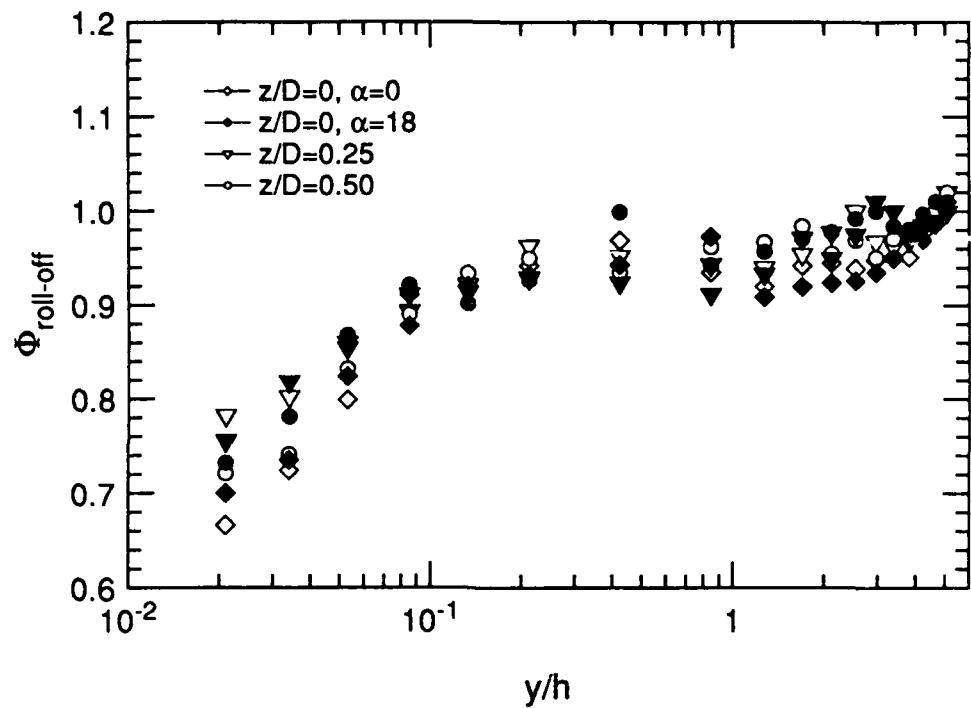
Figure 8.14a $\Phi_{roll-off}$ for $\langle u \rangle$
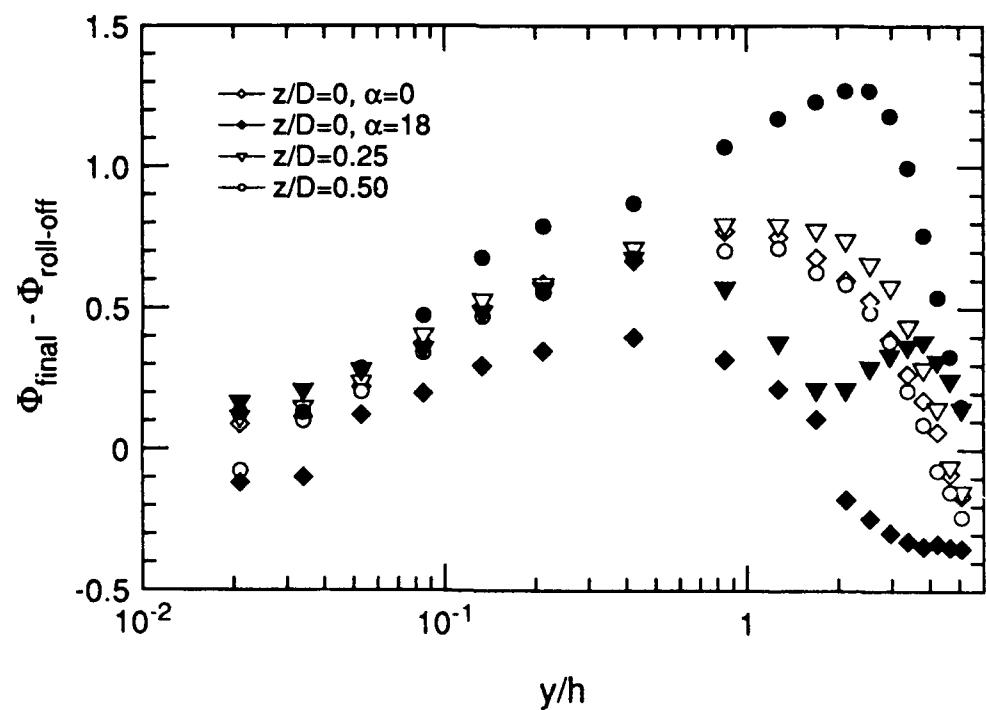
Figure 8.14b $\Phi_{final} - \Phi_{roll-off}$ for $\langle u \rangle$

177
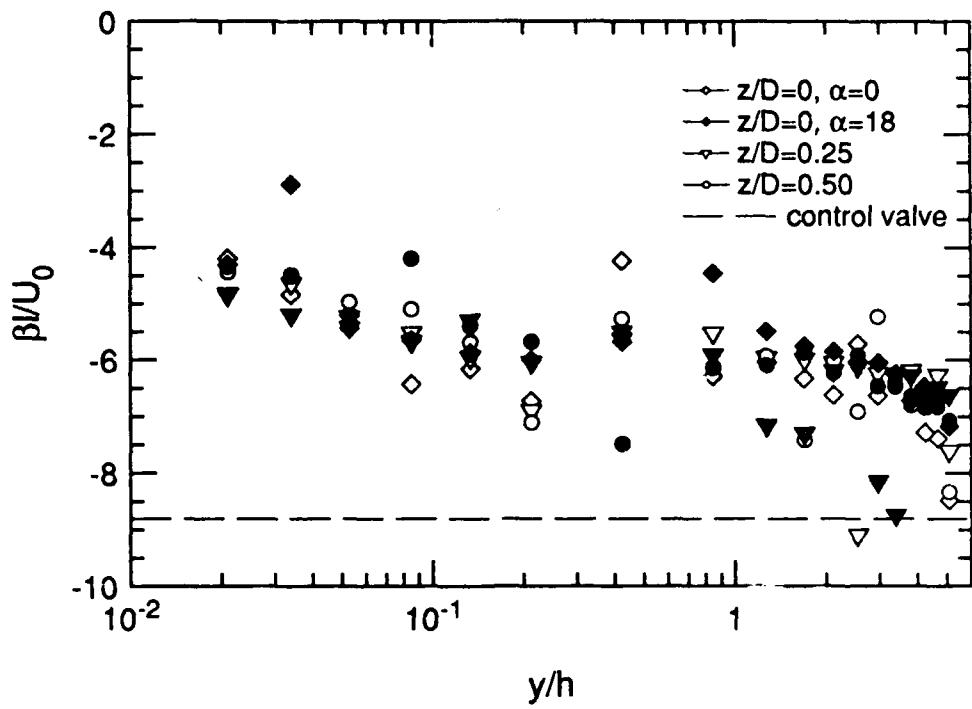
Figure 8.14c Immediate response rate of $\langle u \rangle$
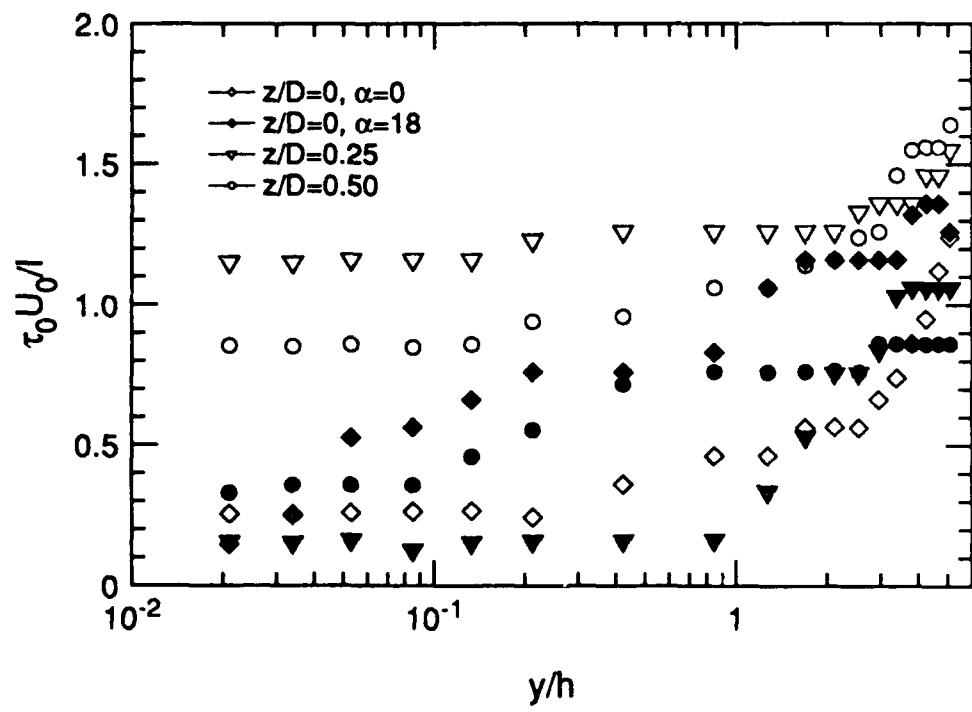
Figure 8.14d Initial delay in response of $\langle u \rangle$

178
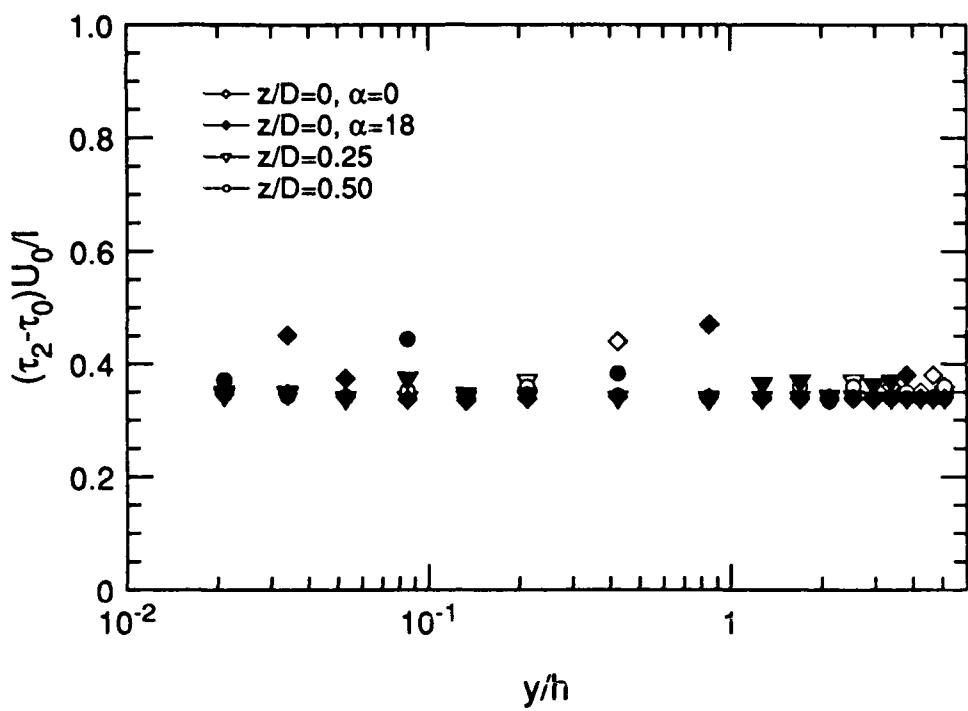
Figure 8.14e Duration of initial response of $\langle u \rangle$
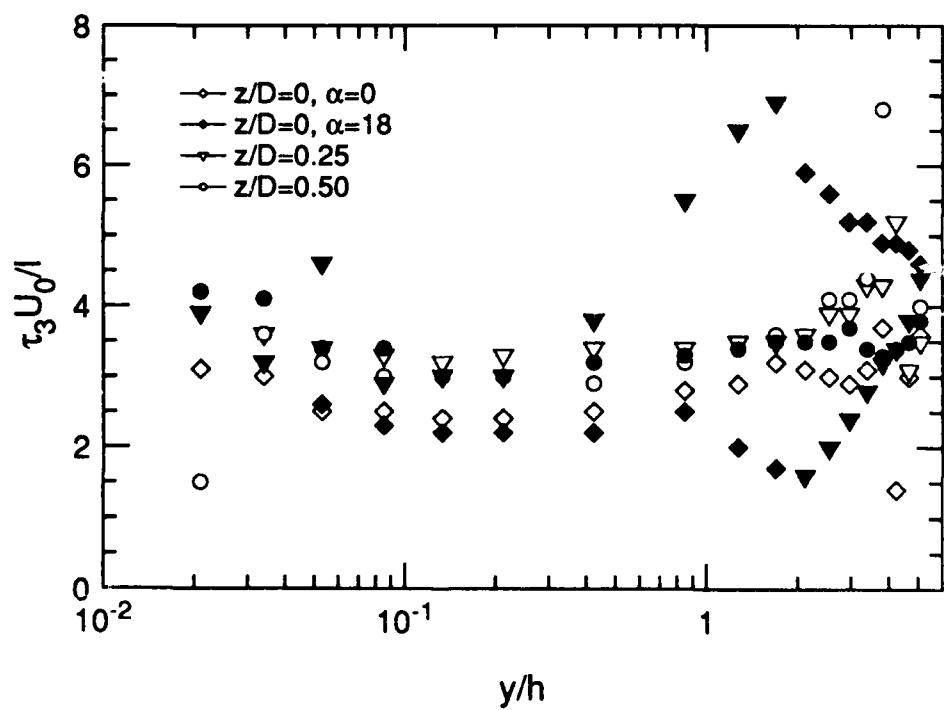
Figure 8.14f Convective time constant for $\langle u \rangle$

179
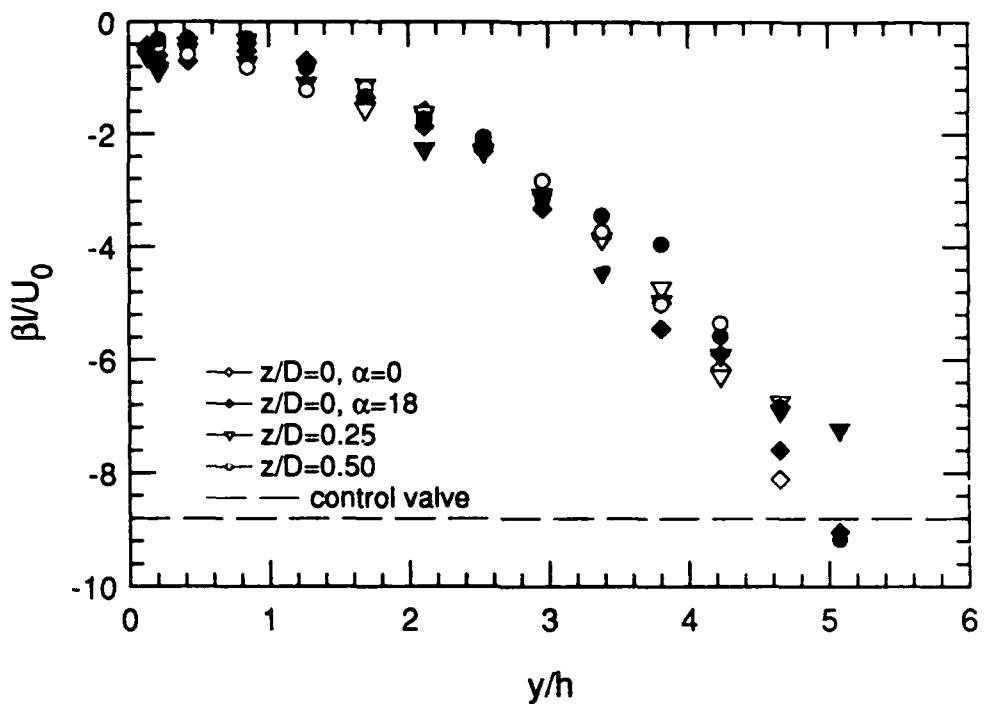
Figure 8.15a Immediate response rate of $\langle v \rangle$
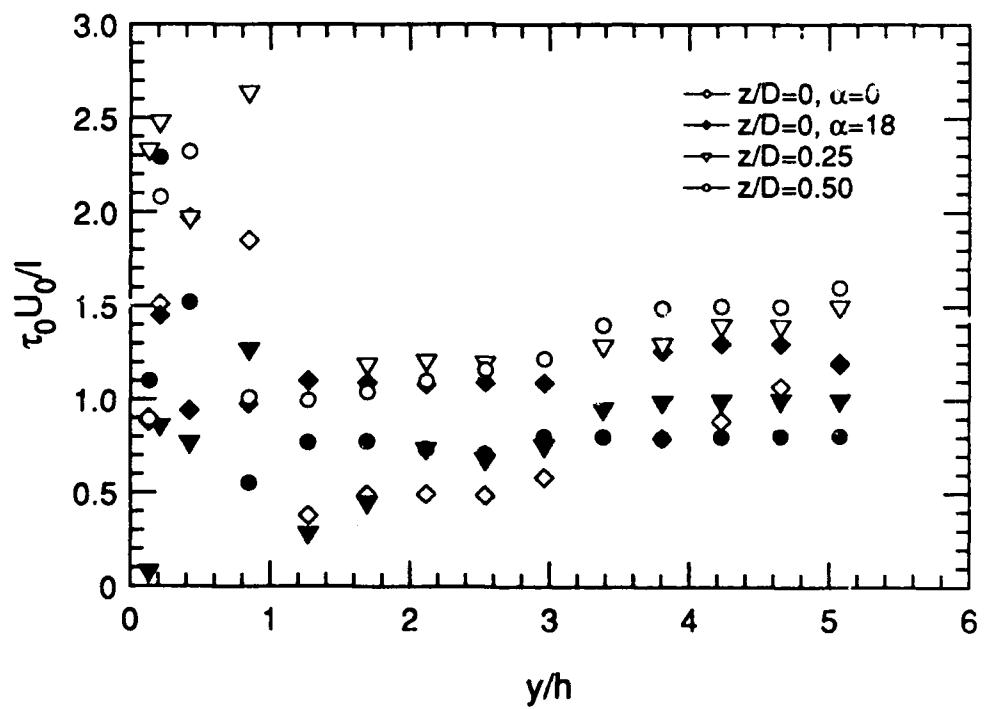
Figure 8.15b Initial delay in response of $\langle v \rangle$
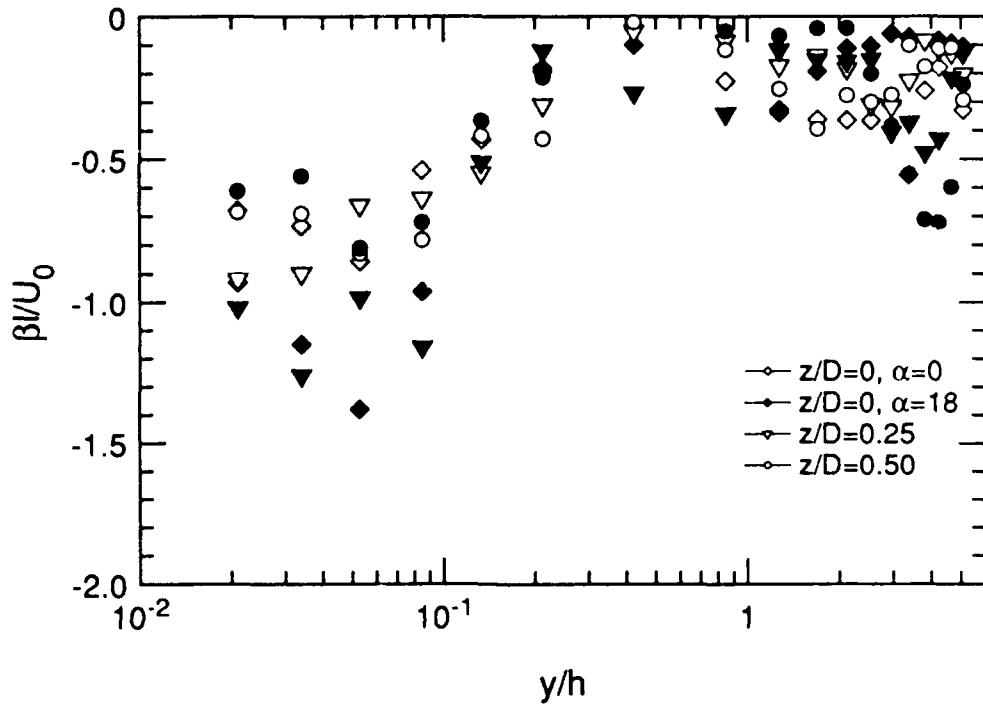
Figure 8.16a Immediate response rate of $\langle u'u' \rangle$
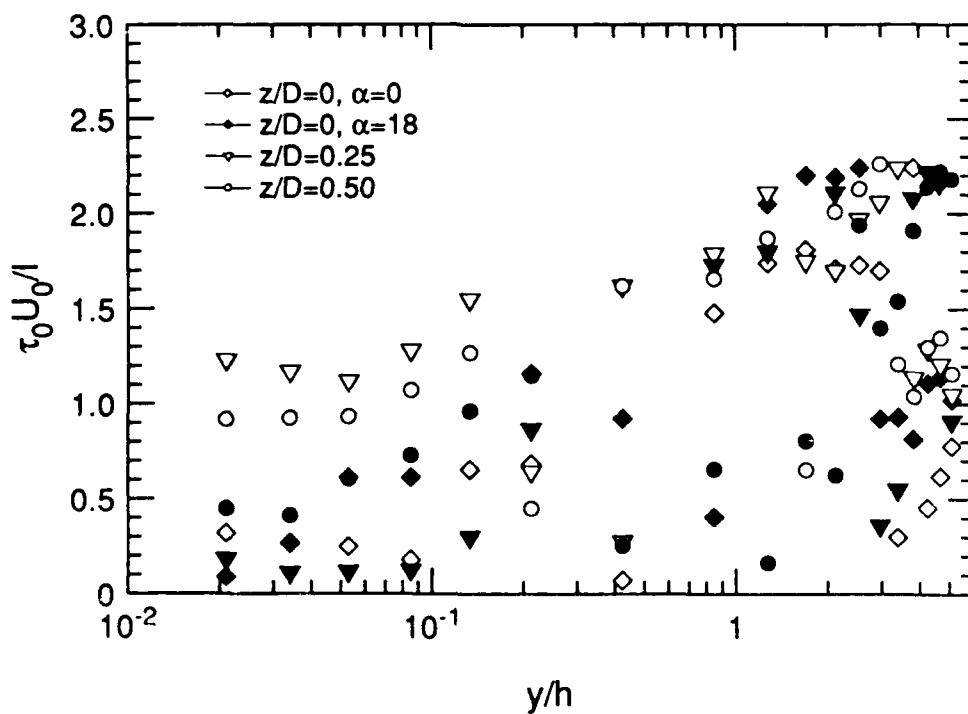
Figure 8.16b Initial delay in response of $\langle u'u' \rangle$

181
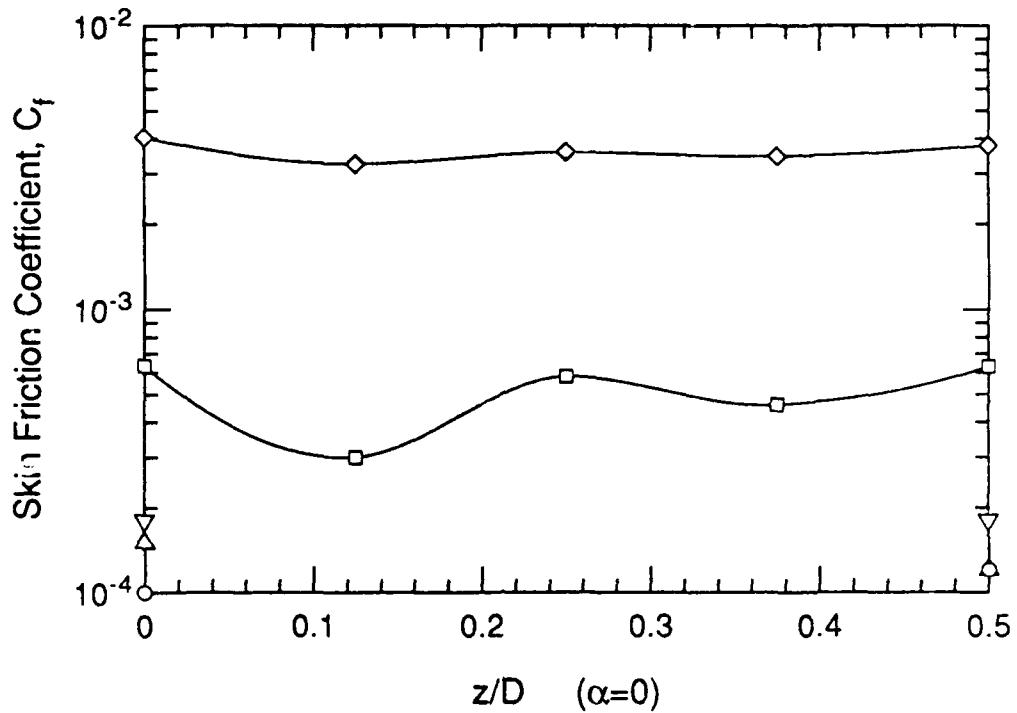
Figure 8.17a Spanwise variation in C_f for $\alpha = 0°$
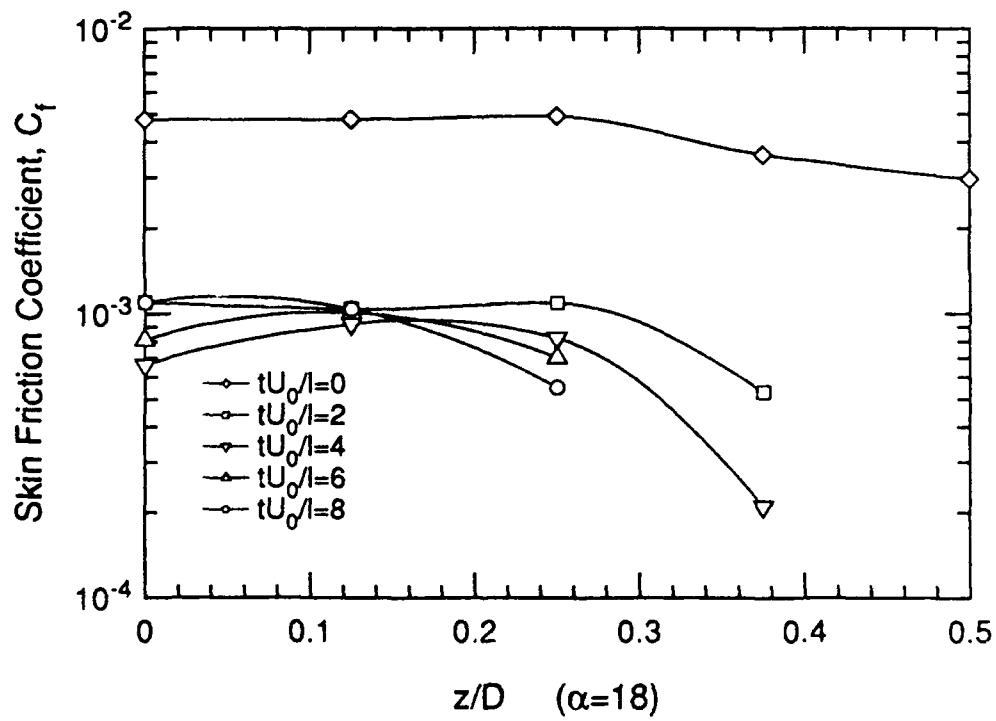
Figure 8.17b Spanwise variation in C_f for $\alpha = 18°$
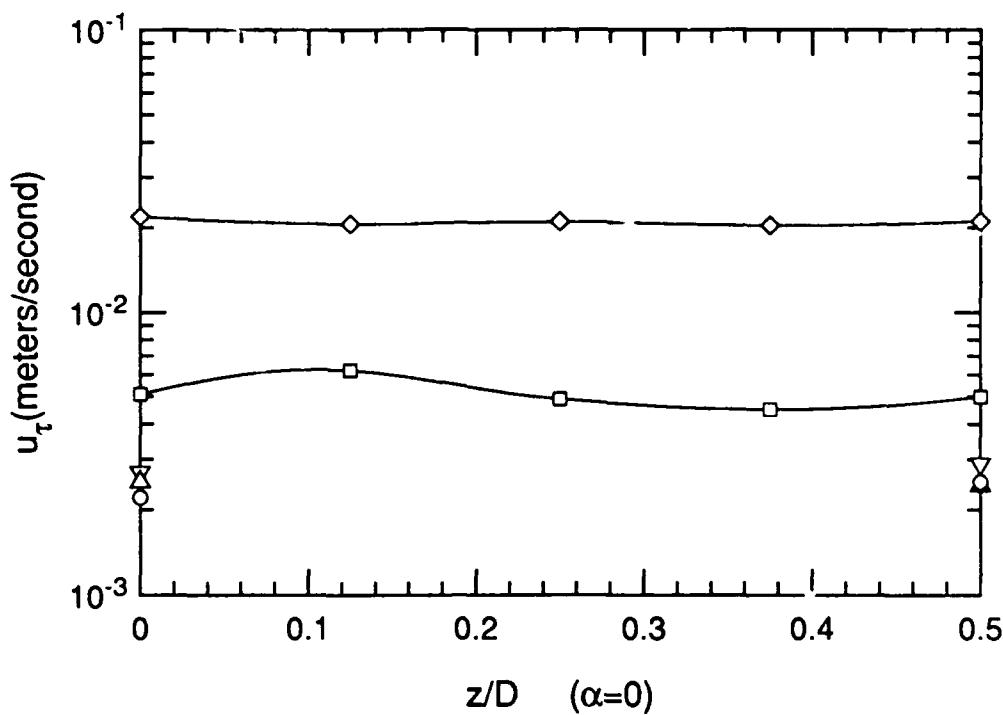
Figure 8.18a Spanwise variation in u_τ for $\alpha = 0°$
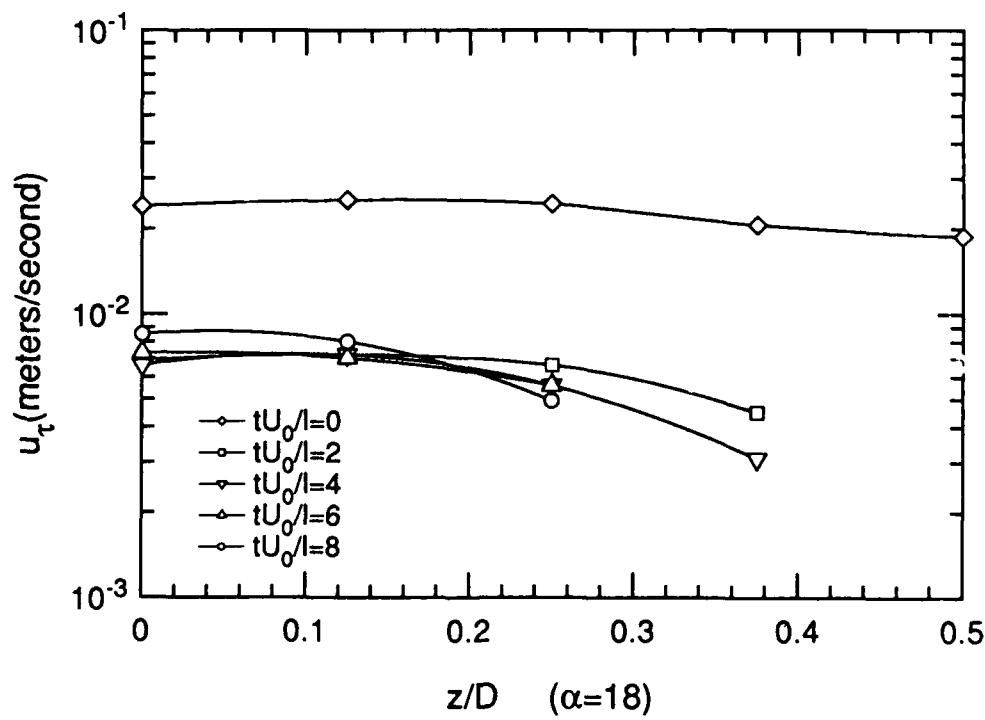
Figure 8.18b Spanwise variation in u_τ for $\alpha = 18°$

183
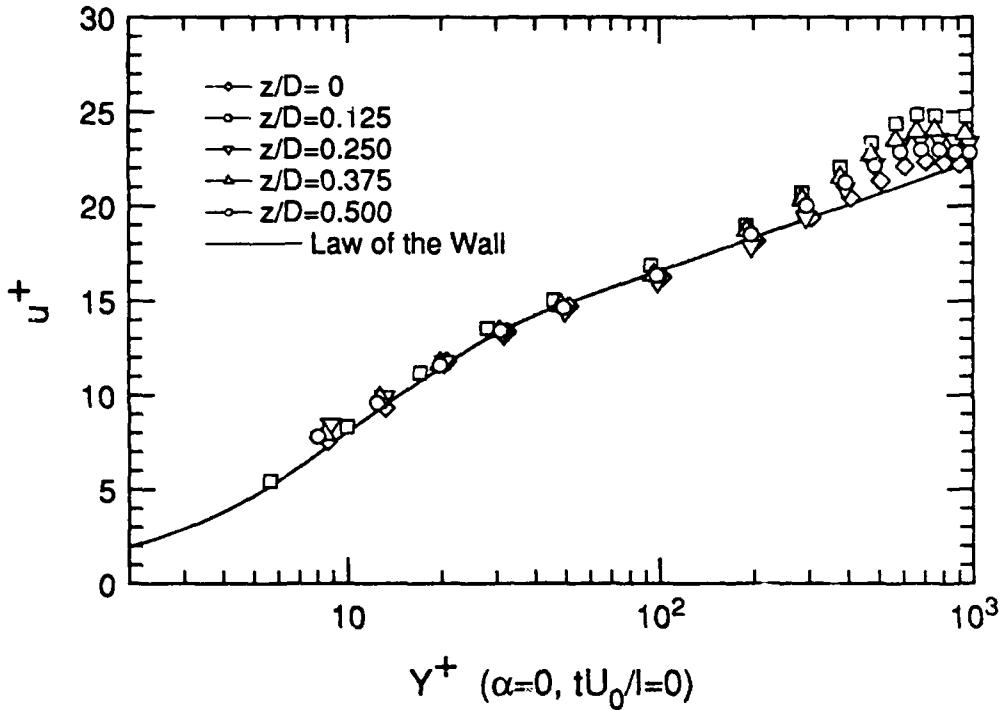
Figure 8.19a $\langle u \rangle$ profiles in wall coordinates for $\alpha = 0°$ at $tU_0/l = 0$
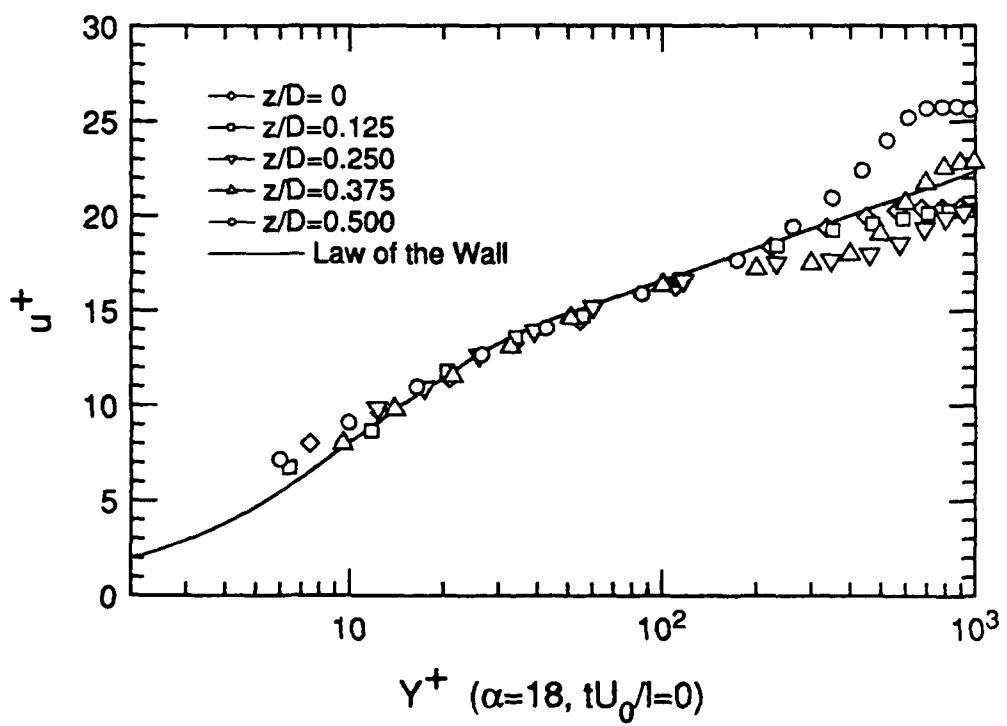
Figure 8.19b $\langle u \rangle$ profiles in wall coordinates for $\alpha = 18°$ at $tU_0/l = 0$
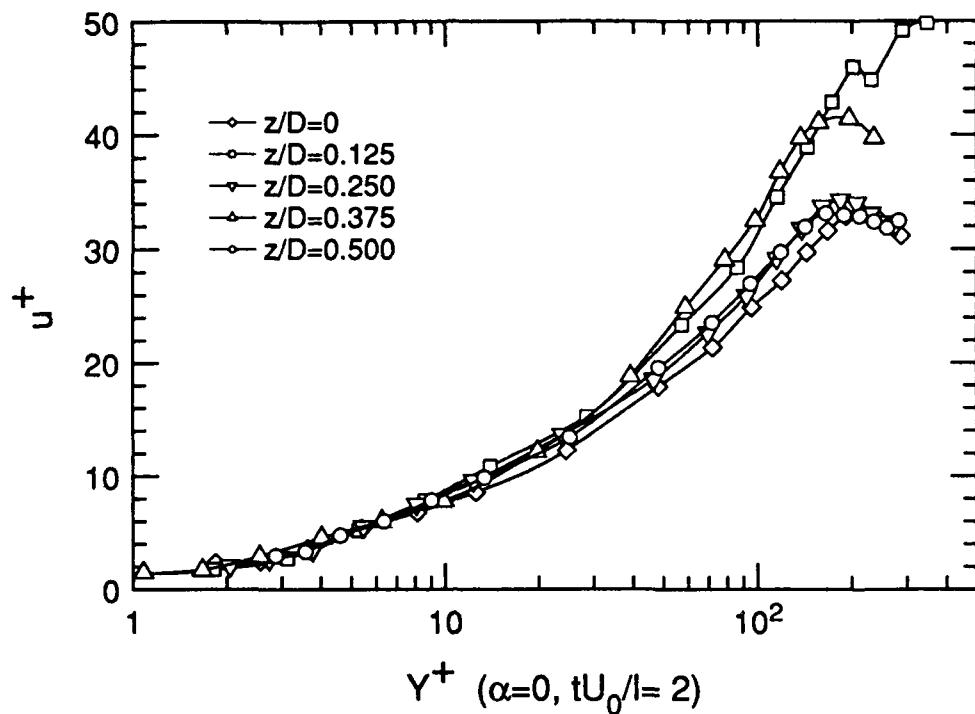
Figure 8.20a $\langle u \rangle$ profiles in wall coordinates for $\alpha = 0°$ at $tU_0/l = 2$
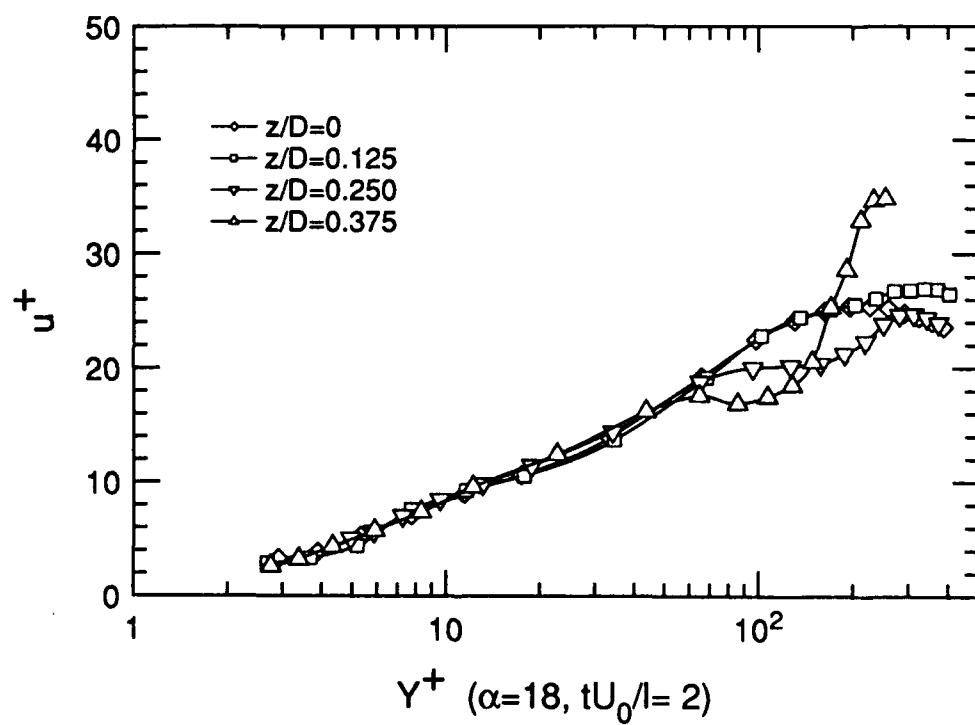
Figure 8.20b $\langle u \rangle$ profiles in wall coordinates for $\alpha = 18°$ at $tU_0/l = 2$

185
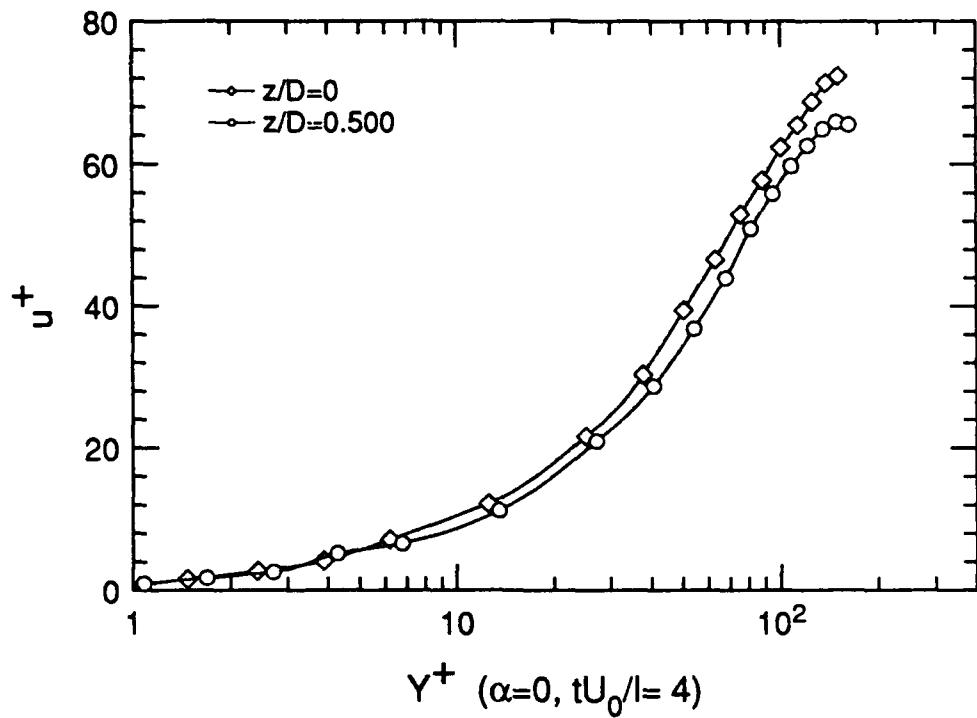
Figure 8.21a $\langle u \rangle$ profiles in wall coordinates for $\alpha = 0°$ at $tU_0/l = 4$
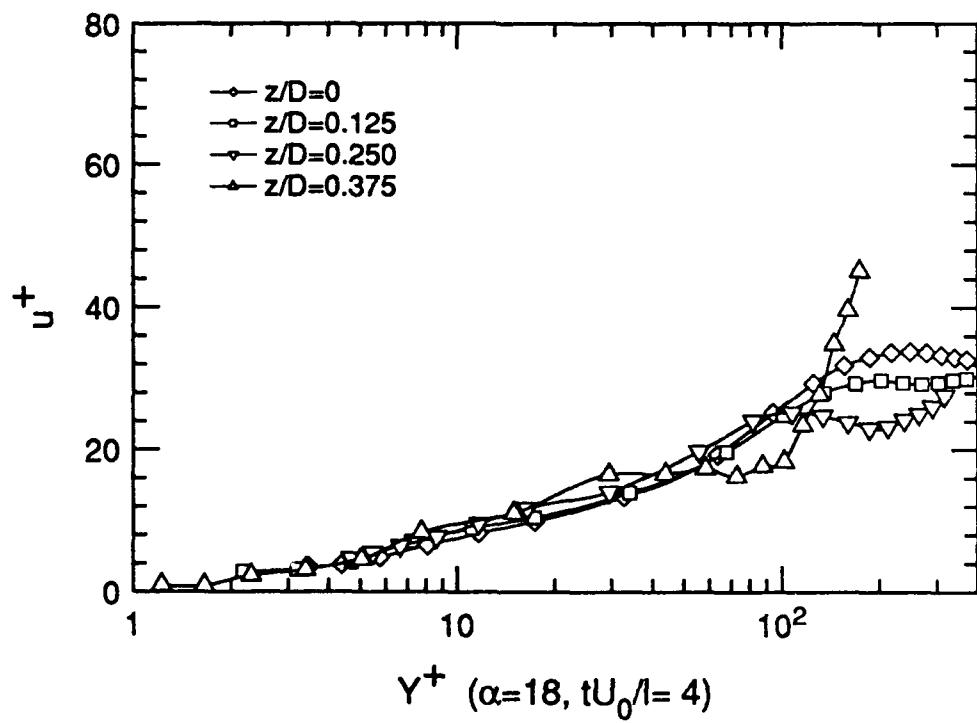
Figure 8.21b $\langle u \rangle$ profiles in wall coordinates for $\alpha = 18°$ at $tU_0/l = 4$

186
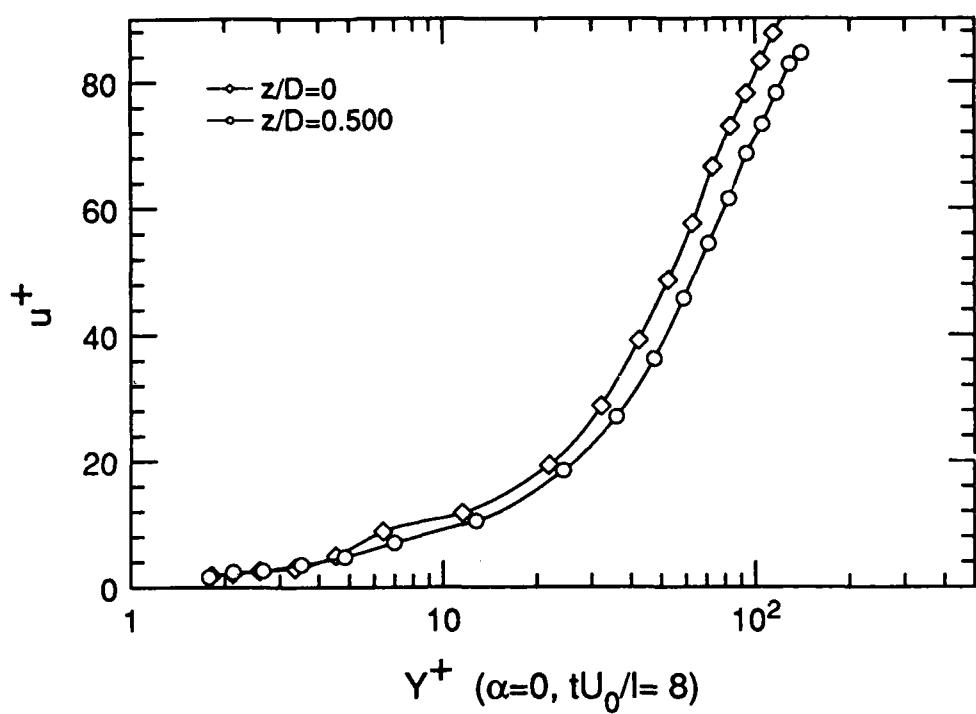
Figure 8.22a $\langle u \rangle$ profiles in wall coordinates for $\alpha = 0°$ at $tU_0/l = 8$
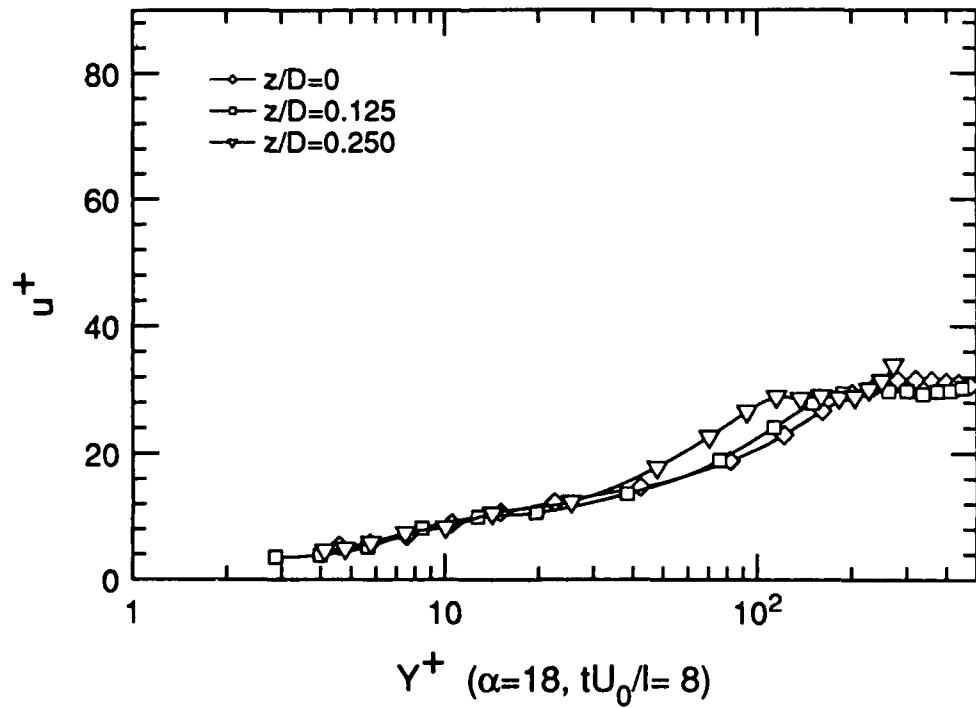
Figure 8.22b $\langle u \rangle$ profiles in wall coordinates for $\alpha = 18°$ at $tU_0/l = 8$

187
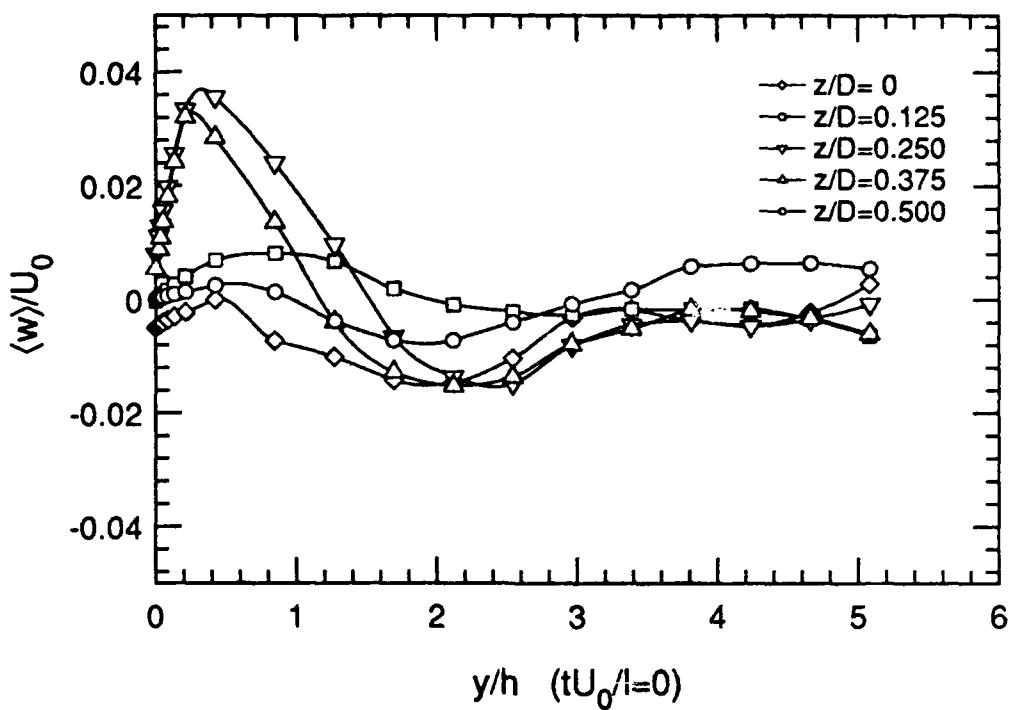
Figure 8.23a $\langle w \rangle$ profiles for $\alpha = 18°$ at $tU_0/l = 0$
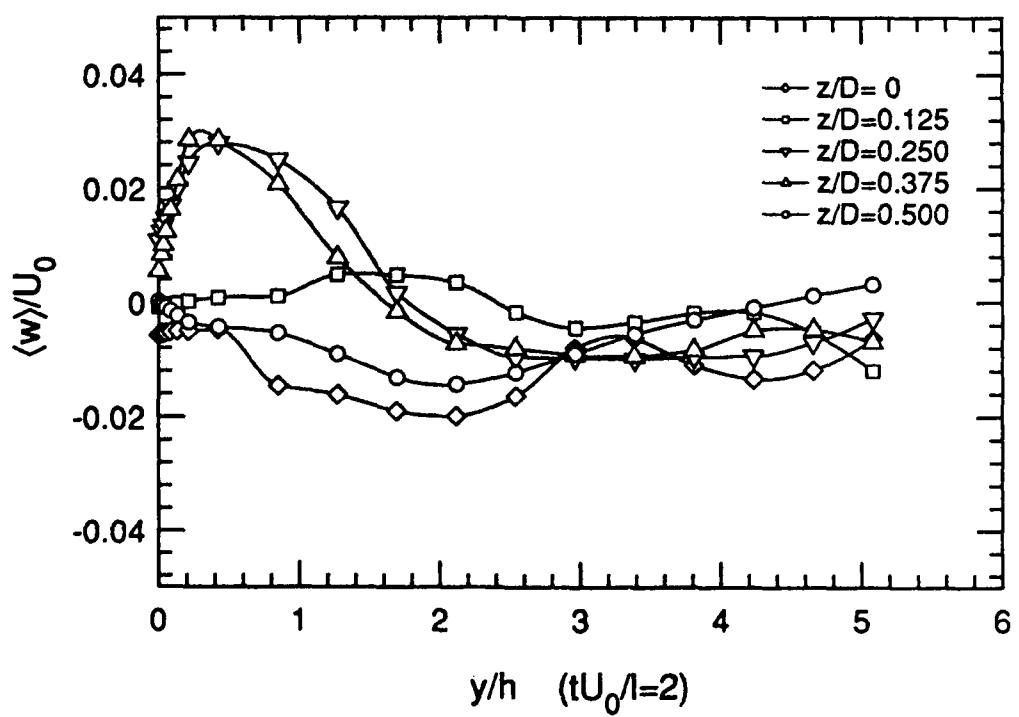
Figure 8.23b $\langle w \rangle$ profiles for $\alpha = 18°$ at $tU_0/l = 2$

188
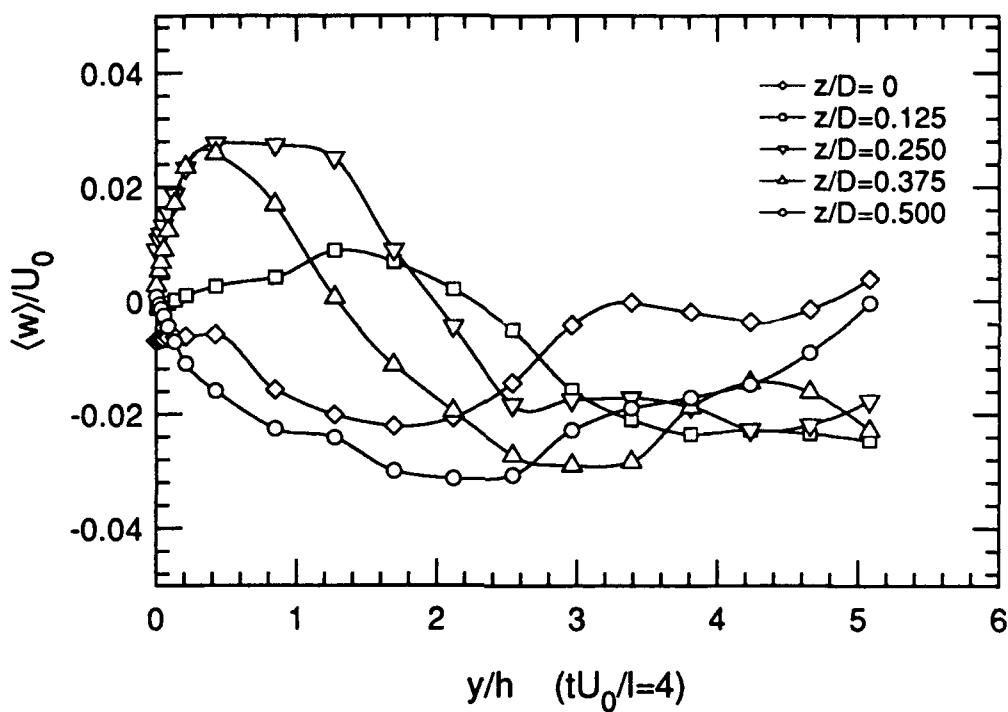
Figure 8.24a $\langle w \rangle$ profiles for $\alpha = 18°$ at $tU_0/l = 4$
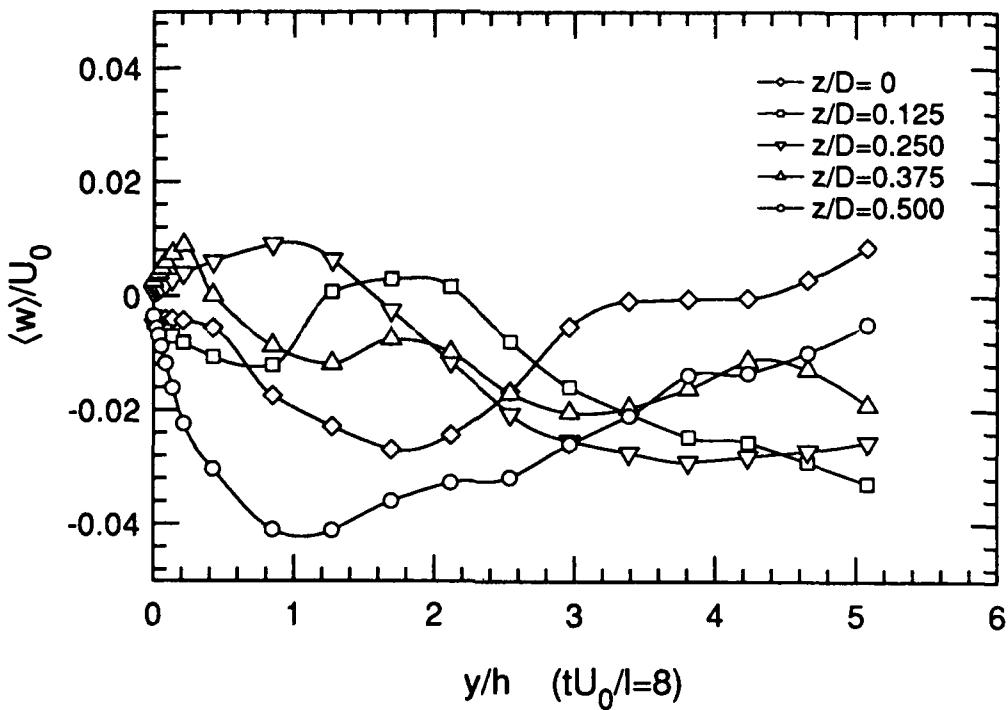
Figure 8.24b $\langle w \rangle$ profiles for $\alpha = 18°$ at $tU_0/l = 8$

189
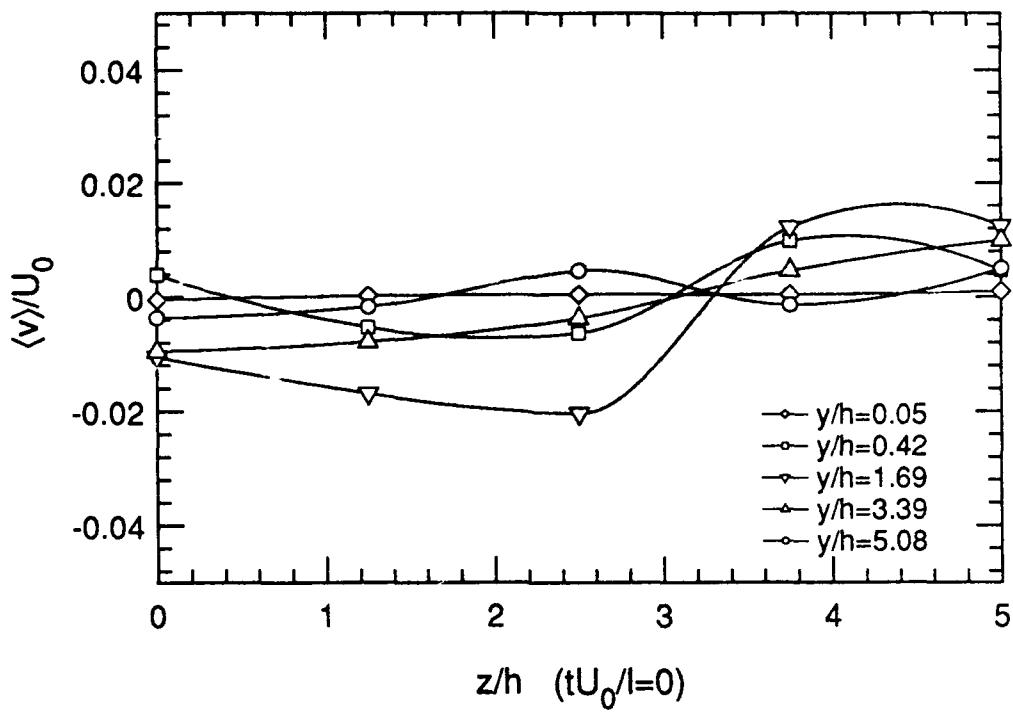
Figure 8.25a Spanwise profiles ot $\langle v \rangle$ for $\alpha = 18°$ at $tU_0/l = 0$
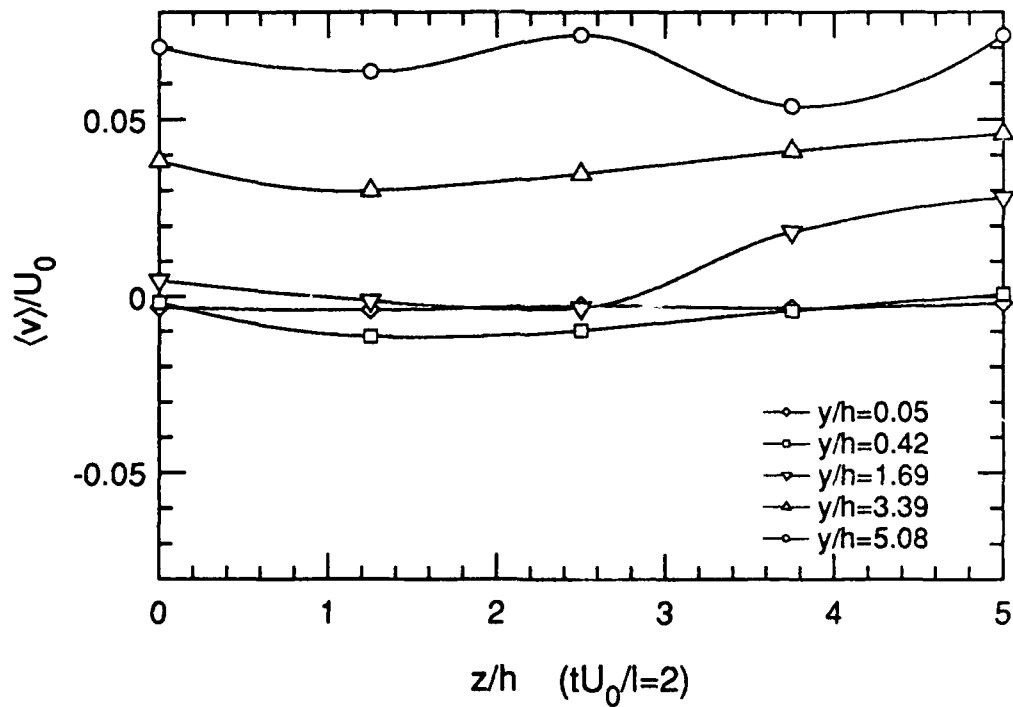
Figure 8.25b Spanwise profiles of $\langle v \rangle$ for $\alpha = 18°$ at $tU_0/l = 2$

190
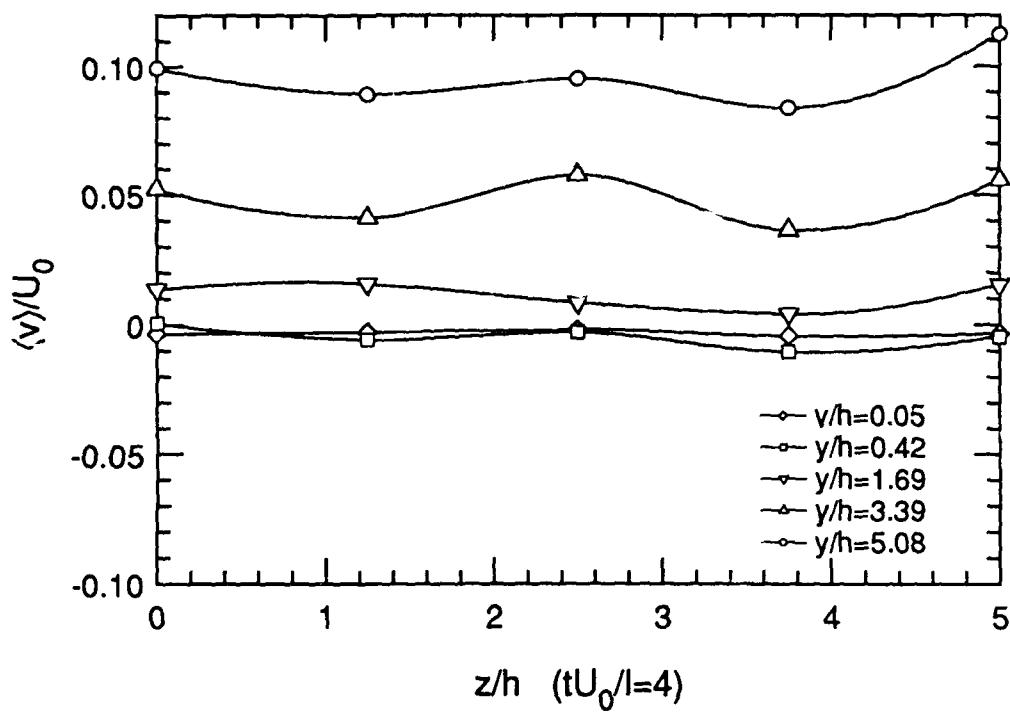
Figure 8.26a Spanwise profiles of $\langle v \rangle$ for $\alpha = 18°$ at $tU_0/l = 4$
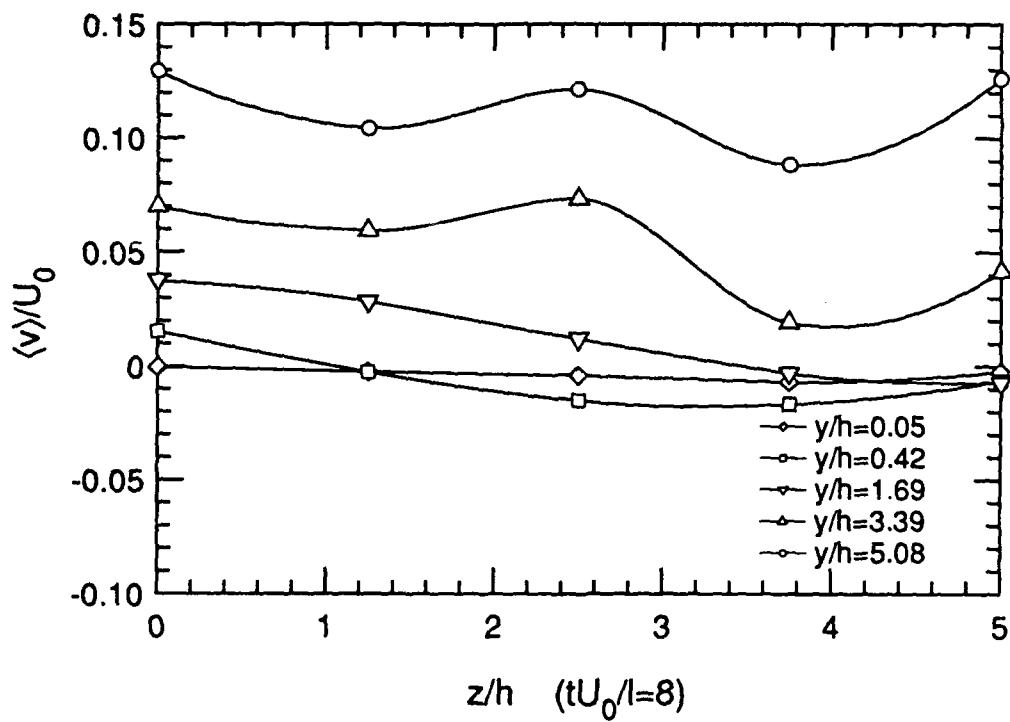
Figure 8.26b Spanwise profiles of $\langle v \rangle$ for $\alpha = 18°$ at $tU_0/l = 8$

191
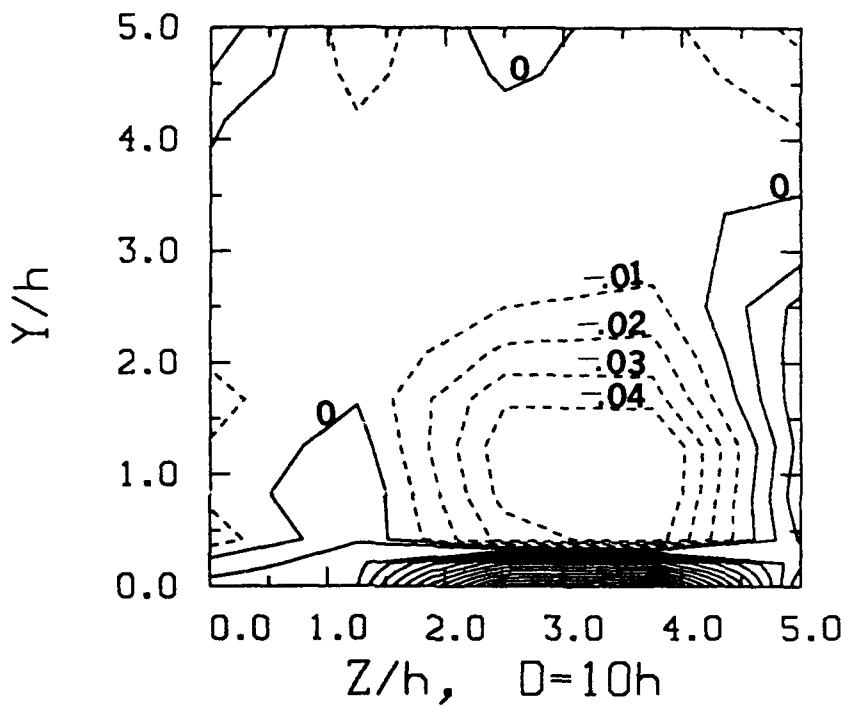
Figure 8.27a Streamwise vorticity, $\langle\omega_x\rangle h/U_0$, at $tU_0/l = 0$
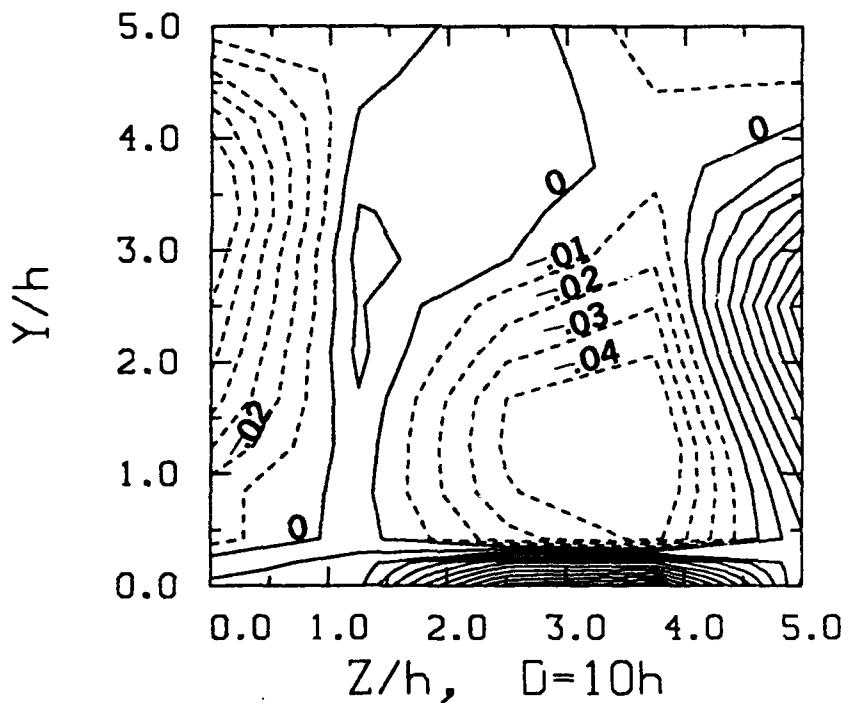
Figure 8.27b Streamwise vorticity, $\langle\omega_x\rangle h/U_0$, at $tU_0/l = 0.4$

192
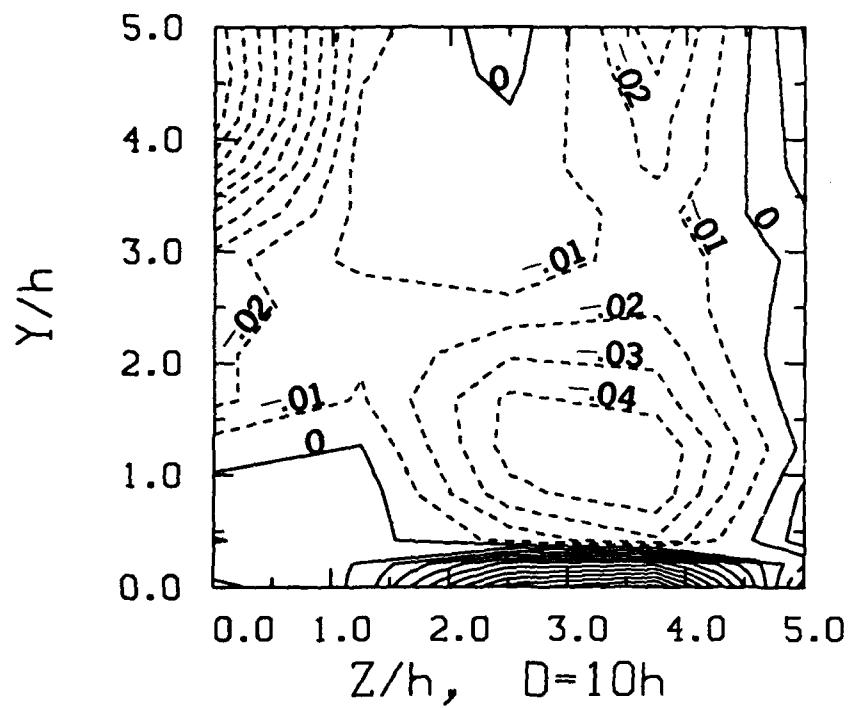
Figure 8.28a Streamwise vorticity, $\langle \omega_x \rangle h / U_0$, at $tU_0/l = 1.2$
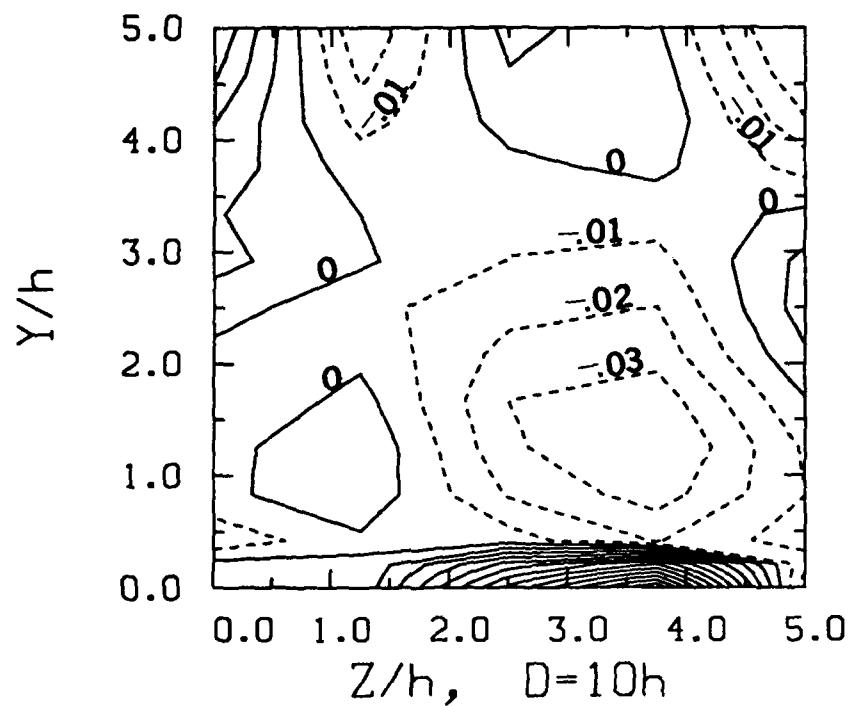
Figure 8.28b Streamwise vorticity, $\langle \omega_x \rangle h / U_0$, at $tU_0/l = 2$

193
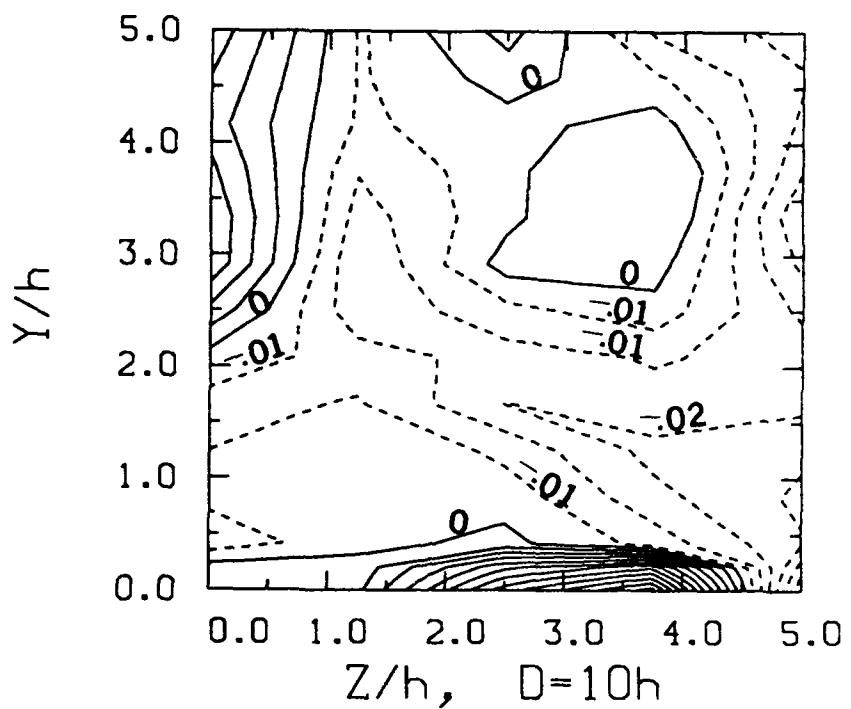
Figure 8.29a Streamwise vorticity, $\langle \omega_x \rangle h/U_0$, at $tU_0/l = 3$
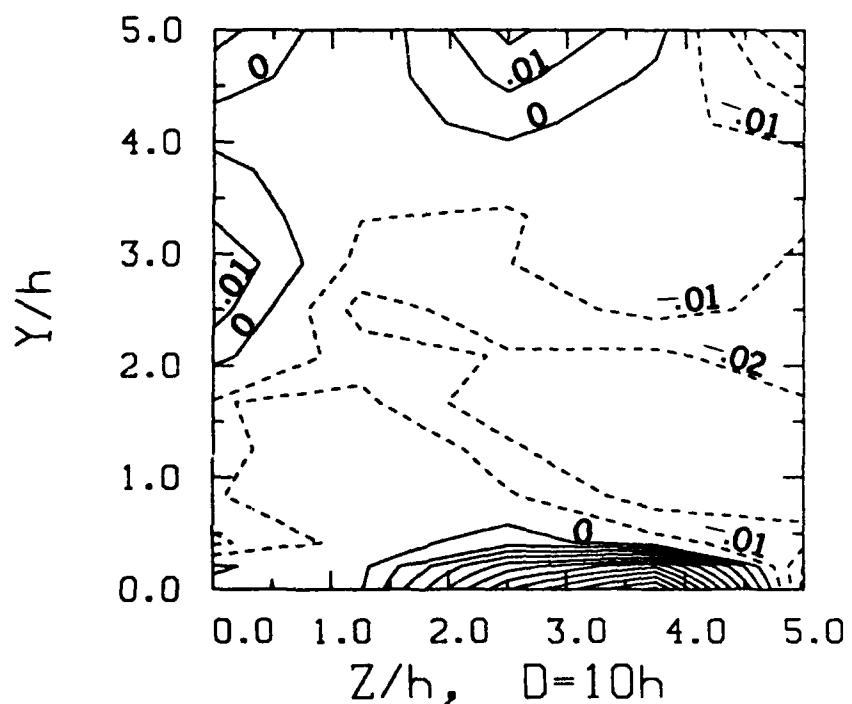
Figure 8.29b Streamwise vorticity, $\langle \omega_x \rangle h/U_0$, at $tU_0/l = 4$

194
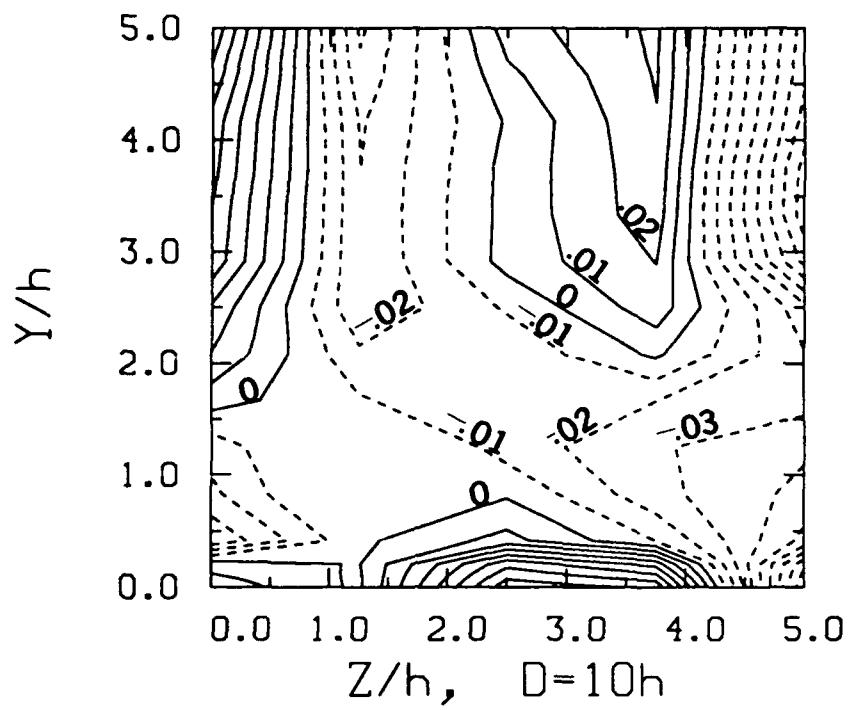
Figure 8.30a Streamwise vorticity, $\langle \omega_x \rangle h/U_0$, at $tU_0/l = 6$
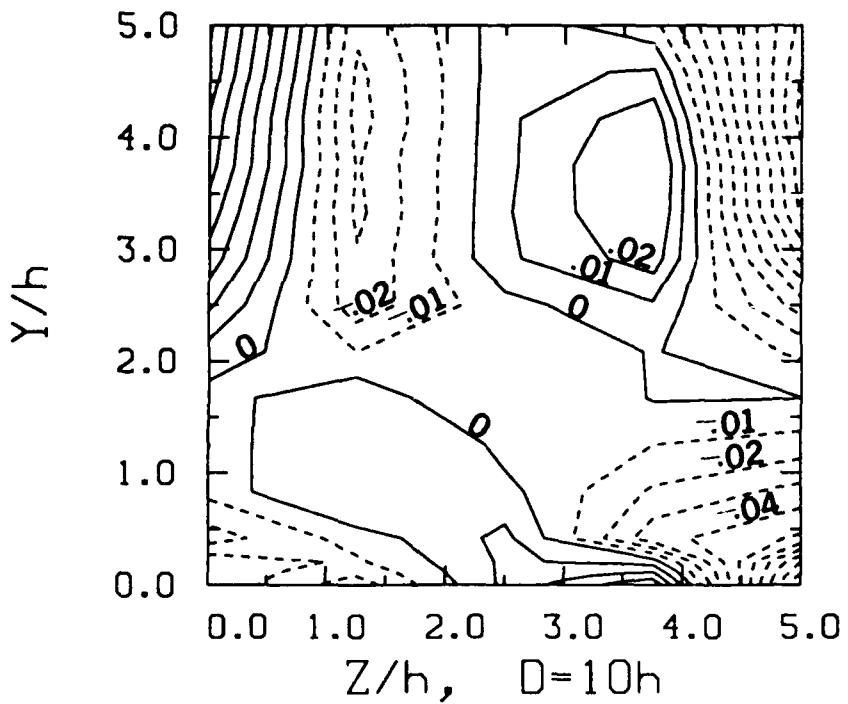
Figure 8.30b Streamwise vorticity, $\langle \omega_x \rangle h/U_0$, at $tU_0/l = 8$

195
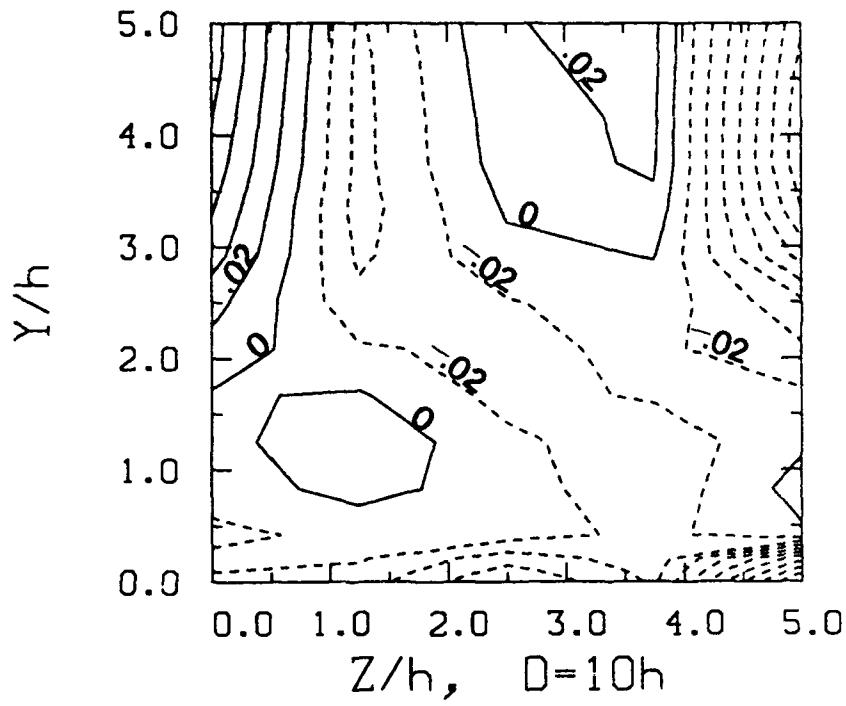
Figure 8.31a Streamwise vorticity, $\langle \omega_x \rangle h/U_0$, at $tU_0/l = 12$
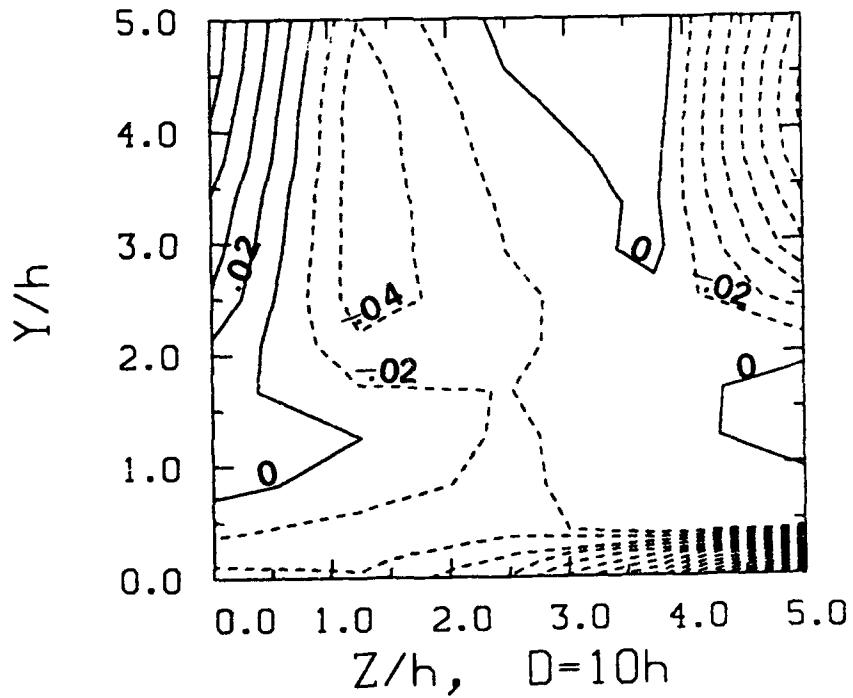
Figure 8.31b Streamwise vorticity, $\langle \omega_x \rangle h/U_0$, at $tU_0/l = 16$
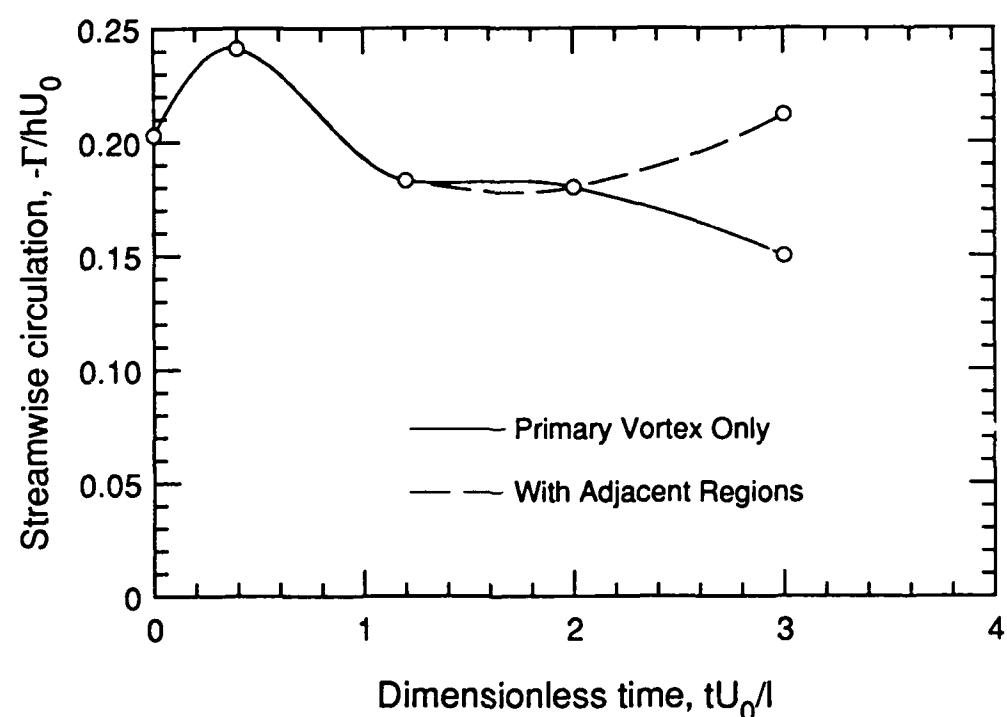
Figure 8.32 History of streamwise circulation
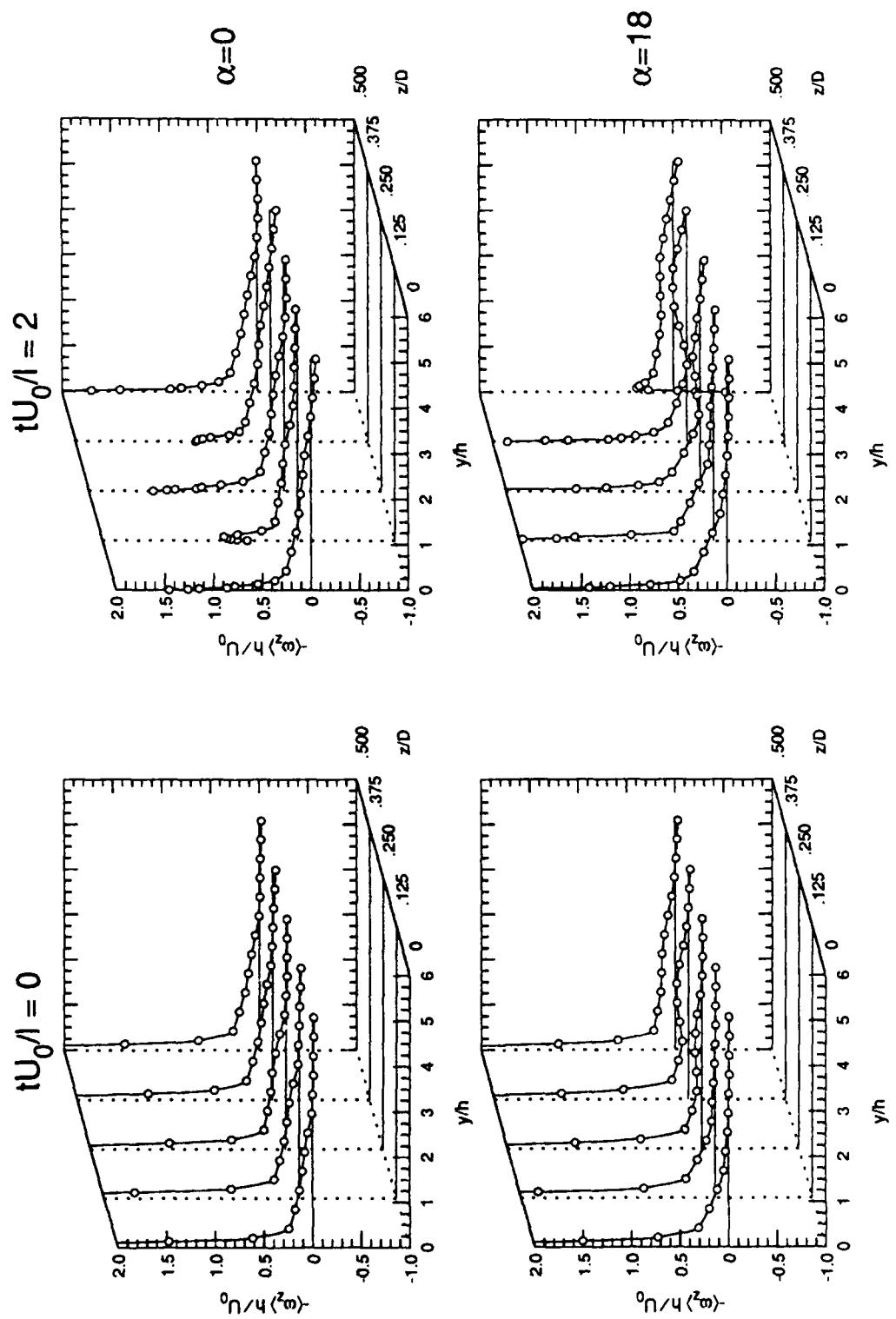
Figure 8.33 Spanwise vorticity, $\langle \omega_z \rangle$ at $tU_0/l = 0$ and $tU_0/l = 2$

198
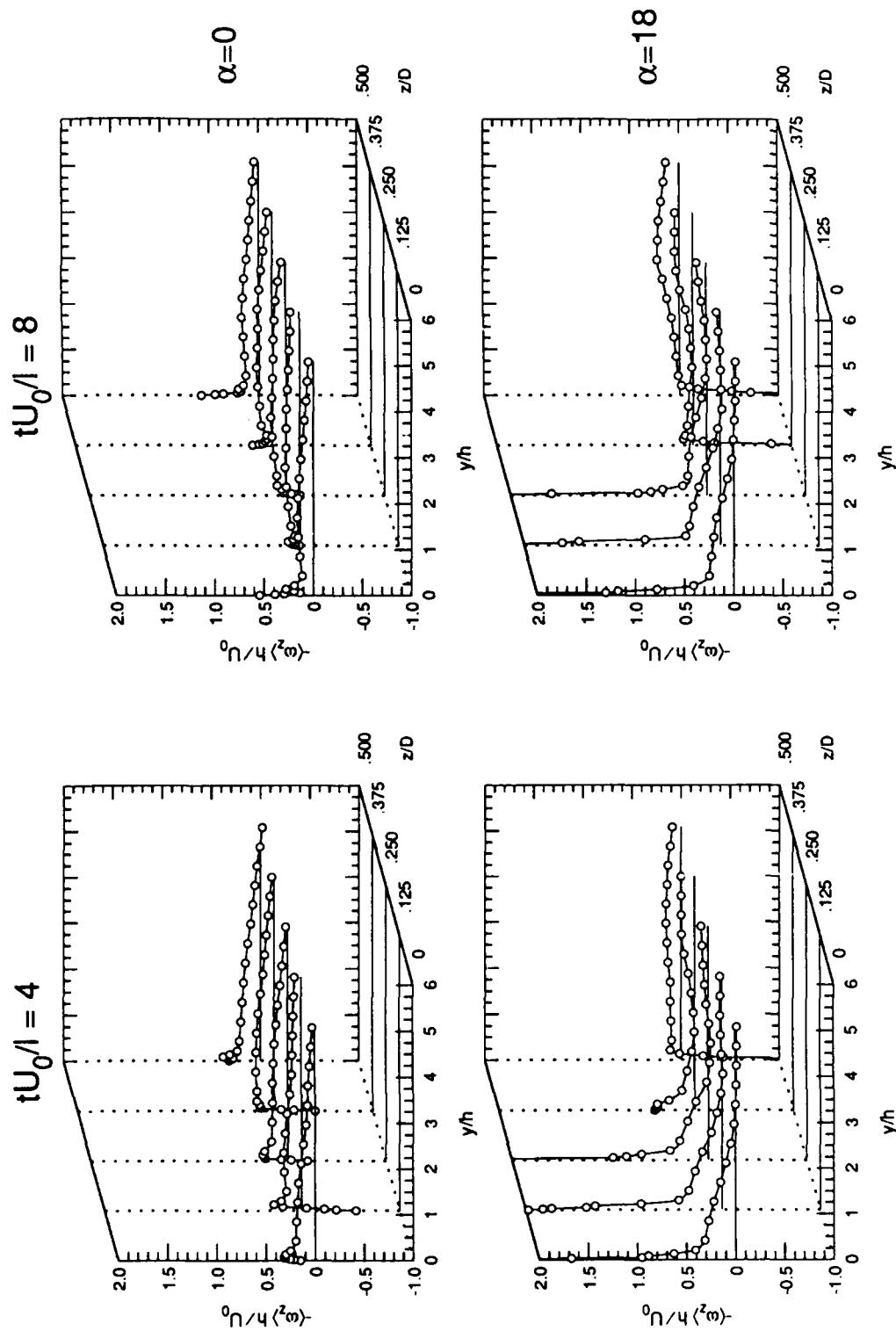
Figure 8.34 Spanwise vorticity, $\langle \omega_z \rangle$ at $tU_0/l = 4$ and $tU_0/l = 8$
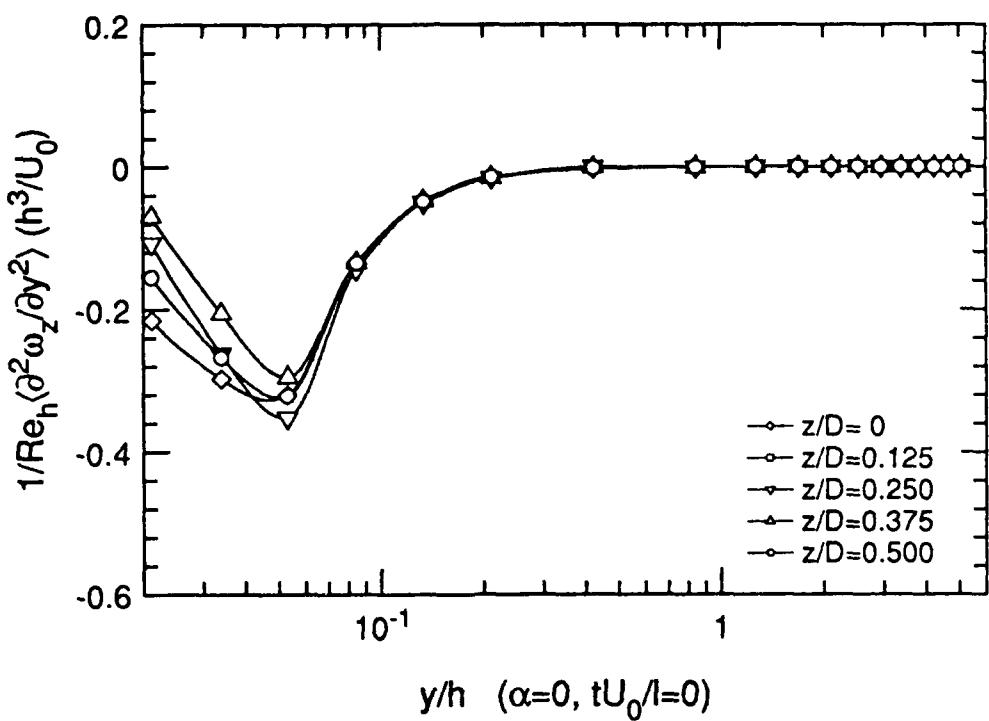
Figure 8.35a Diffusion of spanwise vorticity for $\alpha = 0°$ at $tU_0/l = 0$
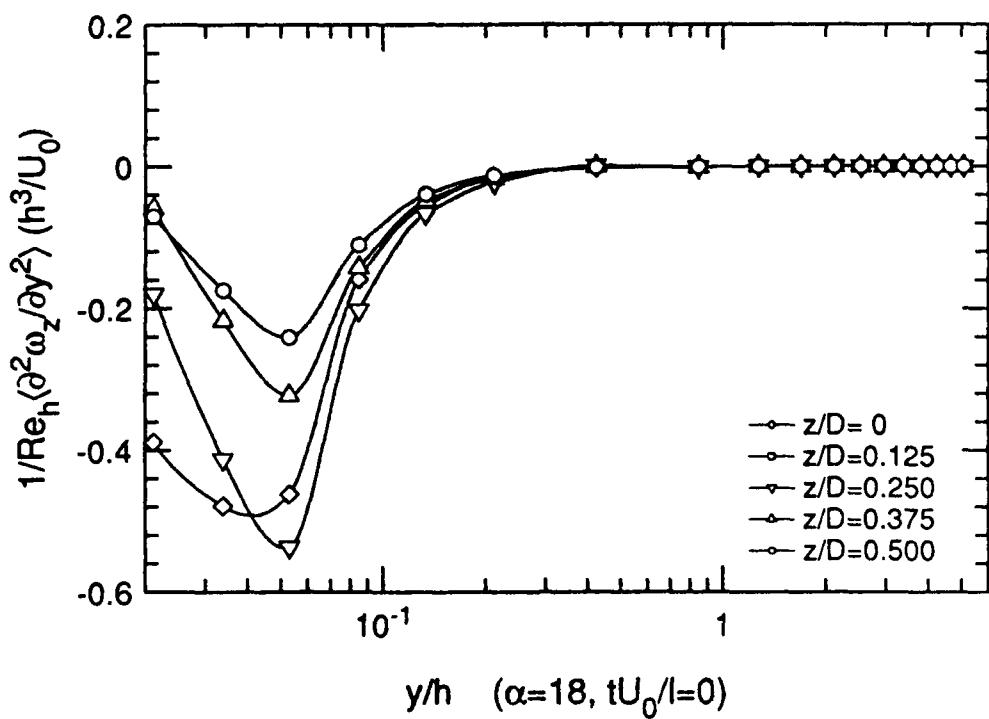
Figure 8.35b Diffusion of spanwise vorticity for $\alpha = 18°$ at $tU_0/l = 0$
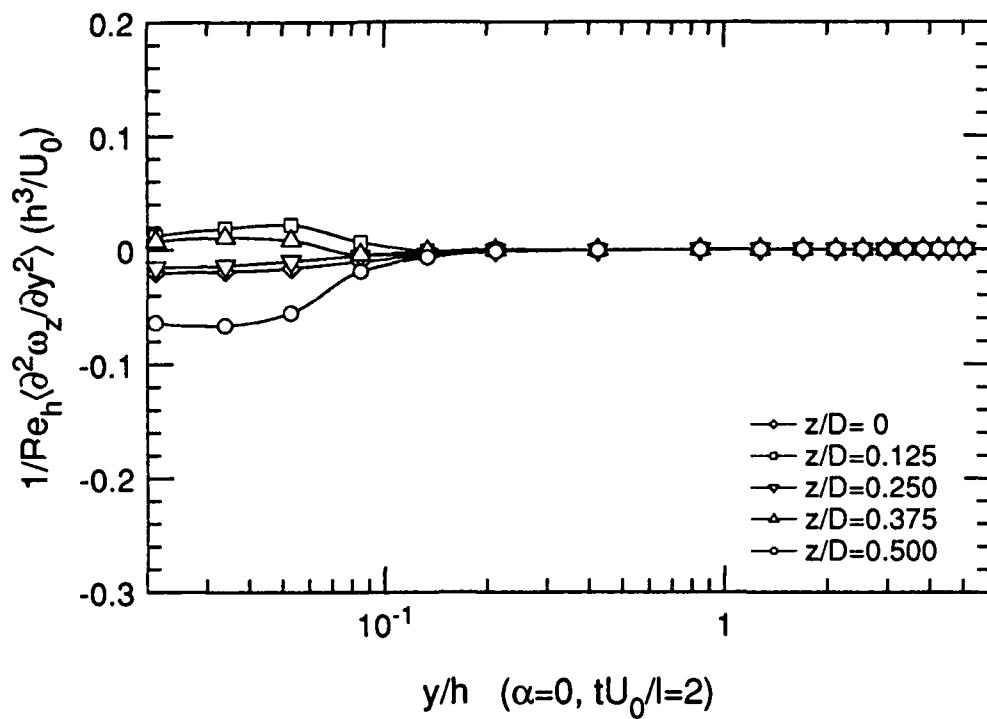
Figure 8.36a Diffusion of spanwise vorticity for $\alpha = 0°$ at $tU_0/l = 2$
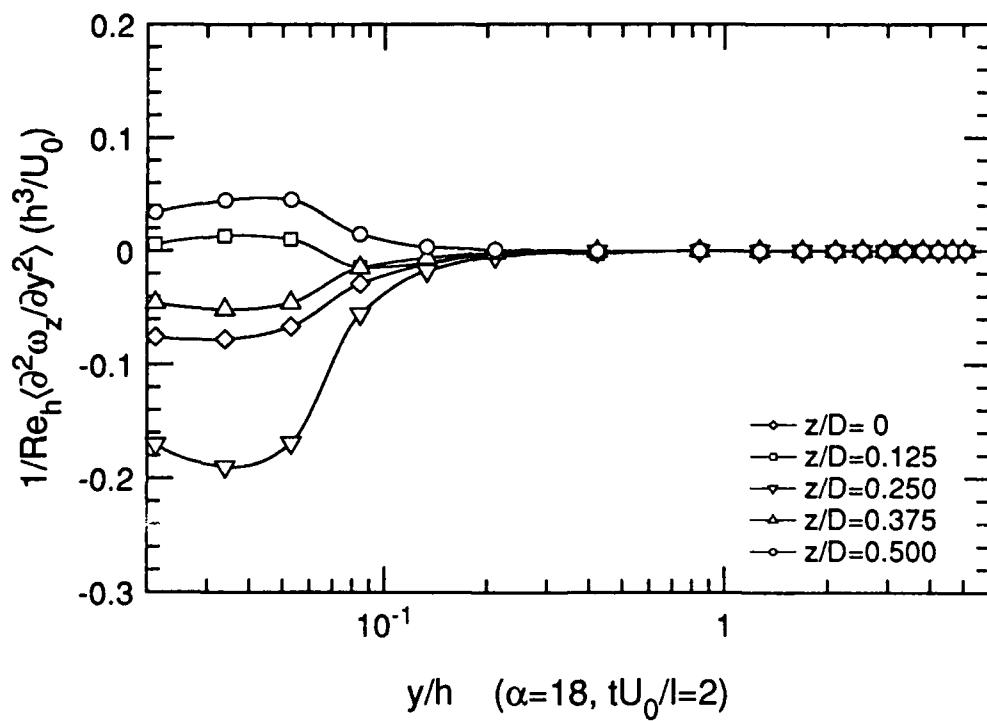
Figure 8.36b Diffusion of spanwise vorticity for $\alpha = 18°$ at $tU_0/l = 2$
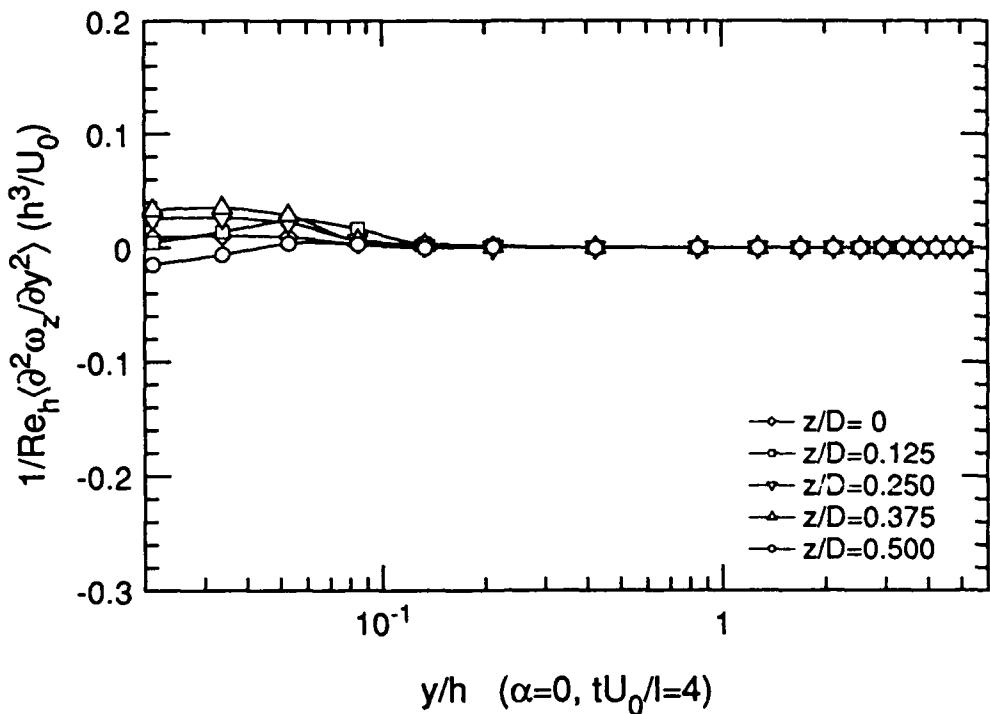
Figure 8.37a Diffusion of spanwise vorticity for $\alpha = 0°$ at $tU_0/l = 4$
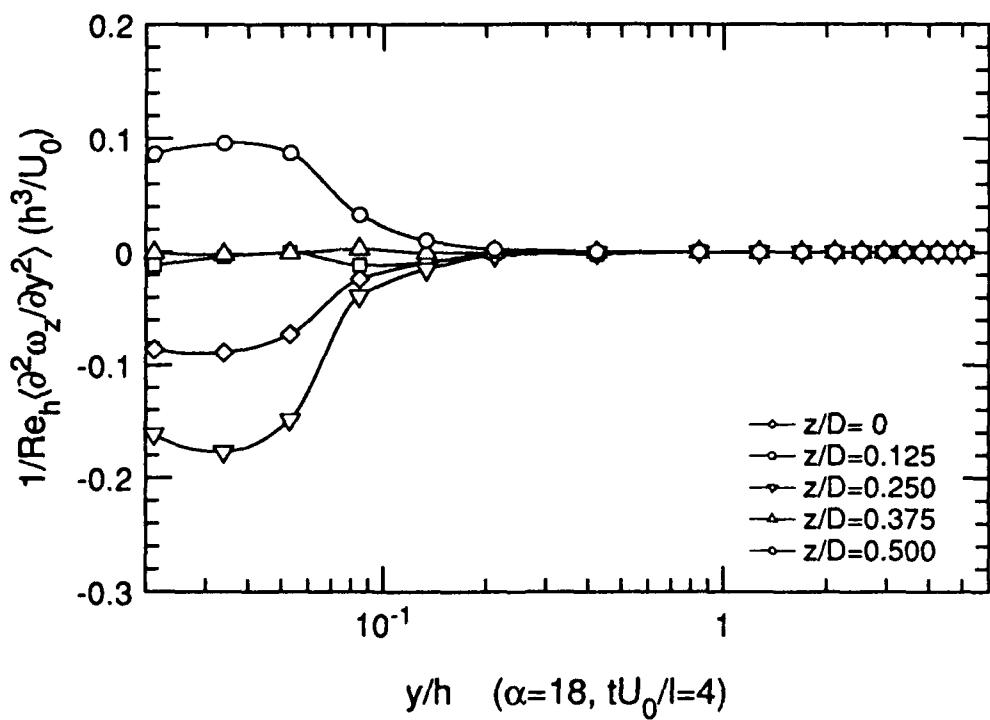
Figure 8.37b Diffusion of spanwise vorticity for $\alpha = 18°$ at $tU_0/l = 4$

202
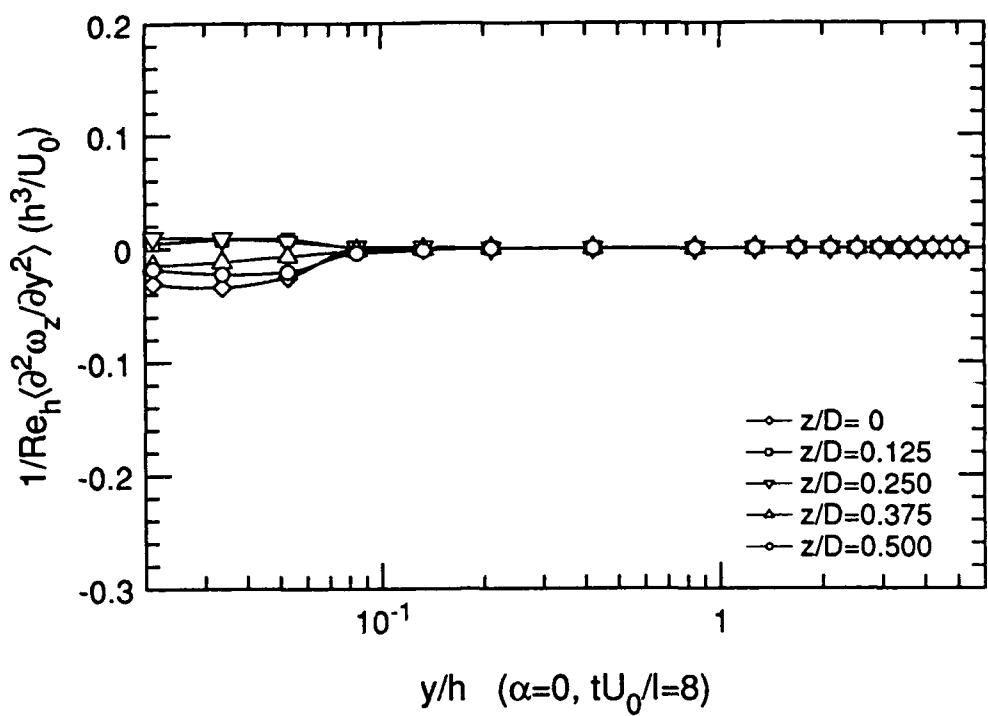
Figure 8.38a Diffusion of spanwise vorticity for $\alpha = 0°$ at $tU_0/l = 8$
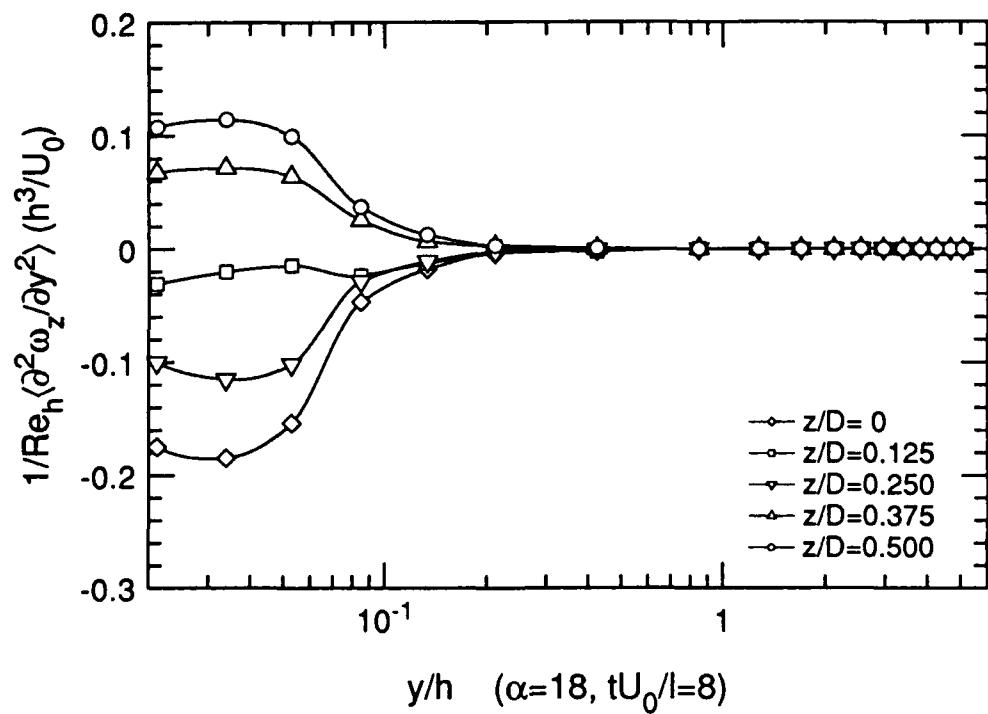
Figure 8.38b Diffusion of spanwise vorticity for $\alpha = 18°$ at $tU_0/l = 8$
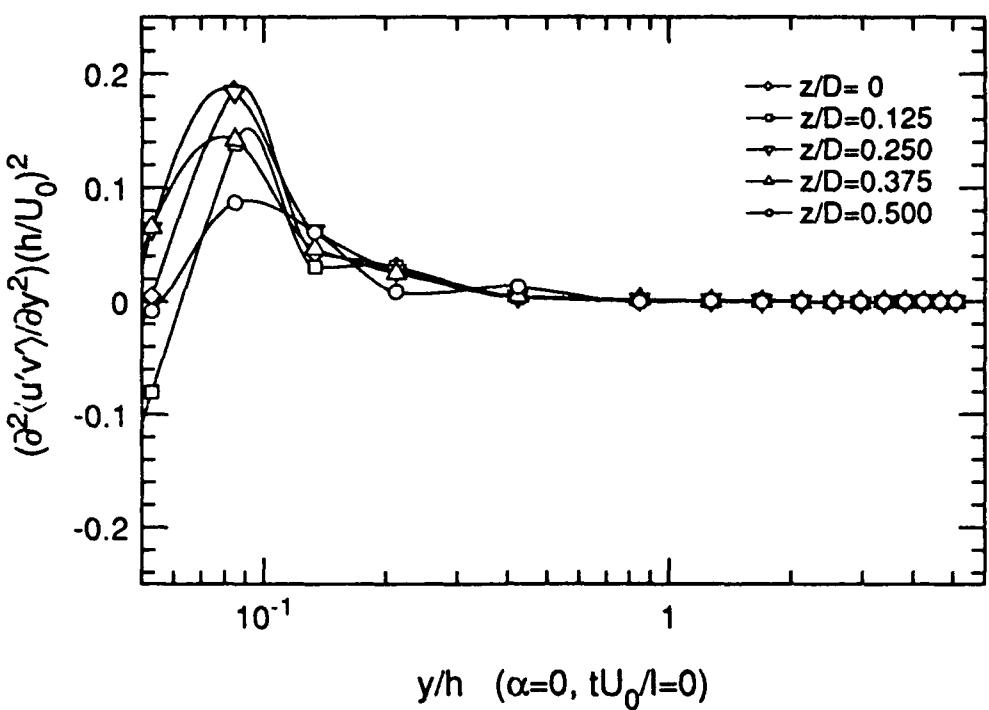
Figure 8.39a Turbulent transport of spanwise vorticity for $\alpha = 0°$ at $tU_0/l = 0$
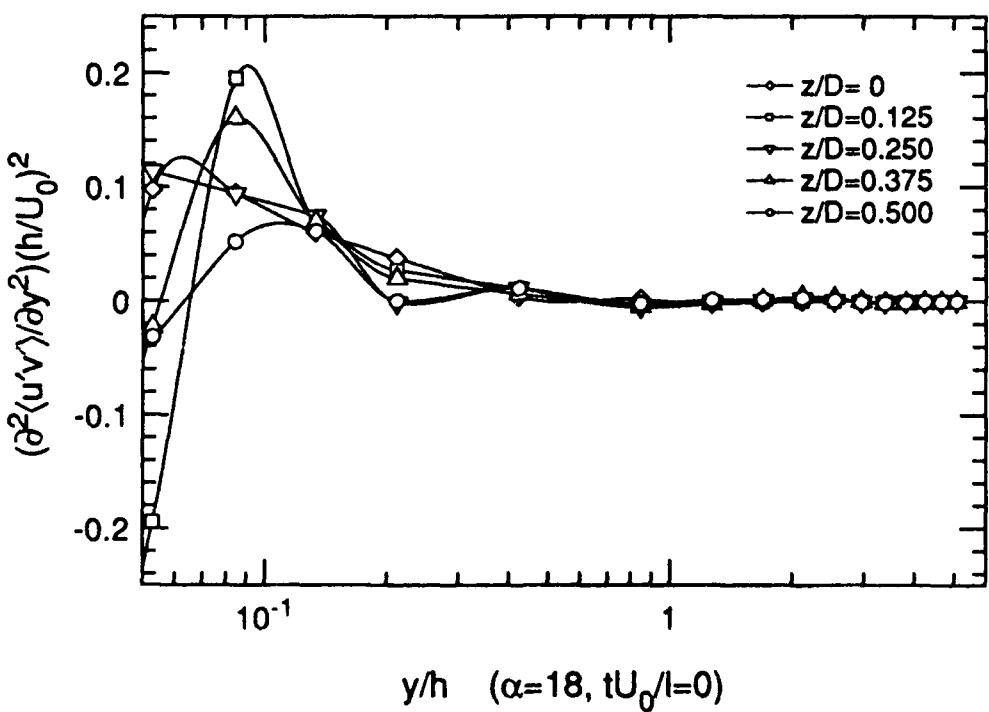
Figure 8.39b Turbulent transport of spanwise vorticity for $\alpha = 18°$ at $tU_0/l = 0$
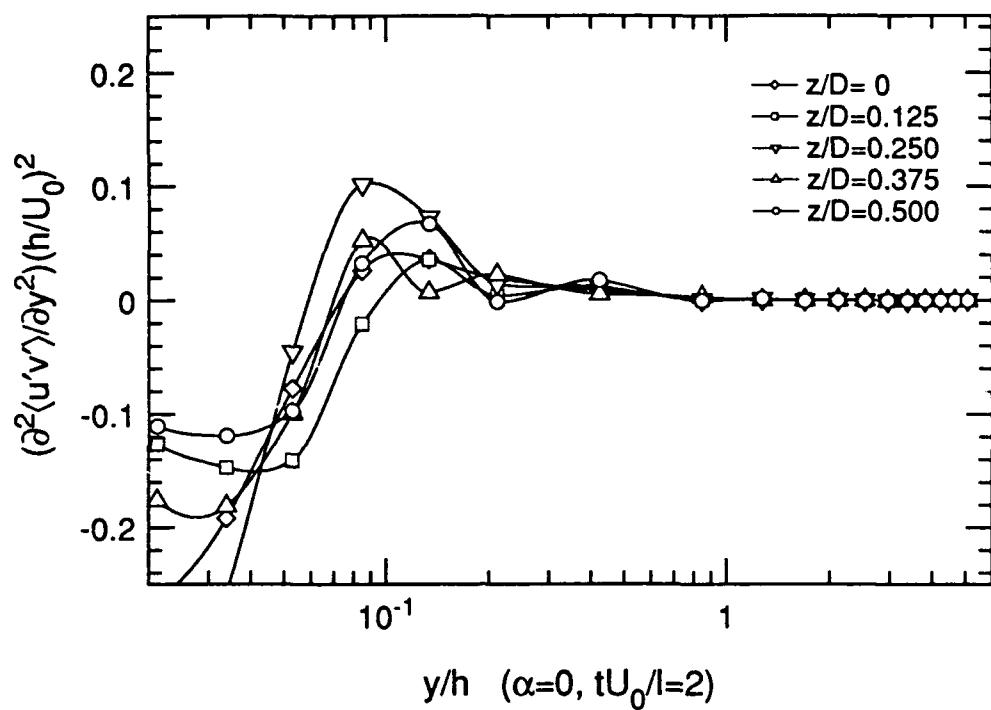
Figure 8.40a Turbulent transport of spanwise vorticity for $\alpha = 0°$ at $tU_0/l = 2$
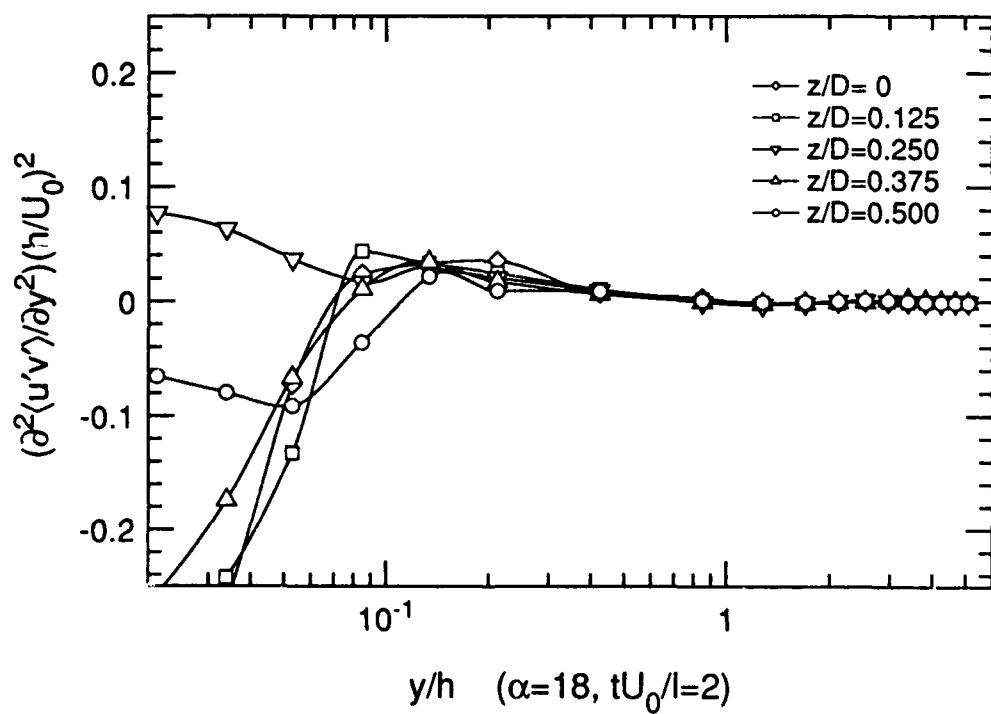
Figure 8.40b Turbulent transport of spanwise vorticity for $\alpha = 18°$ at $tU_0/l = 2$
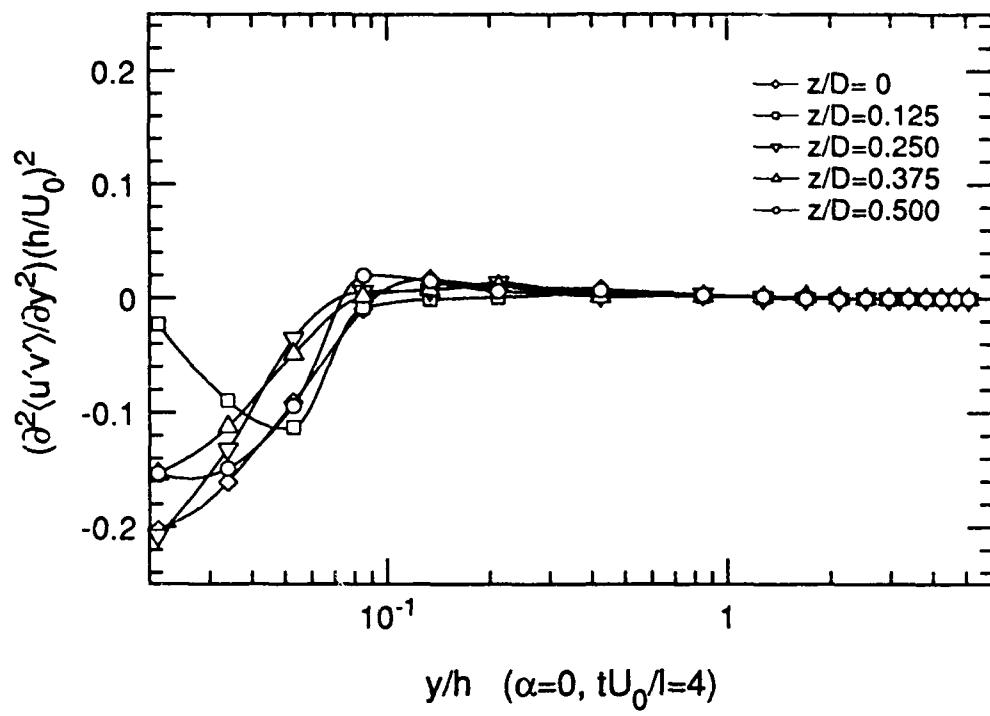
Figure 8.41a Turbulent transport of spanwise vorticity for $\alpha = 0°$ at $tU_0/l = 4$
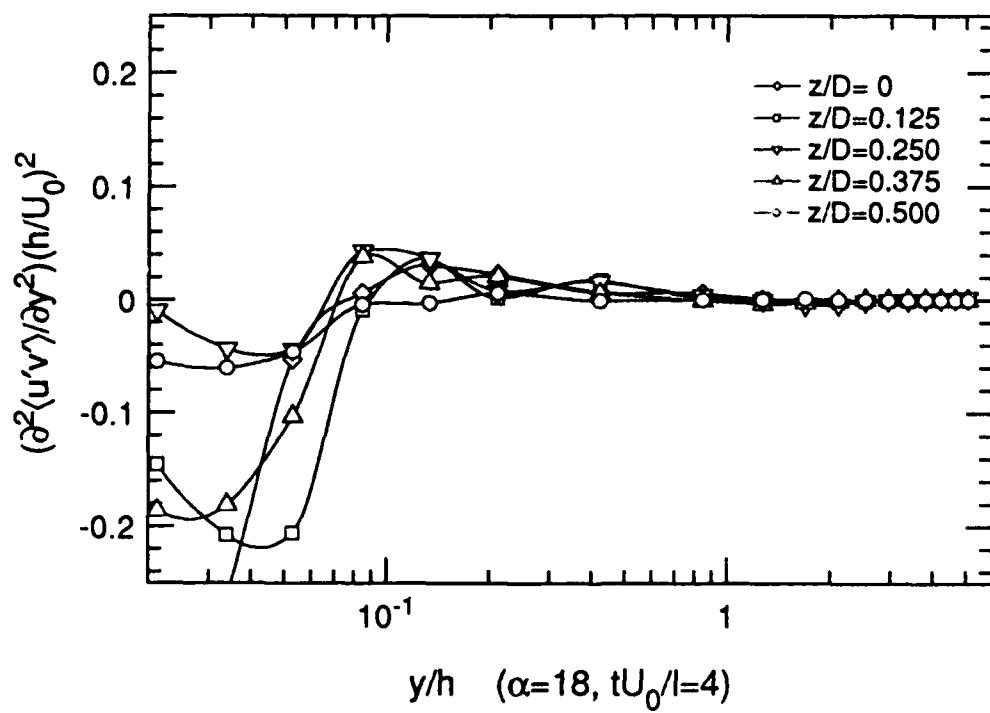
Figure 8.41b Turbulent transport of spanwise vorticity for $\alpha = 18°$ at $tU_0/l = 4$
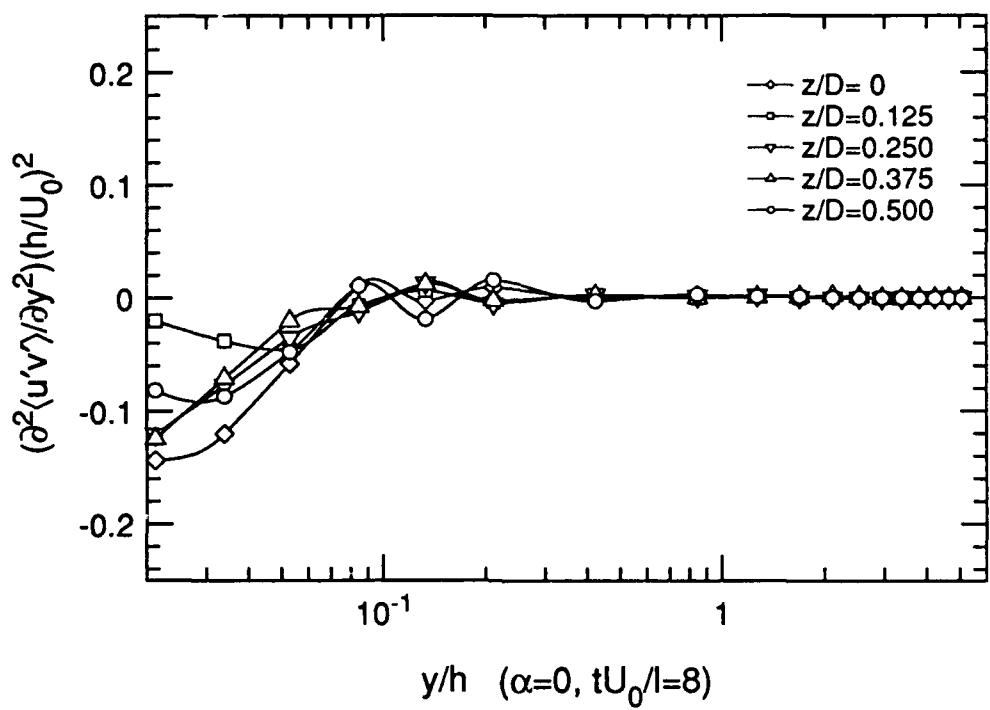
Figure 8.42a Turbulent transport of spanwise vorticity for $\alpha = 0°$ at $tU_0/l = 8$
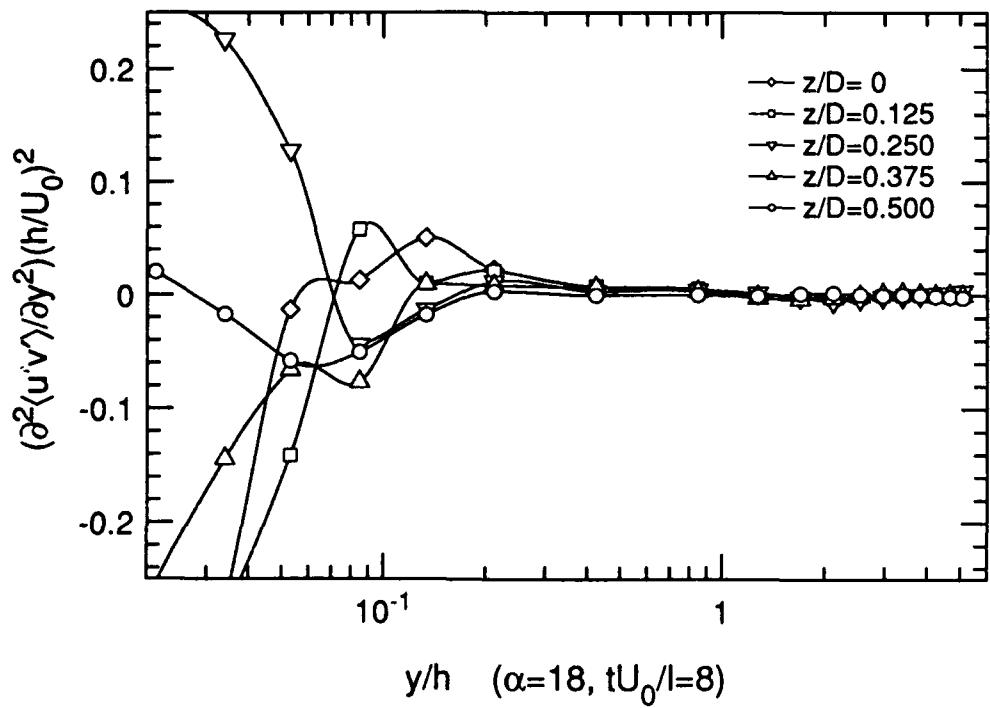
Figure 8.42b Turbulent transport of spanwise vorticity for $\alpha = 18°$ at $tU_0/l = 8$
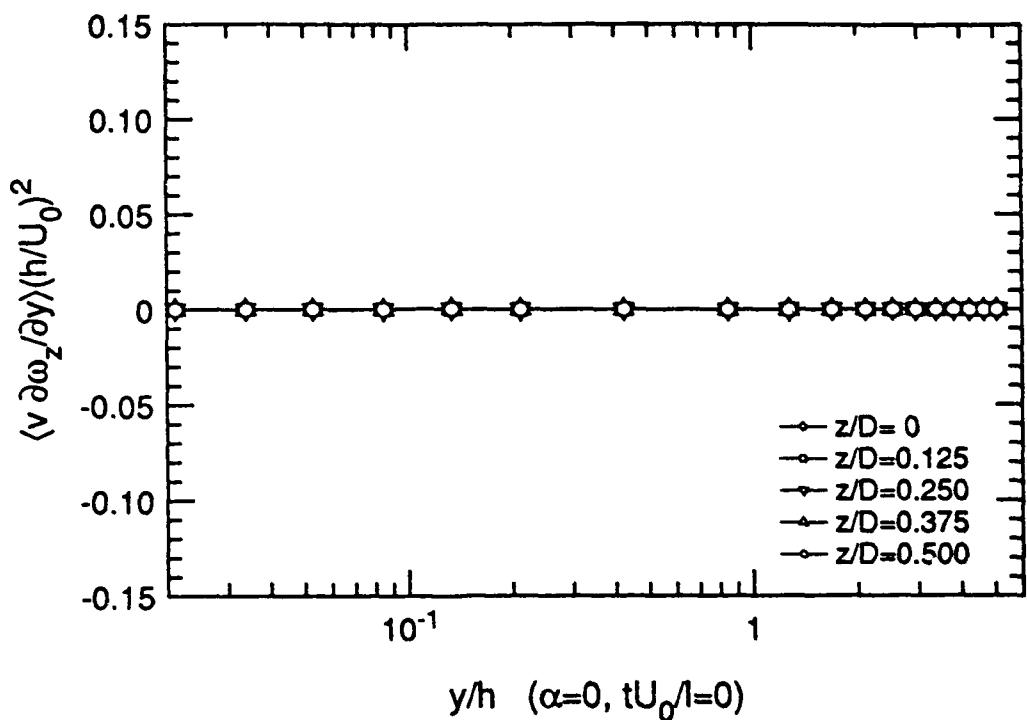
Figure 8.43a Convection of spanwise vorticity by $\langle v \rangle$ for $\alpha = 0°$ at $tU_0/l = 0$
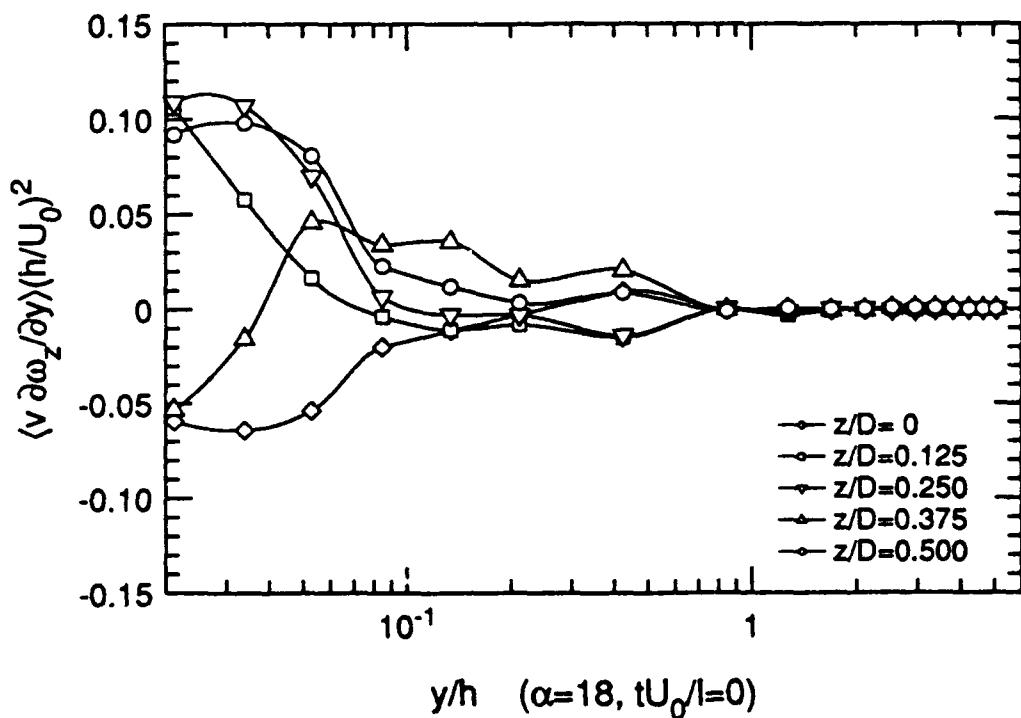
Figure 8.43b Convection of spanwise vorticity by $\langle v \rangle$ for $\alpha = 18°$ at $tU_0/l = 0$
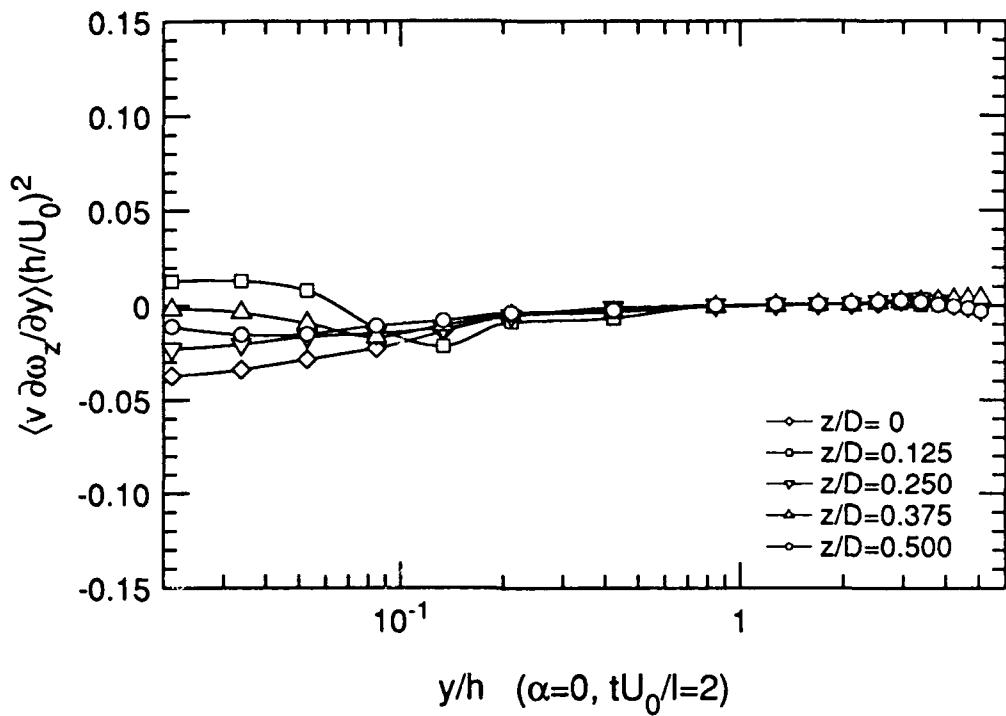
Figure 8.44a Convection of spanwise vorticity by $\langle v \rangle$ for $\alpha = 0°$ at $tU_0/l = 2$
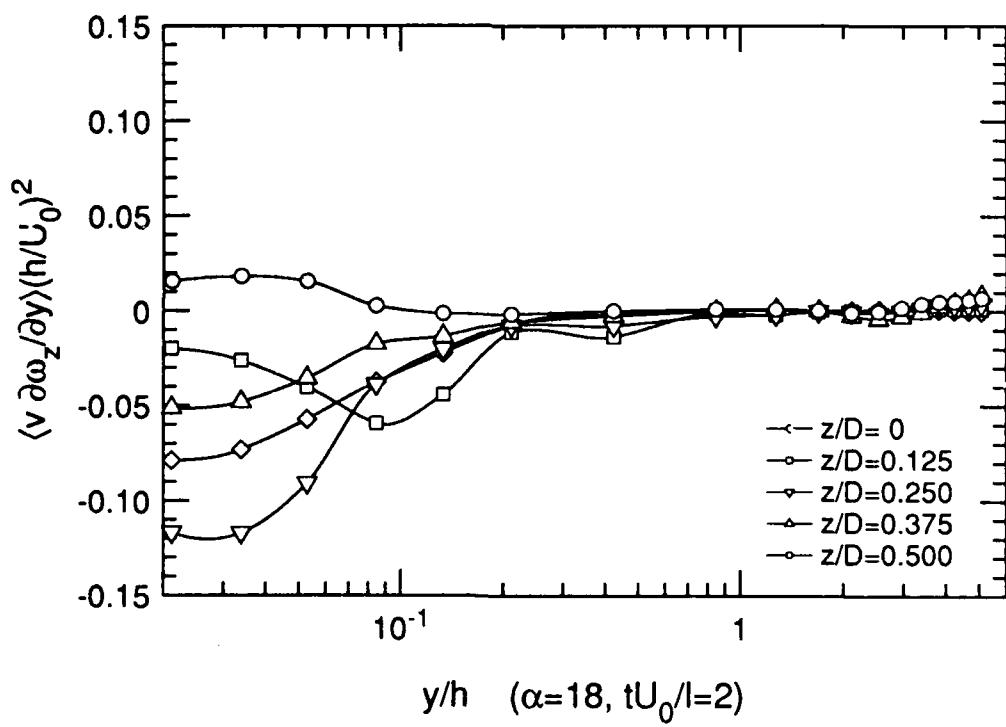
Figure 8.44b Convection of spanwise vorticity by $\langle v \rangle$ for $\alpha = 18°$ at $tU_0/l = 2$

209
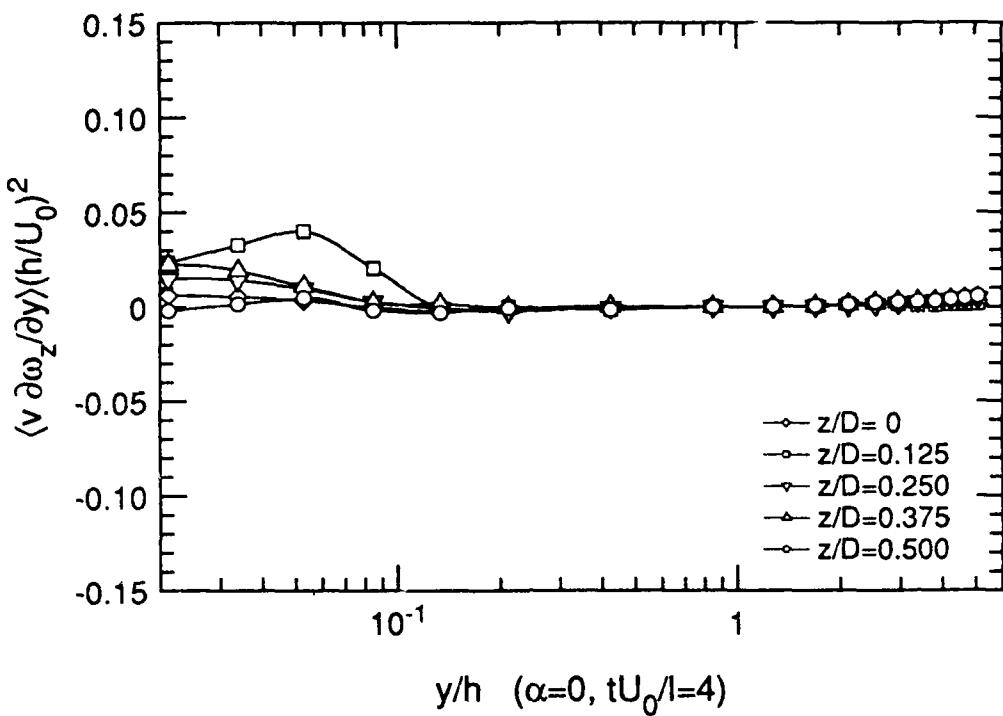
Figure 8.45a Convection of spanwise vorticity by $\langle v \rangle$ for $\alpha = 0°$ at $tU_0/l = 4$
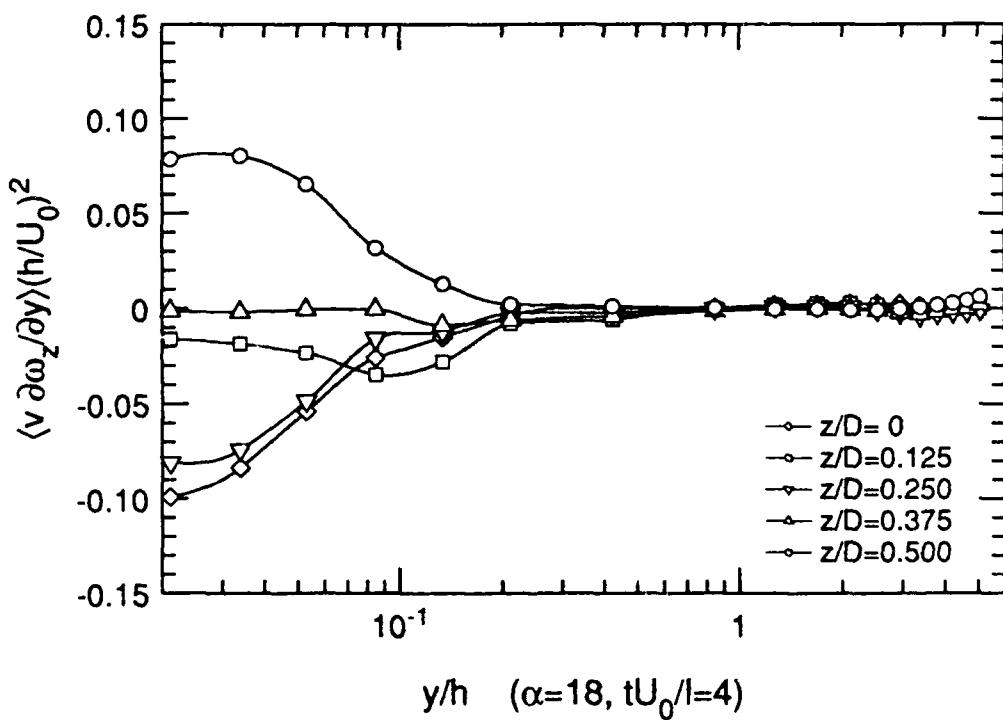
Figure 8.45b Convection of spanwise vorticity by $\langle v \rangle$ for $\alpha = 18°$ at $tU_0/l = 4$
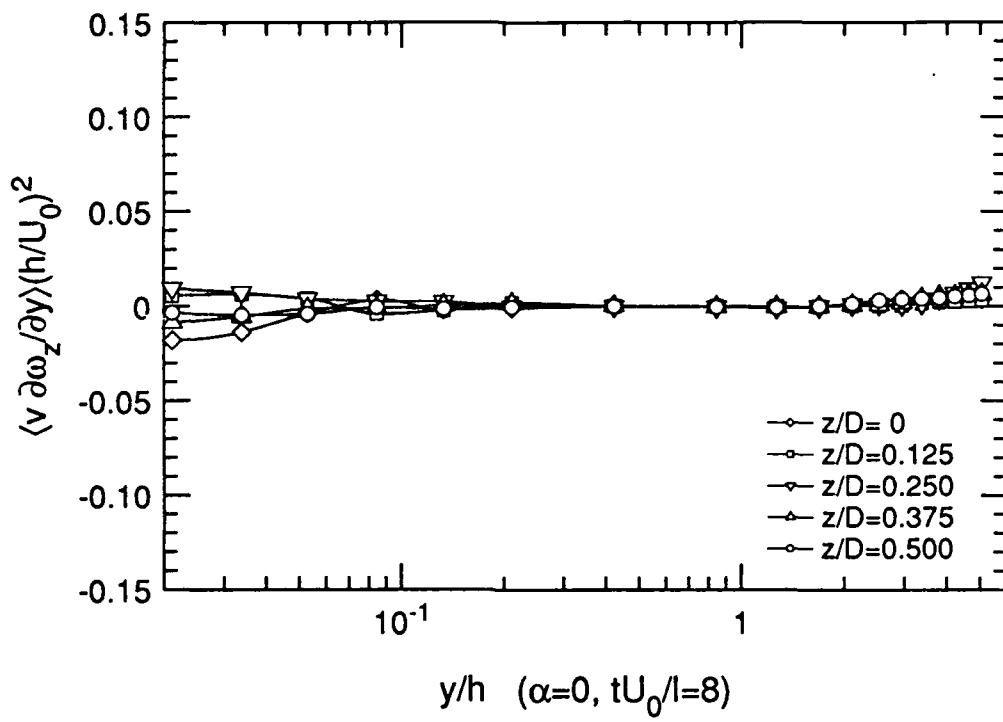
Figure 8.46a Convection of spanwise vorticity by $\langle v \rangle$ for $\alpha = 0°$ at $tU_0/l = 8$
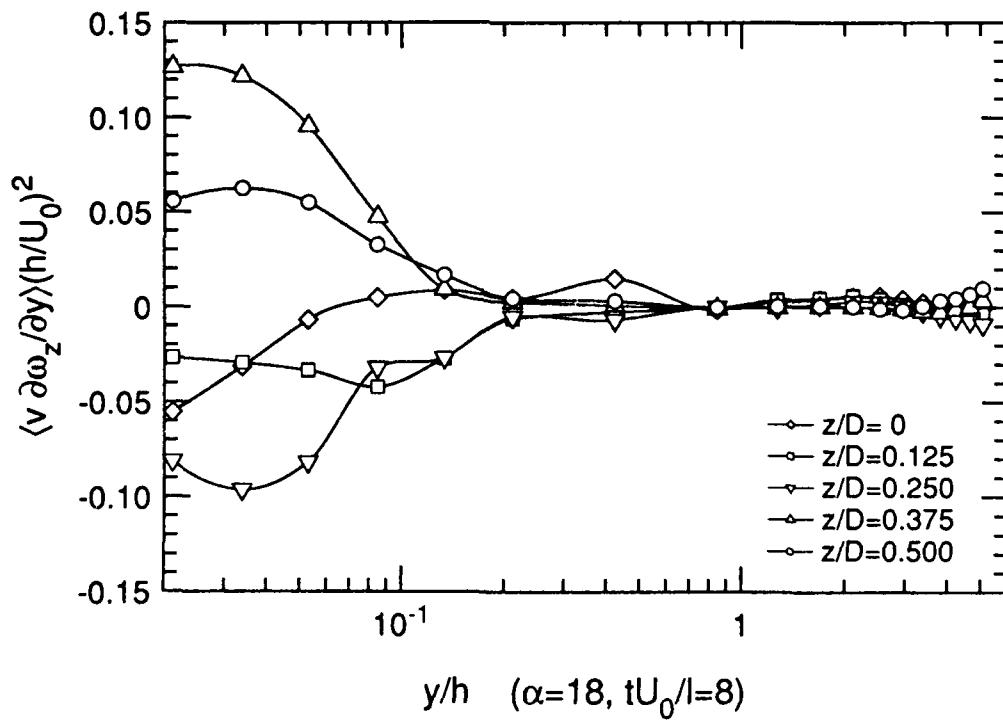
Figure 8.46b Convection of spanwise vorticity by $\langle v \rangle$ for $\alpha = 18°$ at $tU_0/l = 8$

211
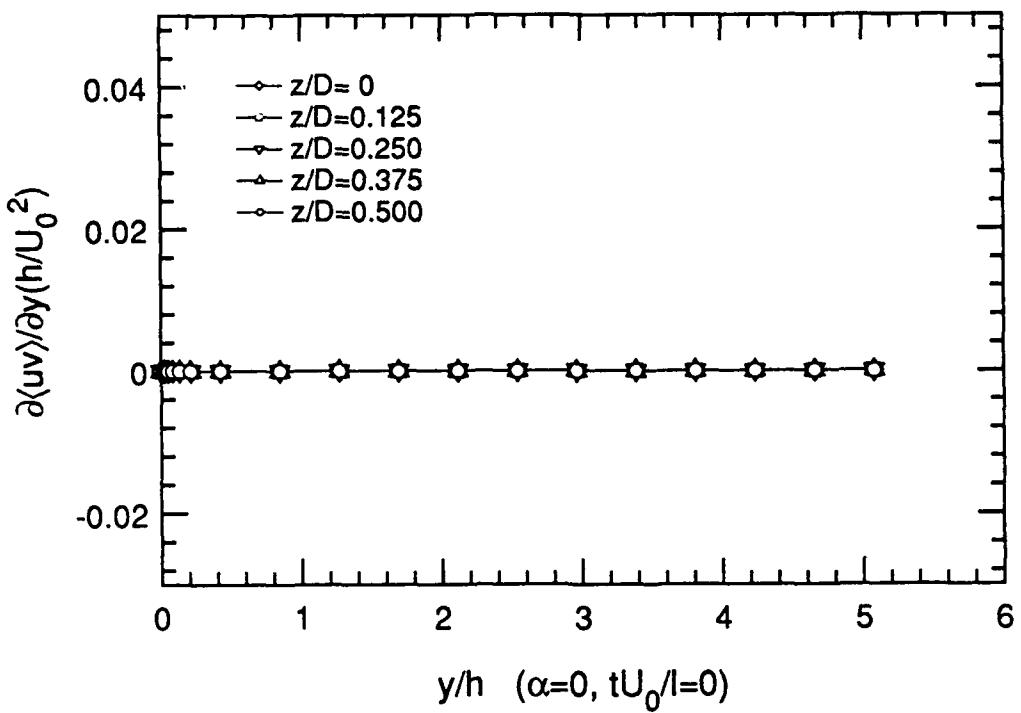
Figure 8.47a Convection of momentum by $\langle v \rangle$ for $\alpha = 0°$ at $tU_0/l = 0$
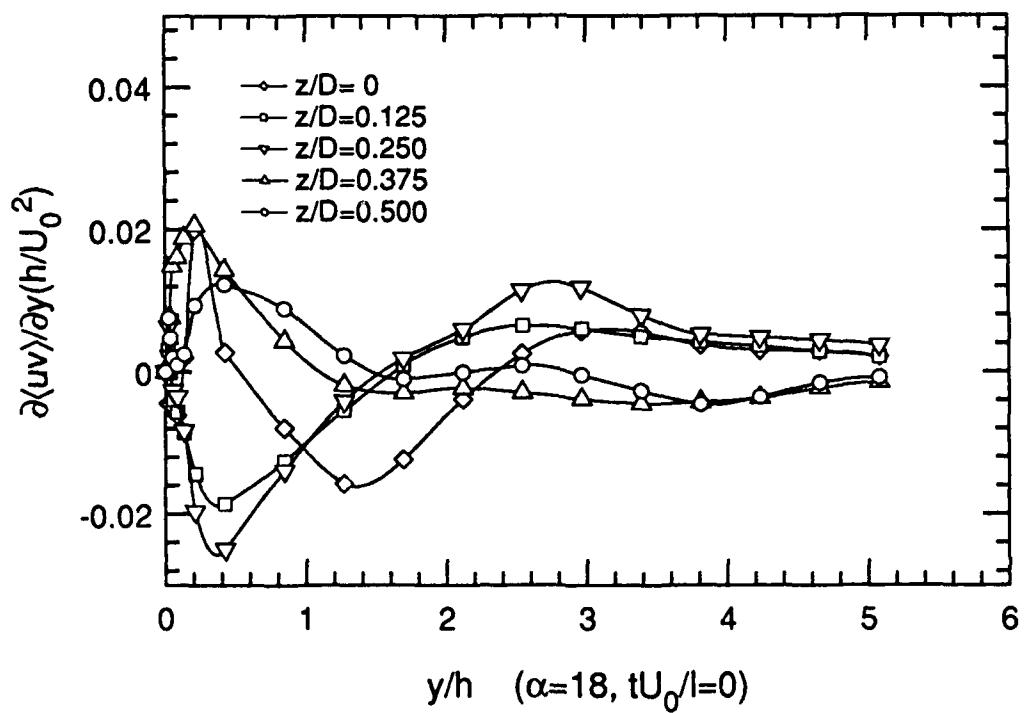
Figure 8.47b Convection of momentum by $\langle v \rangle$ for $\alpha = 18°$ at $tU_0/l = 0$

212
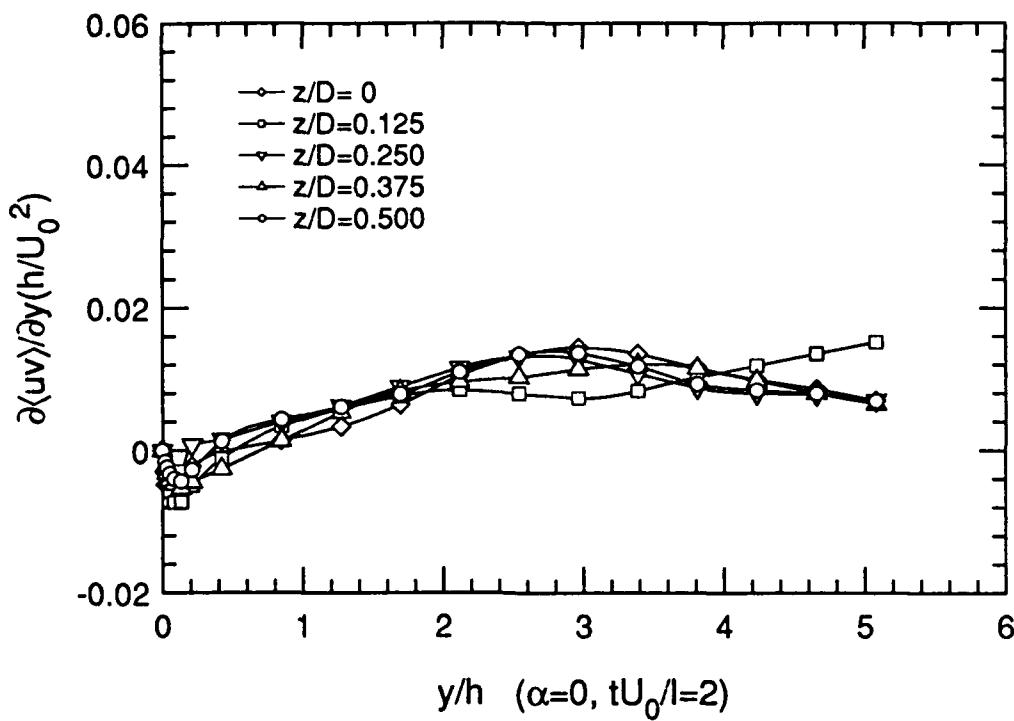
Figure 8.48a Convection of momentum by $\langle v \rangle$ for $\alpha = 0°$ at $tU_0/l = 2$
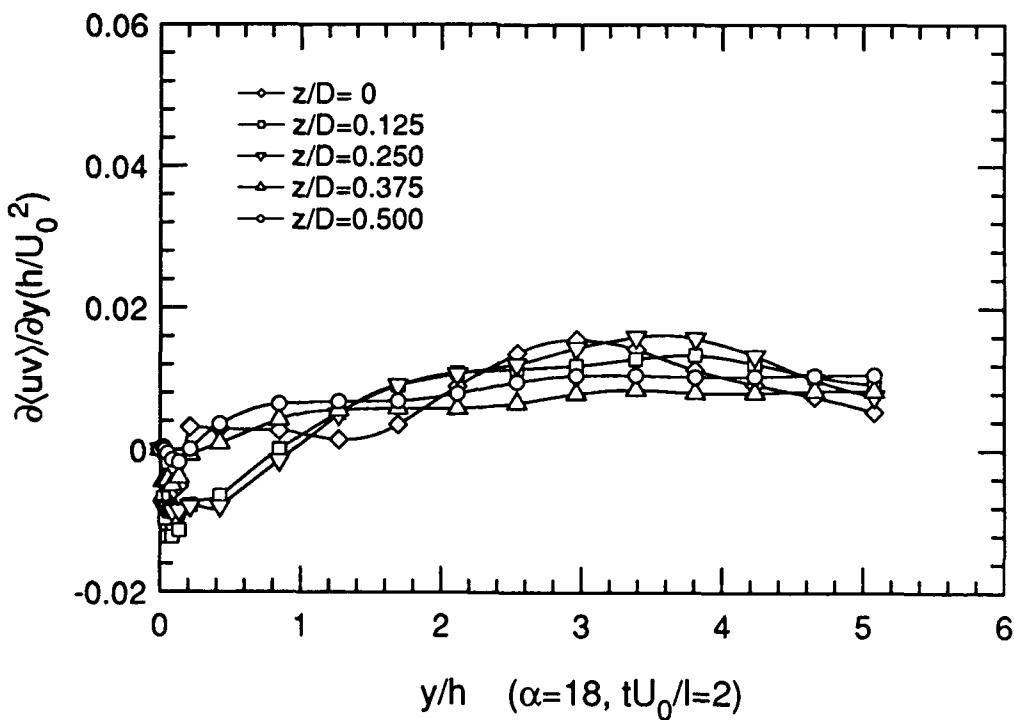
Figure 8.48b Convection of momentum by $\langle v \rangle$ for $\alpha = 18°$ at $tU_0/l = 2$

213
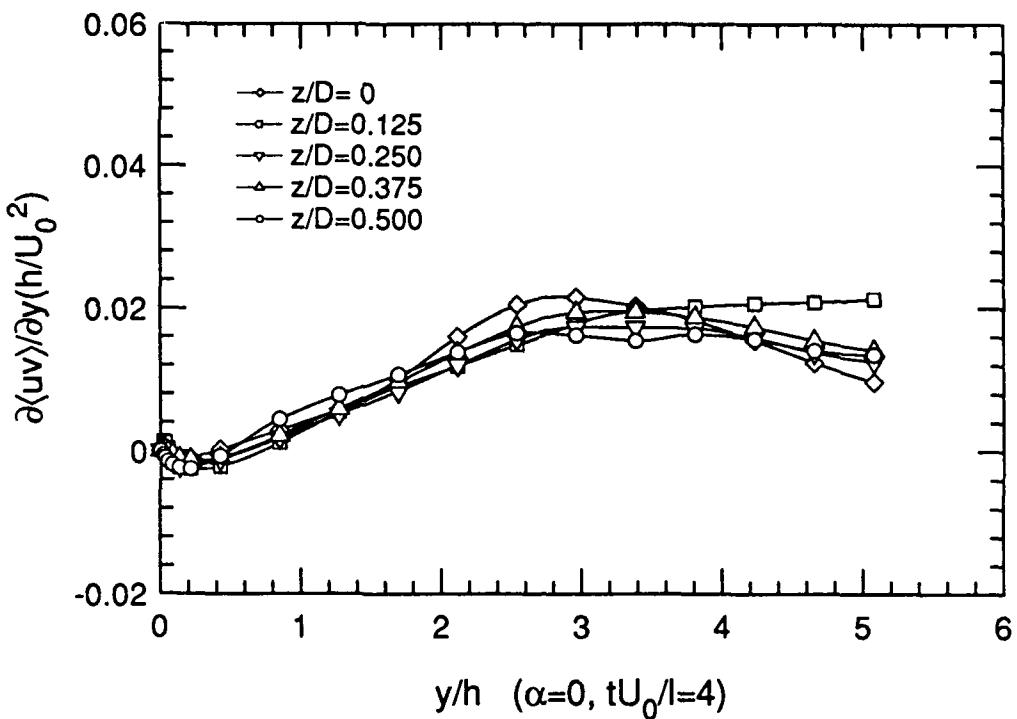
Figure 8.49a Convection of momentum by $\langle v \rangle$ for $\alpha = 0°$ at $tU_0/l = 4$
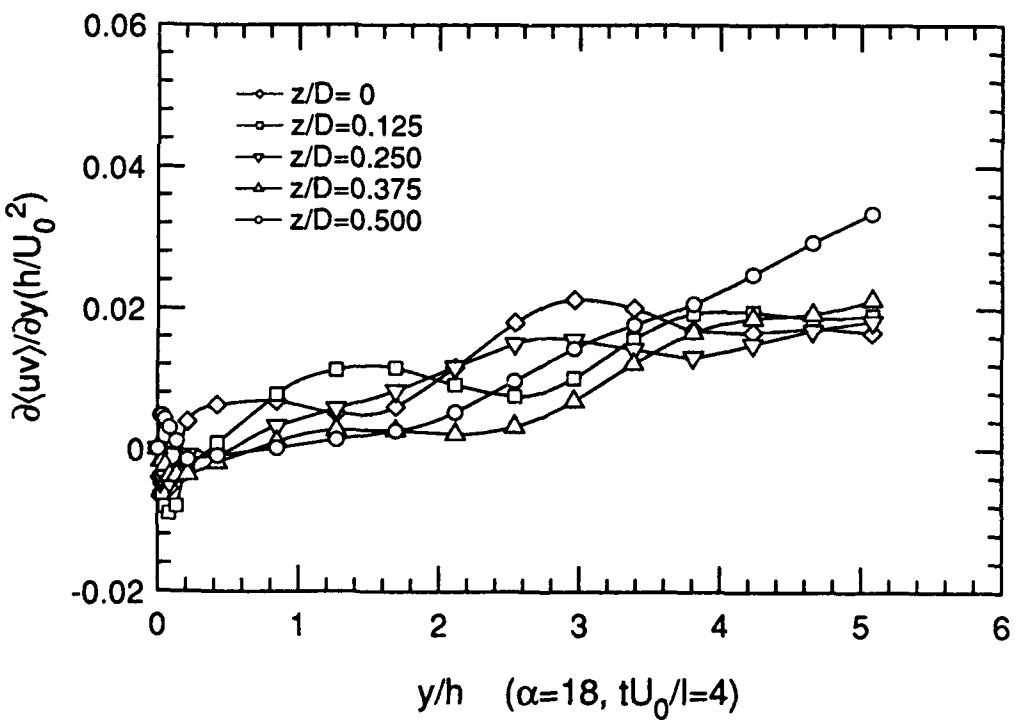
Figure 8.49b Convection of momentum by $\langle v \rangle$ for $\alpha = 18°$ at $tU_0/l = 4$

214
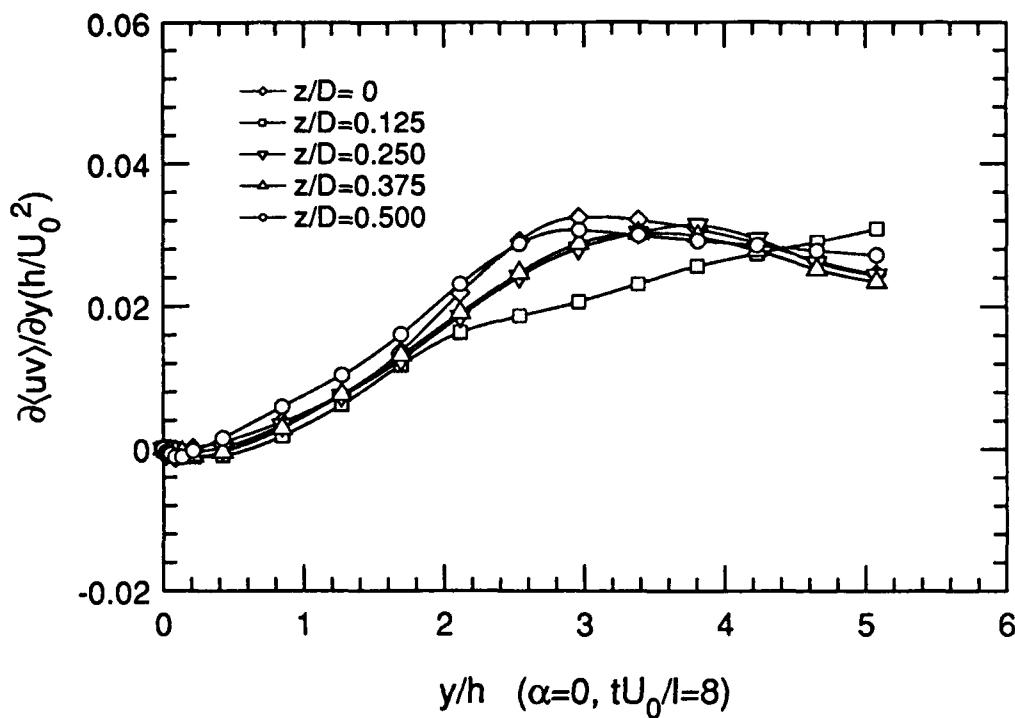
Figure 8.50a Convection of momentum by $\langle v \rangle$ for $\alpha = 0°$ at $tU_0/l = 8$
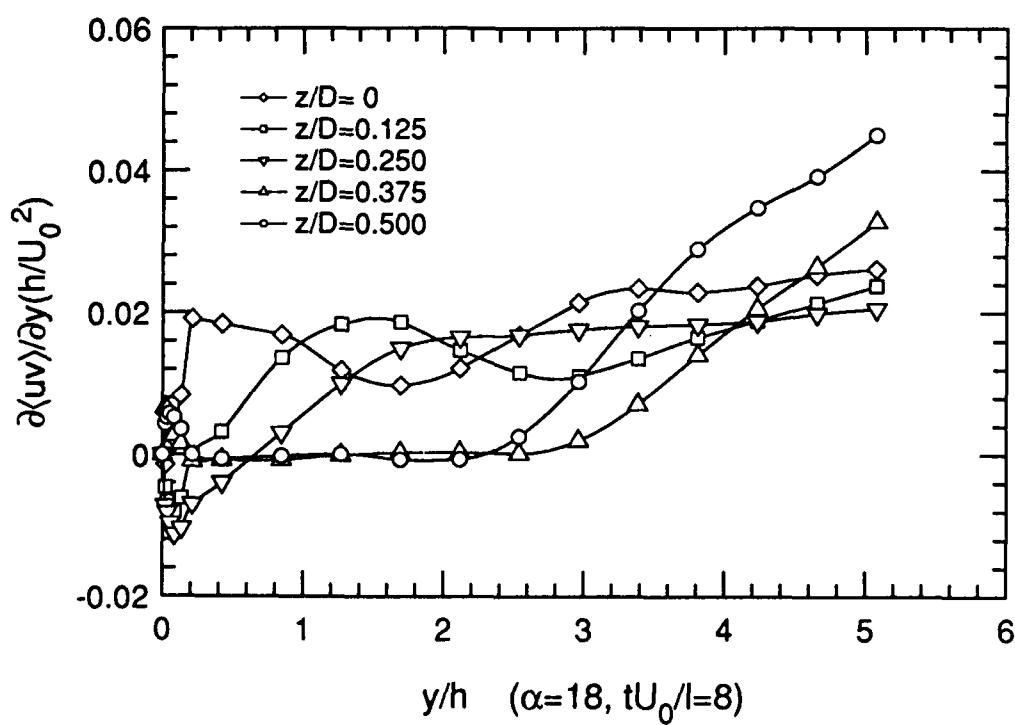
Figure 8.50b Convection of momentum by $\langle v \rangle$ for $\alpha = 18°$ at $tU_0/l = 8$

215
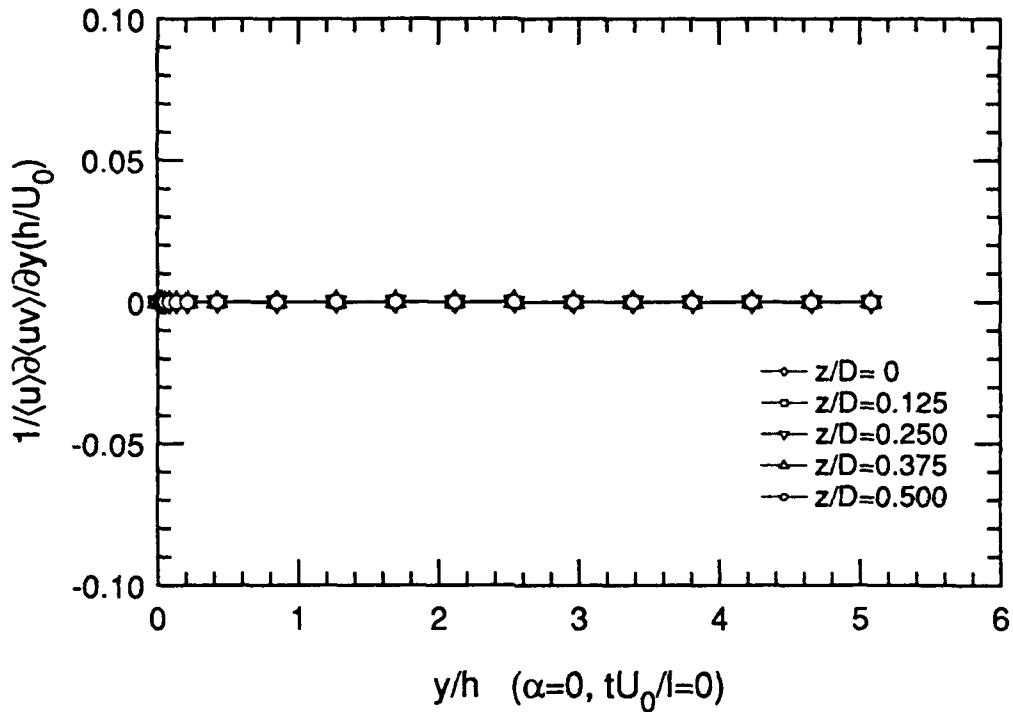
Figure 8.51a Normalized convection of momentum by $\langle v \rangle$ for $\alpha = 0°$
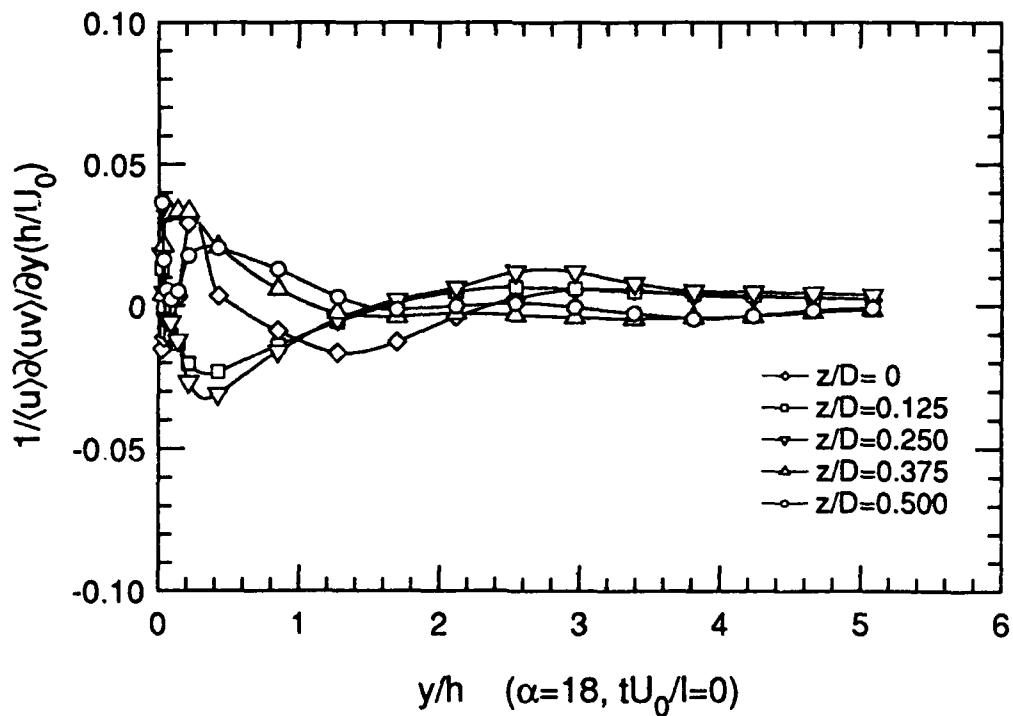
at $tU_0/l = 0$

Figure 8.51b Normalized convection of momentum by $\langle v \rangle$ for $\alpha = 18°$

at $tU_0/l = 0$

216
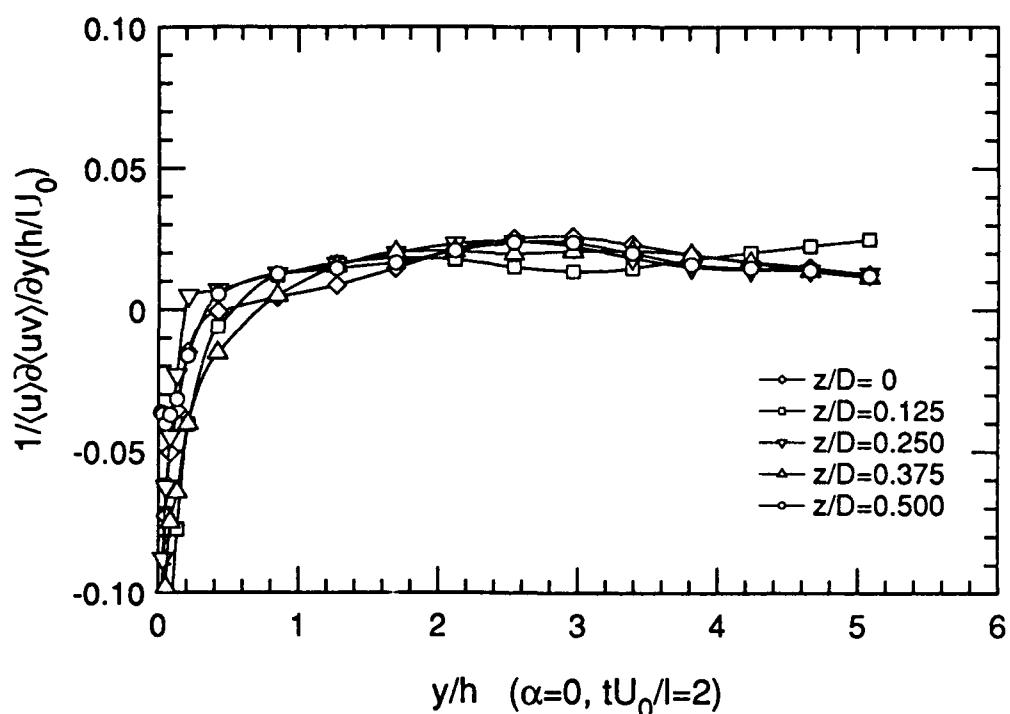
Figure 8.52a Normalized convection of momentum by $\langle v \rangle$ for $\alpha = 0°$
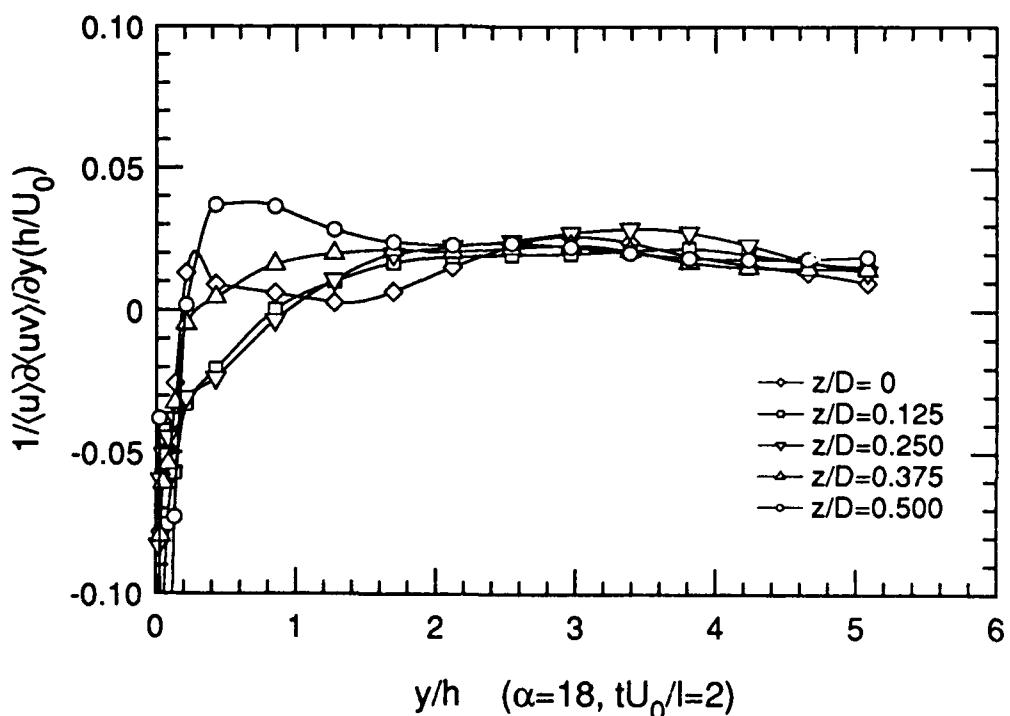
at $tU_0/l = 2$

Figure 8.52b Normalized convection of momentum by $\langle v \rangle$ for $\alpha = 18°$

at $tU_0/l = 2$

217
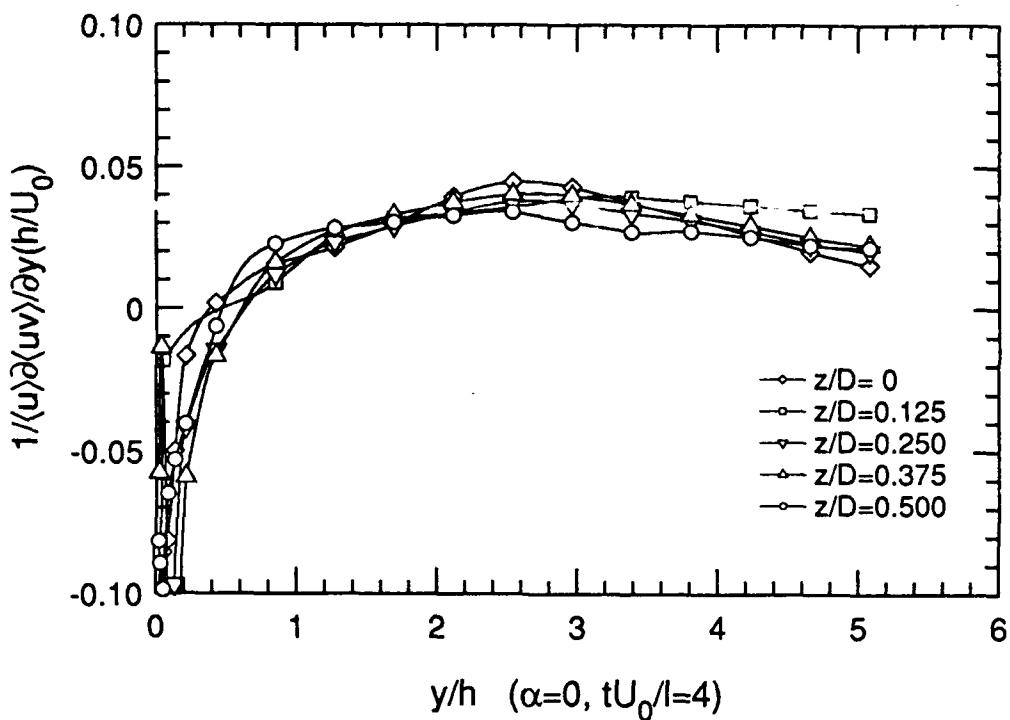
Figure 8.53a Normalized convection of momentum by $\langle v \rangle$ for $\alpha = 0°$
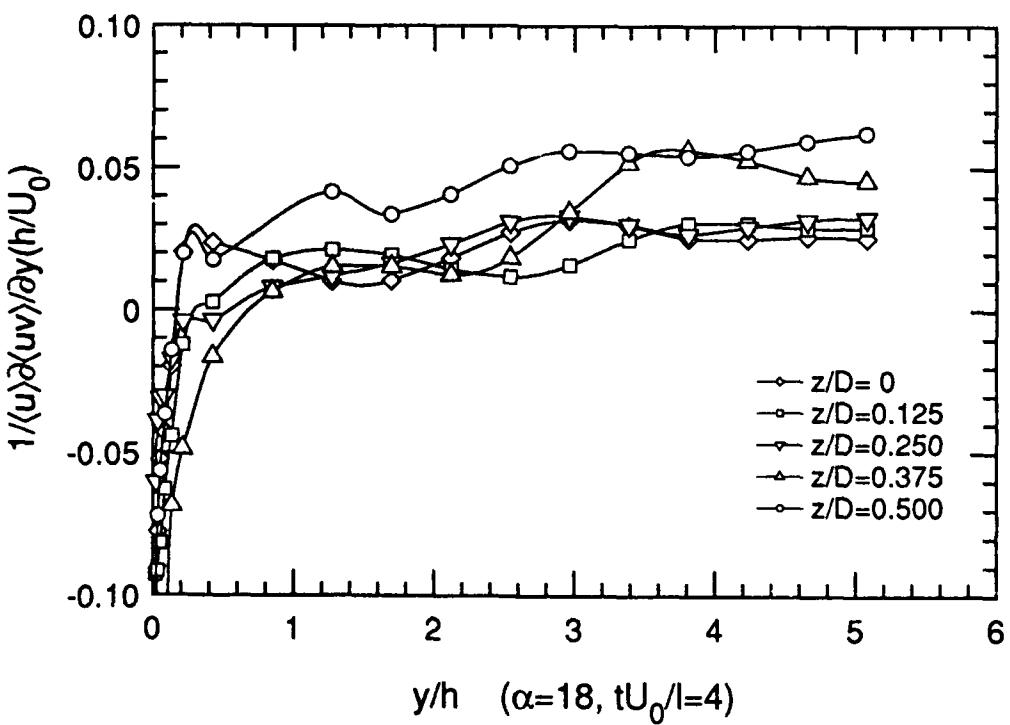
at $tU_0/l = 4$

Figure 8.53b Normalized convection of momentum by $\langle v \rangle$ for $\alpha = 18°$

at $tU_0/l = 4$

218
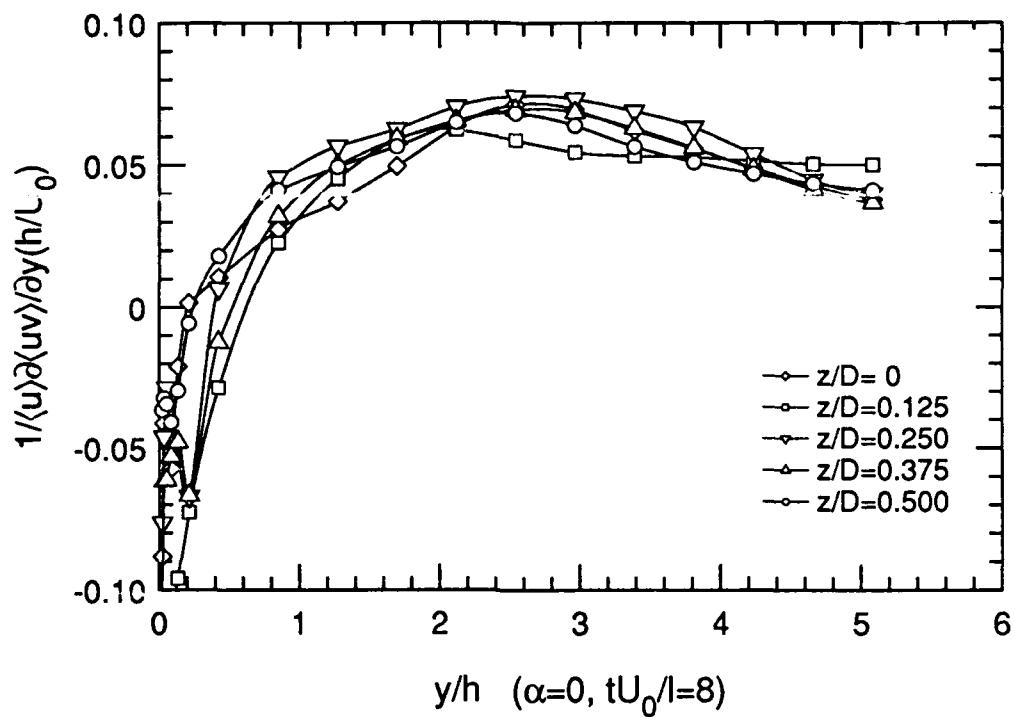
Figure 8.54a Normalized convection of momentum by $\langle v \rangle$ for $\alpha = 0°$
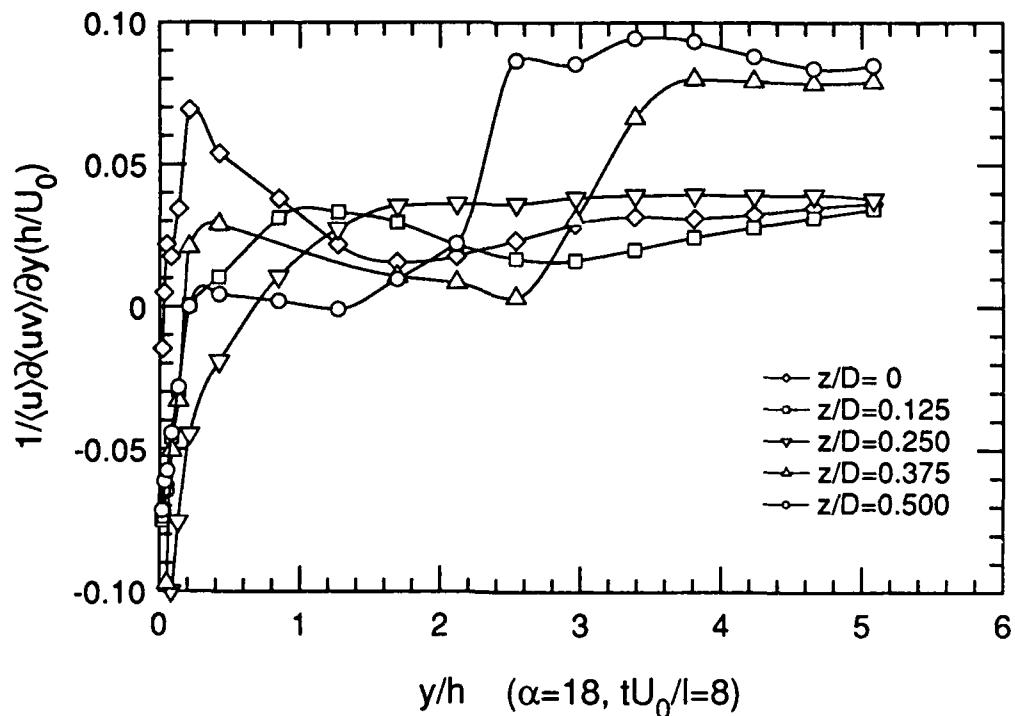
at $tU_0/l = 8$

Figure 8.54b Normalized convection of momentum by $\langle v \rangle$ for $\alpha = 18°$

at $tU_0/l = 8$

219
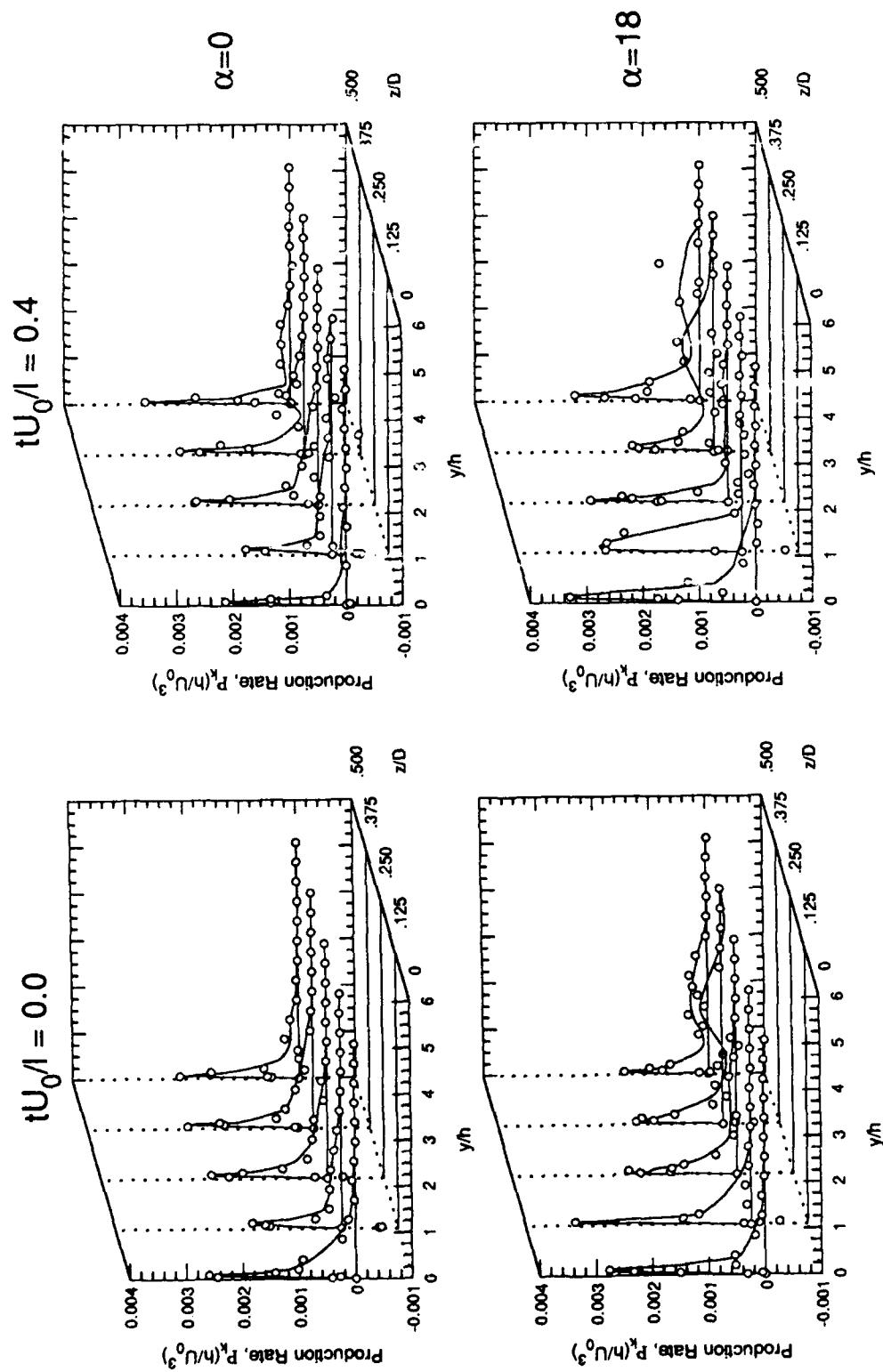
Figure 8.55 Turbulent kinetic energy production at $tU_0/l = 0$ and $tU_0/l = 0.4$

220
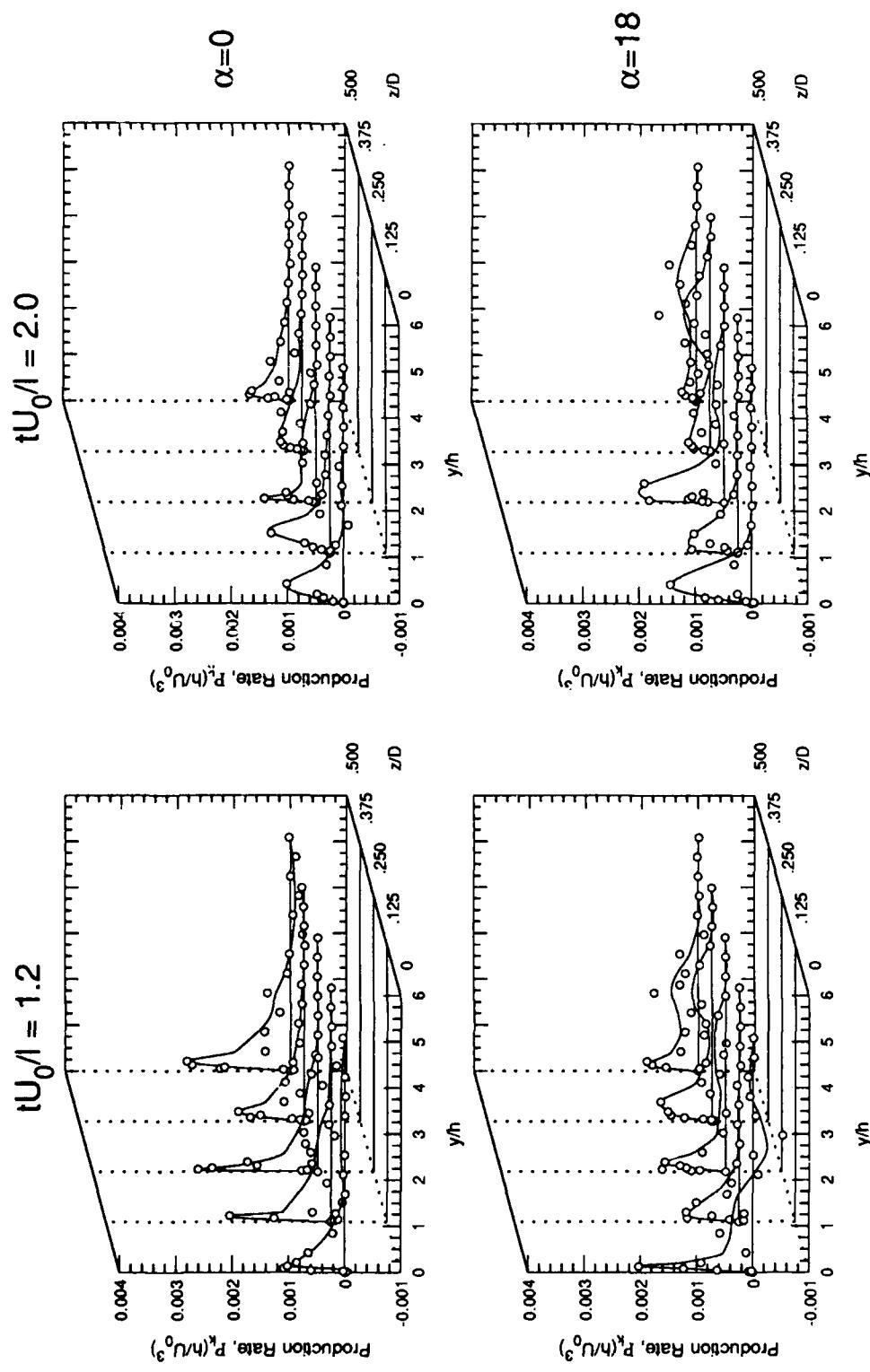
Figure 8.56 Turbulent kinetic energy production at $tU_0/l = 1.2$ and $tU_0/l = 2.0$

221
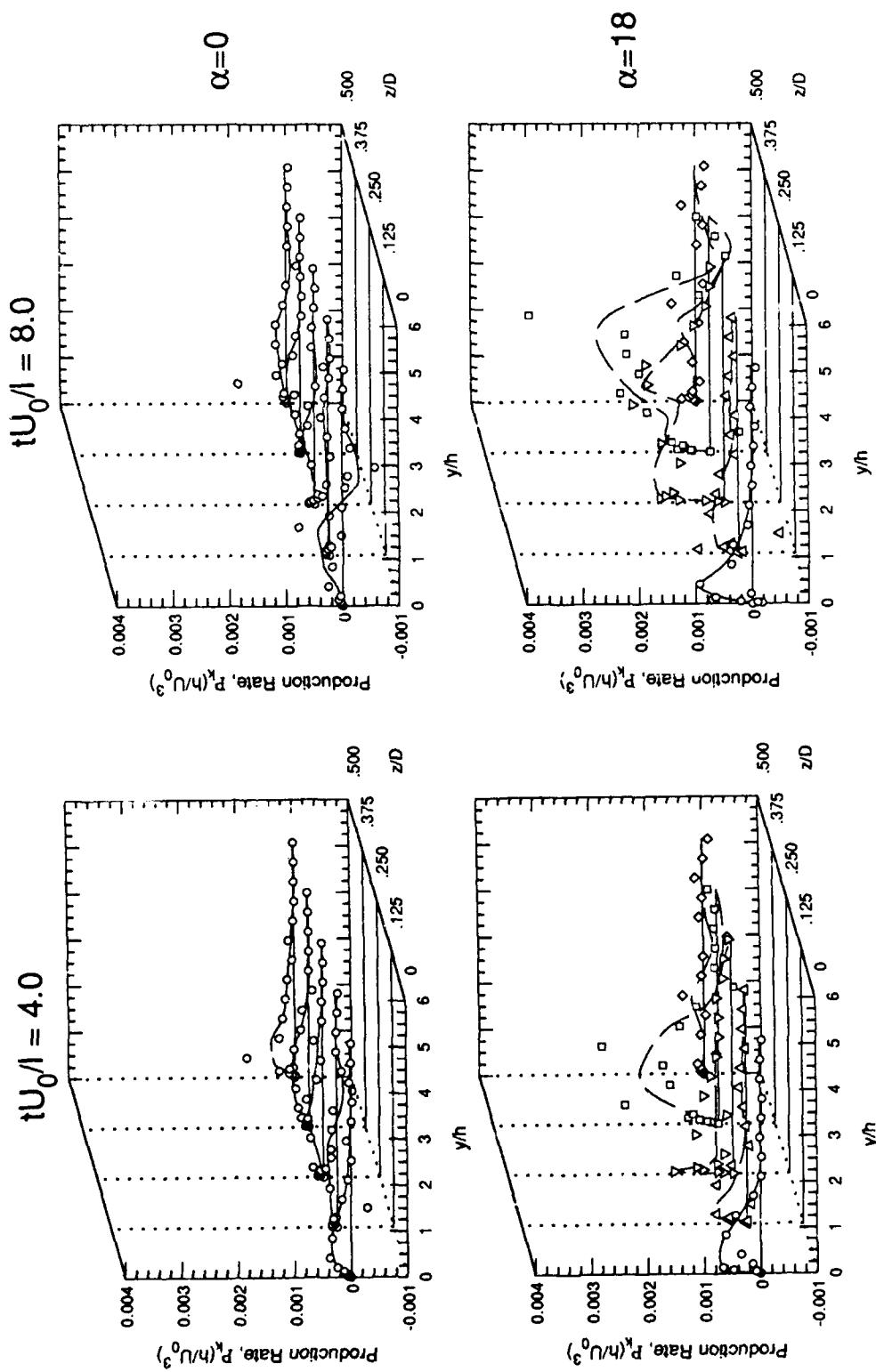
Figure 8.57 Turbulent kinetic energy production at $tU_0/l = 4$ and $tU_0/l = 8$
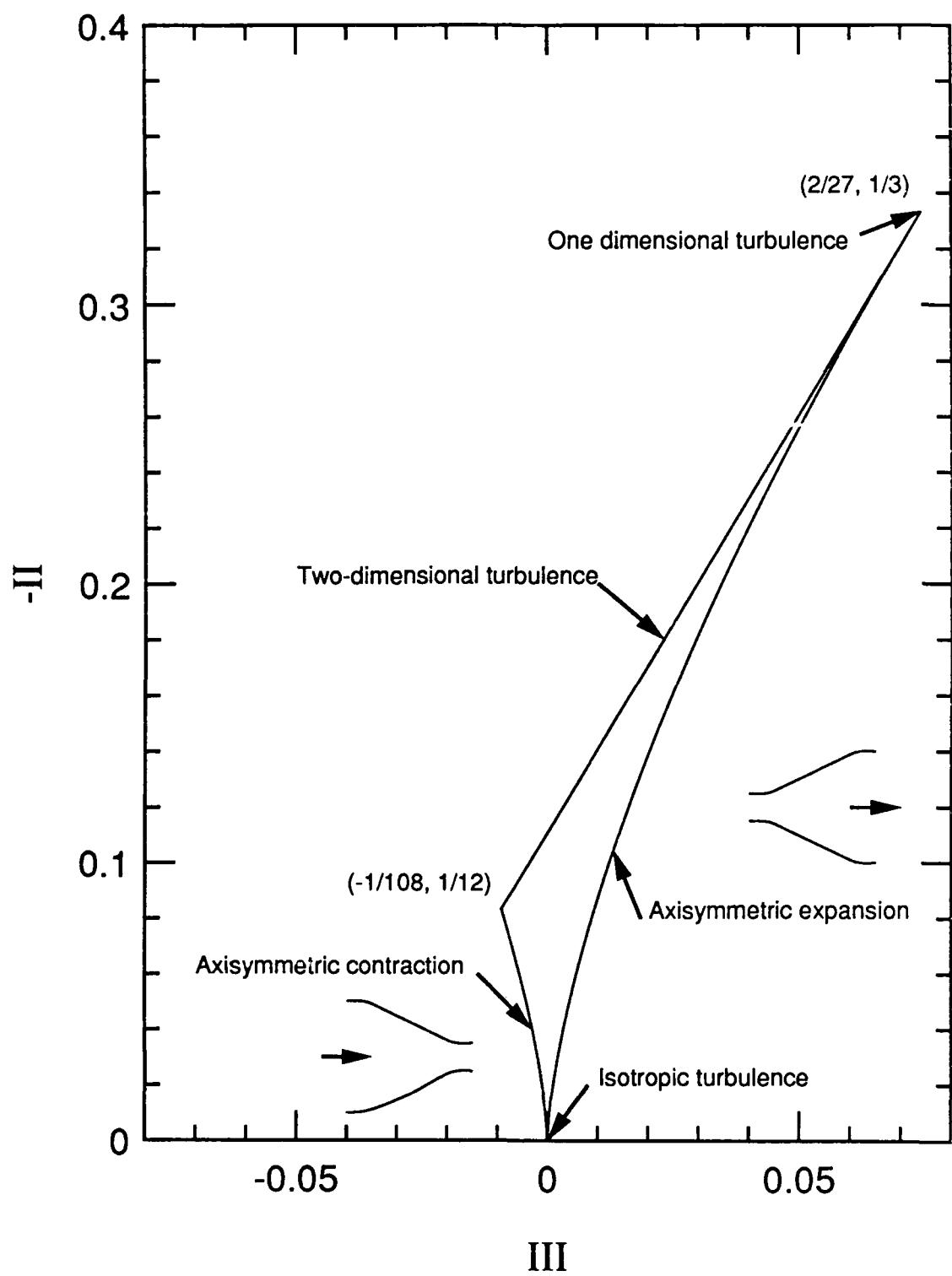
Figure 8.58 Limits of realizability on an invariant map of b_{ij}
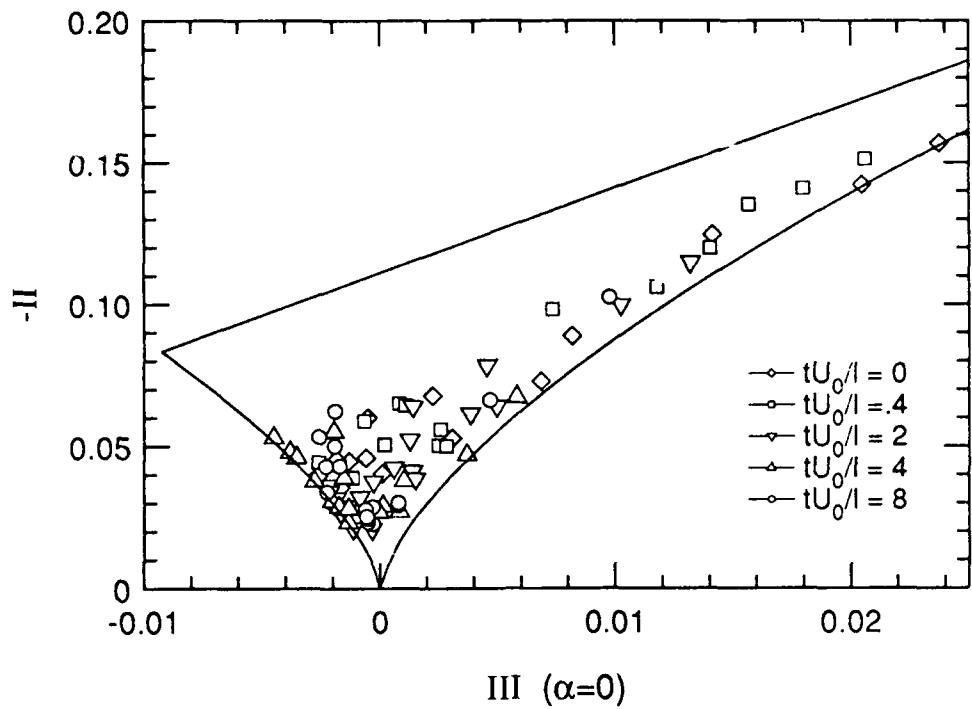
Figure 8.59a Invariant map of b_{ij} for $\alpha = 0°$ at $z/D = 0$
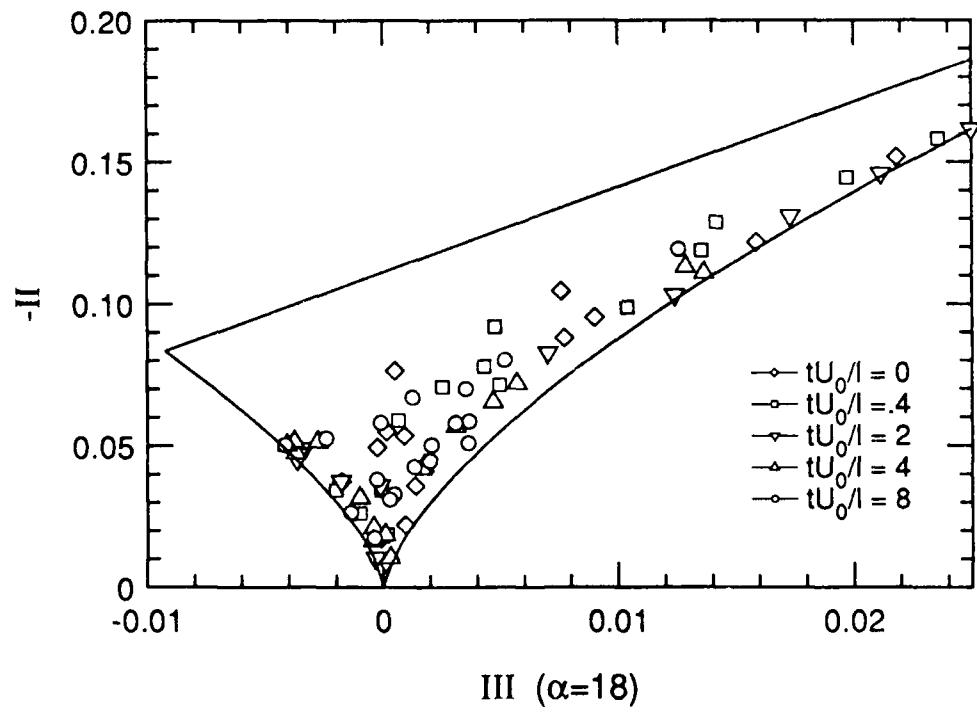
Figure 8.59b Invariant map of b_{ij} for $\alpha = 0°$ at $z/D = 0$
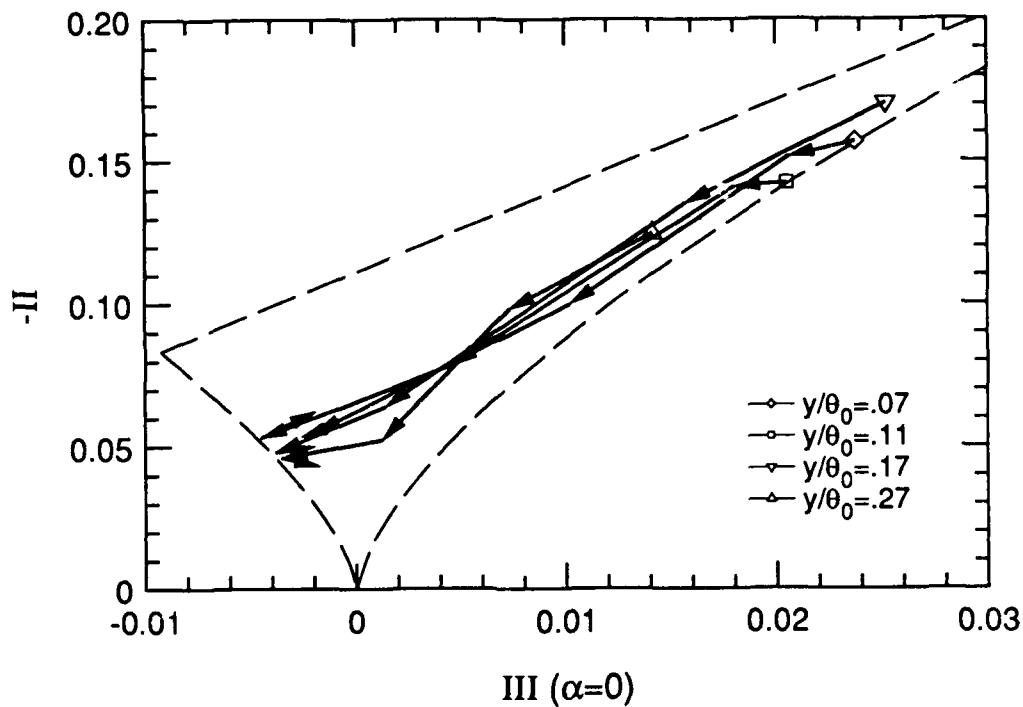
Figure 8.60a Trajectories of b_{ij} for near-wall region with $\alpha = 0°$
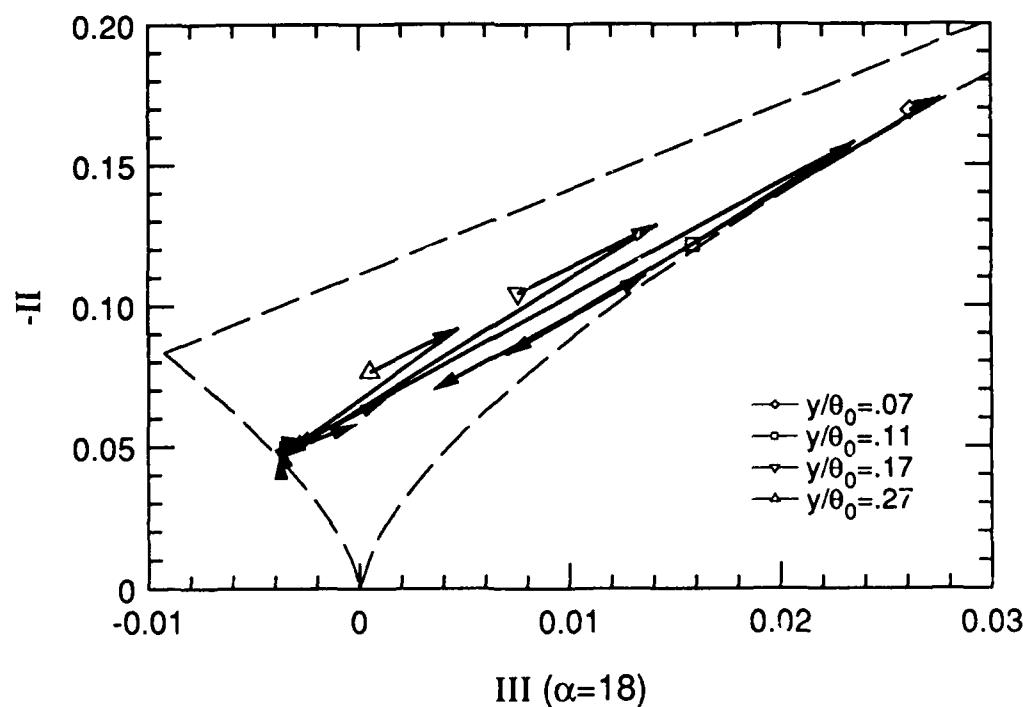
Figure 8.60b Trajectories of b_{ij} for near-wall region with $\alpha = 18°$

225
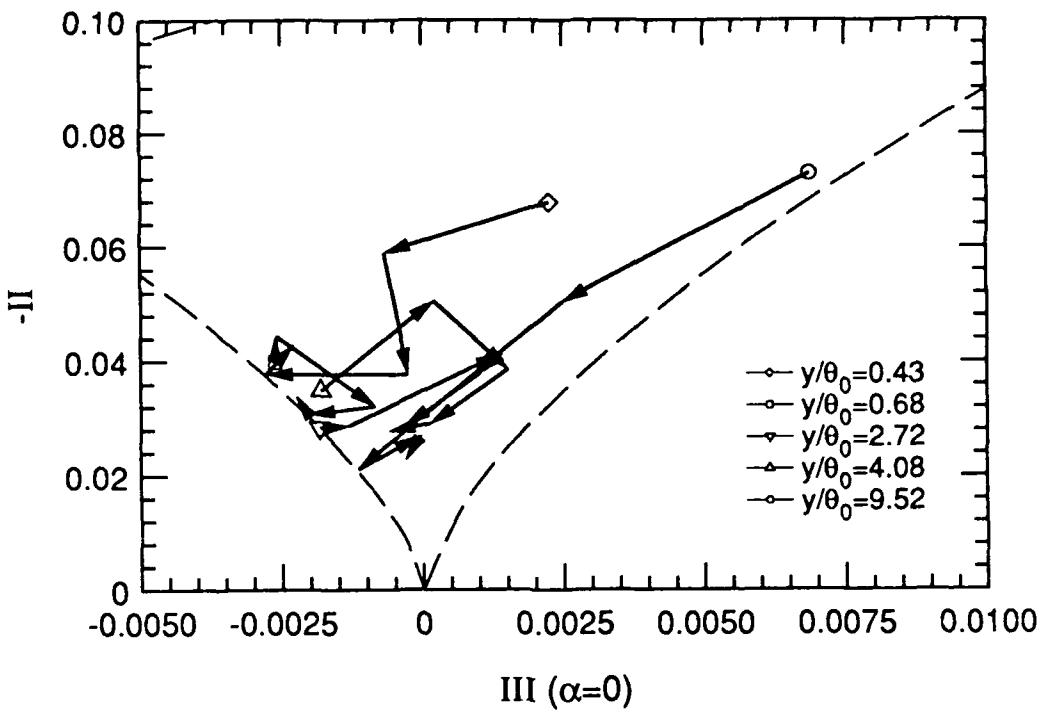
Figure 8.61a Trajectories of b_{ij} for outer boundary layer with $\alpha = 0°$
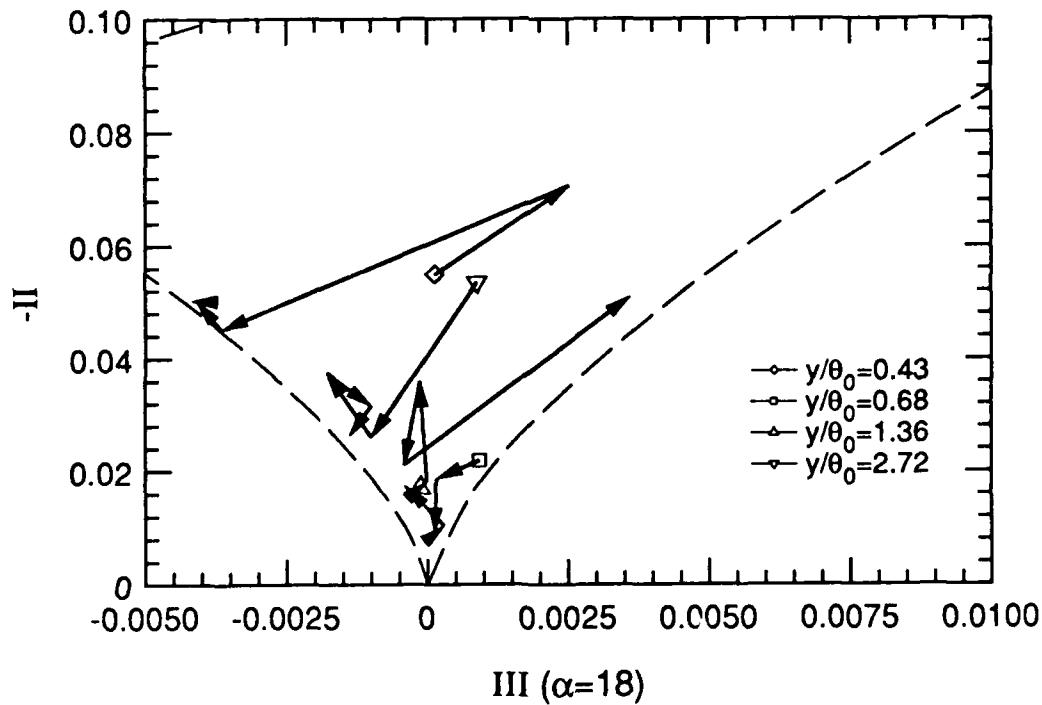
Figure 8.61b Trajectories of b_{ij} for outer boundary layer with $\alpha = 18°$
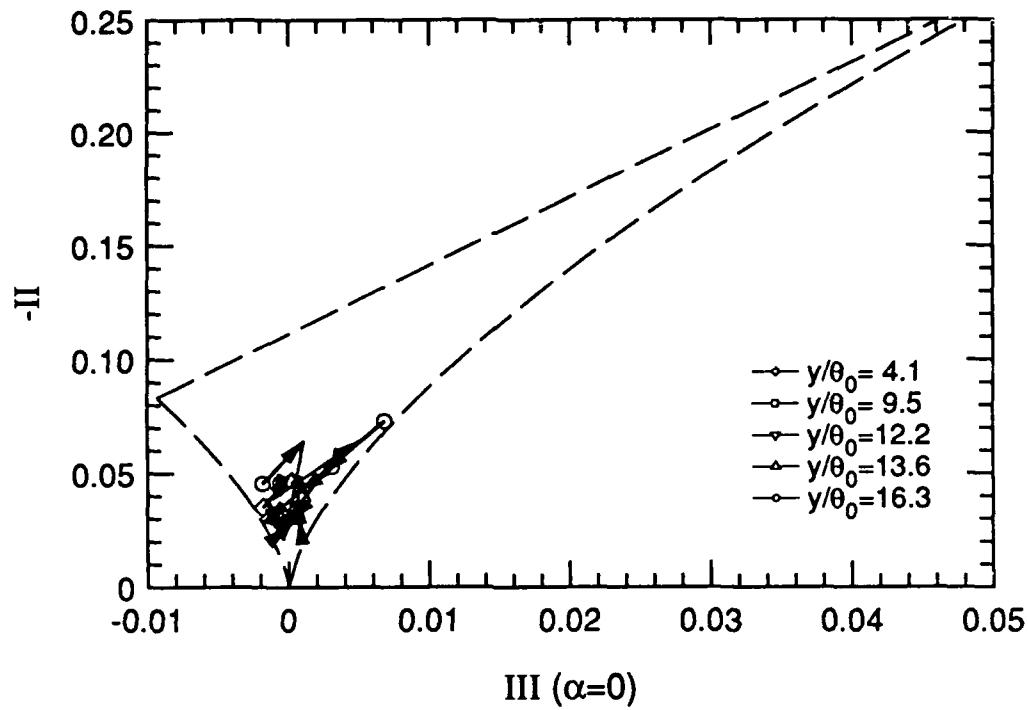
Figure 8.62a Trajectories of b_{ij} for outside boundary layer with $\alpha = 0°$
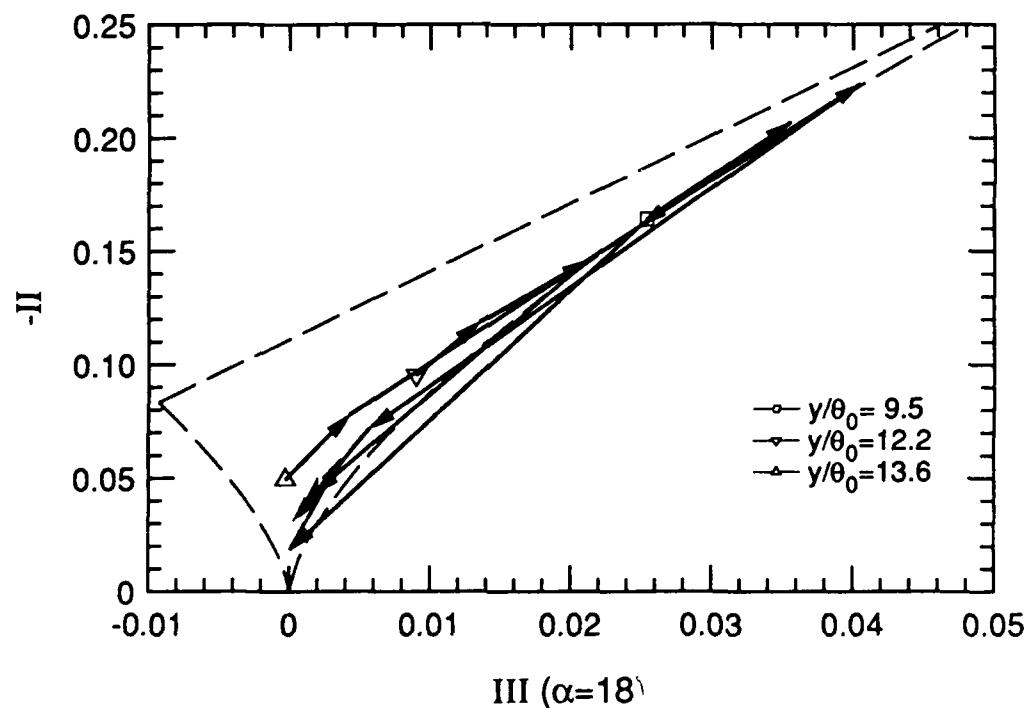
Figure 8.62b Trajectories of b_{ij} for outside boundary layer with $\alpha = 18°$

The principle is most important, not the detail.

— Theodore von Karman, 1954

9. Conclusions and Recommendations for Future Work

9.1 Conclusions

This program has fulfilled the objectives which were identified in chapter 1. Chapters 4 and 5 described the facility and the three-component LDA system that was developed and tested specifically for use in this program. Chapter 7 documented in detail the profiles of each velocity component and all six components of the Reynolds stress tensor. Finally, chapter 8 described the time response of the boundary layer and provided some insight into the mechanisms that make vortex generators work. In particular, figures 8.11 through 8.16 summarize the most significant observations.

Major Conclusions. The major conclusions resulting from this program are as follows:

1. An array of weak counter-rotating vortices markedly alters the nature of the boundary layer, both in steady, zero pressure gradient flows and in unsteady, adverse pressure gradient flows.

2. In steady, zero pressure gradient flows, this experiment confirmed the findings of earlier experiments. Key effects of the vortex generators on the steady boundary layer are:

   a. A decrease in the integral thicknesses in the downwash region and an increase in the upwash region.

   b. An increase in C_f over most of the span, but a decrease in C_f in the upwash region of the vortex pair.

   c. a substantial modification of the wake region with only minor distortion of the 'inner region' of the nominally 2-D turbulent boundary layer.

3. For unsteady flow, the time response of the freestream velocity demonstrates that convection is the mechanism by which vortex generators modify the response of

229

the boundary layer. Modeling the response with two time scales proved to be a useful technique, and led to the following observations:

a. Vortex generators do not affect the basic response *rates* of the boundary layer, but they do affect the *magnitude* of the *convective* portion of the response.

b. There is an initial response throughout the boundary layer which is unaffected by the presence of vortex generators. The duration of this initial response is the same throughout the boundary layer and appears to reflect the control valve response time, but the *rate* and *magnitude* of the initial change are less in the inner region of the boundary layer.

c. There is also a slow or convective response throughout the boundary layer which *is* substantially modified by the presence of the vortex generators.

d. Because the magnitude of the convective response is substantially reduced in the downwash region, a far greater *percentage* of its response occurs during the initial response. The apparent effect of vortex generators in the downwash region, therefore, is that they substantially decrease the time required for the boundary layer to adjust to a step change in the pressure gradient.

4. The response of $\langle v \rangle$ appears to be governed by the same mechanisms that govern the initial response of $\langle u \rangle$, and in the outer region of the boundary layer, the response rates are the same for $\langle u \rangle$ and $\langle v \rangle$. However, near the surface, the magnitude and rate of the response of $\langle v \rangle$ approach zero in the same manner as $\langle v \rangle$ approaches zero.

5. The turbulence in the inner region of the boundary layer begins to respond at the same time as the initial response of $\langle u \rangle$, but responds at a much slower rate. In contrast, the turbulence in the outer portion of the boundary layer responds at the same rate as the growth of the boundary layer, which occurs on the convective time scales of the freestream velocity.

Additional Observations. The following are additional observations that add insight into the behavior of vortex generators:

1. Under unsteady conditions, the displacement thickness increased by only a factor of two in the downwash of the vortex generators, compared to a five-fold increase when the vortex generators were at an angle of attack of 0°.

2. Under unsteady conditions, the strength of the the embedded streamwise vortex, as characterized by the circulation, holds steady for about two convective time periods then begins to decrease. After about three convective time periods, the vorticity from the embedded vortex loses its identity, and the flow appears to become dominated by streamwise vortices of the opposite sign.

3. Plots of the spanwise vorticity reveal the nature of a boundary layer responding to an adverse pressure gradient. With a zero pressure gradient, the boundary layer has a high concentration of negative spanwise vorticity very near the wall. After the adverse pressure gradient is initiated, a portion of this negative vorticity diffuses into the wall due to the pressure gradient, and the remainder redistributes throughout the boundary layer. The vortex generator downwash preserves a higher concentration of negative vorticity near the wall. This results in a healthy velocity profile and precludes the reverse flow that would otherwise occur. Estimates of the terms for transport of spanwise vorticity indicate that the majority of spanwise vorticity transport occurs in the viscous region of the boundary layer, where large vorticity gradients exist, and that the viscous and turbulent diffusion terms dominate.

4. Momentum transport by $\langle v \rangle$ is a significant mechanism by which vortex generators modify the nature of a separating boundary layer. During zero pressure gradient conditions, the downwash convects momentum towards the surface. It continues to carry momentum into the region $40 < y^+ < 200$ for a brief period after the adverse pressure gradient is initiated. As the pressure gradient continues, $\langle v \rangle$ begins to convect momentum away from the entire boundary layer, but the net efflux is significantly less in the downwash regions of the vortex generator than for the case with vortex generators at an angle of attack of 0°.

5. The regions of high turbulent kinetic energy are modified by the presence of the streamwise vortices in the manners observed by previous steady experiments. Under an adverse pressure gradient, the turbulence is amplified and moves outward with the separating boundary layer.

9.2 Recommendations for Future Work

This program has left several questions unanswered which should be pursued in future programs. It has also identified some of the strengths and limitations of this facility for experiments like this. In particular, the strengths of the facility are its computerized flow control and data acquisition which make it ideal for varying many parameters and flow configurations. Water is also ideal for flow visualization. In contrast, unsteady experiments which require mapping the flow field in two or three dimensions, are less ideal because of the very long sampling times required to obtain good converged turbulence statistics. The recommendations that follow are based on these considerations.

Flow Visualization. Some very strong spanwise secondary flow develops during the adverse pressure gradient, particularly in the upwash region (see figures 7.13 and 7.14). Also, the contour plots of streamwise vorticity indicate that vortices of opposite sign are formed (see figures 8.27 through 8.31), perhaps because of the spanwise gradient of the streamwise velocity. Flow visualization would clarify whether this is a significant flow phenomenon or a consequence of irregularities in the facility which are amplified by the adverse pressure gradient. In either case, this is an important question that should be resolved. A new test plate should be constructed that allows the introduction of 'tufts' of dye directly into the regions where the large spanwise flows are occuring.

Parametric Study of Active Control. The time response information from this study provides information that should be useful in the design of an active flow control system. However, a control engineer would actually like to know how

these response parameters vary with the configuration and dimensions of the vortex generators, and how these parameters change when the vortex generators are moved in conjunction with the unsteady pressure gradient. This would require two additions or modifications to the existing test surface: (a) fabricate test surfaces for several alternate configurations, including larger blades and co-rotating pairs; and (b) replace the belt-drive mechanism with a bevel gear mechanism which is driven by one of the valve-control motors. The data acquisition should emphasize time response of the freestream velocity, with very little or no emphasis on three-component LDA measurements. While phase averaging over 300-500 cycles would still be recommended for good convergence of the velocity data, from hindsight, a 4-second cycle would be adequate for the time response information presented in this program. This type of study would provide a wealth of information for design of active flow control system.

9.3 Closure

This program was intended to be a first look at embedded streamwise vorticity in unsteady flows. Since it was a first step, the approach included some very sophisticated techniques, and some rather simple techniques. Because of the complexity of a three-dimensional unsteady flow, the simple time response analysis actually provided the most useful information. If more three-dimensional LDA measurements of turbulent quantities are desired in a flow such as this, then quality data will require many (several thousand) cycles per phase average on a denser spatial data grid than used in this program. The most useful information, however, will probably come from the simpler techniques.
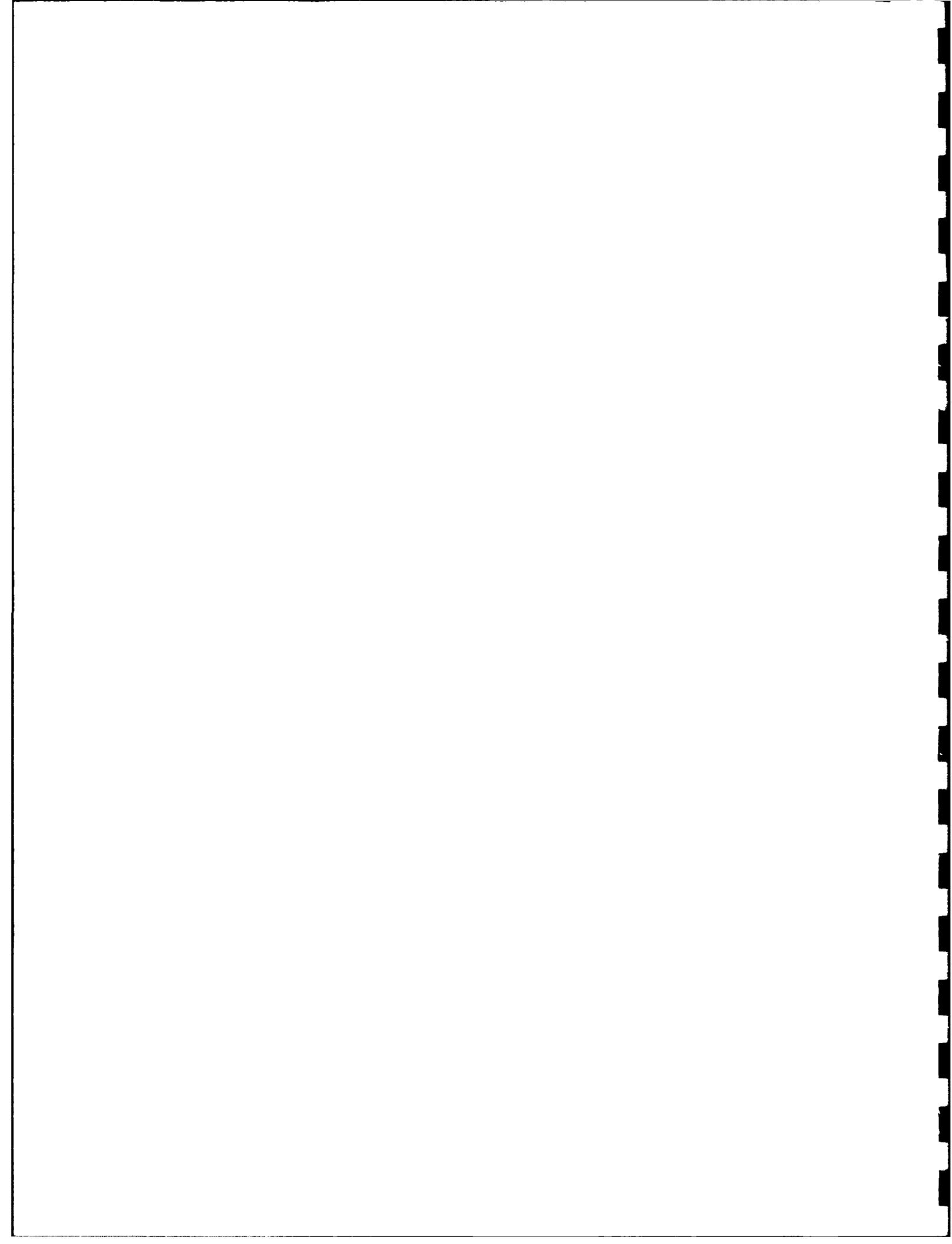
References

BARLOW, R.S. & JOHNSTON, J.P. 1985 Structure of Turbulent Boundary Layers on a Concave Surface. *Report MD-47*, Department of Mechanical Engineering, Stanford University, Stanford, California.

BATCHELOR, G.K. 1967 *Introduction to Fluid Dynamics.* Cambridge University Press, New York.

BHATTACHARJEE, S., SCHEELKE, B., & TROUT, T.R. 1985 Modification of Vortex Interactions in a Reattaching Separated Flow. *AIAA Paper 85-0555.*

BINDER, G., & KUENY, J. 1981 Measurements of the Periodic Velocity Turbulent Channel Flow. *Unsteady Turbulent Shear Flows*, ed. by Michel *et al.*, Springer Verlag.

BINDER, G., TARDU, S., BLACKWELDER, R.F., & KUENY, J.L. 1985 Large Amplitude Periodic Oscillations in the Wall Region of a Turbulent Boundary Layer. *Fifth Symposium on Turbulent Shear Flows*, Cornell University, Ithaca, New York.

BLACKWELDER, R.F. & HARITONIDIS, J.H. 1983 Scaling of Burst Frequencies in Turbulent Boundary Layers. *J. Fluid Mech.* **132**, 87.

BRADSHAW, P. & CUTLER, A.D. 1987 Three-dimensional Flows with Imbedded Longitudinal Vortices. *Perspectives in Turbulence Studies*, Springer-Verlag, 382.

BRERETON, G.J. & REYNOLDS, W.C. 1987 Experimental Study of the Fluid Mechanics of Unsteady Turbulent Boundary Layers. *Report TF-29*, Department of Mechanical Engineering, Stanford University, Stanford, California.

BRERETON, G.J. & REYNOLDS, W.C. 1987 Kinetic Energy Transfer in an Unsteady Turbulent Boundary Layer. *Sixth Symposium on Turbulent Shear Flows*, Toulouse, France.

BRERETON, G.J., REYNOLDS, W.C., & CARR, L.W. 1985 Unsteady Turbulent Boundary Layers: Some Effects of Abrupt Free-Stream Velocity Changes. *Fifth Symposium on Turbulent Shear Flows*, Cornell University, Ithaca, New York.

CARLSON, A.B. & REYNOLDS, W.C. 1989 An Experimental Investigation of Heat Transfer in an Unsteady Turbulent Boundary Layer. (In Preparation), Department of Mechanical Engineering, Stanford University, Stanford, California.

CHEHROUDI, B. & SIMPSON, R.L. 1985 Space-time results for a separating turbulent boundary layer using a rapidly scanning laser anemometer. *J. Fluid Mech.* **160**, 77.

COLES, D.E. 1956 The law of the wake in the turbulent boundary layer. *J. Fluid Mech.* **1**, 191.

COLES, D.E. 1968 The young person's guide to the data. *Proc. Computation of Turbulent Boundary Layers—1968 AFOSR-IFP-Stanford conference* **2**, Department of Mechanical Engineering, Stanford University, Stanford, California.

COOK, W.J. 1986 Turbulent Boundary Layers in Oscillating Flows: An Experimental and Computational Study. *Report ISU-ERI-Ames-86434*, Engineering Research Institute, Iowa State University, Ames, Iowa.

COOK, W.J., MURPHY, J.D., & OWEN, F.K. 1985 An experimental and Computational Study of Turbulent Boundary Layers in Oscillating Flows. *Fifth Symposium on Turbulent Shear Flows*, Cornell University, Ithaca, New York.

COOK, W.J. & MURPHY, J.D. 1987 Measurements of Time-Dependent Boundary Layer Turbulence in an Oscillating Flow. *Sixth Symposium on Turbulent Shear Flows*, Toulouse, France.

COUSTEIX, J., DESOPPER, A., & HOUDEVILLE, R. 1977 Structure and Development of a Turbulent Boundary Layer in an Oscillatory External Flow. *Turbulent Shear Flows, # 1*, ed. Durst *et al.*, Springer-Verlag.

COUSTEIX, J., JAVELLE, J., & HOUDEVILLE, R. 1981 Influence of Strouhal Number on the Structure of Flat Plate Turbulent Boundary Layer, *Turbulent Shear Flows, # 3*, ed. Bradbury *et al.*, Springer-Verlag.

COUSTEIX, J. & HOUDEVILLE, R. 1985 Turbulence and Skin Friction Evolutions in an Oscillating Boundary Layer. *Fifth Symposium on Turbulent Shear Flows*, Cornell University, Ithaca, New York.

COUSTOLES, E., TENAUD, C., & COUSTEIX, J. 1987 Manipulation of Turbulent Boundary Layers in Zero Pressure Gradient Flows: Detailed Experiments and Modelling. *Sixth Symposium on Turbulent Shear Flows*, Toulouse, France.

CUTLER, A.D. & BRADSHAW, P. 1986 The Interaction Between a Strong Longitudinal Vortex and a Turbulent Boundary Layer, *AIAA Paper 86-1071*.

DURST, F., MELLING, A. & WHITELAW, J.H. 1981 *Principles and Practice of Laser-Doppler Anemometry*. Academic Press, London.

EIBECK, P.A. & EATON, J.K. 1985 An Experimental Investigation of the Heat-Transfer Effects of a Longitudinal Vortex Embedded in a Turbulent Boundary Layer. *Report MD-48*, Thermosciences Division, Department of Mechanical Engineering, Stanford University, Stanford, California.

GAD-EL-HAK, M., & BLACKWELDER, R.F. 1987 Control of the Discrete Vortices from a Delta Wing, *AIAA Journal* 25, 1042.

GAD-EL-HAK, M., & HO, C.-M. 1986 Unsteady Vortical Flow Around Three-Dimensional Lifting Surfaces, *AIAA Journal* 24, 713.

GAJDECZKO, B. & RAMAPRIAN, B.R. 1987 Experiments on Periodic Turbulent Boundary Layers in Adverse Pressure Gradient. *Sixth Symposium on Turbulent Shear Flows*, Toulouse, France.

HENK, R.W., & REYNOLDS, W.C. 1989 An Experimental Study of the Fluid Mechanics of an Unsteady, Three-Dimensional Separation. (In Preparation), Department of Mechanical Engineering, Stanford University, Stanford, California.

237

HINZE, J.O. 1981 *Turbulence.* McGraw-Hill, New York.

JAYARAMAN, R., PARIKH, P. & REYNOLDS, W.C. 1982 An experimental study of the dynamics of an unsteady turbulent boundary layer. *Report TF-18,* Department of Mechanical Engineering, Stanford University, Stanford, California.

KARLSSON, S.K.F. 1959 An unsteady turbulent boundary layer. *J. Fluid Mech.* **5,** 622.

KIM, J., MOIN, P. & MOSER, R. 1987 Turbulence statistics in fully developed channel flow at low Reynolds number. *J. Fluid Mech.* **177,** 133.

KLEWICKI, J.C. & FALCO, R.E. 1988 On accurately measuring statistics associated with small scale structure in surbulent boundary layers. *Report TSL-88-4,* Turbulence Structure Laboratory, Department of Mechanical Engineering, Michigan State University.

KLINE, S.J. &McCLINTOCK, F.A. 1953 Describing uncertainties in single-sample experiments. *Mech. Engr.* **75,**3.

LAUFER, J. 1950 Investigation of Turbulent Flow in a Two-Dimensional Channel. *NACA Technical Note 2123.*

LAUFER, J. 1954 The structure of Turbulence in Fully Developed Pipe Flow. *NACA Technical Note 2954.*

Liakopoulos, A. 1983 Explicit Representations of the Complete Velocity Profile in a Turbulent Boundary Layer. *AIAA Journal* **22,** 844.

LIANDRAT, J., AUPOIX, B. & COUSTEIX, J. 1985 Calculation of Longitudinal Vortices Imbedded in a Turbulent Boundary Layer. *Fifth Symposium on Turbulent Shear Flows,* Cornell University, Ithaca, New York.

LUTTGES, M.W. 1987 Unsteady Separated Flows: Vorticity and Turbulence. *Report AFOSR-TR-87-0384,* Department of Aerospace Engineering Sciences, University of Colorado, Boulder, Colorado.

LUTTGES, M.W., ROBINSON, M.C., & KENNEDY, D.A. 1985 Control of Unsteady Separated Flow Structures on Airfoils. *AIAA Paper 85-0531.*

McCOY, W.T. & SARPKAYA, T. 1986 Stability of the Vortex Mostion in Oscillating Flow. *Master's Thesis*, Naval Postgraduate School, Monterey, California.

McCROSKEY, W.J., CARR, L.W., & McALISTER, K.W. 1976 Dynamic Stall Experiments on Oscillating Airfoils. *AIAA Journal* **14**, 57.

MEHTA, R.D. 1984 An Experimental Study of a Vortex/Mixing Layer Interaction. *AIAA Paper 84-1543.*

MEHTA, R.D. 1985 Effect of a Longitudinal Vortex on a Separated Turbulent Boundary Layer. *AIAA Paper 85-0530.*

MEHTA, R.D. 1986 Interaction Between a Long.tudinal Vortex and a Shock-Induced Turbulent Boundary Layer Separation. *AIAA Paper 86-0346.*

MEHTA, R.D. & BRADSHAW, P.B. 1988 Longitudinal vortices imbedded in turbulent boundary layers. Part 2. Vortex pair with 'common flow' upwards. *J. Fluid Mech.* **188**, 529.

MEHTA, R.D. & CANTWELL, E.R. 1985 Properties of a Half-Delta Wing Vortex. *Fifth Symposium on Turbulent Shear Flows*, Cornell University, Ithaca, New York.

MEHTA, R.D., SHABAKA, I.M.M.A, SHIBL, A., & BRADSHAW, P. 1983 Longitudinal Vortices Imbedded in Turbulent Boundary Layers. *AIAA Paper 83-0378.*

MOFFAT, R.J. 1988 Describing the Uncertainties in Experimental Results. *Experimental Thermal and Fluid Science*, **1**, 3, Elsevier Science Publishing Co., Inc., New York.

MOIN, P. & KIM, J. 1985 The Structure of the vorticity field in turbulent channel flow. Part 1. Analysis of instantaneous fields and statistical correlations. *J. Fluid Mech.* **155**, 441.

MURLIS, J., TSAI, H.M., & BRADSHAW, P. 1982 The structure of turbulent boundary layers at low Reynolds numbers. *J. Fluid Mech.* 122,13.

NETER, J., WASSERMAN, W., AND KUTNER, M. 1985. *Applied Linear Statistical Models.* Irwin, Homewood, Illinois.

PAULEY, W.R. & EATON, J.K. 1988 Experiments on the Development of Longitudinal Vortex Pairs Embedded in a Turbulent Boundary Layer *AIAA Journal* **26**, 816.

PAULEY, W.R. & EATON, J.K. 1988 The Fluid Dynamics and Heat Transfer Effects of Streamwise Vortices Embedded in a Turbulent Boundary Layer. *Report MD-51*, Department of Mechanical Engineering, Stanford University, Stanford, California.

PEARCEY, H.H. 1961 Shock-Induced Separation and Its Prevention by Design and Boundary Layer Control, Part IV. *Boundary Layer and Flow Control*, G.V. Lachmann, ed. 1277.

PRANDTL, L. 1952 *Essentials of Fluid Dynamics.* Blackie, London.

REISENTHEL, P., KOGA, D., & NAGIB, H. 1985 Control of Separated Flows Using Forced Unsteadiness, *AIAA Paper 85-0556*.

REYNOLDS, W.C. 1987 Fundamentals of Turbulence for Turbulence Modeling and Simulation. *Class Lecture Notes for ME261B*, Department of Mechanical Engineering, Stanford University, Stanford, California.

REYNOLDS, W.C. & CARR, L.W. 1985 Review of unsteady, driven, separated flows. *AIAA Paper 85-0527*.

RICE, JOHN A. 1988 *Mathematical Statistics and Data Analysis.* Wadsworth & Brooks/Cole, Pacific Grove, California.

ROOS, F.W., & KEGELMAN, J.T. 1985 Control of Coherent Structures in Reattaching Laminar and Turbulent Shear Layers. *AIAA Paper 85-0554*.

SCHUBAUER, G.B. & SPANGENBERG, W.G. 1960 Forced mixing in boundary Layers. *J. Fluid Mech.* **8**, 10.

SHABAKA, I.M.M.A, MEHTA, R.D., & BRADSHAW, P. 1985 Longitudinal vortices imbedded in turbulent boundary layers. Part 1. Single vortex. *J. Fluid Mech.* **155**, 37.

SHILOH, K., SHIVAPRASAD, B.G., & SIMPSON, R.L. 1981 The structure of a separating turbulent boundary layer. Part 3. Transverse velocity measurements. *J. Fluid Mech.* **113**, 75.

SIGURDSON, L.W. & ROSHKO, A. 1985 Controlled Unsteady Excitation of a Reattaching Flow. *AIAA Paper 85-0552.*

SIMPSON, R.L., CHEW, Y.T., & SHIVAPRASAD, B.G. 1981 The structure of a separating turbulent boundary layer. Part 1. Mean flow and Reynolds stresses. *J. Fluid Mech.* **113**, 23.

SIMPSON, R.L., CHEW, Y.T., & SHIVAPRASAD, B.G. 1981 The structure of a separating turbulent boundary layer. Part 2. Higher-order turbulence results. *J. Fluid Mech.* **113**, 53.

SIMPSON, R.L., SHIVAPRASAD, B.G., & CHEW, Y.T. 1983 The structure of a separating turbulent boundary layer. Part 4. Effects of periodic free-stream unsteadiness. *J. Fluid Mech.* **127**, 219.

SIMPSON, R.L., & SHIVAPRASAD, B.G. 1983 The structure of a separating turbulent boundary layer. Part 5. Frequency effects on periodic unsteady free-stream flows. *J. Fluid Mech.* **131**, 319.

SPALART, P.R. 1986 Direct Simulation of a Turbulent Boundary Layer up to $R_\theta = 1410$. *NASA Technical Memorandum 89407*, NASA Ames Research Center, Moffet Field, California.

SPALDING, D.B. 1961 *Trans. A.S.M.E., J. Appl. Mech.*, **28E**, 455.

STOKES, G.G. 1851 On the effect of the internal friction of fluids on the motion of pendulums. *Trans. Camb. Phil. Soc.* ix **8**, [*Papers, iii.* 1].

TARDU, S., BINDER, G., & BLACKWELDER, R. 1987 Modulation of Bursting by Periodic Oscillations Imposed on Channel Flow. *Sixth Symposium on Turbulent Shear Flows*, Toulouse, France.

TENNEKES, H. & LUMLEY, J.L. 1972 *A First Course in Turbulence.* M.I.T. Press, Cambridge, Mass.

WALKER, J., HELIN, H., & CHOU, D. 1985 Unsteady Surface Pressure Measurements on a Pitching Airfoil. *AIAA Paper 85-0532.*

WESTPHAL, R.V., EATON, J.K., & PAULEY, W.R. 1985 Interaction Between a Vortex and a Turbulent Boundary Layer in a Streamwise Pressure Gradient, *Fifth Symposium on Turbulent Shear Flows*, Cornell University, Ithaca, New York.

WESTPHAL, R.V. & MEHTA, R.D. 1987 Interaction of an Oscillating Vortex With a Turbulent Boundary Layer, *AIAA Paper 87-1246.*

WHITE, F.M. 1974 *Viscous Fluid Flow.* McGraw-Hill, New York.

Appendix A: Uncertainty Analysis

A.1 Measured Quantities

Methodology. This analysis is based on two key ingredients of an uncertainty analysis, as described by Kline and McClintock (1953). They are (1) a clearly stated confidence level for which the uncertainty interval applies, and (2) an assumption of linearly independent factors that contribute to the uncertainty. With respect to the first ingredient, all the uncertainty ranges estimated in this report will be stated at 20:1 odds, which is equivalent to a 95% confidence level. With respect to the second item, for n linearly independent sources of uncertainty, the total uncertainty can be visualized as the length of a vector in n dimensional space formed by n orthogonal vectors placed head to tail. The length of the total uncertainty vector is then just the square-root of the sum of the squares of the individual uncertainties.

Moffat (1988) simplifies the categorization of uncertainties as *bias* (fixed) and *random*. He points out that some of the fixed uncertainties actually result from slowly varying effects, but for simplicity here such uncertainties will be considered with the bias. The analysis that follows addresses uncertainties in the three phase-averaged velocities, $\langle u \rangle$, $\langle v \rangle$, and $\langle w \rangle$, the three normal stress terms, $\langle u'u' \rangle$, $\langle v'v' \rangle$, and $\langle w'w' \rangle$, and the three shear stress terms $\langle u'v' \rangle$, $\langle u'w' \rangle$, and $\langle v'w' \rangle$. For each mean velocity, the uncertainty will be calculated for two cases, a representative peak value and a representative low but significant plateau value. These values are presented in table A.1. This table also presents the cumulative results of the discussions that follow.

Bias Uncertainties. The largest fixed uncertainties in LDA measurements of velocity in this facility are (1) those in the calibration resulting from uncertainty in the beam intersection angle, (2) background electronic noise, (3) cross-

243

contamination of the three velocity component signals, and (4) frequency-voltage conversion errors in the downmixing and tracker/counter instrumentation.

Calibration Error. One significant potential source of bias in LDA measurements in this facility comes from determination of the beam intersection angle. For the w calibration, holes are burned in construction paper at several heights above the surface. While the distances are small, the height change is known quite accurately from the stepping motor controller, and the distance between burn spots is determined on a micro-positioning platform. Determination of the angle for u and v involves projecting the beams about $2m$ across the lab onto a wall. Here the distances are greater but the true center of each beam is harder to establish. The calibration constant is proportional to the wavelength of laser light and inversely proportional to the sine of the half-angle of intersection. For u and v, this angle is on the order of $2.8°$, while it is about $7.6°$ for w.

The best indictors of repeatibility and potential bias errors were obtained during the laboratory validation phase. When the two independent LDA systems were operated side by side, repeated tests indicated that the two systems agreed with each other to within about 1% of the freestream velocity. Therefore, 0.01 was used as the relative calibration bias estimator for u and v. Because of the larger crossing angle for w, its sensitivity to the same amount of error is less, about 40% of u, so 0.004 was used as the relative calibration bias estimator for w. An error in the calibration slope affects the fluctuating quantities in a similar manner, except that each must be treated as a product term. That is

$$\frac{\Delta(u'u')}{\Delta\text{slope}} = 2u'\frac{\Delta u'}{\Delta\text{slope}}. \tag{A.1}$$

Electronic Background Noise. Section 5.1 described the facility validation experiments to differentiate between electronic background noise and the true freestream turbulence of the facility. The conclusions of that study were that the down-mixing circuitry added an apparent turbulence of about 1% of the $0.7m/sec$ freestream velocity. In terms of the variance and the parameters of this experiment, this is

244

equivalent to $0.0001U_0^2$. This value was used for terms containing u' and v'. Note that the electronic noise is subtracted from the mean values and therefore does not affect them.

Cross Contamination. In a normal turbulent boundary layer, u is about 30 times larger than v. This means that a small contamination of u can totally obliterate v. Fortunately, during the adverse pressure gradient, the v component grows significantly while u decreases, so the contamination also decreases. While the alignment procedure was geared toward minimizing the cross-contamination, the optics cannot be rotated much better than about $0.5°$. This means there is a potential u contamination in v of about $0.01u$, which shows up as a significant bias in small values of v. The same potential for contamination exists with the w measurements, so the same estimate for bias was used for w.

Remaining Bias Uncertainties. The remaining bias uncertainties that have not specifically been discussed yet are those due to biases in the instrumentation, such as the repeatability of the Bragg cell frequency, the ability of trackers and counters to detect the doppler frequency, the analog to digital conversion process, and the voltage calibration slopes and offsets. The manufacturer of the LDA equipment gives an overall system accuracy of 0.4% of full scale range, which corresponds to 0.02 uncertainty on u. Calibration data indicates that the uncertainty in the analog to digital conversion process is on the order of 0.05%. While these factors were not discussed until now, they were *implicitly* included in the calibration error considered above. That was a system to system comparison, where the indication was that the uncertainty was typically 1% instead of the 2% mentioned above. In addition, these bias errors will be shown to be small in comparison to the random uncertainty that will be considered next.

Random Uncertainties. Analysis of the random uncertainty is based on an assumed statistical distribution, based on past experience, of the variable being measured. The phase-averaged *mean* values, the normal stresses, and the shear stresses each require separate treatment.

245

Mean Values. The velocity usually has a normal distribution, therefore Student's t distribution describes how to estimate the uncertainty from the measured estimate of the variance. In this case, for phase-averaged values $\langle u \rangle$, $\langle v \rangle$, and $\langle w \rangle$, the corresponding measured variance estimates are simply $\langle u'u' \rangle$, $\langle v'v' \rangle$, and $\langle w'w' \rangle$. At $20 : 1$ odds, the uncertainty interval is

$$\pm t_{n-1}(.975) \frac{s}{\sqrt{n}}. \qquad (A.2)$$

In equation A.2, s is the square-root of the measured variance and for phase-averages performed over 500 cycles, $n = 500$. The t distribution has a value of 1.98 for $n = 120$, then it approaches 1.96 as n approaches infinity. These uncertainty calculations used the value 1.98. In addition, the peak normal stress values were *not* used for this estimate because the peak usually applies over a very small portion of the data space and projects an unrealistically large uncertainty for most of the data. After viewing the data presented in chapter 7, a more realistic value for the normalized variance estimate appeared to 0.005 for all three normal stresses. Since this is about one-third the peak value of $\langle u'u' \rangle$, there are regions where the uncertainty is larger than that stated by this analysis.

Normal Stresses. Consistent with the assumption above that the variance of the velocity has a normal distribution, it follows that the variance has a χ^2 distribution. Under these conditions, Rice (1988) defines the confidence interval of the variance as

$$\frac{n\hat{\sigma}^2}{\chi^2_{n-1}(\alpha/2)} \leq \sigma^2 \leq \frac{n\hat{\sigma}^2}{\chi^2_{n-1}(1 - \alpha/2)}, \qquad (A.3)$$

where $\hat{\sigma}^2$ in this case is the estimate of the variance, $\langle u'u' \rangle$, $\langle v'v' \rangle$, or $\langle w'w' \rangle$. Since χ^2 is not a symmetrical distribution, the two values, $\chi^2_{499}(.975)$ and $\chi^2_{499}(.025)$ must each be calculated. For large values of n for which χ^2 is not tabulated, Rice gives a useful approximation

$$\chi^2_p \simeq \frac{1}{2}(z_p \pm \sqrt{2\nu - 1})^2 \qquad (A.4)$$

In equation A.4, z_p is 1.96 for the standard 20:1 odds used in this analysis.

246

Shear Stresses. The confidence interval for the shear stress is a little more complicated. While one can treat the cross-product terms as the product of two χ^2 distributed variables, a more correct approach that yields somewhat tighter intervals is given by Neter, Wasserman, and Kutner (1985). They sight a transformation by R. A. Fisher of the correlation coefficient, r_{12},

$$z' = \frac{1}{2}\ln\left(\frac{1 + r_{12}}{1 - r_{12}}\right). \tag{A.5}$$

Unlike the shear stresses, this transformed variable is approximately normal, with a variance

$$\sigma^2(z') = \frac{1}{n - 3}. \tag{A.6}$$

The confidence interval for z' at the 95% confidence level is therefore

$$\pm 1.96\sigma(z'). \tag{A.7}$$

For estimation purposes, since the $u'v'$ correlation coefficient is on the order of 0.4 across half of the boundary layer, and since the correlation coefficients of $u'w'$ and $v'w'$ approach this value in the regions where vortex generator action is significant, 0.4 is a representative value over most of the regions where the shear stress is significant. This value was transformed into a value of z' to get a confidence interval in z', and then transformed back to obtain a confidence interval of the correlation coefficient. Normalizing this interval by the original value of 0.4 yielded a relative uncertainty estimate for the shear stress terms of 0.36.

Summary. Table A.1 presents the significant numbers used in and obtained from this uncertainty analysis. Figure A.1 helps to visualize the total relative uncertainties in bar graph form. Figure A.1 and table A.1 indicate that the smallest uncertainties occur in the larger values of the mean velocities but the largest uncertainties occur in the very small values of v and w. This uncertainty is due mostly to the potential contamination by u. Fortunately, these small values mostly occur under zero pressure-gradient conditions without vortex generators, where not much interesting is happening anyway. Errors in the normal and shear stresses were

about the same for small and large values, hence only a single representative value is shown. With the exception of small values of v and w, the dominant uncertainty is random in nature.

A.2 Calculated Quantities

In general, the goal of this program was to estimate the general magnitude of various terms that describe the transport of momentum and vorticity. In contrast to many engineering studies where regressions yield engineering coefficients with a small relative uncertainty, this study required multiple derivatives of the data, a *dangerous* process which results in large uncertainty intervals. This section will attempt to place some uncertainty intervals on the computations presented in chapter 8. While the *philosophy* regarding 20:1 odds will carry over from section A.1, the attempt at statistical rigor will not. The following paragraphs summarize the general assumptions and judgements that went into the estimates of computational uncertainty.

The determination of u_τ and C_f were based on curve-fits to the $\langle u \rangle$ profiles. Curve-fits generally have a lower uncertainty than that of the individual points on the curve. As stated in chapter 8, comparison of the different methods for determination of u_τ indicated a repeatability to within about 2% to 3%. This is the basis for the uncertainty estimate for u_τ. Since C_f is computed from u_τ^2, its uncertainty is double that of u_τ.

All the remaining computations involved derivatives of the data. In all cases, a piece-wise least-squares parabolic fit of the data was obtained, and then a cubic spline was used to estimate the slope. The curve fit should generally be better than the uncertainty in the individual points on the curve, but because of the variety of curves fit, no improvement was assumed here. To test the uncertainty in the spline determination of derivatives, the spline was tested agai⌐st a rather *nasty* non-polynomial curve representative of the shear stress profiles. The spline showed

248

a worst-case deviation of about 10% from the analytical slope, so 10% was added to the uncertainty of each velocity first-derivative. For subsequent derivatives of the velocity and for *both* derivatives of $\langle u'v' \rangle$, various manipulations of the data seemed to indicate that it was more appropriate to *double* the uncertainty with each operation. Finally, computational products were treated according to the standard practice square-root of the sum of the squares. The resulting estimates are summarized in table A.2.

Table A.1 Estimates of Measurement Uncertainty

	Value	Calibration		Contam./Bkd.		Random		Total	
		Abs.	Rel.	Abs.	Rel.	Abs.	Rel.	Abs.	Rel.
$\langle U \rangle$	1.0E-1	1.0E-3	1.0E-2	0.0	0.0	6.2E-3	6.2E-2	6.3E-3	6.3E-2
$\langle U \rangle$	1.0	1.0E-2	1.0E-2	0.0	0.0	1.1E-2	1.1E-2	1.5E-2	1.5E-2
$\langle V \rangle$	3.0E-2	3.0E-4	1.0E-2	1.0E-2	3.3E-1	6.2E-3	2.1E-1	1.2E-2	3.9E-1
$\langle V \rangle$	1.5E-1	1.5E-3	1.0E-2	1.0E-2	6.7E-2	1.1E-2	7.2E-2	1.5E-2	9.8E-2
$\langle W \rangle$	3.0E-2	1.2E-4	4.0E-3	1.0E-2	3.3E-1	6.2E-3	2.1E-1	1.2E-2	3.9E-1
$\langle W \rangle$	5.0E-2	2.0E-4	4.0E-3	1.0E-2	2.0E-1	1.1E-2	2.1E-1	1.5E-2	2.9E-1
$\langle u'u' \rangle$	1.5E-2	3.0E-4	2.0E-2	5.0E-5	3.3E-3	3.7E-3	2.5E-1	3.7E-3	2.5E-1
$\langle v'v' \rangle$	1.5E-2	3.0E-4	2.0E-2	5.0E-5	3.3E-3	3.7E-3	2.5E-1	3.7E-3	2.5E-1
$\langle w'w' \rangle$	1.5E-2	3.0E-4	2.0E-2	5.0E-5	3.3E-3	3.7E-3	2.5E-1	3.7E-3	2.5E-1
$\langle u'v' \rangle$	2.5E-3	5.0E-5	2.0E-2	5.0E-5	2.0E-2	9.1E-4	3.6E-1	9.1E-4	3.6E-1
$\langle u'w' \rangle$	5.0E-3	1.0E-4	2.0E-2	5.0E-5	1.0E-2	1.8E-3	3.6E-1	1.8E-3	3.6E-1
$\langle v'w' \rangle$	2.5E-3	5.0E-5	2.0E-2	5.0E-5	2.0E-2	9.1E-4	3.6E-1	9.1E-4	3.6E-1

Table A.2 Estimates of Computational Uncertainty

| Quantity	Uncertainty
u_τ	3%
C_f	5%
$\langle \omega_x \rangle$	25% − 50%
$\langle \omega_z \rangle$	10%
$\langle v \rangle \langle \omega_z \rangle_{,y}$	22% − 45%
$\langle \omega_z \rangle_{,yy}$	40%
$\langle u'v' \rangle_{,yy}$	100%
$\langle uv \rangle_{,y}$	20% − 40%

Relative Uncertainty in Measurements
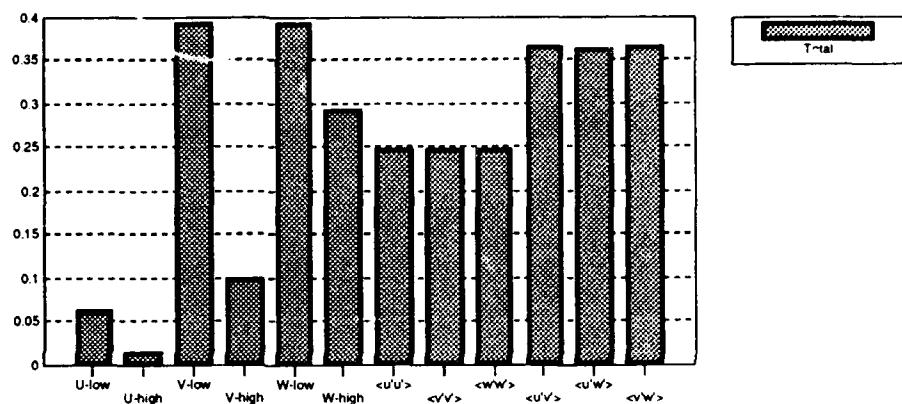
Figure A.1 Relative uncertainty in measurements